

# Quantum computation in solid-state systems

INAUGURALDISSERTATION

zur

Erlangung der Würde eines Doktors der  
Philosophie

vorgelegt der

Philosophisch-Naturwissenschaftlichen Fakultät

der Universität Basel

von

Bence Hetényi

Basel, 2022

Originaldokument gespeichert auf dem Dokumentenserver der Universität Basel  
[edoc.unibas.ch](http://edoc.unibas.ch)



Dieses Werk ist unter dem Vertrag „Creative Commons Namensnennung-Keine  
kommerzielle Nutzung-Keine Bearbeitung 2.5 Schweiz“ lizenziert. Die vollständige Lizenz  
kann unter

[creativecommons.org/licences/by-nc-nd/2.5/ch](http://creativecommons.org/licences/by-nc-nd/2.5/ch)  
eingesehen werden.

Genehmigt von der Philosophisch-Naturwissenschaftlichen  
Fakultät auf Antrag von

Prof. Dr. Daniel Loss

Prof. Dr. Jelena Klinovaja

Prof. Dr. Oded Zilberberg

Basel, 21. Juni 2022

Prof. Dr. Marcel Mayor  
Dekan

# Summary

In the last few years, as superconducting devices reached tens and later hundred qubits on a single chip, quantum computing has become a reality [1,2], tackling problems that would be prohibitively time-consuming even with the most powerful classical supercomputers. These early quantum computers (QC) are called noisy intermediate-scale quantum computers, since environmental noise cannot be efficiently counteracted in such small qubit arrays. While certain algorithms can indeed leverage the potential of hundreds of imperfect qubits [3], the great promises of quantum computing require perfect qubits that can be realized only in qubit arrays of much larger scales, using quantum error correction (QEC) [4,5].

Spin qubits in semiconductors [6,7] are the only platform to date that has the potential of reaching such scales, paving way for fault-tolerant quantum computing. Qubits hosted in quantum dots (QDs) [6] have dimensions of few tens of nanometers, facilitating the integration of potentially millions of qubit on a single chip. Especially compelling candidates are spin qubits in silicon nanostructures. With decades of experience coming from the semiconductor industry, silicon is one of the most studied elements with the prosperity of uniquely advanced manufacturing techniques.

Electron spin qubits in silicon have immensely matured in the last few years reaching single- and two-qubit gate fidelities matching the error thresholds of QEC algorithms [8, 9]. However, the weak intrinsic spin-orbit interaction (SOI) in the conduction band necessitates the use of micromagnets to aid the all-electrical qubit control. This additional complication presents new challenges in device design and fabrication. Hole spin qubits in silicon and germanium QDs, on the other hand, benefit from strong direct Rashba SOI [10] accelerating qubit control speeds to several hundreds of megahertz [11,12], without the need to integrate additional elements in the device.

In this thesis, we start with an introduction and a brief overview of

the field, in Chapter 1, where we discuss the fundamental physics of hole quantum dots and how they satisfy the stringent prerequisites of quantum computing. Furthermore, we take a glimpse at the various components of scalable architectures and the requirements on the qubit architecture posed by QEC codes. In the subsequent chapters we address the question how the enhanced anisotropy and SOI affect two-qubit gates in hole QDs. In particular, we discuss exchange anisotropy due to orbital effects of the magnetic field and crystalline anisotropy in Chapter 2. We also confirm the emergence of the zero-field splitting of triplet states in hole QDs numerically, and develop an analytical model linking the effect to the cubic Rashba SOI in Chapter 3. This work presents the first theoretical model to explain this recently observed effect in hole QDs [13]. Afterwards, in collaboration with the Zumbühl lab, we decipher the strong spin-orbit effects in an experiment on Ge/Si nanowire QDs, where we also identify the strong  $g$  factor renormalization caused by enhanced SOI (Chapter 4). Furthermore, we study the tunability of SOI in silicon FinFET devices in Chapter 5, identifying sweet spots where the qubit lifetime is greatly prolonged. Finally, we study the prospects of coupling distant spin qubits by a chiral magnon mode localized at the edge of a two-dimensional ferromagnet in Chapter 6.



# Contents

<b>Contents</b>	<b>v</b>
<b>1 Introduction</b>	<b>1</b>
1.1 Holes in group-IV semiconductors . . . . .	1
1.2 Single-qubit control . . . . .	5
1.3 Two-qubit gates . . . . .	9
1.4 Initialization and readout . . . . .	14
1.5 Decoherence . . . . .	17
1.6 Scalability . . . . .	22
1.7 Quantum error correction on scalable spin qubit arrays . .	25
1.A Details of the particle density calculation in a double QD .	27
<b>Bibliography</b>	<b>29</b>
<b>2 Exchange interaction of hole-spin qubits in double quantum dots</b>	<b>42</b>
2.1 Introduction . . . . .	43
2.2 Single hole-spin qubit . . . . .	45
2.3 Symmetry considerations . . . . .	47
2.4 Low-energy basis of a DQD . . . . .	51
2.5 Low-energy Hamiltonian of a DQD . . . . .	52
2.6 Coupled hole-spin qubits in silicon NWs . . . . .	53
2.7 Discussion . . . . .	61
2.8 Conclusion . . . . .	63
2.A Magnetic field along an $N$ -fold symmetry axis, generaliza- tion of Bloch's theorem . . . . .	63
2.B Lowest-energy Kramers doublet . . . . .	65
2.C Conservation of the effective spin . . . . .	66
2.D Orthonormalization method . . . . .	67
2.E Single-particle basis for the numerics . . . . .	70
2.F $S_{01}$ as a figure of merit for the effective spin mixing . . . .	71

2.G	Slow $\sqrt{\text{SWAP}}$ gates and anisotropy-limited fidelity . . . . .	74
2.H	Comparison of the exchange interaction between silicon and Ge/Si core/shell NWs . . . . .	76
<b>Bibliography</b>		<b>78</b>
<b>3</b>	<b>Zero-field splitting in Si and Ge quantum dots</b>	<b>85</b>
3.1	Introduction . . . . .	86
3.2	Analytical theory . . . . .	87
3.3	Numerics . . . . .	91
3.4	Conclusions . . . . .	94
3.A	Zero-field splitting induced by cubic spin-orbit interaction	94
3.B	Details of the numerical calculation . . . . .	102
3.C	Symmetry analysis of the triplet degeneracy . . . . .	108
<b>Bibliography</b>		<b>111</b>
<b>4</b>	<b>Strong spin-orbit interaction and <math>g</math>-factor renormalization</b>	<b>119</b>
4.1	Introduction . . . . .	120
4.2	Device and measurement setup . . . . .	123
4.3	Double quantum dot and Pauli spin blockade . . . . .	124
4.4	Lifting of Pauli Spin Blockade . . . . .	125
4.5	Possible Spin-mixing mechanisms . . . . .	126
4.6	Model of the two transitions . . . . .	128
4.7	Varying the strength of interdot tunnel coupling . . . . .	132
4.8	Spin-orbit length . . . . .	134
4.9	Conclusions and outlook . . . . .	136
4.A	Model Hamiltonian . . . . .	137
4.B	Double-dot Hamiltonian . . . . .	141
4.C	Singlet-Triplet basis . . . . .	143
<b>Bibliography</b>		<b>146</b>
<b>5</b>	<b>Fully tunable spin-orbit interaction in Si FinFETs</b>	<b>152</b>
5.1	Introduction . . . . .	153
5.2	Theoretical Model . . . . .	155
5.3	Equilateral FinFETs . . . . .	159
5.4	Effect of the SOHs . . . . .	167
5.5	Suppressing charge noise in FinFET Qubits . . . . .	169
5.6	Conclusion . . . . .	173
5.A	Electric field simulation . . . . .	174
5.B	Orbital eigenstates . . . . .	175
5.C	Spin-orbit interaction in perturbation theory . . . . .	176
5.D	Spin-orbit coupling against $\delta E_{ii}$ . . . . .	186
5.E	Effect of strain . . . . .	187
5.F	Compensating for the SOHs . . . . .	190

<b>Bibliography</b>	<b>209</b>
<b>6 Long-distance coupling of spin qubits via topological magnons</b>	<b>219</b>
6.1 Introduction . . . . .	220
6.2 Theory . . . . .	222
6.3 Results . . . . .	233
6.4 Qubit entanglement via chiral magnon transduction . . . .	242
6.5 Discussion . . . . .	246
6.6 Conclusion . . . . .	247
6.A Conventions . . . . .	248
6.B Effective qubit-magnon coupling: analytical formulas . . .	249
6.C Including spectral broadening in the Schrieffer-Wolff trans- formation . . . . .	251
6.D Effective qubit-qubit coupling . . . . .	254
6.E Decoherence . . . . .	258
6.F Exchange interaction — Analytical formulas . . . . .	261
6.G Dipole-dipole interaction analytical formulas . . . . .	262
<b>Bibliography</b>	<b>267</b>

# CHAPTER 1

## Introduction

In this Chapter we revisit the basic requirements for quantum computation with spin qubits, focusing on the already achieved milestones in hole-spin qubits and the challenges on the road ahead. We will keep returning to the importance of spin-orbit interaction (SOI) as it is a crucial element of the spin manipulation and readout techniques, but also have a prominent effect on the two-qubit operations and lead to decoherence channels, setting a trade-off between fast operations and information loss time scales.

Many of the frameworks used for quantum computing with spin qubits [6] have been developed with the focus on electron spin qubits. As it will be shown in Section 1.1, the low-energy physics of hole quantum dots (QDs) share some of the key properties with that of electrons. Therefore in most sections of this introduction, electrons and holes (referred to as particles) will be treated on the same footing, and only the pivotal qualitative and quantitative differences between electrons and holes are discussed.

### 1.1 Holes in group-IV semiconductors

In this section we first consider the band structure of group-IV semiconductors, e.g., silicon or germanium, then we discuss the effect of various external fields. In particular the effect of magnetic and electric fields, as well as strain in the top of the valence bands is discussed.

The structure of the valence bands in semiconductors with a diamond lattice, can be understood in the tight binding picture. While the states of the conduction band have  $s$  like wavefunctions (with orbital angular momentum  $l = 0$ ), the valence bands consist of three degenerate  $p$  type wavefunctions ( $l = 1$ ). Since the two basis atoms each reside in an inversion asymmetric (tetrahedral) position, spin-orbit interaction splits up the 6 states with  $l = 1$  and  $s = 1/2$  as

$$1_l \otimes \frac{1}{2}_s = \frac{3}{2}_{\text{HH-LH}} \oplus \frac{1}{2}_{\text{SO}}, \quad (1.1)$$

where the heavy- and light-hole (HH and LH) bands are degenerate at the  $\Gamma$  point ( $\mathbf{k} = 0$ ) of the Brillouin zone with a total angular momentum  $j = 3/2$ . The spin-orbit splitt-off bands (SO) with  $j = 1/2$  have a lower energy than the former two pairs of bands. The elementary unit cell in a diamond lattice is a cube that contains two atoms that are located at  $1/4$  and  $3/4$  of the body diagonal of a cube, respectively. Therefore the elementary unit cell is inversion symmetric, implying no spin splitting in the band structure at finite momentum, i.e., every band is doubly degenerate throughout the Brillouin zone.

Due to the cubic symmetry of the Bravais lattice, the valence bands can be described by a few parameters at zero magnetic field. Here we restrict our attention to the case of the HH and LH bands since these are the ones hosting the lowest energy hole excitations. This model is commonly referred to as the Luttinger-Kohn model [14, 15] with the Hamiltonian

$$H_{LK} = \frac{\hbar^2}{2m_e} \left[ \left( \gamma_1 + \frac{5}{2}\gamma_2 \right) k^2 - 2\gamma_2 (k_x^2 J_x^2 + c.p.) - 4\gamma_3 (\{k_x, k_y\} \{J_x, J_y\} + c.p.) \right], \quad (1.2)$$

where  $m_e$  is the vacuum electron mass,  $\gamma_i$  are the (dimensionless) Luttinger parameters, and  $k_i$  are the momenta along the  $\langle 100 \rangle$  crystallographic axes. Moreover,  $\hbar J_i$  is the  $i$ th component of the atomic angular momentum operator in the spin-3/2 subspace, i.e., where  $J^2 = 3/2(3/2 + 1)$ , the anticommutator is defined as  $\{A, B\} = (AB + BA)/2$ , and  $c.p.$  denotes cyclic permutations. Note that, since conduction bands are not included explicitly in Eq. (1.2), we can use the convention that holes have positive energy.

Later on we will include the effect of the QD confinement and define a qubit basis based on the lowest-energy eigenstates of the hole-QD. In order to split the degeneracy of the lowest pair of eigenstates, we will

need the Zeeman interaction in the HH and LH bands. This also acquires an anisotropic correction and reads

$$H_Z = 2\mu_B\kappa\mathbf{B} \cdot \mathbf{J} + 2\mu_Bq(B_xJ_x^3 + c.p.), \quad (1.3)$$

where  $\kappa$  and  $q$  are the coefficients of the isotropic and anisotropic terms with typically  $\kappa \gg q$  and  $B_i$  are the magnetic field component along the  $\langle 100 \rangle$  directions. Here we neglected the orbital effects of the magnetic field for simplicity, but we will account for this correction in Chapter 2 where this contribution have a qualitative effect on the exchange anisotropy, and also in Chapter 4 where the strength of the applied magnetic field lead to clearly observable effects on the g-factor renormalization.

The contribution of the electric field is twofold. Its homogeneous part, i.e.,  $H_E = -e\mathbf{E} \cdot \mathbf{r}$  breaks inversion symmetry, giving rise to Rashba spin-orbit interaction, while its gradient, e.g.,  $-e(\partial_z E_z)z^2/2$ , will be used later for the confinement of the QD. Furthermore, we discuss how the strain enters the Hamiltonian of holes. The strain term, also called Bir-Pikus Hamiltonian [82], can be written as

$$H_{BP} = \left( -D_d + \frac{5}{6}D_u \right) \text{tr}\epsilon - \frac{2}{3}D_u(\epsilon_{xx}^2 J_x^2 + c.p.) - \frac{4}{3}D'_u(\epsilon_{xy}\{J_x, J_y\} + c.p.), \quad (1.4)$$

where  $\epsilon_{ij}$  are the components of the strain tensor and the deformation potentials  $D_d$ ,  $D_u$ , and  $D'_u$  are of the order of electronvolts. As opposed to the conduction band at  $\mathbf{k} = 0$ , where strain only enters via the renormalization of the fundamental bandgap, for holes it mixes different angular momenta leading to rich new physics.

Both the Luttinger-Kohn and the Bir-Pikus Hamiltonians in Eqs. (1.2) and (1.4) can be interpreted via the directionality of the  $p$  like atomic wavefunctions. The hopping strength (i.e., the momentum term) could vary if the electron is hopping from a site with  $p_i$  to a neighbouring site with a different  $p_j$  atomic wavefunction. Similarly, the  $p$  orbitals are more sensitive to the direction of deformation (i.e., the strain term), as there is a difference whether the  $p_i$  orbital is compressed along its axis or perpendicular to it. All these issues are absent in the mesoscopic physics of conduction electrons as their atomic wavefunction is of  $s$  type that is lacking such an orientation dependence.

It is in general hard to find the exact eigenvalues and eigenvectors of Eq. (1.2) due to the mixing of different momentum and angular momentum components. One example where such a solution is known is when

$\gamma_2 = \gamma_3$  and the last two terms of Eq. (1.2) can be written as  $-2\gamma_2(\mathbf{k} \cdot \mathbf{J})^2$ , that is the *spherical approximation* (or *axial approximation* in the presence of a magnetic field). This approximation is expected to perform well for germanium where  $(\gamma_3 - \gamma_2)/(\gamma_3 + \gamma_2) \sim 10\%$  [17], and is particularly useful in systems where the confinement of the holes has a cylindrical symmetry [18,19], like in the case of Ge/Si core/shell nanowires where the holes are confined in the cylindrically symmetric germanium core. However, it should be kept in mind that the neglected anisotropic corrections can lead to important qualitative effects.

### Elongated hole quantum dots

In order to describe the low-energy physics of holes confined in a QD, we need to extend the Hamiltonian  $H_{LK} + H_Z + H_E + H_{BP}$  with the effect of confinement. This is usually done either by considering hardwall boundary conditions at some interfaces, or by applying a harmonic confinement. While the former approach is suitable to describe the effect of bandgap mismatch between two semiconductors or a semiconductor-oxide interface, the latter is a better approximation for the smooth confinement provided by electrostatic gates. In quasi-2D systems there is one strong axis of confinement, e.g., in a two-dimensional electron/hole gas realized in a semiconductor sandwich structure, where electrostatic gates are used to confine a QD in the in-plane directions. Another approach is taking a nanowire, where the confinement is only provided by gates along the wire direction. Herein we will focus on this latter case.

Here we briefly discuss a way to describe quasi one-dimensional systems with a harmonic potential along the axis of weak confinement (the  $z$  axis). The total Hamiltonian can be written as

$$H_{\text{QD}} = H_0 + H_1 k_z + H_2 k_z^2 + V, \quad (1.5)$$

where the four terms are

$$H_0 = H_{LK}|_{k_z=0} + H_Z + H_E^{x,y} + H_{BP}, \quad (1.6a)$$

$$H_1 = \partial_{k_z} H_{LK}|_{k_z=0}, \quad (1.6b)$$

$$H_2 = \frac{1}{2} \partial_{k_z}^2 H_{LK}|_{k_z=0}, \quad (1.6c)$$

$$V = -eE_z z + \frac{\hbar^2 \gamma_1}{2m_e L_z^4} z^2, \quad (1.6d)$$

with  $m_e/\gamma_1$  being the average HH-LH mass and  $L_z$  is the harmonic confinement length [20]. Using the lowest-energy eigenstates  $|m\rangle$  of  $H_0$  with energy  $\varepsilon_m$ , one can project the Hamiltonian into a few transversal subbands as

$$H_{\text{QD}}^{mn} = \varepsilon_m \delta^{mn} + H_1^{mn} k_z + H_2^{mn} k_z^2 - eE_z \delta^{mn} z + \frac{\hbar^2 \gamma_1}{2m_e l_z^4} \delta^{mn} z^2, \quad (1.7)$$

where the coupling between the subbands is given by powers of  $k_z$ . Finally, accounting for higher subbands perturbatively, we write the effective Hamiltonian of the lowest two subbands as

$$H_{\text{eff}} = \frac{\hbar^2 k_z^2}{2m^*} + \frac{1}{2} g \mu_B B \sigma_z + \hbar k_z \mathbf{v}_{so} \cdot \boldsymbol{\sigma} - eE_z z + \frac{\hbar^2}{2m^* l_z^4} z^2 + \mathcal{O}(k_z^3), \quad (1.8)$$

where  $g \mu_B B = \varepsilon_2 - \varepsilon_1$  is the qubit splitting, the Pauli matrices  $\sigma_i$  act on the subband or ‘spin’ degrees of freedom, and the effective mass  $m^*$  in the first term incorporates corrections of higher subbands. Moreover, the confinement length  $l_z$  is now defined with the effective mass as  $l_z = L_z(m_e/m^* \gamma_1)^{1/4}$ , and the effective spin-orbit term  $\hbar k_z \mathbf{v}_{so} \cdot \boldsymbol{\sigma}$  is simply the projection of  $H_1 k_z$  to the subspace of  $|m\rangle \in \{|1\rangle, |2\rangle\}$ . This approach will be used in Chapter 3 and 5 to treat the linear- and cubic Rashba SOI, respectively. This consideration also allows us in the following sections to discuss the requirements for hole-spin qubits to be used for quantum computing in a simple way.

A qubit can be encoded in the lowest spin-doublet eigenstates of the Hamiltonian (1.8) and the qubit splitting is controlled by the strength of the Zeeman term  $\Delta_z = g \mu_B B$ . In the absence of spin-orbit interaction, the qubit basis states are simply product states of the harmonic oscillator ground state and the eigenstates of  $\sigma_z$ , i.e.,  $|0\rangle \equiv |\uparrow\rangle$  and  $|1\rangle \equiv |\downarrow\rangle$ . When the SOI term is nonzero, spin-qubits can still be defined, but the spin and orbital degrees of freedom are not be separable any more.

## 1.2 Single-qubit control

In order to perform the single-qubit rotations required for universal quantum computing, rotations of the spin around two perpendicular axes need to be achieved. The concept to achieve such rotations originates from the electron spin-resonance (ESR) experiments [21]. In a homogeneous magnetic field, the spin undergoes the Larmor precession around the axis of the magnetic field. If the precessing spin is exposed to a



transversal ac magnetic field oscillating with a frequency that matches the precession frequency  $\omega_L$ , the spin will also rotate continuously around the axis of the oscillating field. The latter rotation is referred to as Rabi oscillation [22].

Even though, two-axis control might seem to be straightforward to achieve using static and alternating magnetic fields, both of these mechanisms are obstructed by the low temperatures, the small size of the QDs, and the requirement of individual qubit control in a multi-qubit system. The spin rotation due to Larmor precession only requires a static magnetic field, however, the Zeeman field  $\Delta_z$  would need to be controlled individually for each qubit to induce a relative phase difference between them. Changing the strength of the magnetic field  $B$  over tens of nanometers is challenging, especially since fast temporal switching would be required to induce precise relative phase shifts from qubit to qubit. This problem can be circumvented by electrical tunability of the  $g$  factor [23–25], as it will be shown later.

Oscillating magnetic fields are also unfavorable since fast qubit drive would require strong ac currents in close proximity to the qubits [6, 26]. The heat dissipation of such alternating currents can have a detrimental effect on the low-temperature physics of the QD. Fortunately, spin-orbit interaction offers a solution to this problem by translating the effect of an ac electric field to oscillations of the spin degree of freedom [27, 28].

In order to obtain a simple picture how all-electrical control is realized, let us consider a simple model with strong confinement along  $x$  and  $y$ , and harmonic confinement along the  $z$  direction. We include a static transversal electric field  $E_y$  entering the effective Hamiltonian (1.8) as a Rashba spin-orbit term, and an ac electric field along the confinement direction, shaking the QD as

$$H_{\text{eff}} = \frac{\hbar^2 k_z^2}{2m^*} + \frac{\hbar^2}{2m^* l_z^4} z^2 + \frac{1}{2} g \mu_B B \sigma_z + \alpha E_y k_z \sigma_x - e E_{z,0} z \cos(\omega_{\text{ac}} t), \quad (1.9)$$

where  $\alpha$  is the coefficient of the Rashba SOI, corresponding to a spin-orbit vector of  $\mathbf{v}_{so} = \hbar^{-1} \alpha E_y \hat{\mathbf{x}}$  in Eq. (1.8), and  $E_{z,0}$  is the amplitude of the oscillating electric field. Writing the momentum and the  $z$  coordinate in terms of harmonic oscillator creation and annihilation operators  $a$  and  $a^\dagger$ , we get

$$H_{\text{eff}} = \Delta_{\text{orb}} a^\dagger a + \frac{1}{2} \Delta_z \sigma_z + i t_{so} (a^\dagger - a) \sigma_x + \mathcal{E}_z \cos(\omega_{\text{ac}} t) (a^\dagger + a), \quad (1.10)$$

where  $\Delta_{\text{orb}} = \hbar^2/m^*l_z^2$  is the orbital splitting,  $\Delta_z = g\mu_B B$  is the Zeeman energy,  $t_{so} = \alpha E_y/\sqrt{2}l_z$  is the spin-orbit coupling strength, and  $\mathcal{E}_z = -eE_{z,0}l_z/\sqrt{2}$ . In order to find the lowest order contribution of SOI to the Zeeman field and the oscillating transversal Zeeman field needed for the two-axis qubit control, we consider two orbital levels and perform second order perturbation theory. The effective qubit Hamiltonian then reads

$$H = \frac{1}{2}\tilde{\Delta}_z\sigma_z + \nu_0 \cos(\omega_{\text{ac}}t)\sigma_x, \quad (1.11)$$

with the coefficients being

$$\tilde{\Delta}_z = \Delta_z \left( 1 - 2\frac{t_{so}^2}{\Delta_{\text{orb}}^2} \right), \quad (1.12a)$$

$$\nu_0 = \frac{\mathcal{E}_z t_{so} \Delta_z}{\Delta_{\text{orb}}^2}, \quad (1.12b)$$

where we assumed  $\mathcal{E}_z, t_{so}, \Delta_z \ll \Delta_{\text{orb}}$ . Even from this simplistic model, it is apparent that SOI facilitates the replacement of both the local static magnetic field and the ac magnetic field required for ESR, by static and alternating electric fields that are more compatible with low temperatures and the small feature size of semiconductor devices.

For small Zeeman splitting  $\Delta_z$  and spin-orbit interaction  $t_{so}$  Eq. (1.12a) yields a correction to the qubit splitting that is proportional to the Zeeman splitting. As long as the splitting of the qubit levels is linear in the magnetic field, the effect of SOI is a small electric field dependent renormalization of the  $g$  factor,  $g \rightarrow \tilde{g}(E_y)$ . This small renormalization is already enough for selective qubit phase control. By changing their  $g$  factor for a certain time period, a relative phase is assigned to the corresponding qubit. The electrical tunability of the  $g$  factor has been observed in several experiments by now providing means of accomplishing phase gates, and also individual qubit addressability for the Rabi drive [23–25]. When the magnetic field is not small any more, orbital effects of the magnetic field can enter the  $g$  factor via SOI making it dependent on the magnetic field strength [29, 30]. Furthermore, for holes where the SOI strength can be profoundly strong, the renormalization of the  $g$  factor is not perturbative but depends exponentially on the magnetic field, as it will be shown in Chapter 4.

The strength of the oscillating coupling in Eq. (1.12b) determines the rotation frequency of the qubit along an axis perpendicular to the static Zeeman field. Due to the electric dipole moment  $el_z/\sqrt{2}$  involved in the

process, the SOI-assisted ESR is commonly referred to as electric-dipole spin resonance (EDSR) [27, 31]. Other than being linearly dependent on the electric fields and the Zeeman splitting, the driving strength  $\nu_0$  in Eq. (1.12b) depends strongly on the effective mass and the QD length, i.e.,  $\nu_0 \propto l_z^4$ . Therefore elongating the QD along the direction of the drive is a key to achieve fast Rabi oscillations [27, 31]. The EDSR mechanism has been used in recent experiments on hole QDs in germanium, to induce the fastest Rabi oscillations to date [11, 12], the success of which relies on the strong direct Rashba SOI of holes [10].

Besides EDSR, another alternative to obtain an effective oscillating magnetic field is to electrically modulate the anisotropy of the  $g$  tensor [32]. If the qubit Zeeman splitting can be written as  $\Delta_Z^0 = \mathbf{B} \cdot \hat{\mathbf{g}}(V_0)$ , where  $\hat{\mathbf{g}}$  is the  $g$  tensor that depends on the gate voltage  $V_0$ , small changes in the gate voltage lead to a change in the Zeeman field  $\delta\Delta_Z = \mathbf{B} \cdot \partial_V \hat{\mathbf{g}}(V_0) dV$ . However, due to the change of anisotropy in the  $g$  tensor, the modulation of the Zeeman field –as opposed to Eq. (1.12a)– can have two components e.g.,  $\delta\Delta_Z = \delta\Delta_Z^{\parallel} + \delta\Delta_Z^{\perp}$ . If a periodic drive is applied to the gate voltage with a frequency  $|\Delta_Z^0|/\hbar$ , the perpendicular Zeeman field component  $\delta\Delta_Z^{\perp}$  acts as a transversal oscillating field that is needed for the coherent spin rotations.

We have seen two ways to connect the oscillating magnetic field of the ESR experiment to oscillating electric fields that are more compatible with further requirements of QD systems. However, as opposed to the ESR experiments –where the emphasis is on the population difference between spin-up and spin-down electrons in an ensemble– for single qubit control it is profoundly important how accurately one can flip the spin state of a single particle [26]. Therefore, it is worthwhile to take a closer look at the dynamics of a single spin subjected to a resonant transversal field.

## The rotating wave approximation

Here we consider the time-evolution under the Hamiltonian with a periodically modulated coupling of Eq. (1.11) [33]. Taking the state  $|\psi\rangle = U(t)|\tilde{\psi}\rangle$  the Schrödinger equation can be written as

$$\begin{aligned} \frac{d}{dt} |\tilde{\psi}\rangle &= -\frac{i}{\hbar} \left( U^\dagger H U - i\hbar U^\dagger \dot{U} \right) |\tilde{\psi}\rangle \\ &= -\frac{i}{\hbar} \tilde{H} |\tilde{\psi}\rangle \end{aligned} \tag{1.13}$$

where the unitary transformation is chosen such that the frame is rotating around the quantization axis by the frequency of the oscillating coupling, i.e.,  $U(t) = \exp(-i\omega_{\text{ac}}t\sigma_z/2)$ . In this case the Hamiltonian in the rotating frame reads as

$$\tilde{H} = \frac{1}{2}(\Delta_z - \hbar\omega_{\text{ac}})\sigma_z + \frac{1}{2}\nu_0[1 + \cos(2\omega_{\text{ac}}t)]\sigma_x + \frac{1}{2}\nu_0\sin(2\omega_{\text{ac}}t)\sigma_y, \quad (1.14)$$

where the rapidly oscillating terms can be neglected if  $\Delta_z/\hbar - \omega_{\text{ac}}, \nu_0/\hbar \ll 2\omega_{\text{ac}}$ . This approximation is referred to as the rotating wave approximation with

$$H_{\text{RWA}} = \frac{1}{2}(\Delta_z - \hbar\omega_{\text{ac}})\sigma_z + \frac{1}{2}\nu_0\sigma_x. \quad (1.15)$$

If the ac drive is resonant with the qubit frequency, i.e.,  $\Delta_z/\hbar = \omega_{\text{ac}}$ , the total time evolution of the qubit state then includes coherent rotations of the spin state around the  $x$  axis on top of the usual Larmor precession as  $|\psi(t)\rangle = \exp(-i\Delta_z t\sigma_z/2\hbar) \exp(-i\nu_0 t\sigma_x/2\hbar) |\psi(0)\rangle$ , where  $|\psi(0)\rangle = |0\rangle$ . This driven rotation of the spin state provides a spin-flip time of  $t_{\text{op}} = \hbar/2\nu_0$  that is the operation time of the single-qubit gate  $X$ .

The exact time evolution is illustrated in Fig. 1.1(a)-(b) for weak drive ( $\nu_0/\Delta_z = 0.01$ ), where the RWA is a very good approximation, and for  $\nu_0/\Delta_z = 0.2$ , where the effect of the counter-rotating terms is not negligible any more. The plotted quantity is the expectation value of the polarization operator  $(1 + \sigma_z)/2$ , that is unity for the state  $|0\rangle$  and zero for  $|1\rangle$ . The small modulation on top of the sinusoidal oscillations in Fig. 1.1(b) seems harmless at first, but have serious implications on the qubit-flip probability. Namely, after time  $t_{\text{op}}$ , the state does not end up exactly in the other qubit basis state  $|1\rangle$ . This effect can be interpreted as a gate error and is shown as a function of coupling strength in Fig. 1.1(c). It should be also noted that the drive cannot be switched on abruptly, and the pulse shape can also have a negative effect on the overall gate fidelity. These issues have been addressed by Zeuch *et al.*, where it is shown that the imperfect time-evolution can be corrected by considering  $1/\Delta_z$  corrections to the RWA [34].

### 1.3 Two-qubit gates

Two-qubit gates are essential parts of a quantum computer, since they are used to establish entanglement between qubit states. Depending on their

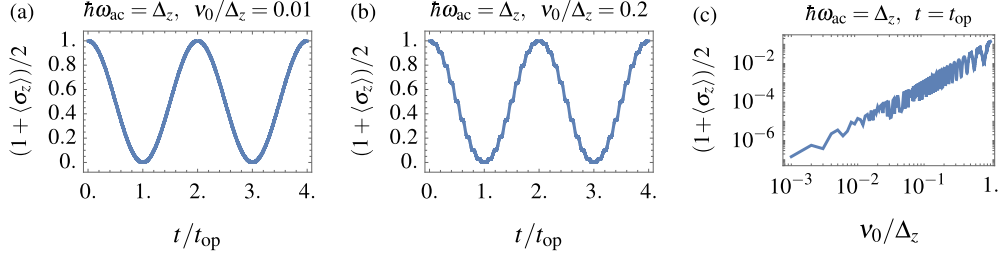


Figure 1.1: (a)-(b) polarization of the state  $|\psi(t)\rangle$  during the exact time-evolution according to Eq. (1.13) with resonant drive, starting from the state  $|\psi(0)\rangle = |0\rangle$ . (c) Spin-flip fidelity, i.e., qubit polarization at  $t = t_{\text{op}}$ , as a function of driving strength  $\nu_0/\Delta_z$ .

role in the quantum architecture one can distinguish short- and long-range entangling gates. Short-ranged two-qubit gates connect neighbouring qubits in the array, while long-range gates can act as coherent links between dense-qubit arrays [35], that are discussed in more detail in Section. 1.6. Spin qubits offer a natural way to realize entanglement between neighboring qubits, that is the inter-dot *exchange interaction* between tunnel-coupled QDs.

For example, the eigenstates of two decoupled qubits  $|\uparrow\downarrow\rangle$  and  $|\downarrow\uparrow\rangle$  are degenerate if the  $g$  factors are identical. As the shape of QDs is adjusted by electrostatic gates, a tunnelling channel opens between QDs facilitating overlap between the wavefunctions of the two particles. Owing to Pauli's exclusion principle, the spin triplets, i.e.,  $(|\uparrow\downarrow\rangle + |\downarrow\uparrow\rangle)/\sqrt{2}$ , need to be paired with an antisymmetric orbital wavefunction, while the spin singlet, i.e.,  $(|\uparrow\downarrow\rangle - |\downarrow\uparrow\rangle)/\sqrt{2}$ , has a symmetric orbital part that is lower in energy [36]. In this simple case, where we have assumed that the wavefunction can be written as a product of orbital and spin parts, the low-energy dynamics of the system is described by the Heisenberg Hamiltonian

$$H_H = \frac{J}{4} \boldsymbol{\sigma}_1 \cdot \boldsymbol{\sigma}_2 \quad (1.16)$$

where  $J$  is the exchange splitting, separating the singlet from the triplets, and  $\boldsymbol{\sigma}_i$  is the vector of Pauli matrices acting on the  $i$ th qubit. The time evolution according to the static Heisenberg Hamiltonian of Eq. (1.16) for a time  $t = \hbar/4J$  results in a  $\sqrt{\text{SWAP}}$  operation on the qubit. This is an entangling gate which can be used to construct a controlled-NOT gate [6], that is required by some of the most potent quantum error correction algorithms (see Section 1.7).

In order to find a model that correctly describes the low-energy behavior of our coupled-QD system, we assume that switching on the Coulomb interaction between the two particles does not change the two-particle ground state<sup>1</sup>. In this case one can write down the two-site Fermi-Hubbard model as,

$$H_{\text{FH}} = \sum_{s=\uparrow,\downarrow} \frac{\epsilon}{2} (c_{L,s}^\dagger c_{L,s} - c_{R,s}^\dagger c_{R,s}) + t_c (c_{L,s}^\dagger c_{R,s} + c_{R,s}^\dagger c_{L,s}) + U(n_{L,s}n_{L,-s} + n_{R,s}n_{R,-s}), \quad (1.17)$$

where  $c_{j,s}^\dagger$  creates a particle on site  $j \in \{L, R\}$  with spin  $s \in \{\uparrow, \downarrow\}$ , obeying fermionic commutation relations. Furthermore we use the convention that  $-s = \downarrow$  if  $s = \uparrow$ , and *vice versa*, and define the particle number operator for site  $j$  as  $n_{j,s} = c_{j,s}^\dagger c_{j,s}$ . In this simple model each site contains a single orbital level (higher orbitals are neglected), and have an onsite potential  $\pm\epsilon/2$  for left and right, respectively. Particles can tunnel to the neighboring site by a hopping  $t_c$ , and the double occupation of each site is penalized by the charging energy  $U$  [37]. Projecting  $H_{\text{FM}}$  onto the two-particle sector leads to the commonly used effective Hamiltonian of double QDs,

$$H_{\text{DQD}} = \begin{pmatrix} U + \epsilon & 0 & \sqrt{2}t_c & 0 \\ 0 & U - \epsilon & \sqrt{2}t_c & 0 \\ \sqrt{2}t_c & \sqrt{2}t_c & 0 & 0 \\ 0 & 0 & 0 & 0 \end{pmatrix} \begin{matrix} S_{(2,0)} \\ S_{(0,2)} \\ S_{(1,1)} \\ T_{(1,1)} \end{matrix} \quad (1.18)$$

where the order of the basis states is shown next to the matrix, with singlet states being defined as  $|S_{(2,0)}\rangle = c_{L,\uparrow}^\dagger c_{L,\downarrow}^\dagger |0\rangle$ ,  $|S_{(0,2)}\rangle = c_{R,\uparrow}^\dagger c_{R,\downarrow}^\dagger |0\rangle$ , and  $|S_{(1,1)}\rangle = 1/\sqrt{2}(c_{L,\uparrow}^\dagger c_{R,\downarrow}^\dagger - c_{L,\downarrow}^\dagger c_{R,\uparrow}^\dagger) |0\rangle$ . The notation  $T_{(1,1)}$  comprises the three degenerate triplets  $|T_{ss}\rangle = c_{L,s}^\dagger c_{R,s}^\dagger |0\rangle$  and  $|T_0\rangle = 1/\sqrt{2}(c_{L,\uparrow}^\dagger c_{R,\downarrow}^\dagger + c_{L,\downarrow}^\dagger c_{R,\uparrow}^\dagger) |0\rangle$ . In a symmetric double QD, i.e.,  $\epsilon = 0$ , due to the coupling between  $S_{(1,1)}$  and the doubly occupied singlets, the  $S_{(1,1)}$  will become the ground state with energy  $-J \approx -4t_c^2/U$  for weak tunnel-coupling.

This model is widely used in both theoretical and experimental works to describe the inter-dot exchange interaction phenomenologically, since it provides a correct qualitative description [38]. Furthermore the model can be extended by spin-orbit or hyperfine interaction terms [29, 39].

---

<sup>1</sup>In other words, the lowest two-particle eigenstates are mainly composed of combinations of the lowest energy single-particle states.

Despite the simple form of the Hamiltonian in Eq. (1.18), it is remarkably difficult to obtain its parameters from first principles. The Heitler-London and Hund-Mulliken methods are using linear combinations of single QD eigenstates of the left and right dot to project the full Hamiltonian of the tunnel-coupled QDs onto the low-energy subspace [40]. These methods rely on the assumption that the tunnel-coupling between the QDs is weak and the low-energy two-particle eigenstates can be described by products of single particle wavefunctions that are localized on the left and right QD respectively. However, in many cases the electrostatic contribution of the Coulomb potential has an important influence on the shape of the two-particle wavefunction. For double QDs that are much longer than the Bohr radius  $a_B$  (for Si  $a_B \sim 3$  nm, while in Ge  $a_B \sim 12$  nm), the Coulomb repulsion is strong enough to force the two particles apart even if the potential barrier between the QDs is reduced to zero [41, 42].

This phenomenon, also referred to as Wigner molecularization [43, 44], and is illustrated in Fig. 1.2. The naive picture, when the left and right peaks of the two-particle density merge into a single peak as the potential barrier  $v_B$  is reduced to zero corresponds to the weak interaction or short QD limit (first row of figures, for  $a_B = 5L$ ). However, in materials with short Bohr radius, like silicon, the the Coulomb repulsion acts as an effective tunnel barrier between the QDs, maintaining the bimodal character of the particle density even in the single QD limit (second row of figures, for  $a_B = 0.2L$ ). The details of the two-particle density calculation can be found in Section 1.A. Importantly, the exchange splitting is strongly suppressed in the latter case, since it is determined by the overlap of the wavefunctions [43, 44]. Furthermore, we note that the strong electrostatic contribution of the Coulomb interaction can also result in an effective spin-spin interaction, by virtue of spin orbit interaction, even if the QDs are not tunnel coupled [45].

Concluding the discussion on short-range entangling gates, we give a brief overview on the experimental progress with two-qubit gates. Two qubit gates in group-IV semiconductors have been realized with electron QDs in silicon first [46]. Since then, two-qubit gate fidelities in Si improved continuously [47] and already have reached the fault-tolerance threshold [8, 9]. Fast two-qubit logic has also been demonstrated for holes in planar germanium [48, 49], but achieving such a milestone for hole QDs in silicon still lies in the future.

Establishing long-range two-qubit gates is an essential element of the prospective large-scale quantum computers. Such gates act as coherent

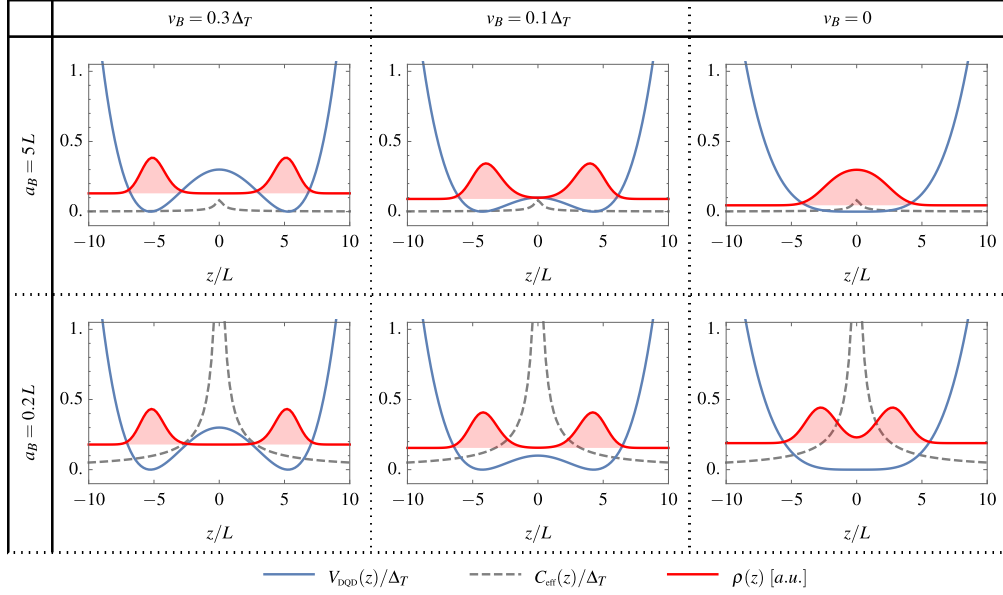


Figure 1.2: Double QD potential for an elongated dot along the weak confinement axis  $z$ , with reducing barrier height  $v_B$  from left to right (blue curves). First row corresponds to the weak interaction regime, while the second row is the strong interaction case (this latter is practically more feasible e.g., in Si). The effective one-dimensional Coulomb pair-potential as in Ref. [50], is shown as dashed gray lines. Reduced two-particle density  $\rho(z)$  is shown in red (in arbitrary units). The energy offset of particle density corresponds to the ground state energy. The length unit  $L$  is the side length of the cross section (square), while  $\Delta_T = \hbar^2/2m^*L^2$  is the orbital splitting in the transversal direction.

links coupling dense qubit clusters and thereby transmitting entanglement over a larger scale quantum processor, while leaving room for classical control electronics on the same chip [35]. Due to the large spatial separation (tens or hundreds of micrometers) such quantum gates require a mediator between the distant spin qubits to be entangled. Some proposals use fermionic particles (e.g., electrons or holes) for such a transmitter, while others rely on bosons (e.g., photons in a cavity or magnonic modes of a ferromagnet). Here we briefly review some of these proposals.

Entangling gates based on electronic mediators use tunnel coupling between the QD and a delocalized electron state (unoccupied). The chemical potential of the QD is tuned below the resonance of the respective



mode, making the overlap with the delocalized state highly tunable. The mediator mode can be, e.g., a quantum Hall edge mode of a two-dimensional electron gas [51], or an electronic cavity mode. The latter case has been confirmed experimentally by achieving coherent tunnelling between QDs mediated by a circular electronic cavity in GaAs [52]. A slightly different approach is to coherently transfer an electron from dot to dot [53] using a few sets of gates [54].

On the other hand, entanglement can also be transferred by bosonic modes, e.g., photons. Qubits can be coupled to the cavity photons of a microwave resonator via the electric dipole moment of the QD which in turn couples to the spin due to SOI [55, 56]. Owing to their high quality factors superconducting resonators are often subject of theoretical proposals [57] and experimental studies [26, 27] for coupling qubits to the lowest photonic mode of the resonator. In state-of-the-art experiments 20 MHz of qubit-qubit coupling strength can be achieved between silicon QDs separated by a distance of  $250\ \mu\text{m}$  [27]. While numerous works are targeting the so called transversal coupling regime, when the interaction of the qubit with the cavity mode relies on the qubit splitting being close the resonance, another opportunity is to couple the qubits longitudinally. The main advantage of this coupling regime is that it does not require near-resonant coupling with the cavity mode, since no spin-flip occurs, while still facilitating two-qubit entangling gates [60].

Finally, magnonic modes in a ferromagnet can also be leveraged for long distance entanglement using dipole-dipole or direct exchange interaction to couple the spin-qubits to the FM. Here, the interaction strength depends on the transverse spin-susceptibility, that decays slower with the distance in quasi-1D systems, providing longer range for the two-qubit entangling gate [61]. As we will see in Chapter 6, chiral magnonic modes provide such a one-dimensional channel, allowing for fast and high-fidelity coupling between distant qubits.

## 1.4 Initialization and readout

Several qubit readout protocols have been developed along the two decades of research in the field of semiconductor spin-qubits [6]. Early experiments have measured the current through a double QD, where the detuning between the two QDs is set such that the energy of the doubly occupied singlet  $S_{(2,0)}$  lies close to the states of  $(1, 1)$  charge configuration [62], that is  $\epsilon \sim -U$  in Eq. (1.18). A current of particles from left to

right can flow uninterrupted through the  $S_{(2,0)} \rightarrow S_{(1,1)} \rightarrow (1,0)$  transition<sup>2</sup>. However, in the reversed biased case, when the double QD is refilled from the right i.e.,  $(1,0) \rightarrow S_{(1,1)}/T_{(1,1)}$ , the system will (eventually) fall into one of the triplet states, blocking the flow of the current in the absence of the spin-flip transition  $T_{(1,1)} \rightarrow S_{(2,0)}$ . This phenomenon is called the Pauli spin blockade (PSB), and the measurement scheme established in Ref. [62] is widely used to date for the demonstration of strong spin-orbit interaction (as in the case of Chapter 4), or coherent Rabi oscillations [11,63]. The key property of PSB that is leveraged in those measurements is that it converts spin to charge, by allowing  $|\uparrow\downarrow\rangle = (|S\rangle + |T\rangle_0)/\sqrt{2}$  (and also  $|\downarrow\uparrow\rangle$ ) to tunnel into the  $|S_{(2,0)}\rangle$  state that is the only energetically available state in the  $(2,0)$  charge configuration, whereas  $|\uparrow\uparrow\rangle$  and  $|\downarrow\downarrow\rangle$  will stay in the  $(1,1)$  charge configuration.

The above mentioned readout technique has several advantages such as being fast and working reliably at high temperatures [63]. On the other hand, the particle hosting the spin-qubit is lost to the reservoir during the protocol, making the measurement destructive. Furthermore the measured signal relies on several tunnelling events as opposed to measuring the spin in a single process. In the following we will consider single-shot readout schemes that can measure the spin of the particle without driving current through the QD hosting it.

The spin state of an individual electron in a QD was first read out by Elzerman *et al.* [64]. In this readout protocol two additional components are required, e.g., a reservoir on one side of the QD and a quantum point contact (QPC) on the other side. The QD is coupled to the reservoir by a gate-tunable coupling and its chemical potential with respect to the Fermi level of the reservoir is also adjustable by an electrostatic gate. If the Zeeman splitting of the spin states is sufficiently large, the spin-to-charge conversion can be achieved by tuning the QD chemical potential such that the electron from a spin-up state can tunnel to the reservoir but not from the spin-down state. Once the spin information is converted into 1 or 0 charge on the QD, the charge state is measured via the QPC [65]. The QPC is tuned such that the conductance is very sensitive to the electrostatic potential of the QD, thus the escape of the electron from the QD is observable in the QPC current.

Since the experiment of Elzerman *et al.*, several improvements have been proposed and implemented on the spin readout of quantum dots.

---

<sup>2</sup>The notation  $(m, n)$  refers to  $m$  ( $n$ ) particles on the left (right) QD. Forward bias means that particles can enter to the left QD and escape from the right.

The spin-to-charge conversion in the original experiment has been severely limited by the temperature, i.e., the Zeeman splitting of the QD needs to be much larger than  $k_B T$ . As we will see later, this condition is compromised by the qubit relaxation process that requires small Zeeman splitting for long qubit coherence. The charge readout based on the dc current measurement of the QPC can also be made significantly faster by radio frequency (RF) reflectometry. Furthermore, the readout is still destructive, since the electron that hosts the qubit gets lost in the reservoir.

Using a sensor QD instead of the reservoir significantly reduces the constraint on the Zeeman energy and temperature. A commonly employed technique is using the PSB for the spin-to-charge conversion and initialization [66]. Here the qubit QD and the sensor QD contain a single particle each, the qubit is in an unknown state  $|\psi_q\rangle$  while the particle on the sensor QD is in the  $|\downarrow_s\rangle$  state. The spin-to-charge conversion follows the same scheme as we have seen above with the left QD being the sensor and the right QD the qubit. If the charge measurement collapsed the two-electron wavefunction to the  $|S_{(2,0)}\rangle$  state, the quantum dot can be brought back to the  $(1, 1)$  charge configuration by raising the chemical potential of the sensor dot. Provided that this step is adiabatic with respect to the  $|S_{(2,0)}\rangle - |T_{\downarrow\downarrow}\rangle$  anticrossing (i.e., caused by SOI), the state is initialized in the  $|\downarrow_s\rangle |\downarrow_q\rangle$  state. If no excess charge was observed in the charge measurement, the system is already projected into the  $|\downarrow_s\rangle |\downarrow_q\rangle$  state, and there is no need for an additional gate pulse on the sensor dot.

## Readout based on charge sensing

Charge sensors have also developed remarkably since the early works using QPC-current based charge readout [64, 65]. Connecting the sensor QPC or a single-electron transistor (SET) to a high frequency resonant circuit, the reflection of a resonant carrier signal can be used to infer the charge state of the nearby QD [67]. This RF reflectometry based readout has been used in numerous works ever since to measure the charge state [68–72] down to (potentially) nanosecond timescales for donor based spin qubits [73], providing a crucial advantage over the QPC-current measurement. Using this charge readout scheme, the spin state of a single particle in a QD can be read out by spin-to-charge conversion [73–75] in  $1.5 \mu\text{s}$  microseconds and up to 97% fidelity [73]. Similar method for gate-defined hole QDs result in  $6 \mu\text{s}$  readout time [66] with a fidelity limited by triplet relaxation in the PSB. There have been also potent theoretical proposals for current-based charge sensors using Aharonov-Bohm in-

terferometers [76], but their experimental realization is yet to be achieved. Moreover, further improvement is required from the scalability standpoint, since the charge sensing circuitry would increase the single qubit footprint tremendously.

Instead of having a separate tunnel junction to measure its absolute charge, the QD can be coupled directly to the RF circuit [77, 78]. When the particle on the QD tunnels to the neighboring site (e.g., to an other QD), the quantum capacitance changes, shifting the resonance frequency of the RF circuit. This readout protocol is called dispersive readout, since the information is encoded in the dispersive shift of the reflected signal, rather than the damping of the resonant circuit as for the previously considered RF-QPC (or RF-SET) readout. The advantage of the dispersive approach is the low back action on the qubit as well as the fact that the readout circuitry does not contain a mesoscopic charge detector. On the other hand, dispersive charge sensing to date is still outperformed in operation speed by the other reflectometry-based readout schemes. The best charge sensing times range from milliseconds to hundreds of nanoseconds [77–79], whereas the measurement times are down to the nanosecond regime for the RF-SETs [73]. Gate-based spin readout has been achieved in  $6\mu\text{s}$  with 98% fidelity in Si using superconducting resonators [79], while normal off-chip resonators require milliseconds for single-shot readout of about 70% fidelity [80].

While single and two qubit gates improved tremendously reaching the error thresholds of quantum error correction algorithms [8, 9], spin readout remained to this date a “skeleton in the closet”, down-performing quantum gates in both operation times and fidelities. In fact new quantum gate benchmarking techniques needed to be developed such as randomized benchmarking [81] and gate set tomography [82], in order to measure gate fidelities that exceed the performance of the qubit readout. Additionally, gate set tomography also allows for the identification of systematic errors caused by the time evolution under an “imperfect” Hamiltonian [8, 82].

## 1.5 Decoherence

In this section we present some of the common frameworks to treat qubit decoherence due to stationary classical noise. Here we follow the more extensive review of Burkard *et al.* [37] and the lecture notes of Christoph Kloeffer on “*Spin-based Quantum Information Science*”. In the first subsec-

tion general considerations and formulas are presented, assuming a stationary noise with a given noise power spectrum  $S(\omega)$ , while the noise sources relevant for practical applications in semiconductor structures are discussed in the subsection to follow.

### Qubit decoherence due to classical noise

In the two-dimensional qubit subspace, the noise can be divided into longitudinal, i.e.,  $\propto \sigma_z$ , and transversal, i.e.,  $\propto \sigma_{\pm}$ , components. The qubit Hamiltonian  $\Delta_z \sigma_z / 2$  extended with the time-dependent noise terms reads

$$H = \frac{1}{2}[\Delta_z + b_z(t)]\sigma_z + \frac{1}{4}b_+(t)\sigma_- + \frac{1}{4}b_-(t)\sigma_+, \quad (1.19)$$

where  $b_z(t)$  [ $b_{\pm}(t)$ ] is the noise term coupling longitudinally (transversally) to the qubit. Within the framework of the Bloch-Redfield theory [83] two important timescales can be deduced: the relaxation time  $T_1$  and the dephasing time  $T_2$ . In analogy with the Bloch equations in the context of nuclear magnetic resonance, the relaxation time  $T_1$  describes the (exponential) decay of the qubit polarization, i.e.,  $\langle \sigma_z \rangle$ , due to transversal noise, whereas  $\langle \sigma_{\pm} \rangle$  decays with the dephasing time  $T_2$  as a result of longitudinal noise.

The relaxation time can be derived straightforwardly, using Fermi's golden rule. Considering the spontaneous flipping of the qubit ( $|0\rangle$  to  $|1\rangle$  and *vice versa*)

$$\frac{1}{T_1} = \Gamma_{|0\rangle \rightarrow |1\rangle} + \Gamma_{|1\rangle \rightarrow |0\rangle} = \frac{1}{4\hbar^2} S_{b_-}(\Delta_z/\hbar), \quad (1.20)$$

where the transition rates are expressed in terms of the power spectral function of the transversal noise,

$$S_{b_-}(\omega) = \int dt e^{-i\omega t} (\langle b_+(t)b_-(0) \rangle + \langle b_-(0)b_+(t) \rangle). \quad (1.21)$$

In the formula for the relaxation rate the noise power spectrum shows up at  $\omega = \Delta_z/\hbar$ . This is intuitive, since the qubit needs to emit/absorb an energy of  $\Delta_z$  to flip its spin state. Similarly, the dephasing time in the Bloch-Redfield approximation can be obtained as

$$\frac{1}{T_2} = \frac{1}{2T_1} + \frac{1}{4\hbar^2} S_{b_z}(0), \quad (1.22)$$

where the second term is called the pure dephasing, often denoted as  $1/T_2^*$ , and the spectral function of the longitudinal noise  $S_{b_z}(\omega)$  is defined analogous to Eq. (1.21).

The Bloch-Redfield approximation is valid only if the noise is Markovian and decoherence times are much longer than the correlation time of the noise, i.e., the noise is local in time. Or equivalently, the power spectrum needs to change slowly on the scale of the respective decoherence rates, i.e.,  $S_{b_-}(\Delta_z/\hbar) \approx S_{b_-}(\Delta_z/\hbar \pm T_1^{-1})$  for relaxation and  $S_{b_z}(0) \approx S_{b_z}(T_2^{-1})$  for dephasing [84]. The condition for the relaxation time  $T_1$  is usually fulfilled, but the one for dephasing breaks down for some of the practically relevant noise spectra, e.g., the  $1/f$  charge-noise with  $S_{b_z}(\omega) \propto 1/\omega$ .

In order to find a better description for the pure dephasing  $1/T_2^*$ , we abandon the Bloch-Redfield approximation and consider the so called filter function formalism [37, 85–87]. This method accounts for the time-evolution of the qubit spin due to external drive, e.g., when pulses are applied to prolong the coherence of the qubit. Assuming the amplitude of the noise is much smaller than the qubit Zeeman splitting, i.e.,  $b/\Delta_z \ll 1$ , and the applied  $\pi$  pulses are instantaneously flipping the qubit spin as  $\tilde{\sigma}_z = r(t)\sigma_z$  with  $r(t) \in \{-1, 1\}$ , the decay due to pure dephasing is  $\langle \sigma_{\pm}(t) \rangle \sim \exp(-\chi(t))$ , where

$$\chi(t) = \frac{1}{8\pi\hbar^2} \int_{-\infty}^{\infty} d\omega S_{b_z}(\omega) \frac{F(\omega t)}{\omega^2}, \quad (1.23)$$

with the filter function given by

$$F(\omega t) = \omega^2 \left| \int_0^t r(t') e^{i\omega t'} dt' \right|^2. \quad (1.24)$$

For a given pulse sequence the filter function can be straightforwardly evaluated. In the case of a Ramsey experiment where no pulses are applied, the filter function is  $F(\omega t) = 4 \sin^2(\omega t/2)$ . That is the filter function of free induction decay (FID), shown in Fig. 1.3. The pure dephasing time is then defined by  $\chi(T_2^*) = 1$ , that is when the transversal qubit polarization decays to  $1/e$ . As opposed to the result of Eq. (1.22) obtained in the Bloch-Redfield approximation, the pure dephasing in the filter function formalism accounts for fluctuations with finite frequencies as well.

If the noise is longitudinal and its spectrum is well approximated by a power-law, i.e.,  $S_{b_z}(\omega) \propto |\omega|^{-\beta}$ , the decay of the transversal component of

the qubit polarization reads  $\langle \sigma_{\pm}(t) \rangle \sim \exp[-(t/T_2^*)^{1+\beta}]$ . This can be seen by a simple substitution of the integration variable  $\tau = \omega t$  in Eq. (1.23). Since the filter function of FID is finite at  $\omega = 0$ , the divergence of the noise power-spectrum necessitates the introduction of a low-frequency cutoff  $\omega_{ir}$ , that is the averaging time of the Ramsey experiment. In other words, noise components changing slower than the measurement time only give a constant contribution of the qubit splitting during the Ramsey experiment.

If pulses are applied, the low-frequency noise components, i.e.,  $\omega < 1/t$  can be mitigated. For example in a Hahn echo experiment, where an  $\pi$  pulse is applied at  $t' = t/2$  the filter function is  $F(\omega t) = 16 \sin^4(\omega t/4)$ . For low frequencies,  $F(\omega t)/\omega^2 \sim \omega^2$  in (1.23), hence providing a natural low-frequency cutoff for the  $1/f$ -noise, (see Fig. 1.3). Another important example is the static noise, i.e.,  $S_{b_z}(\omega) \propto \delta(\omega)$ , the effect of which is completely eliminated by the echo pulse.

Furthermore, a timescale often reported in experiments is  $T_{2,\text{Rabi}}$ , the decay of  $\langle \sigma_z \rangle$  during continuous Rabi drive. This decay is analogous to a Hahn echo type of experiment with several  $\pi$  pulses, hence the notation  $T_{2,\text{Rabi}}$ . The driven case analogue of the relaxation process is the decay timescale  $T_{1\rho}$ , when the qubit is initialized along the axis of rotation. In that case the filter function is sampling the noise spectrum at the Rabi frequency (see Fig. 1.3), rather than  $\omega = 0$ , and therefore  $T_{2,\text{Rabi}} > T_2^*$  for low-frequency noise.

Finally, for the sake of completeness, we note that the pure dephasing formula in Eq. (1.22) in the Bloch-Redfield approximation can be obtained from the filter function formalism, exploiting that  $F(\omega t)/\omega^2$  in Eq. (1.23) is strongly peaked around  $\omega < 1/t$ . If the spectral function varies slowly on the scale of the dephasing rate, it can be factored out as  $S_{b_z}(0)$  for timescales  $t \sim T_2^*$ . The remaining frequency integral yields  $2\pi t$ , regardless of the form of the filter function, thus leading to Eq. (1.22).

## Noise sources

In the early days of semiconductor based quantum computing, the coherence of electron spin qubits in GaAs heterostructures has been severely limited by the fluctuating nuclear spin environment that couples to the qubit via (contact) hyperfine interaction [38]. Even though group-IV semiconductors like Si and Ge contain a significantly lower proportion of nuclear-spinful isotopes, hyperfine noise is still present. Owing to the slow dynamics of the nuclear spins, the spectral function of hyperfine

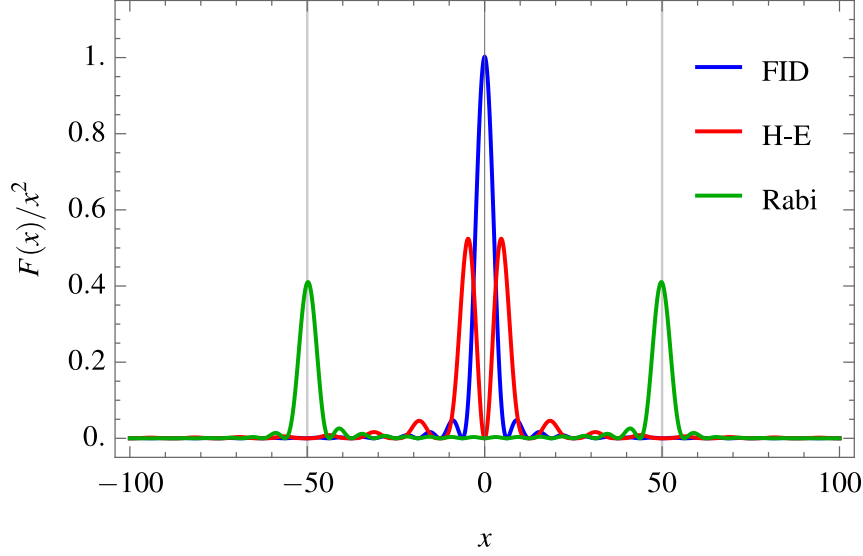


Figure 1.3: Filter function defined in Eq. (1.24), for three practically important cases: free induction decay (FID) shown in blue, Hahn-Echo pulse (H-E) shown in red, and Rabi drive (Rabi) shown in green. Vertical guidelines correspond to  $x = \pm 2\pi f_{\text{Rabi}} t$ .

noise can be approximated as  $S_{b_z}(\omega) = \sigma_b^2 \delta(\omega)$ , where  $\sigma_b^2 \propto 1/N_{\text{nuc}}$  is the variance of the Zeeman field fluctuations due to the nuclear spins. In hole states, owing to their  $p$ -type Bloch function, the contact hyperfine interaction is suppressed, however, other hyperfine contributions can still act as a source of decoherence [88]. While the respective noise spectrum is qualitatively similar, the coupling mechanism can be strikingly different from that of electrons, showing nontrivial dependence on strain, device geometry and electric field [89, 90].

Further inevitable sources of noise include charge noise or  $1/f$ -noise that is the fluctuation of electric field due to fluctuations of gate voltage, or fluctuating charge traps formed at the interfaces or the gate oxide. Even though the origin of the noise is not well understood, it has been confirmed by several experiments that the low-frequency part of the spectral density is inversely proportional to the noise frequency, hence the name  $1/f$ -noise [91–93]. Charge noise couples to the qubit via spin-orbit interaction or a magnetic field gradient. Due to the strong Rashba type of spin-orbit interaction, the coherence of hole-spin qubits is often limited by charge noise. However, in certain geometries and growth di-



rections the spin-orbit interaction can be switched off, leading to dephasing sweet spots, where  $T_2^* \rightarrow \infty$ , at finite electric fields in Si FinFET devices [20].

Dynamical deformations of the lattice, i.e., phonons, also generate a fluctuating electric field that can couple to the qubit in a similar way as we have seen for the case of charge noise. In Si and Ge the coupling to phonons happens via the deformational potential mechanism. The piezoelectric contribution is not present as the basis atoms do not have a net polarization. The primary phonon-induced decoherence mechanism is relaxation [89, 95] where an acoustic phonon is emitted, having an energy equal to the qubit splitting. Dephasing mechanisms on the other hand require a two phonon processes [96] due to the conservation of energy. The spectral function of the phonon bath is determined by the phonon density of states and therefore, depending on the dimensionality of the device, it is proportional to some high power of the frequency for small qubit splittings.

Having discussed quantum gate and readout protocols as well as decoherence timescales, we provide a summary of these relevant timescales and error rates for some of the most recent and most influential experiments on electron spin-qubits in silicon (see Table 1.1) where we distinguish experiments according to the qubit temperature. The corresponding quantities are collected for hole-spin qubits as well in Table. 1.2. Comparison of the timescales in the two tables reflects on the accelerated life of hole-spin qubits that is driven by the strong direct Rashba SOI [10]. Finally, we also remark that decoherence timescales have been measured already in hundreds of experiments. For a detailed quantitative comparison in different materials, qubit definitions, and noise sources we refer the reader to the extensive review of Ref. [97].

## 1.6 Scalability

So far we have been considering the so called qubit layer of the quantum computer, that is expected to work at sub-kelvin temperatures. We have seen that one of the key challenges is the compactification of the readout circuitry. Until this point, the goal has been to identify a qubit architecture with fast operation and long coherence times in a scalable fashion, that is the qubit footprint facilitates control, readout, and sufficient qubit-to-qubit connectivity for quantum error correction (QEC) algorithms. However, scalability of the quantum layer is only a neces-

Electrons	electrons in Si [8,9]	hot electrons in Si [98,99]
$X$ gate	4 MHz, $\mathcal{F} = 99.7\%$	1-2 MHz, $\mathcal{F} = 98.7\%$
$Z$ gate	$\sim$	$\sim$
$T_1$	$> 10$ ms	2-20 ms
$T_2^*$	6-20 $\mu$ s	2 $\mu$ s
$T_{2,\text{Rabi}}$	50 $\mu$ s	8 $\mu$ s
two-qubit gate	5 MHz, $\mathcal{F} = 99.5\%$	2.5 MHz, $\mathcal{F} = 86.1\%$
readout	$v \sim 0.6$ (RF)	$v \sim 0.2$ (SET)
long-range gate	20 MHz, $d = 250$ $\mu$ m [27]	–

Table 1.1: Characteristic timescales and fidelities for a few state-of-the-art experiments on electrons. The first column, ‘electrons in Si’ correspond to measurements at the usual dilution refrigerator temperatures (tens of mK), while the temperature of ‘hot’ electrons is  $\sim 1$  K. ‘RF’ refers to RF-SET readout, while ‘SET’ is normal SET based charge readout.  $\mathcal{F}$  is gate fidelity,  $v$  is the readout visibility, and  $d$  qubit-to-qubit distance.

Holes	holes in planar Ge [48,49]	hot holes in Si [63]
$X$ gate	20 MHz, $\mathcal{F} = 99.4\%$	147 MHz, $\mathcal{F} = 98.9\%$
$Z$ gate	$\sim$	45 MHz
$T_1$	1-16 ms	$> 10$ $\mu$ s
$T_2^*$	150-400 ns	70-200 ns
$T_{2,\text{Rabi}}$	$> 100$ $\mu$ s (CPMG)	$> 2$ $\mu$ s
two-qubit gate	10-100 MHz	–
readout	10 $\mu$ s, $v \sim 0.8$ (RF)	(dc)
long-range gate	–	–

Table 1.2: Characteristic timescales and fidelities for a few state-of-the-art experiments on holes. Holes in planar Ge correspond to measurements at the usual dilution refrigerator temperatures (tens of mK), while the temperature of ‘hot’ holes in Si is  $\sim 1$ -4 K. In the parentheses ‘dc’ refers to dc current based readout, i.e., a particle current is flowing through the measured QD. Furthermore  $T_{2,\text{Rabi}}$  is replaced by  $T_{2,\text{CPMG}}$  (where the qubit coherence is prolonged by ‘CPMG’ refocusing pulses) for Ge in the absence of the former data.

sary condition for scalable quantum computing. Scalability has to be successfully implemented also for the quantum-classical interface that connects the qubit layer with the room temperature classical control. To date, the largest quantum chips consist of a few tens or hundred qubits controlled by a large number of analog cables, limiting the expansion of the qubit array [1, 2]. Making use of the advanced fabrication techniques and decades of experience with the material, the silicon CMOS technology is envisioned to expedite the progress towards truly scalable quantum computers.

The aforementioned QEC algorithms require repeated feedback between the qubits and the classical control. One of such feedback loops would consist of a digital signal sent from the classical driver to a digital-analog converter (DAC) that translates the digital signal into analog dc signals, pulses, and microwave signals used to communicate with an array of qubits. This analog signal needs to be demultiplexed –i.e., separated with respect to the addressed qubit– and then sent toward the respective qubits. Some qubits are then read out, the signals (analog) are multiplexed and converted back to a digital signal (ADC) that arrives at the classical control thus closing the loop.

Few-qubit devices can be controlled directly by room temperature electronics skipping the multiplexing step, but this approach cannot be carried over for thousands or millions of qubits. While the multiplexing still needs to happen at the qubit temperatures to minimize the number of input and output lines to and from the higher temperature electronics, the conversion between analog and digital signals can be deferred to cryogenic temperatures where higher cooling powers are available [100]. For the qubit control, the cryogenic electronics should be able to generate ns pulses and microwave signals as well. These requirements are fulfilled by the cryo-CMOS technology [100–104].

So far we have discussed that the elements of the analog control circuitry can be deferred to cryogenic temperatures. Another step forward toward full scalability would be to bring the qubits and multiplexers to the same temperature as the ADC/DAC layer. One approach is to develop electronics that are suitable for the even smaller cooling powers of a dilution refrigerator, working at 100 mK temperatures [105, 106]. Another promising alternative is to use hot spin-qubits in silicon that operate in cryogenic temperatures [63, 98, 99], therefore –leveraging the full potential of the CMOS technology– in the future they are expected to facilitate the integration of the electronics and the qubits on the same die. Such an approach requires clever device design to bring the electronics

as close as possible to the qubit array that they control.

A recent proposal suggests to arrange small, dense qubit arrays in a checkerboard pattern with their corresponding control electronics [35]. In order to connect the qubit islands –forming a quantum processor of a larger scale– coherent links bridging over micrometer distances are highly desired. These links can be thought of as long-range two-qubit gates that mediate entanglement between qubit islands. There have been several theoretical proposals to realize such a long-range entanglement [53, 56, 57, 60, 61, 107–109], and the experimental realization of such a coherent link –using electronic cavities and superconducting resonators– is a recently achieved milestone in the field [26, 27, 52].

## 1.7 Quantum error correction on scalable spin qubit arrays

Most of the quantum algorithms promising exponential speed up for solving certain problems require decoherence free qubits (at least on the time-scale of the total running time) and a universal set of quantum gates. However, as we have seen in Section 1.5 this is practically not achievable in the real world due to the finite coupling to the environment. In order to tackle such problems we need to convert noisy qubits into a smaller number of logical qubits that maintain their coherence ‘indefinitely’. One of the early proposals from Peter Shor was inspired by the classical repetition code and used 9 qubits to encode a logical qubit, where both bit- and phase-flip error probabilities are reduced from  $p$  to  $p^2$  [110]. This simple error correction approach, however, requires rich connectivity between the physical qubits in order to realize two-qubit gates between logical qubits. More generally, quantum error correction (QEC) algorithms aim to encode a logical qubit in a quantum state that is distributed among a large number of qubits such that individual qubit errors can be detected without influencing the logical qubit [4, 5].

Here we briefly discuss one of the most popular topological error correction codes, the *surface code*, based on the review article of James Wootton [4]. We take a square grid of qubits and divide them into two groups (data and ancilla qubits) distributed in a checkerboard pattern. For each ancilla qubit we define a plaquette enclosed by the four neighbouring data qubits. The ancillas are used to measure the eigenvalue of the X (Z) stabilizer of a given plaquette, that is the product of  $\sigma_i^x$  ( $\sigma_i^z$ ) operators

with  $i$  indexing the four nearest-neighbour data qubits. The  $X$  and  $Z$  stabilizers are defined for each plaquette in an alternating pattern, leading to a set of mutually commuting operators with eigenvalues  $\pm 1$ . The stabilizer space is then the subspace of the total Hilbert space for which all stabilizers have eigenvalue  $+1$ . Note that a single bit-flip error changes the eigenvalues of two  $Z$  stabilizers from  $+1$  to  $-1$ , thereby helping to keep track or correct such error types (similarly  $X$  stabilizers monitor phase-flips) in the periodically applied stabilizer measurements. For the definition of logical qubits, it is crucial how stabilizers are defined on the boundaries. Stabilizers on the boundaries of the system are defined as merging all the incomplete plaquettes of the same type ( $X$  or  $Z$ ) that touch in the corners. Internal boundaries can be realized as well by switching off stabilizer measurements thereby deactivating some plaquettes on the lattice<sup>3</sup>.

It can be shown that the  $Z$  stabilizers with  $-1$  eigenvalue can be associated with anyonic quasiparticles of one flavour while  $X$  stabilizers with  $-1$  eigenvalue correspond to anyons of a different flavour<sup>4</sup>. Due to the definition of stabilizers such anyons can be localized either on the plaquettes or the boundaries of the lattice. This brings us in position to define a logical qubit in the  $Z$  basis using an internal boundary of partial  $Z$  plaquettes: the state  $|0\rangle$  ( $|1\rangle$ ) represents zero (one) anyon on the internal boundary. We only keep track of anyons on the plaquettes, therefore the qubit can be in a superposition of zero and one anyon. Furthermore, by switching on and off certain ancilla measurements, the logical qubit can be moved on the lattice, allowing one to make use of the anyonic exchange statistics. Exploiting the pairwise creation and the exchange statistics of anyons, single qubit  $X$  and  $Z$  gates can be applied on the logical qubit as well as CNOT gates by braiding of logical qubits.

In order to realize the stabilizer measurements and the qubit operations on the lattice, it is sufficient to have a large number of spin qubits in a square grid with single qubit rotations, nearest neighbour CNOT gates, and projective measurements on the physical qubits available [4]. E.g., the  $Z$ -type stabilizer requires four CNOT gates each of them targeted on the ancilla and controlled on the nearest-neighbour data qubits. Measuring the ancilla on the  $Z$  basis yields the eigenvalue of the corre-

---

<sup>3</sup>It is important to note that boundary stabilizers do not participate in the periodic stabilizer measurement cycles.

<sup>4</sup>Anyons are quasiparticles in 2D, obeying a peculiar exchange statistics. Here the important property is that two subsequent exchanges of two anyons with different flavours lead to a phase shift of  $-1$ .

sponding stabilizer [111]. Defining the  $X$ -stabilizers follows the same logic. Therefore we conclude that scalable spin qubit arrays are viable platforms to achieve fault tolerant quantum computing. Assuming that the single-, two-qubit and readout error probabilities within a stabilizer measurement cycle are equal, e.g.,  $p_c$ , the most efficient error correction algorithms [111–113] manage to achieve a fault tolerance error threshold of  $p_c \sim 1\%$ .

## 1.A Details of the particle density calculation in a double QD

In Fig. 1.2 we have considered a double QD in a nanowire geometry with square cross section of side length  $L$ , and a corresponding ‘transversal’ orbital energy  $\Delta_T = \hbar^2/2m^*L^2$ . Assuming that the double QD is significantly longer than the side length of the wire, we restrict our analysis to the lowest transversal subband. This allows us to use the simple fitting formula derived in Ref. [50] for the effective one-dimensional Coulomb interaction, that is

$$C_{\text{eff}}(z) = \frac{e^2}{4\pi\epsilon} \frac{1}{\sqrt{z^2 + (L/4)^2}}, \quad (1.25)$$

where  $\epsilon$  is the dielectric constant of the material and  $L/4$  acts as a short-range cutoff for the Coulomb potential. Using this formula, we write the spin-independent Hamiltonian of the double QD as

$$H_{\text{DQD}} = -\frac{\hbar^2}{2m^*}(\partial_{z_1}^2 + \partial_{z_2}^2) + V_{\text{DQD}}(z_1) + V_{\text{DQD}}(z_2) + C_{\text{eff}}(z_1 - z_2), \quad (1.26)$$

where  $V_{\text{DQD}}(z) = v_B(z^2/a^2 - 1)^2$  with  $a = 10L(\sqrt{2\Delta_T/v_B} + 1)^{-1/2}$  being the position of the minimum, fixed by the condition that  $V_{\text{DQD}}(z = \pm 10L) = 2\Delta_T$ . This parametrization of the double QD potential allows for a meaningful comparison between different barrier heights. Then we calculate  $\psi(z_1, z_2)$ , the lowest energy eigenstate of the Hamiltonian. Owing to the particle exchange symmetry of the Hamiltonian (that is  $z_1 \leftrightarrow z_2$ ) one can simply define the reduced two-particle density as

$$\rho(z) = \int dz' |\psi(z, z')|^2. \quad (1.27)$$

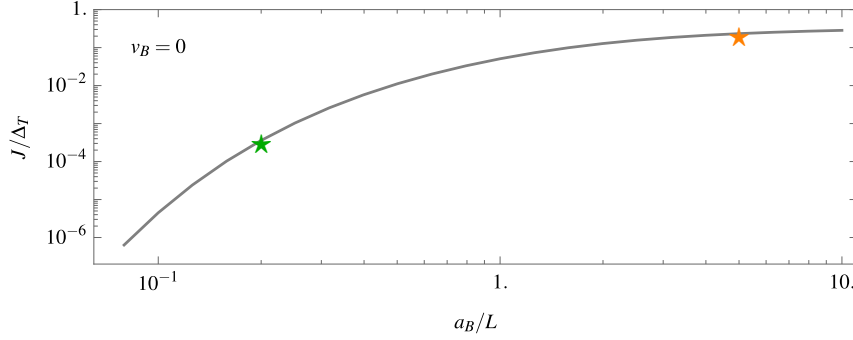


Figure 1.4: Exchange splitting as a function of interaction strength. The markers correspond to the strong (green) and weak interaction limit (orange) for  $v_B = 0$  in Fig. 1.2.

Finally, we deduced the exchange splitting from the eigenvalues of the Hamiltonian in Eq. (1.26). We define the exchange splitting  $J$  as the energy difference between the lowest odd and even orbital states. The exchange splitting as a function of  $a_B/L$  is shown in Fig. 1.4, quantifying the suppression of the exchange in the strong interaction case, when the wavefunction overlap is reduced by the strong Coulomb repulsion. Note that we refer to the strength of the Coulomb interaction via the Bohr radius that is defined as  $a_B = 4\pi\epsilon\hbar^2/e^2m^*$  (small value means strong interaction).

# Bibliography

- [1] F. Arute, K. Arya, R. Babbush, D. Bacon, J. C. Bardin, R. Barends, R. Biswas, S. Boixo, F. G. S. L. Brandao, D. A. Buell, B. Burkett, Y. Chen, Z. Chen, B. Chiaro, R. Collins, W. Courtney, A. Dunsworth, E. Farhi, B. Foxen, A. Fowler, C. Gidney, M. Giustina, R. Graff, K. Guerin, S. Habegger, M. P. Harrigan, M. J. Hartmann, A. Ho, M. Hoffmann, T. Huang, T. S. Humble, S. V. Isakov, E. Jeffrey, Z. Jiang, D. Kafri, K. Kechedzhi, J. Kelly, P. V. Klimov, S. Knysh, A. Korotkov, F. Kostritsa, D. Landhuis, M. Lindmark, E. Lucero, D. Lyakh, S. Mandrà, J. R. McClean, M. McEwen, A. Megrant, X. Mi, K. Michielsen, M. Mohseni, J. Mutus, O. Naaman, M. Neeley, C. Neill, M. Y. Niu, E. Ostby, A. Petukhov, J. C. Platt, C. Quintana, E. G. Rieffel, P. Roushan, N. C. Rubin, D. Sank, K. J. Satzinger, V. Smelyanskiy, K. J. Sung, M. D. Trevithick, A. Vainsencher, B. Villalonga, T. White, Z. J. Yao, P. Yeh, A. Zalcman, H. Neven, and J. M. Martinis, “Quantum supremacy using a programmable superconducting processor,” *Nature*, vol. 574, no. 7779, pp. 505–510, 2019.
- [2] J. Chow, O. Dial, and J. Gambetta, “Ibm quantum breaks the 100-qubit processor barrier,” *IBM Research Blog*, available in [https://research. ibm. com/blog/127-qubit-quantum-process-or-eagle](https://research.ibm.com/blog/127-qubit-quantum-process-or-eagle), 2021.
- [3] K. Bharti, A. Cervera-Lierta, T. H. Kyaw, T. Haug, S. Alperin-Lea, A. Anand, M. Degroote, H. Heimonen, J. S. Kottmann, T. Menke, W.-K. Mok, S. Sim, L.-C. Kwek, and A. Aspuru-Guzik, “Noisy intermediate-scale quantum algorithms,” *Rev. Mod. Phys.*, vol. 94, p. 015004, Feb 2022.
- [4] J. R. Wootton, “Quantum memories and error correction,” *Journal of Modern Optics*, vol. 59, no. 20, pp. 1717–1738, 2012.



- [5] B. M. Terhal, "Quantum error correction for quantum memories," *Reviews of Modern Physics*, vol. 87, no. 2, p. 307, 2015.
- [6] D. Loss and D. P. DiVincenzo, "Quantum computation with quantum dots," *Phys. Rev. A*, vol. 57, pp. 120–126, Jan. 1998.
- [7] B. E. Kane, "A silicon-based nuclear spin quantum computer," *nature*, vol. 393, no. 6681, pp. 133–137, 1998.
- [8] X. Xue, M. Russ, N. Samkharadze, B. Undseth, A. Sammak, G. Scappucci, and L. M. Vandersypen, "Quantum logic with spin qubits crossing the surface code threshold," *Nature*, vol. 601, no. 7893, pp. 343–347, 2022.
- [9] A. Noiri, K. Takeda, T. Nakajima, T. Kobayashi, A. Sammak, G. Scappucci, and S. Tarucha, "Fast universal quantum gate above the fault-tolerance threshold in silicon," *Nature*, vol. 601, no. 7893, pp. 338–342, 2022.
- [10] C. Kloeffel, M. Trif, and D. Loss, "Strong spin-orbit interaction and helical hole states in Ge/Si nanowires," *Phys. Rev. B*, vol. 84, p. 195314, Nov. 2011.
- [11] F. N. Froning, L. C. Camenzind, O. A. van der Molen, A. Li, E. P. Bakkers, D. M. Zumbühl, and F. R. Braakman, "Ultrafast hole spin qubit with gate-tunable spin-orbit switch functionality," *Nature Nanotechnology*, vol. 16, no. 3, pp. 308–312, 2021.
- [12] K. Wang, G. Xu, F. Gao, H. Liu, R.-L. Ma, X. Zhang, Z. Wang, G. Cao, T. Wang, J.-J. Zhang, D. Culcer, X. Hu, H.-W. Jiang, H.-O. Li, G.-C. Guo, and G.-P. Guo, "Ultrafast coherent control of a hole spin qubit in a germanium quantum dot," *Nature Communications*, vol. 13, no. 1, p. 206, 2022.
- [13] G. Katsaros, J. Kukučka, L. Vukušić, H. Watzinger, F. Gao, T. Wang, J.-J. Zhang, and K. Held, "Zero field splitting of heavy-hole states in quantum dots," *Nano Letters*, vol. 20, no. 7, pp. 5201–5206, 2020. PMID: 32479090.
- [14] J. M. Luttinger and W. Kohn, "Motion of electrons and holes in perturbed periodic fields," *Physical Review*, vol. 97, no. 4, p. 869, 1955.

- [15] J. M. Luttinger, "Quantum theory of cyclotron resonance in semi-conductors: General theory," *Phys. Rev.*, vol. 102, pp. 1030–1041, May 1956.
- [16] G. L. Bir and G. E. Pikus, *Symmetry and strain-induced effects in semi-conductors*, vol. 484. Wiley New York, 1974.
- [17] R. Winkler, *Spin–Orbit Coupling Effects in Two-Dimensional Electron and Hole Systems*, vol. 191 of *Springer Tracts in Modern Physics*. Berlin, Heidelberg: Springer Berlin Heidelberg, 2003.
- [18] P. C. Sercel and K. J. Vahala, "Analytical formalism for determining quantum-wire and quantum-dot band structure in the multiband envelope-function approximation," *Phys. Rev. B*, vol. 42, pp. 3690–3710, Aug 1990.
- [19] D. Csontos, P. Brusheim, U. Zülicke, and H. Q. Xu, "Spin- $\frac{3}{2}$  physics of semiconductor hole nanowires: Valence-band mixing and tunable interplay between bulk-material and orbital bound-state spin splittings," *Phys. Rev. B*, vol. 79, p. 155323, Apr 2009.
- [20] S. Bosco, B. Hetényi, and D. Loss, "Hole spin qubits in Si finfets with fully tunable spin-orbit coupling and sweet spots for charge noise," *PRX Quantum*, vol. 2, no. 1, p. 010348, 2021.
- [21] E. Zavoisky, "Spin-magnetic resonance in paramagnetics," *J Phys Ussr*, vol. 9, pp. 211–245, 1945.
- [22] I. I. Rabi, "Space quantization in a gyrating magnetic field," *Phys. Rev.*, vol. 51, pp. 652–654, Apr 1937.
- [23] S. Nadj-Perge, S. Frolov, E. Bakkers, and L. P. Kouwenhoven, "Spin–orbit qubit in a semiconductor nanowire," *Nature*, vol. 468, no. 7327, pp. 1084–1087, 2010.
- [24] M. Veldhorst, J. C. C. Hwang, C. H. Yang, A. W. Leenstra, B. de Ronde, J. P. Dehollain, J. T. Muhonen, F. E. Hudson, K. M. Itoh, A. Morello, and A. S. Dzurak, "An addressable quantum dot qubit with fault-tolerant control-fidelity," *Nature Nanotechnology*, vol. 9, no. 12, pp. 981–985, 2014.
- [25] B. Voisin, R. Maurand, S. Barraud, M. Vinet, X. Jehl, M. Sanquer, J. Renard, and S. De Franceschi, "Electrical control of g-factor in

- a few-hole silicon nanowire mosfet," *Nano letters*, vol. 16, no. 1, pp. 88–92, 2016.
- [26] F. H. L. Koppens, C. Buizert, K. J. Tielrooij, I. T. Vink, K. C. Nowack, T. Meunier, L. P. Kouwenhoven, and L. M. K. Vandersypen, "Driven coherent oscillations of a single electron spin in a quantum dot," *Nature*, vol. 442, no. 7104, pp. 766–771, 2006.
  - [27] V. N. Golovach, M. Borhani, and D. Loss, "Electric-dipole-induced spin resonance in quantum dots," *Phys. Rev. B*, vol. 74, p. 165319, Oct 2006.
  - [28] K. C. Nowack, F. H. L. Koppens, Y. V. Nazarov, and L. M. K. Vandersypen, "Coherent Control of a Single Electron Spin with Electric Fields," *Science*, vol. 318, pp. 1430–1433, Nov. 2007.
  - [29] F. N. M. Froning, M. J. Rančić, B. Hetényi, S. Bosco, M. K. Rehmann, A. Li, E. P. A. M. Bakkers, F. A. Zwanenburg, D. Loss, D. M. Zumbühl, and F. R. Braakman, "Strong spin-orbit interaction and  $g$ -factor renormalization of hole spins in ge/si nanowire quantum dots," *arXiv preprint arXiv:2007.04308*, 2020.
  - [30] C. Adelsberger, M. Benito, S. Bosco, J. Klinovaja, and D. Loss, "Hole-spin qubits in ge nanowire quantum dots: Interplay of orbital magnetic field, strain, and growth direction," *Phys. Rev. B*, vol. 105, p. 075308, Feb 2022.
  - [31] C. Kloeffel, M. Trif, P. Stano, and D. Loss, "Circuit qed with hole-spin qubits in ge/si nanowire quantum dots," *Phys. Rev. B*, vol. 88, p. 241405, Dec 2013.
  - [32] Y. Kato, R. C. Myers, D. C. Driscoll, A. C. Gossard, J. Levy, and D. D. Awschalom, "Gigahertz electron spin manipulation using voltage-controlled  $g$ -tensor modulation," *Science*, vol. 299, no. 5610, pp. 1201–1204, 2003.
  - [33] F. Bloch and A. Siegert, "Magnetic resonance for nonrotating fields," *Phys. Rev.*, vol. 57, pp. 522–527, Mar 1940.
  - [34] D. Zeuch, F. Hassler, J. J. Slim, and D. P. DiVincenzo, "Exact rotating wave approximation," *Annals of physics*, vol. 423, p. 168327, 2020.

- [35] L. M. K. Vandersypen, H. Bluhm, J. S. Clarke, A. S. Dzurak, R. Ishihara, A. Morello, D. J. Reilly, L. R. Schreiber, and M. Veldhorst, "Interfacing spin qubits in quantum dots and donors—hot, dense, and coherent," *Npj Quantum Inf.*, vol. 3, pp. 1–10, Sept. 2017.
- [36] D. C. Mattis, *Theory Of Magnetism Made Simple, The: An Introduction To Physical Concepts And To Some Useful Mathematical Methods*. World Scientific Publishing Company, 2006.
- [37] G. Burkard, T. D. Ladd, J. M. Nichol, A. Pan, and J. R. Petta, "Semiconductor spin qubits," *arXiv preprint arXiv:2112.08863*, 2021.
- [38] J. R. Petta, A. C. Johnson, J. M. Taylor, E. A. Laird, A. Yacoby, M. D. Lukin, C. M. Marcus, M. P. Hanson, and A. C. Gossard, "Coherent manipulation of coupled electron spins in semiconductor quantum dots," *Science*, vol. 309, no. 5744, pp. 2180–2184, 2005.
- [39] D. Stepanenko, M. Rudner, B. I. Halperin, and D. Loss, "Singlet-triplet splitting in double quantum dots due to spin-orbit and hyperfine interactions," *Phys. Rev. B*, vol. 85, p. 075416, Feb. 2012.
- [40] G. Burkard, D. Loss, and D. P. DiVincenzo, "Coupled quantum dots as quantum gates," *Physical Review B*, vol. 59, no. 3, p. 2070, 1999.
- [41] M. Taut, "Two electrons in an external oscillator potential: Particular analytic solutions of a coulomb correlation problem," *Physical Review A*, vol. 48, no. 5, p. 3561, 1993.
- [42] F. Gao, J.-H. Wang, H. Watzinger, H. Hu, M. J. Rančić, J.-Y. Zhang, T. Wang, Y. Yao, G.-L. Wang, J. Kukučka, *et al.*, "Site-controlled uniform ge/si hut wires with electrically tunable spin-orbit coupling," *Advanced Materials*, vol. 32, no. 16, p. 1906523, 2020.
- [43] J. C. Abadillo-Uriel, B. Martinez, M. Filippone, and Y.-M. Niquet, "Two-body wigner molecularization in asymmetric quantum dot spin qubits," *Physical Review B*, vol. 104, no. 19, p. 195305, 2021.
- [44] H. E. Ercan, S. N. Coppersmith, and M. Friesen, "Strong electron-electron interactions in si/sige quantum dots," *Phys. Rev. B*, vol. 104, p. 235302, Dec 2021.

- [45] M. Trif, V. N. Golovach, and D. Loss, "Spin-spin coupling in electrostatically coupled quantum dots," *Phys. Rev. B*, vol. 75, p. 085307, Feb 2007.
- [46] M. Veldhorst, C. H. Yang, J. C. C. Hwang, W. Huang, J. P. Dehollain, J. T. Muhonen, S. Simmons, A. Laucht, F. E. Hudson, K. M. Itoh, A. Morello, and A. S. Dzurak, "A two-qubit logic gate in silicon," *Nature*, vol. 526, no. 7573, pp. 410–414, 2015.
- [47] W. Huang, C. H. Yang, K. W. Chan, T. Tanttu, B. Hensen, R. C. C. Leon, M. A. Fogarty, J. C. C. Hwang, F. E. Hudson, K. M. Itoh, A. Morello, A. Laucht, and A. S. Dzurak, "Fidelity benchmarks for two-qubit gates in silicon," *Nature*, vol. 569, no. 7757, pp. 532–536, 2019.
- [48] N. W. Hendrickx, D. P. Franke, A. Sammak, G. Scappucci, and M. Veldhorst, "Fast two-qubit logic with holes in germanium," *Nature*, vol. 577, pp. 487–491, Jan. 2020.
- [49] N. W. Hendrickx, W. I. L. Lawrie, M. Russ, F. van Riggelen, S. L. de Snoo, R. N. Schouten, A. Sammak, G. Scappucci, and M. Veldhorst, "A four-qubit germanium quantum processor," *Nature*, vol. 591, no. 7851, pp. 580–585, 2021.
- [50] B. Hetényi, S. Bosco, and D. Loss, "Anomalous zero-field splitting for hole spin qubits in si and ge quantum dots," *arXiv preprint arXiv:2205.02582*, 2022.
- [51] G. Yang, C.-H. Hsu, P. Stano, J. Klinovaja, and D. Loss, "Long-distance entanglement of spin qubits via quantum hall edge states," *Physical Review B*, vol. 93, no. 7, p. 075301, 2016.
- [52] G. Nicolí, M. S. Ferguson, C. Rössler, A. Wolfertz, G. Blatter, T. Ihn, K. Ensslin, C. Reichl, W. Wegscheider, and O. Zilberberg, "Cavity-mediated coherent coupling between distant quantum dots," *Phys. Rev. Lett.*, vol. 120, p. 236801, Jun 2018.
- [53] J. Yoneda, W. Huang, M. Feng, C. H. Yang, K. W. Chan, T. Tanttu, W. Gilbert, R. C. C. Leon, F. E. Hudson, K. M. Itoh, A. Morello, S. D. Bartlett, A. Laucht, A. Saraiva, and A. S. Dzurak, "Coherent spin qubit transport in silicon," *Nature Communications*, vol. 12, no. 1, p. 4114, 2021.

- [54] I. Seidler, T. Struck, R. Xue, N. Focke, S. Trellenkamp, H. Bluhm, and L. R. Schreiber, "Conveyor-mode single-electron shuttling in Si/SiGe for a scalable quantum computing architecture," *arXiv preprint arXiv:2108.00879*, 2021.
- [55] A. Blais, R.-S. Huang, A. Wallraff, S. M. Girvin, and R. J. Schoelkopf, "Cavity quantum electrodynamics for superconducting electrical circuits: An architecture for quantum computation," *Physical Review A*, vol. 69, no. 6, p. 062320, 2004.
- [56] C. Kloeffer, M. Trif, P. Stano, and D. Loss, "Circuit QED with hole-spin qubits in Ge/Si nanowire quantum dots," *Phys. Rev. B*, vol. 88, p. 241405, Dec. 2013.
- [57] S. E. Nigg, A. Fuhrer, and D. Loss, "Superconducting grid-bus surface code architecture for hole-spin qubits," *Physical review letters*, vol. 118, no. 14, p. 147701, 2017.
- [58] F. Borjans, X. G. Croot, X. Mi, M. J. Gullans, and J. R. Petta, "Resonant microwave-mediated interactions between distant electron spins," *Nature*, vol. 577, no. 7789, pp. 195–198, 2020.
- [59] P. Harvey-Collard, J. Dijkema, G. Zheng, A. Sammak, G. Scappucci, and L. M. K. Vandersypen, "Coherent spin-spin coupling mediated by virtual microwave photons," *Phys. Rev. X*, vol. 12, p. 021026, May 2022.
- [60] S. Bosco, P. Scarlino, J. Klinovaja, and D. Loss, "Fully tunable longitudinal spin-photon interactions in si and ge quantum dots," *arXiv preprint arXiv:2203.17163*, 2022.
- [61] L. Trifunovic, O. Dial, M. Trif, J. R. Wootton, R. Abebe, A. Yacoby, and D. Loss, "Long-Distance Spin-Spin Coupling via Floating Gates," *Phys. Rev. X*, vol. 2, p. 011006, Jan. 2012.
- [62] K. Ono, D. G. Austing, Y. Tokura, and S. Tarucha, "Current Rectification by Pauli Exclusion in a Weakly Coupled Double Quantum Dot System," *Science*, vol. 297, pp. 1313–1317, Aug. 2002.
- [63] L. C. Camenzind, S. Geyer, A. Fuhrer, R. J. Warburton, D. M. Zumbühl, and A. V. Kuhlmann, "A hole spin qubit in a fin field-effect transistor above 4 kelvin," *Nature Electronics*, vol. 5, no. 3, pp. 178–183, 2022.

- [64] J. Elzerman, R. Hanson, L. Willems van Beveren, B. Witkamp, L. Vandersypen, and L. P. Kouwenhoven, "Single-shot read-out of an individual electron spin in a quantum dot," *nature*, vol. 430, no. 6998, pp. 431–435, 2004.
- [65] M. Field, C. Smith, M. Pepper, D. Ritchie, J. Frost, G. Jones, and D. Hasko, "Measurements of coulomb blockade with a noninvasive voltage probe," *Physical Review Letters*, vol. 70, no. 9, p. 1311, 1993.
- [66] N. Hendrickx, W. Lawrie, L. Petit, A. Sammak, G. Scappucci, and M. Veldhorst, "A single-hole spin qubit," *Nature communications*, vol. 11, no. 1, pp. 1–6, 2020.
- [67] R. Schoelkopf, P. Wahlgren, A. Kozhevnikov, P. Delsing, and D. Prober, "The radio-frequency single-electron transistor (rf-set): A fast and ultrasensitive electrometer," *science*, vol. 280, no. 5367, pp. 1238–1242, 1998.
- [68] D. Reilly, C. Marcus, M. Hanson, and A. Gossard, "Fast single-charge sensing with a rf quantum point contact," *Applied Physics Letters*, vol. 91, no. 16, p. 162101, 2007.
- [69] M. Cassidy, A. Dzurak, R. Clark, K. Petersson, I. Farrer, D. Ritchie, and C. Smith, "Single shot charge detection using a radio-frequency quantum point contact," *Applied Physics Letters*, vol. 91, no. 22, p. 222104, 2007.
- [70] C. Barthel, M. Kjærgaard, J. Medford, M. Stopa, C. M. Marcus, M. Hanson, and A. C. Gossard, "Fast sensing of double-dot charge arrangement and spin state with a radio-frequency sensor quantum dot," *Physical Review B*, vol. 81, no. 16, p. 161308, 2010.
- [71] M. House, I. Bartlett, P. Pakkiam, M. Koch, E. Peretz, J. van der Heijden, T. Kobayashi, S. Rogge, and M. Simmons, "High-sensitivity charge detection with a single-lead quantum dot for scalable quantum computation," *Physical Review Applied*, vol. 6, no. 4, p. 044016, 2016.
- [72] A. Noiri, K. Takeda, J. Yoneda, T. Nakajima, T. Koder, and S. Tarucha, "Radio-frequency-detected fast charge sensing in undoped silicon quantum dots," *Nano Letters*, vol. 20, no. 2, pp. 947–952, 2020. PMID: 31944116.

- [73] D. Keith, M. House, M. Donnelly, T. Watson, B. Weber, and M. Simmons, "Single-shot spin readout in semiconductors near the shot-noise sensitivity limit," *Physical Review X*, vol. 9, no. 4, p. 041003, 2019.
- [74] A. Morello, J. J. Pla, F. A. Zwanenburg, K. W. Chan, K. Y. Tan, H. Huebl, M. Möttönen, C. D. Nugroho, C. Yang, J. A. Van Donckelaar, *et al.*, "Single-shot readout of an electron spin in silicon," *Nature*, vol. 467, no. 7316, pp. 687–691, 2010.
- [75] L. Vukusic, J. Kukucka, H. Watzinger, J. M. Milem, F. Schaffler, and G. Katsaros, "Single-shot readout of hole spins in ge," *Nano letters*, vol. 18, no. 11, pp. 7141–7145, 2018.
- [76] O. Zilberberg, A. Romito, and Y. Gefen, "Charge sensing amplification via weak values measurement," *Phys. Rev. Lett.*, vol. 106, p. 080405, Feb 2011.
- [77] K. D. Petersson, C. G. Smith, D. Anderson, P. Atkinson, G. A. C. Jones, and D. A. Ritchie, "Charge and spin state readout of a double quantum dot coupled to a resonator," *Nano Letters*, vol. 10, pp. 2789–2793, 08 2010.
- [78] J. I. Colless, A. C. Mahoney, J. M. Hornibrook, A. C. Doherty, H. Lu, A. C. Gossard, and D. J. Reilly, "Dispersive readout of a few-electron double quantum dot with fast rf gate sensors," *Phys. Rev. Lett.*, vol. 110, p. 046805, Jan 2013.
- [79] G. Zheng, N. Samkharadze, M. L. Noordam, N. Kalhor, D. Brousse, A. Sammak, G. Scappucci, and L. M. K. Vandersypen, "Rapid gate-based spin read-out in silicon using an on-chip resonator," *Nature Nanotechnology*, vol. 14, no. 8, pp. 742–746, 2019.
- [80] A. West, B. Hensen, A. Jouan, T. Tanttu, C.-H. Yang, A. Rossi, M. F. Gonzalez-Zalba, F. Hudson, A. Morello, D. J. Reilly, and A. S. Dzurak, "Gate-based single-shot readout of spins in silicon," *Nat. Nanotechnol.*, vol. 14, pp. 437–441, May 2019.
- [81] E. Magesan, J. M. Gambetta, and J. Emerson, "Characterizing quantum gates via randomized benchmarking," *Physical Review A*, vol. 85, no. 4, p. 042311, 2012.



- [82] R. Blume-Kohout, J. K. Gamble, E. Nielsen, K. Rudinger, J. Mizrahi, K. Fortier, and P. Maunz, "Demonstration of qubit operations below a rigorous fault tolerance threshold with gate set tomography," *Nature communications*, vol. 8, no. 1, pp. 1–13, 2017.
- [83] A. Abragam, *The principles of nuclear magnetism*. No. 32, Oxford university press, 1961.
- [84] Y. Makhlin, G. Schön, and A. Shnirman, "Dissipative effects in josephson qubits," *Chemical Physics*, vol. 296, no. 2, pp. 315 – 324, 2004.
- [85] G. Ithier, E. Collin, P. Joyez, P. Meeson, D. Vion, D. Esteve, F. Chiarello, A. Shnirman, Y. Makhlin, J. Schrieffer, *et al.*, "Decoherence in a superconducting quantum bit circuit," *Physical Review B*, vol. 72, no. 13, p. 134519, 2005.
- [86] G. S. Uhrig, "Keeping a quantum bit alive by optimized  $\pi$ -pulse sequences," *Physical Review Letters*, vol. 98, no. 10, p. 100504, 2007.
- [87] Ł. Cywiński, R. M. Lutchyn, C. P. Nave, and S. D. Sarma, "How to enhance dephasing time in superconducting qubits," *Physical Review B*, vol. 77, no. 17, p. 174509, 2008.
- [88] J. Fischer, W. A. Coish, D. V. Bulaev, and D. Loss, "Spin decoherence of a heavy hole coupled to nuclear spins in a quantum dot," *Phys. Rev. B*, vol. 78, p. 155329, Oct. 2008.
- [89] F. Maier and D. Loss, "Effect of strain on hyperfine-induced hole-spin decoherence in quantum dots," *Phys. Rev. B*, vol. 85, p. 195323, May 2012.
- [90] S. Bosco and D. Loss, "Fully tunable hyperfine interactions of hole spin qubits in si and ge quantum dots," *Physical review letters*, vol. 127, no. 19, p. 190501, 2021.
- [91] J. Yoneda, K. Takeda, T. Otsuka, T. Nakajima, M. R. Delbecq, G. Allison, T. Honda, T. Koderu, S. Oda, Y. Hoshi, N. Usami, K. M. Itoh, and S. Tarucha, "A quantum-dot spin qubit with coherence limited by charge noise and fidelity higher than 99.9%," *Nat. Nanotechnol.*, vol. 13, p. 102, Feb. 2018.

- [92] X. Mi, M. Benito, S. Putz, D. M. Zajac, J. M. Taylor, G. Burkard, and J. R. Petta, "A coherent spin-photon interface in silicon," *Nature*, vol. 555, no. 7698, pp. 599–603, 2018.
- [93] E. J. Connors, J. Nelson, L. F. Edge, and J. M. Nichol, "Charge-noise spectroscopy of si/sige quantum dots via dynamically-decoupled exchange oscillations," *Nature communications*, vol. 13, no. 1, pp. 1–9, 2022.
- [94] F. Maier, C. Kloeffel, and D. Loss, "Tunable  $g$  factor and phonon-mediated hole spin relaxation in ge/si nanowire quantum dots," *Phys. Rev. B*, vol. 87, p. 161305, Apr 2013.
- [95] J. Li, B. Venitucci, and Y.-M. Niquet, "Hole-phonon interactions in quantum dots: Effects of phonon confinement and encapsulation materials on spin-orbit qubits," *Physical Review B*, vol. 102, no. 7, p. 075415, 2020.
- [96] V. Kornich, C. Kloeffel, and D. Loss, "Phonon-mediated decay of singlet-triplet qubits in double quantum dots," *Physical Review B*, vol. 89, no. 8, p. 085410, 2014.
- [97] P. Stano and D. Loss, "Review of performance metrics of spin qubits in gated semiconducting nanostructures," *arXiv preprint arXiv:2107.06485*, 2021.
- [98] C. H. Yang, R. Leon, J. Hwang, A. Saraiva, T. Tanttu, W. Huang, J. Camirand Lemyre, K. W. Chan, K. Tan, F. E. Hudson, *et al.*, "Operation of a silicon quantum processor unit cell above one kelvin," *Nature*, vol. 580, no. 7803, pp. 350–354, 2020.
- [99] L. Petit, H. G. J. Eenink, M. Russ, W. I. L. Lawrie, N. W. Hendrickx, S. G. J. Philips, J. S. Clarke, L. M. K. Vandersypen, and M. Veldhorst, "Universal quantum logic in hot silicon qubits," *Nature*, vol. 580, no. 7803, pp. 355–359, 2020.  
N. Hendrickx, D. Franke, A. Sammak, G. Scappucci, and M. Veldhorst, "Fast two-qubit logic with holes in germanium," *Nature*, vol. 577, no. 7791, pp. 487–491, 2020.
- [100] F. Sebastiano, J. Van Dijk, B. Patra, J. van Staveren, X. Xue, C. Almudever, G. Scappucci, M. Veldhorst, L. Vandersypen,

- A. Vladimirescu, *et al.*, "Cryo-cmos interfaces for large-scale quantum computers," in *2020 IEEE International Electron Devices Meeting (IEDM)*, pp. 25–2, IEEE, 2020.
- [101] B. Patra, R. M. Incandela, J. P. Van Dijk, H. A. Homulle, L. Song, M. Shahmohammadi, R. B. Staszewski, A. Vladimirescu, M. Babaie, F. Sebastiano, *et al.*, "Cryo-cmos circuits and systems for quantum computing applications," *IEEE Journal of Solid-State Circuits*, vol. 53, no. 1, pp. 309–321, 2017.
- [102] E. Charbon, F. Sebastiano, A. Vladimirescu, H. Homulle, S. Visser, L. Song, and R. M. Incandela, "Cryo-cmos for quantum computing," in *2016 IEEE International Electron Devices Meeting (IEDM)*, pp. 13–5, IEEE, 2016.
- [103] B. Patra, J. P. Van Dijk, A. Corna, X. Xue, N. Samkharadze, A. Sammak, G. Scappucci, M. Veldhorst, L. M. Vandersypen, M. Babaie, *et al.*, "A scalable cryo-cmos 2-to-20ghz digitally intensive controller for  $4 \times 32$  frequency multiplexed spin qubits/transmons in 22nm finfet technology for quantum computers," in *2020 IEEE International Solid-State Circuits Conference, ISSCC 2020*, pp. 304–306, Institute of Electrical and Electronics Engineers (IEEE), 2020.
- [104] H. Homulle, S. Visser, and E. Charbon, "A cryogenic 1 gsa/s, soft-core fpga adc for quantum computing applications," *IEEE Transactions on Circuits and Systems I: Regular Papers*, vol. 63, no. 11, pp. 1854–1865, 2016.
- [105] S. J. Pauka, K. Das, R. Kalra, A. Moini, Y. Yang, M. Trainer, A. Bousquet, C. Cantaloube, N. Dick, G. C. Gardner, M. J. Manfra, and D. J. Reilly, "A cryogenic cmos chip for generating control signals for multiple qubits," *Nature Electronics*, vol. 4, no. 1, pp. 64–70, 2021.
- [106] M. Veldhorst, H. G. J. Eenink, C. H. Yang, and A. S. Dzurak, "Silicon cmos architecture for a spin-based quantum computer," *Nature Communications*, vol. 8, no. 1, p. 1766, 2017.
- [107] P. Szumniak, J. Pawłowski, S. Bednarek, and D. Loss, "Long-distance entanglement of soliton spin qubits in gated nanowires," *Physical Review B*, vol. 92, no. 3, p. 035403, 2015.

- [108] R. McNeil, M. Kataoka, C. Ford, C. Barnes, D. Anderson, G. Jones, I. Farrer, and D. Ritchie, "On-demand single-electron transfer between distant quantum dots," *Nature*, vol. 477, no. 7365, pp. 439–442, 2011.
- [109] J. M. Boter, J. P. Dehollain, J. P. van Dijk, T. Hensgens, R. Versluis, J. S. Clarke, M. Veldhorst, F. Sebastiano, and L. M. Vandersypen, "A sparse spin qubit array with integrated control electronics," in *2019 IEEE International Electron Devices Meeting (IEDM)*, pp. 31–4, IEEE, 2019.
- [110] P. W. Shor, "Scheme for reducing decoherence in quantum computer memory," *Physical review A*, vol. 52, no. 4, p. R2493, 1995.
- [111] A. G. Fowler, M. Mariantoni, J. M. Martinis, and A. N. Cleland, "Surface codes: Towards practical large-scale quantum computation," *Physical Review A*, vol. 86, no. 3, p. 032324, 2012.
- [112] D. S. Wang, A. G. Fowler, and L. C. Hollenberg, "Surface code quantum computing with error rates over 1%," *Physical Review A*, vol. 83, no. 2, p. 020302, 2011.
- [113] A. G. Fowler, A. C. Whiteside, and L. C. Hollenberg, "Towards practical classical processing for the surface code," *Physical review letters*, vol. 108, no. 18, p. 180501, 2012.

## CHAPTER 2

# Exchange interaction of hole-spin qubits in double quantum dots

*Adapted from:*  
Bence Hetényi, Christoph Kloeffel, and Daniel Loss  
“Exchange interaction of hole-spin qubits in double quantum dots in highly anisotropic semiconductors”,  
Phys. Rev. Research **2**, 033036 (2020)

We study the exchange interaction between two hole-spin qubits in a double quantum dot setup in a silicon nanowire in the presence of magnetic and electric fields. Based on symmetry arguments we show that there exists an effective spin that is conserved even in highly anisotropic semiconductors, provided that the system has a twofold symmetry with respect to the direction of the applied magnetic field. This finding facilitates the definition of qubit basis states and simplifies the form of exchange interaction for two-qubit gates in coupled quantum dots. If the magnetic field is applied along a generic direction, cubic anisotropy terms act as an effective spin-orbit interaction introducing novel exchange couplings even for an inversion symmetric setup. Considering the example of a silicon nanowire double dot, we present the relative strength of these anisotropic exchange interaction terms and calculate the fidelity of the  $\sqrt{\text{SWAP}}$  gate. Furthermore, we show that the anisotropy-induced spin-orbit effects can be comparable to that of the direct Rashba spin-orbit interaction for experimentally feasible electric field strengths.

## 2.1 Introduction

Over the last two decades localized spins in quantum dots (QDs) became a promising candidate for scalable quantum computing [1,2]. Electron spins confined in semiconductor heterostructures benefit from the feasibility of coherent control via electric-dipole-induced spin resonance (EDSR) [3–6] and exchange based two-qubit gates [7–9]. On the other hand, besides charge noise and phonon induced decoherence, electrons are also exposed to fluctuating nuclear spins [10–12].

Holes confined in quantum dots [13,14] have recently attracted much attention due to the possibility of fast single-qubit control by virtue of a strong spin-orbit interaction (SOI) [15–21], and slow decoherence owing to the suppressed hyperfine interaction [19,22–25]. Single-shot readout [26], exchange-coupled quantum dots [27,28] and two-qubit gates [29] have recently been realized in systems, where the heavy-hole (HH) and light-hole (LH) states are well separated.

As opposed to planar QDs, eigenstates of holes being strongly confined in more than one directions have significant contributions from both the HH and LH states [30,31]. These systems benefit from an even stronger Rashba type of SOI that relies on the HH-LH mixing and is not suppressed by the fundamental band gap [32,33]. In agreement with recent experiments [15,17,34–41], Si and Ge/Si core/shell nanowires (NWs) are particularly promising platforms for such low-dimensional hole systems. Remarkably, these NWs and QDs therein can be formed with a complementary metal-oxide-semiconductor (CMOS) compatible fabrication process [17,36,38,42,43], which indicates an exceptional scalability. Furthermore, both Si and Ge are bulk inversion symmetric, leading to a suppressed piezoelectric interaction between holes and phonons, and can be isotopically enriched, allowing to reduce the number of nuclear spins to nearly zero [44–47].

Two-qubit gates between hole-spin qubits in NW QDs can be implemented in different ways. For example, the qubits can be coupled over long distances via floating metallic gates [48] or via the cavity photons of transmission-line resonators [16,49] by harnessing the strong, direct Rashba SOI (DRSOI) [32,33]. Nearby qubits, on the other hand, can be coupled by electrically controlling the wave function overlap and thereby inducing an exchange interaction. However, this important possibility has not been explored yet since the HH-LH mixing renders the interaction multifaceted.

In this paper, we address the question how the HH-LH mixing affects the form of the exchange interaction in tunnel-coupled QDs. This question is relevant not only for two-qubit operations but also for, e.g., the implementation of singlet-triplet qubits [50–52] and spin-to-charge readout schemes [1, 7, 53] with holes. In the most general case the form

$$H_{(1,1)} = \frac{1}{4} \boldsymbol{\sigma}^L \cdot \bar{\mathbf{J}} \boldsymbol{\sigma}^R + \frac{1}{2} (\boldsymbol{\Delta}^L \cdot \boldsymbol{\sigma}^L + \boldsymbol{\Delta}^R \cdot \boldsymbol{\sigma}^R) \quad (2.1)$$

needs to be assumed for the interaction between the qubit basis-states  $|0\rangle$  and  $|1\rangle$  of the left ( $L$ ) and right ( $R$ ) QDs, where  $\bar{\mathbf{J}}$  is the exchange-matrix and the coefficients in the single-qubit part  $\boldsymbol{\Delta}^{L(R)}$  are related to the  $g$ -tensor  $\bar{\mathbf{g}}^{L(R)}$  via  $\boldsymbol{\Delta}^{L(R)} = \mu_B \bar{\mathbf{g}}^{L(R)} \mathbf{B}$ . The Pauli-matrices (e.g.,  $\sigma_z^L = |0_L\rangle\langle 0_L| - |1_L\rangle\langle 1_L|$ ) are acting on the energetically lowest two eigenstates of the QDs.

For electrons, the exchange matrix obtains the simple form  $J_{ij} = JR_{ij}(\mathbf{n}, \theta)$ , where the parameters of the rotation  $R_{ij}$  depend on the spin-orbit couplings [54]. However due to the strong anisotropy of the hole states in materials like silicon, the exchange interaction acquires anisotropic corrections even in the case of an inversion symmetric setup. As reported earlier, these anisotropic effects can enhance the role of spatial symmetries in the theoretical description [38, 55, 56].

We discuss the possible symmetries of a generic double quantum dot (DQD) setup. If the confinement, the crystal structure, and the external fields respect the same symmetry, an effective spin can be associated to the qubit states of each QD. The conservation of this effective spin allows one to identify selection rules for the exchange interaction  $\bar{\mathbf{J}}$ .

We consider coupled hole-spin qubits in a silicon NW and identify the high symmetry axes of the magnetic field along which the effective spin is conserved. However, effective spin projections can get mixed upon application of an external electric field (inducing DRSOI), or by changing the direction of the magnetic field due to crystalline anisotropy (anisotropy-induced spin mixing). One of our central results is shown in Fig. 2.4, where we present the effect of the hitherto neglected anisotropy-induced spin mixing mechanism on the exchange interaction  $\bar{\mathbf{J}}$  and the induced Zeeman splittings  $\boldsymbol{\Delta}$ . This mixing will lead to anisotropic corrections to the exchange interaction even in the presence of inversion symmetry. Furthermore, we compare our results obtained for silicon NWs with that of Ge/Si core/shell NWs, where crystalline anisotropy manifests itself rather weakly in the valence band.

If coupling is established between two QDs each hosting a single hole-spin qubit, the exchange interaction can be utilized to implement a fundamental entangling gate such as the  $\sqrt{\text{SWAP}}$  [1]. However, in silicon the anisotropic corrections can lead to systematic gate errors limiting the fidelity of the  $\sqrt{\text{SWAP}}$  gate. We calculate the gate fidelities in the coherent system and find that anisotropic corrections can be mitigated if the gate is sufficiently fast.

This paper is organized as follows: In Sec. 2.2 we review the simple model of conduction band electrons and present the Hamiltonian of the valence band holes together with the commonly used axial approximation. In Sec. 2.3 we introduce an effective spin and discuss its advantages for the application as spin qubits. Projecting the Hamiltonian of coupled quantum dots to the low-energy basis in Secs. 2.4 and 2.5, we study the selection rules that apply for the exchange interaction if the quantum dots respect a mutual twofold symmetry. In Sec. 2.6 we propose a symmetry-decomposition of the Hamiltonian that reveals the different effective spin mixing terms, compare the spin mixing effect of the cubic anisotropy and the DRSOI, present the relative energy scales of the anisotropic corrections to the exchange interaction, and calculate the anisotropy-limited fidelities of a  $\sqrt{\text{SWAP}}$  gate. We conclude with a few remarks and a short summary in Secs. 6.5 and 6.6. Technical details are deferred to Apps. 2.A-2.H.

## 2.2 Single hole-spin qubit

We consider a single hole confined by electric gates either in a NW or in a two-dimensional hole gas in a heterostructure. Provided that the energy scale associated with the temperature is much lower than the orbital splittings, the hole will occupy the lowest orbital state. If the confinement is significantly stronger along one or two axes, the lowest state will retain only two-fold degeneracy in the absence of magnetic field due to the different effective masses corresponding to the HH and the LH states [32,33]. Splitting of these eigenstates by magnetic field establishes an effective two-level system  $|0\rangle, |1\rangle$  to be referred to as hole-spin qubit later on.

First we consider the general Hamiltonian of a single quasiparticle, an electron (+) or a hole (−) confined in a QD

$$H_{\text{QD}} = H_{\text{b}}(\mathbf{k}, \hat{\mathbf{J}}) + H_{\text{Z}}(\hat{\mathbf{J}}, \mathbf{B}) \pm e\mathbf{E} \cdot \mathbf{r} + V_{\text{QD}}(\mathbf{r}) + H^{\text{c}}, \quad (2.2)$$



where  $H_b(\mathbf{k}, \hat{\mathbf{J}})$  is the bulk Hamiltonian of either the conduction band or the valence bands with the vector operator  $\hbar \hat{\mathbf{J}}$  combining the atomic orbital angular momentum [ $l = 0(1)$  for the conduction band (valence bands)] and the spin. The crystal-momentum including the vector potential  $\mathbf{A}$  is  $\hbar \mathbf{k} = -i\hbar \nabla + e\mathbf{A}$ , where  $e$  is the positive elementary charge. The Zeeman term  $H_Z(\hat{\mathbf{J}}, \mathbf{B})$  contains the spherical and anisotropic corrections coupling the magnetic field  $\mathbf{B} = \nabla \times \mathbf{A}$  to the angular momentum  $\hbar \hat{\mathbf{J}}$ . The electric field is taken into account via the term  $\pm e\mathbf{E} \cdot \mathbf{r}$  and the inversion symmetric confinement potential  $V_{\text{QD}}(\mathbf{r})$ , where  $\mathbf{r}$  is the position operator of the quasiparticle. The last term  $H^c$  contains further corrections such as the Rashba and the Dresselhaus spin-orbit interaction (which are higher order terms in the multi-band perturbation theory) as well as the strain and the interface effects.

In the case of the conduction band the  $s$ -wave property of the Bloch-functions (i.e., zero orbital angular momentum) implies that the angular momentum components are given by the three Pauli matrices i.e.,  $\hbar \hat{J}_i = \frac{\hbar}{2} \sigma_i$ . Since the Pauli matrices together with the identity matrix form a complete basis, the effective Hamiltonian of the conduction band electrons in a homogeneous magnetic field can be written in the simple form

$$H_{\text{cond}}(\mathbf{k}) + H_Z(\hat{\mathbf{J}}, \mathbf{B}) = \frac{\hbar^2 k^2}{2m^*} + g^* \mu_B \mathbf{B} \cdot \hat{\mathbf{J}}, \quad (2.3)$$

with the effective band mass  $m^*$  and  $g$ -factor  $g^*$ . The special property of the Pauli matrices then imply that the Hamiltonian of Eq. (2.3) has continuous axial symmetry (the Hamiltonian commutes with the spin projection  $\hat{J}_B$  along the magnetic field).

In the presence of magnetic field the Luttinger-Kohn Hamiltonian  $H_{\text{LK}} + H_Z$  describing the top of the HH-LH bands for cubic crystals can be written as

$$\begin{aligned} H_{\text{LK}}(\mathbf{k}, \hat{\mathbf{J}}) + H_Z(\hat{\mathbf{J}}, \mathbf{B}) = & \\ & \frac{\hbar^2}{2m} \left[ \left( \gamma_1 + \frac{5}{2} \bar{\gamma} \right) k^2 - 2\bar{\gamma}(\mathbf{k} \cdot \hat{\mathbf{J}})^2 \right] \\ & + (2\kappa + \bar{\gamma}) \mu_B \mathbf{B} \cdot \hat{\mathbf{J}} + \Delta\gamma K(\mathbf{k}, \hat{\mathbf{J}}) + 2q\mu_B \mathbf{B} \cdot \hat{\mathbf{J}} \end{aligned} \quad (2.4)$$

where  $m$  is the bare electron mass,  $\gamma_1$  is the first Luttinger parameter,  $\bar{\gamma} = (2\gamma_2 + 3\gamma_3)/5$  is the averaged Luttinger parameter, and  $\Delta\gamma = \gamma_3 - \gamma_2$  is the prefactor of the terms with cubic symmetry [57–61]. The spin-3/2

vector operator  $\hbar \hat{\mathbf{J}}$  is combining the atomic orbital angular momentum ( $l = 1$ ) and the spin. The Zeeman part  $H_Z(\hat{\mathbf{J}}, \mathbf{B}) = 2\kappa\mu_B \mathbf{B} \cdot \hat{\mathbf{J}} + 2q\mu_B \mathbf{B} \cdot \hat{\mathbf{J}}$  is composed of the isotropic and anisotropic terms [62] with coefficients  $\kappa$  and  $q$ , respectively.

The first two terms of the Hamiltonian in Eq. (2.4) are invariant under arbitrary rotations around the magnetic field axis i.e.,  $[H^{(1,2)}, e^{-i\phi\hat{F}_B}] = 0$  holds for any angle  $\phi$ , where  $\hbar \hat{F}_B$  is the total angular momentum  $\hbar \hat{\mathbf{F}} = \hbar \hat{\mathbf{J}} + \hbar \hat{\mathbf{L}}$  projected along the magnetic field, with the orbital angular momentum being  $\hbar \hat{\mathbf{L}} = -i\hbar \mathbf{r} \times \nabla$  [61]. For materials like Ge, InAs, and GaAs these terms give the main contributions, since  $\Delta\gamma \ll \bar{\gamma}$  and  $q \ll |\kappa|$  (e.g., the anisotropy parameters  $\Delta\gamma/\bar{\gamma}$  obtained from Ref. [63] are 0.28, 0.091, and 0.31, respectively), and the last two terms are treated only perturbatively within the framework of the *axial approximation* [30, 31, 63–65].

While for electrons even the spin  $\hbar \hat{J}_B$  is approximately conserved, only the total angular momentum conservation could be considered for the valence band states. However, corrections due to cubic anisotropy can play important role [20], especially for materials with strong cubic anisotropy (e.g., silicon where  $\Delta\gamma/\bar{\gamma} = 1.1$ ) corrections to the axial approximation cannot be treated perturbatively. We wish to identify an effective spin as a good quantum number that is conserved by the Hamiltonian in Eq. (2.4), for the highly anisotropic case. For this we consider the point symmetry group of the QD system in the next section.

## 2.3 Symmetry considerations

To properly define a qubit, we first consider the symmetries of the bulk crystal in the presence of magnetic and electric fields and identify high symmetry axes. This will allow us to identify an effective spin  $\alpha = \text{mod}_2(F_B) \in \{-1/2, 1/2\}$  [66], which is related to the eigenvalues of a twofold symmetry operator such as  $D(C_{2B}) = e^{-i\pi\hat{F}_B}$ , where  $\hat{F}_B$  is the total angular momentum operator and has half-odd-integer eigenvalues  $F_B$ . The eigenstates in a QD are also characterized by this quantum number  $\alpha$  and can be used as a qubit, provided that the confinement respects the considered symmetry. Finally, we present DQD geometries where a twofold symmetry is maintained implying spin selection rules for the interaction between the two quantum dots.

The Bravais lattice of a bulk crystal is defined by discrete translations in the three spatial directions. The Bravais lattice can be invariant un-

der further symmetry transformations, e.g.,  $N$ -fold rotations  $C_{Na}$  about an axis  $a$ , inversion  $I$ , or their combinations, the so called roto-reflections  $S_{Na} = I \cdot C_{Na}$ . The set of symmetry elements taking the lattice into itself constitute the point group of the crystal [67]. The external fields can also be described in the language of point groups as follows. The homogeneous electric and magnetic fields  $\mathbf{E}$  and  $\mathbf{B}$  are invariant under any rotations around their axis. In addition,  $\mathbf{E}$  is symmetric and under reflections with respect to any mirror plane that contains its axis. However, since  $\mathbf{B}$  is a pseudo-vector it only respects inversion symmetry and reflection symmetry with respect to the single mirror plane being perpendicular to it.

Comparing the symmetries of a cubic crystal with that of the external fields one obtains the reduced point group of the crystal in the presence of external fields which we summarize in Tab. 2.1 for different directions of the external fields. The resulting point group is non-trivial, only if the magnetic field is applied along a high-symmetry axis, e.g., the point group  $C_4$ , which contains the elements of a four-fold rotation around the axis of the magnetic field  $\mathbf{B}$ , i.e.,  $C_4 = \{E, C_{4B}, C_{2B}, C_{4B}^3\}$ , where  $E$  is the identity element.

	$B \parallel \langle 100 \rangle$	$B \parallel \langle 110 \rangle$	$B \parallel \langle 111 \rangle$	other
$E = 0$	$C_{4h} \rightarrow \alpha_4$	$C_{2h} \rightarrow \alpha$	$C_{3i} \rightarrow \alpha_3$	$C_i$
$E \parallel B$	$C_4 \rightarrow \alpha_4$	$C_2 \rightarrow \alpha$	$C_3 \rightarrow \alpha_3$	$C_1$
$E \perp B$	$C_s \rightarrow \alpha$	$C_s \rightarrow \alpha$	$C_1$	$C_1$

Table 2.1: Reduction of the cubic point group (using Schoenflies symbols) with diamond structure  $O_h$  upon application of external electric and magnetic fields [63]. To each point group containing an  $N$ -fold symmetry one can associate (indicated by an arrow) a generalized effective spin  $\alpha_N = \text{mod}_N(F_B)$  as discussed in App. 2.A. The special case of a two-level system in the ground state of a single QD with  $\alpha \equiv \alpha_2$  is used here as qubit basis.

We have seen, that the bulk crystal can have a non-trivial point group even if external fields are applied. Moreover, if we consider a quasi-particle confined in a QD, the point group of this system consists of the symmetry elements that respect the symmetries of the crystal, the fields, and the confinement (i.e., the intersection of the corresponding point groups). Fig. 2.1 illustrates confinement geometries respecting only a single twofold symmetry of the magnetic field. The resulting point

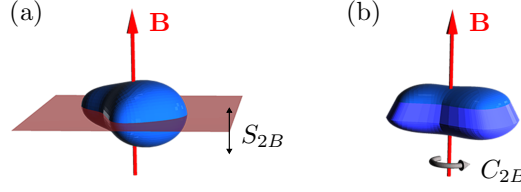


Figure 2.1: Sketch of single QDs with two-fold symmetry  $\mathcal{R}_2$  in the presence of a magnetic field  $\mathbf{B}$  (red) where the blue objects illustrate the shape of the QDs in real space, e.g., the geometry of the confinement or the charge density of the confined holes. (a) The QD possesses a mirror symmetry  $\mathcal{R}_2 = S_{2B}$ ; the only direction of the magnetic field respecting the symmetry of the QD is perpendicular to the symmetry plane (red transparent). (b) The QD possesses a twofold rotation symmetry  $\mathcal{R}_2 = C_{2B}$ ; the only direction of the magnetic field respecting the symmetry is along the symmetry axis (red).

group is  $S_2 = \{E, S_{2B}\}$  for the system in Fig. 2.1(a) and  $C_2 = \{E, C_{2B}\}$  for Fig. 2.1(b).

If  $\mathcal{R}_2 \in \{C_{2B}, S_{2B}\}$  is a twofold symmetry element of the point group of the QD system, the Hamiltonian of Eq. (2.2) has to commute with the symmetry operator  $D(\mathcal{R}_2)$ , the representation of  $\mathcal{R}_2$  on the Hilbert space [67]. As a consequence, the (non-degenerate) eigenstates  $|m\rangle \in \{|0\rangle, |1\rangle, |2\rangle, \dots\}$  of the Hamiltonian are also eigenstates of  $D(\mathcal{R}_2)$ ,

$$D(\mathcal{R}_2) |m\alpha\rangle = e^{-i\pi\alpha} |m\alpha\rangle, \quad (2.5)$$

where  $\alpha = \text{mod}_2(F_B)$  is a spin-like quantum number of the state  $|m\alpha\rangle \equiv |m\rangle$ , where, again,  $\alpha = \pm 1/2$ . Furthermore, it can be shown that the two states of a Kramers doublet (states that are transformed to each other by time-reversal) correspond to effective spin  $\alpha$  and  $-\alpha$  (see App. 2.B). With this finding we conclude that spin qubits can be defined as the lowest Kramers doublet of a quantum dot in any crystal or confinement geometry, as long as a twofold symmetry is preserved in the system.

The effective spin  $\alpha$  is rooted in the discrete rotational (roto-reflectional) symmetry and gives rise to a discrete conservation law for the total angular momentum expressed as  $\alpha = \text{mod}_2(F_B)$ . This relation can be proven in general for an  $N$ -fold symmetry axis (with  $N \geq 2$ ) which gives rise to a quantum number  $\alpha_N = \text{mod}_N(F_B)$  that is conserved modulo  $N$ . This result can be seen as Bloch's theorem for angular momenta (see App. 2.A for further details).

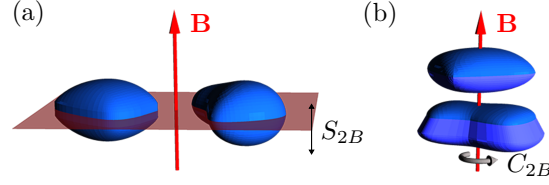


Figure 2.2: DQD geometries where the symmetry-induced quantum numbers  $\alpha_{L(R)} = \pm 1/2$  are conserved and can be used to label a qubit in each QD. The DQD axis (a) lies in the symmetry plane (red transparent plane) that is perpendicular to the magnetic field  $\mathbf{B}$  or (b) coincides with both the magnetic field and the twofold rotation axis.

The interaction between holes with their effective spin gives rise to matrix elements of the interaction which satisfy certain selection rules due to the underlying conservation laws. In particular, we find that the matrix elements for the Hamiltonian of coupled QDs  $H_{\text{DQD}}$  obey the following selection rules:

$$\langle m\alpha, n\beta | H_{\text{DQD}} | p\chi, q\xi \rangle \propto \delta_{0, \text{mod}_2(\alpha+\beta-\chi-\xi)}, \quad (2.6)$$

provided that the DQD setup respects the twofold symmetry of the left and right QDs (for details see App. 2.C). The two-particle states above,  $|m\alpha, n\beta\rangle = |m\alpha\rangle_1 \otimes |n\beta\rangle_2$ , are product states of the single-particle states  $|m\alpha\rangle_1$  and  $|n\beta\rangle_2$  for the first and second particle, respectively. The indices  $m, n, p, q \in \{0_L, 0_R, 1_L, 1_R, 2_L, \dots\}$  label the single-particle eigenstates of the left or right QD, and  $\alpha, \beta, \chi, \xi = \pm 1/2$  stand for the effective spins associated with the single-particle states.

We have seen that the point group of the crystal may contain two-, three- or fourfold symmetry axes, even if external fields are applied. However, the confinement potential defining the DQD should also respect these symmetries in order to benefit from the selection rules given in Eq. (2.6). A DQD setup can obey a twofold symmetry in two ways: (i) The DQD axis (i.e., the axis connecting the centers of the two coupled QDs) lies in the common symmetry plane of the QDs being perpendicular to the magnetic field [as illustrated in Fig. 2.2(a)]. (ii) The DQD axis coincides with the common rotation axis, see Fig. 2.2(b).

## 2.4 Low-energy basis of a DQD

In order to determine the interaction between the two qubits in a DQD system the low-energy solutions of the following Hamiltonian [68] have to be considered,

$$H_{\text{DQD}} = H_L(1) + \delta V_L(1) + H_R(2) + \delta V_R(2) + C(1, 2), \quad (2.7)$$

where  $H_{L(R)}$  is the single-QD Hamiltonian in Eq. (2.2) of the left (right) QD with  $V_{\text{QD}} = V_{L(R)}$ ,  $\delta V_{L(R)} = V_{\text{DQD}} - V_{L(R)}$  is the difference between the double- and single-dot potentials, and  $C(1, 2) = e^2/(4\pi\epsilon|\mathbf{r}_1 - \mathbf{r}_2|)$  is the Coulomb interaction with the single-particle coordinates  $\mathbf{r}_{1,2}$  and the dielectric constant  $\epsilon = \epsilon_0\epsilon_r$ , where  $\epsilon_0$  is the vacuum permittivity.

In order to construct a basis for the low-energy effective Hamiltonian of the DQD, the energetically lowest eigenstates (for qubits)  $|0_L\rangle$ ,  $|1_L\rangle$  of the single QD Hamiltonian  $H_L$  need to be orthonormalized with respect to the ones in the right well  $|0_R\rangle$ ,  $|1_R\rangle$  [69]. In general, these eigenstates can not be written as a product of an orbital and a spin part [70,71] (e.g., due to spin-orbit interaction or the HH-LH mixing) and therefore the  $|0\rangle$  and  $|1\rangle$  eigenstates of different QDs are not necessarily orthogonal. To characterize this mutual non-orthogonalities, we introduce the overlap matrix elements

$$S_{ab} = \langle a_L | b_R \rangle, \quad (2.8)$$

where  $a, b \in \{0, 1\}$ . Even though the wave functions of electrons in the presence of inversion symmetry is separable into orbital and spin part, ensuring  $S_{01} = 0$  and  $S_{00} = S_{11}$  regardless of the magnetic field, for holes these relations hold only for zero magnetic field [54]. Nevertheless we find that  $S_{01}$  can also vanish provided the magnetic field preserves a twofold symmetry in the DQD system, while the difference of the diagonal elements is proportional to the applied magnetic field, i.e.,  $S_{00} - S_{11} \propto B$  for small magnetic fields.

The overlap  $S_{ab}$  is suppressed exponentially with distance between the dots, therefore the orthonormalization can be performed in such a way that the same quantum numbers can be used to label the orthonormalized states, e.g.,  $|0_L\rangle_{\text{ON}} = \sum_m C_{m,0_L} |m\rangle$ , where  $C_{m,0_L} \sim \delta_{m,0_L} + \mathcal{O}(S_{ab})$  (the precise form is given in App. 2.D). Further on the subscript “ON” will be suppressed for simplicity, and the non-orthogonal states are used only in the definition in Eq. (2.8).

From the orthonormalized low-energy single-particle states, six fermionic two-particle states can be constructed in accordance with the Pauli prin-

ciple. Three of them are analogous to triplet states,  $|T_{0\pm}\rangle$  [e.g.,  $|T_+\rangle = (|0_L, 0_R\rangle - |0_R, 0_L\rangle)/\sqrt{2}$ ], one corresponds to a singlet state with a single particle on each dot  $|S\rangle$ , and there are two singlet states  $|S_{L(R)}\rangle$  with both particles on the left (right) dot. Within the framework of the Hund-Mulliken approximation these six states are used to project the Hamiltonian of Eq. (2.7) onto the low-energy Hilbert space.

## 2.5 Low-energy Hamiltonian of a DQD

Exchange coupling is known to be adequate for implementation of two-qubit gates [1]. However the effect of the doubly occupied singlets ( $|S_{L(R)}\rangle$ ) can be crucial for correct quantitative analysis [69], for simplicity we restrict the DQD Hamiltonian of Eq. (2.7) to the lowest energy subspace  $\{S, T_0, T_+, T_-\}$  for the qualitative discussion here and take the higher singlets into account only for the numerical results in Sec. 2.6 via Schrieffer-Wolff transformation [72].

Changing the confinement of the left QD (initially described by the Hamiltonian  $\frac{1}{2}\Delta_0^L \sigma_z^L$ ) results in a modification of the Zeeman splittings  $\Delta^L$  inducing coupling between the qubit basis states [38, 56]. To lowest order in the potential difference  $\delta V_L = V_{\text{DQD}} - V_L$  one obtains

$$\Delta_z^L = \Delta_0^L + \langle 0_L | \delta V_L | 0_L \rangle - \langle 1_L | \delta V_L | 1_L \rangle, \quad (2.9a)$$

$$\Delta_x^L - i\Delta_y^L = 2 \langle 0_L | \delta V_L | 1_L \rangle, \quad (2.9b)$$

for the coefficients of the single-qubit effective Hamiltonian  $\frac{1}{2}\Delta^L \cdot \sigma^L$ , where the Pauli matrices  $\sigma_{x,y,z}^L$  are defined with the orthonormalized states  $|a_L\rangle$  (e.g.,  $\sigma_z^L = |0_L\rangle\langle 0_L| - |1_L\rangle\langle 1_L|$ ). If the DQD respects the same twofold symmetry as the left and right QDs, the couplings vanish, i.e.,  $\Delta_x^L = \Delta_y^L = 0$  due to the modulo-2 conservation law. On the other hand, the energy splitting  $\Delta_z^L$  can still be affected by the potential. The results given by Eqs. (2.9a) and (2.9b) are in correspondence with those obtained from the study of mirror symmetries in the  $g$ -matrix formalism [56].

Next, we turn to a discussion of the exchange couplings. First we point out that, in the presence of a twofold symmetry, due to Eq. (2.6) the  $T_{\pm}$ -triplet sector is decoupled from the rest of the subspace. This is so because the triplets  $|T_{\pm}\rangle$  are composed from products of two single-particle states with the same quantum number  $\alpha$ , whereas all the other states contain products of single-particle states with opposite quantum numbers  $\alpha$ . While this decoupling also exists for conduction band states,

the matrix elements  $\langle T_+|C|T_- \rangle$  and  $\langle S|C|T_0 \rangle$  (which vanish for electrons) do not need to vanish for valence band holes.

In the most general case, the Hamiltonian of two coupled qubits is given in Eq. (2.1). Rewriting this expression in the singlet-triplet basis  $\{S, T_0, T_+, T_-\}$ , we obtain the effective Hamiltonian

$$H_{(1,1)} = \frac{1}{4} \begin{pmatrix} -J_{xx} - J_{yy} - J_{zz} & 2iJ_{xy}^a & \sqrt{2}(-J_{xz}^a - iJ_{yz}^a) & \sqrt{2}(-J_{xz}^a + iJ_{yz}^a) \\ -2iJ_{xy}^a & J_{xx} + J_{yy} - J_{zz} & \sqrt{2}(J_{xz}^s + iJ_{yz}^s) & -\sqrt{2}(J_{xz}^s - iJ_{yz}^s) \\ \sqrt{2}(-J_{xz}^a + iJ_{yz}^a) & \sqrt{2}(J_{xz}^s - iJ_{yz}^s) & J_{zz} & J_{xx} - J_{yy} - 2iJ_{xy}^s \\ \sqrt{2}(-J_{xz}^a - iJ_{yz}^a) & \sqrt{2}(-J_{xz}^s - iJ_{yz}^s) & J_{xx} - J_{yy} + 2iJ_{xy}^s & J_{zz} \end{pmatrix} + \frac{1}{2} \begin{pmatrix} 0 & 2\Delta_z^a & \sqrt{2}(-\Delta_x^a - i\Delta_y^a) & \sqrt{2}(\Delta_x^a - i\Delta_y^a) \\ 2\Delta_z^a & 0 & \sqrt{2}(\Delta_x^s + i\Delta_y^s) & \sqrt{2}(\Delta_x^s - i\Delta_y^s) \\ \sqrt{2}(-\Delta_x^a + i\Delta_y^a) & \sqrt{2}(\Delta_x^s - i\Delta_y^s) & 2\Delta_z^s & 0 \\ \sqrt{2}(\Delta_x^a + i\Delta_y^a) & \sqrt{2}(\Delta_x^s + i\Delta_y^s) & 0 & -2\Delta_z^s \end{pmatrix}, \quad (2.10)$$

where  $\bar{\mathbf{J}}^s = (\bar{\mathbf{J}} + \bar{\mathbf{J}}^T)/2$  is the symmetric part,  $\bar{\mathbf{J}}^a = (\bar{\mathbf{J}} - \bar{\mathbf{J}}^T)/2$  is the antisymmetric part of the exchange matrix, and the Zeeman terms  $\Delta^s = (\Delta^L + \Delta^R)/2$  account for the homogeneous part of the magnetic field, while  $\Delta^a = (\Delta^L - \Delta^R)/2$  for the inhomogeneous part. In general, these terms can also arise if the g-factors of the dots are different. If the magnetic field is oriented along a high-symmetry axis, the  $T_\pm$  sector becomes independent of the  $ST_0$  sector, and therefore the off-diagonal elements of the exchange matrix  $J_{xz}^s, J_{xz}^a, J_{yz}^s$ , and  $J_{yz}^a$  have to vanish.

## 2.6 Coupled hole-spin qubits in silicon NWs

In this section we consider a cylindrical NW fabricated from silicon. A coupled QD setup is established by means of electrostatic gates such that each QD is occupied by a single hole. First we discuss what assumptions were made and which parameter values were used to describe the system, then in Sec. 2.6 we decompose the Hamiltonian of a single QD into an effective spin conserving and a symmetry breaking part. We compare the effect of different mechanisms that can lead to anisotropic exchange interaction in Sec. 2.6, namely the DRSOI and the anisotropy-induced spin mixing (to be clarified below). In Sec. 2.6 we provide numerical examples for the parameters characterizing the effective  $4 \times 4$  Hamiltonian in Eq. (2.10) for the inversion symmetric limit, where the



anisotropic exchange couplings can only appear by virtue of the strong cubic anisotropy in silicon. Finally, the effect of anisotropic corrections on the fidelity of a  $\sqrt{\text{SWAP}}$  gate is discussed in Sec. 2.6.

To be concrete for the numerical evaluations to follow, we focus on a silicon NW with circular cross section and cylinder axis along the [001] direction of the silicon crystal. We use  $\gamma_1 = 4.285$ ,  $\gamma_2 = 0.339$ ,  $\gamma_3 = 1.446$ ,  $\kappa = -0.42$ , and  $q = 0.01$  for the Luttinger-parameters and  $\epsilon_r = 12.1$  for the dielectric constant [63]. The axes  $x, y, z$  correspond to the [100], [010], [001] crystallographic axes, respectively. The magnetic field  $\mathbf{B} = B(\cos \varphi, \sin \varphi, 0)$  is applied in the plane perpendicular to the cylinder axis, and it is parametrized by the angle  $\varphi$  it encloses with the  $x$  axis [see Fig. 2.3(a)].

For the confinement potential in Hamiltonian of Eq. (2.7) we assume the form  $V_{\text{DQD}}(\mathbf{r}) = V_{\text{NW}}(x, y) + \frac{v_B}{a^4}(z^2 - a^2)^2$  with  $v_B$  being the height of the quartic-potential barrier, and  $V_{\text{NW}}(x, y)$  is the transverse confinement potential. In order to efficiently approximate the wells of the DQD potential by independent harmonic potentials  $V_{L(R)}(z)$ , the barrier height should be larger than the orbital energy of the harmonic confinement, or equivalently  $v_B > 2\hbar^2\gamma_1/(ma^2)$  ( $\sim 2.9$  meV for the parameters of our example of Si NW). The confinement potential  $V_{\text{DQD}}(\mathbf{r})$  is inversion symmetric [due to the cylindrical shape of the NW, i.e.  $V_{\text{NW}}(x, y) = V_{\text{NW}}(x^2 + y^2)$ ] and the inversion-asymmetric part of the electric fields is taken into account via the term  $-e\mathbf{E} \cdot \mathbf{r}$ , where  $\mathbf{E}$  is a homogeneous electric field.

## Corrections beyond the conservation of effective spin

Since the magnetic field  $\mathbf{B}$  in the present case is always perpendicular to the DQD axis ( $z$  axis), only reflection symmetry  $S_{2B}$  can be maintained [see Fig. 2.2(a)]. For example, if the magnetic field is applied along the [100] axis ( $\varphi = 0$ ) and  $\mathbf{E} = 0$ , the system respects the symmetry  $S_{2B}$ , facilitating the definition of the effective spin  $\alpha$ . The modulo-2 conservation of this effective spin simplifies the form of the exchange interaction matrix and the induced Zeeman splittings (as we discussed in Sec. 2.5).

Changing the direction of the magnetic field or the application of a homogeneous electric field can break the symmetry. Since the confinement potential  $V_{\text{DQD}}(\mathbf{r})$  and the Coulomb interaction  $C(\mathbf{r}_1 - \mathbf{r}_2)$  both respect the symmetry  $S_{2B}$  for any  $\varphi$ , the symmetry breaking contribution in the Hamiltonian of Eq. (2.7) has to be a part of the single QD Hamiltonian  $H_{\text{QD}}$ . In this case, the mixing of effective spins has a strong similarity with the case of localized electron spins in the presence of Rashba or

Dresselhaus spin-orbit interaction [70,71]. Therefore, we are motivated to decompose the single QD Hamiltonian in the following way,

$$H_0 = H_{\text{QD}} - H_{\text{SO}}, \quad (2.11a)$$

$$H_{\text{SO}} = \frac{1}{2}[D(S_{2B}), H_{\text{QD}}]D(S_{2B}), \quad (2.11b)$$

where  $H_0$  commutes with the symmetry operator  $D(S_{2B})$  conserving the effective spin, and the analogue of the SOI,  $H_{\text{SO}}$ , anti-commutes with the symmetry and thus leads to couplings only of sectors with different quantum numbers.

Performing the decomposition given in Eq. (2.11) on the Hamiltonian of Eq. (2.2), one obtains the following three terms for the spin-non-conserving part  $H_{\text{SO}}$ :

$$\begin{aligned} \frac{\hbar^2}{2m} \Delta\gamma \sin(4\varphi) \left[ (k_{\perp}^2 - k_B^2) \{ \hat{J}_B, \hat{J}_{\perp} \} \right. \\ \left. + \{ k_B, k_{\perp} \} (\hat{J}_{\perp}^2 - \hat{J}_B^2) \right], \end{aligned} \quad (2.12a)$$

$$2q\mu_B B \frac{\sin(4\varphi)}{4} \left[ \hat{J}_{\perp} (\hat{J}_{\perp}^2 - \hat{J}_B^2) - 2\hat{J}_B \{ \hat{J}_B, \hat{J}_{\perp} \} \right], \quad (2.12b)$$

$$- eE_B r_B, \quad (2.12c)$$

where  $\{A, B\} = (AB + BA)/2$  defines the anti-commutator. The momenta rotated to the frame of the magnetic field are defined as  $k_B = k_x \cos(\varphi) + k_y \sin(\varphi)$  and  $k_{\perp} = -k_x \sin(\varphi) + k_y \cos(\varphi)$ , analogously  $\hbar \hat{J}_B$  and  $\hbar \hat{J}_{\perp}$  are the rotated angular momenta and  $r_B$  is the rotated coordinate. The first term, Eq. (2.12a) is coming from the momentum-resolved part of the LK Hamiltonian, the second, Eq. (2.12b) is related to the anisotropic Zeeman term, and the third term, Eq. (2.12c) arises from the electric field component  $E_B$  perpendicular to the symmetry plane, i.e., parallel to the magnetic field  $\mathbf{B}$ .

Note that the anisotropic spin-orbit corrections of Eqs. (2.12a) and (2.12b) are proportional to  $\sin(4\varphi)$  and therefore vanish if  $\mathbf{B} \parallel [100]$ ,  $\mathbf{B} \parallel [110]$ , etc., in correspondence with the expectations from the symmetry arguments. Below we will see that this oscillatory  $\varphi$ -dependence manifests itself in the overlap matrix element  $S_{01}$  [see Figs. 2.3(b)-(c)], the induced Zeeman splittings  $\Delta_{x,y}$ , and the off-diagonal exchange couplings  $J_{xy}$ ,  $J_{xz}$  and  $J_{yz}$  [see Figs. 2.4(b)-(c)].

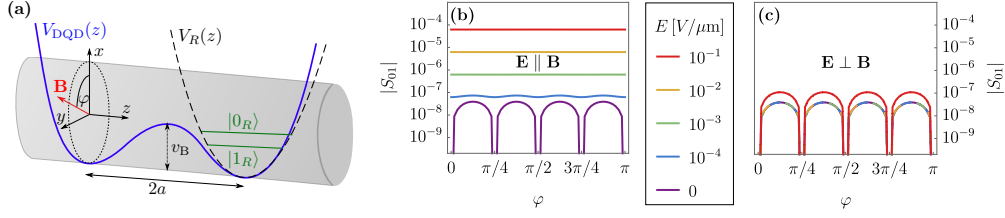


Figure 2.3: (a) Schematic figure of the DQD system realized in a silicon NW. (b)-(c) Absolute value of the anti-aligned overlap  $|S_{01}| = |\langle 0_L | 1_R \rangle|$ , as a function of  $\varphi$ , the angle enclosed by the magnetic field  $\mathbf{B} = B(\cos \varphi, \sin \varphi, 0)$  and the  $x \parallel [100]$  axis, (b) when the electric field  $\mathbf{E} = E(\cos \varphi, \sin \varphi, 0)$  is applied parallel to the magnetic field, and (c) when applied perpendicular to the magnetic field,  $\mathbf{E} = E(-\sin \varphi, \cos \varphi, 0)$ . For this calculation we used a distance of  $2a = 30$  nm between the QDs, barrier height of  $v_B = 3$  meV, magnetic field of  $B = 1$  T, and cylindrical hard-wall confinement with a radius of  $R = 7$  nm. Details on the basis choice and adopted assumptions can be found in App. 2.E.

## Effects of homogeneous electric fields on the effective spin mixing

As we have seen for the spin-non-conserving part  $H_{\text{SO}}$  of the Hamiltonian  $H_{\text{QD}}$ , the symmetry  $S_{2B}$  can be broken by terms with cubic anisotropy in Eqs. (2.12a) and (2.12b) or due to a finite electric field component  $E_B$  along the magnetic field in Eq. (2.12c). As a consequence, the qubit states of different QDs are no longer orthogonal to each other. In order to qualify and compare these two anisotropy effects, we take the overlap matrix element  $|S_{01}| = |\langle 0_L | 1_R \rangle|$  as a figure of merit for this qubit mixing, since it is usually nonzero but vanishes when the QDs respect the symmetry  $S_{2B}$ . Furthermore,  $S_{01}$  can be shown to be proportional to the off-diagonal exchange interaction  $J_{xz}$  and  $J_{yz}$  and the induced Zeeman splittings  $\Delta_x$  and  $\Delta_y$  (see App. 2.F).

For the results presented in Figs. 2.3(b)-(c) we used a cylindrically symmetric hard-wall confinement in the transverse directions for  $V_{\text{NW}}(x, y)$  and studied the effect of asymmetries via the homogeneous electric field term  $-e\mathbf{E} \cdot \mathbf{r}$  with  $\mathbf{E} = (E_x, E_y, 0)$ . The standard Rashba SOI is also taken into account with the coefficient  $\alpha_h = 0.002 \text{ nm}^2 e$  (according to Ref. [33]), although the effect of this term is dominated by the DRSOI [32, 33]. For the example above the relative deviation from the  $\alpha_h = 0$  case is less than 1%.

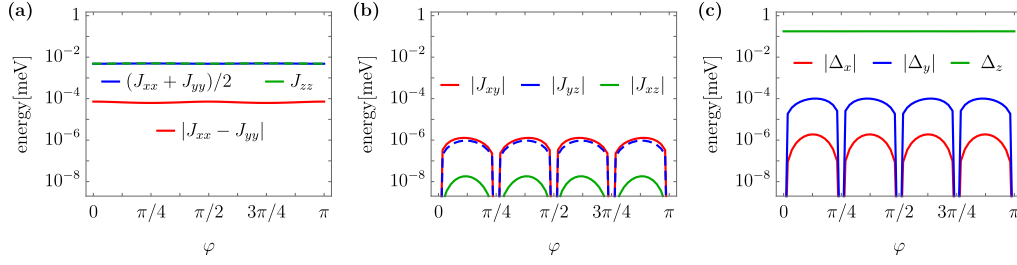


Figure 2.4: (a)-(c) Coefficients characterizing the exchange matrix  $J_{ij}$  and the single-particle Hamiltonian  $\Delta_i$  as a function of the magnetic field direction  $\varphi$ , for a silicon NW. For the numerical simulation the following parameters were used: DQD distance  $2a = 30$  nm; barrier height  $v_B = 3$  meV; magnetic field  $B = 1$  T; harmonic potential of Eq. (2.13) with a confinement length of  $2l_T = 8$  nm. For details on the basis states used for the numerics see App. 2.E.

In Fig. 2.3(b) a homogeneous electric field  $\mathbf{E}$  is applied parallel to the magnetic field, i.e.,  $\mathbf{E} \cdot \mathbf{r} = E_B r_B$ . We plot  $|S_{01}|$  as a function of the magnetic field direction  $\varphi$  for different strength of the electric field between 0 and  $0.1$  V/ $\mu\text{m}$ . Even for relatively small electric fields, e.g.,  $E_B \sim 10^{-3}$  V/ $\mu\text{m}$ , the overlap  $|S_{01}|$  becomes independent of  $\varphi$  and changes roughly linearly with the electric field  $E_B$ . These findings are in agreement with the strong DRSOI predicted for this growth direction [32, 33].

In Fig. 2.3(c) the electric field is applied perpendicular to the magnetic field and the wire axis, therefore  $E_B = 0$  and the symmetry  $S_{2B}$  can only be broken by the cubic anisotropy terms. Importantly,  $S_{01}$  obtains the same angular dependence  $\sin(4\varphi)$  as the terms of the spin non-conserving part of the Hamiltonian  $H_{\text{SO}}$  (see also App. 2.F). Unlike the DRSOI contribution, this effect does not have an analogue in the case of conduction band electrons, since it appears even in the presence of inversion symmetry ( $\mathbf{E} = 0$ ). We refer to this phenomenon as anisotropy-induced spin mixing (see below).

### Anisotropic exchange interaction in the presence of inversion symmetry

In the absence of the homogeneous electric field, i.e.,  $\mathbf{E} = 0$ , the Hamiltonian of Eq. (2.7) is inversion-symmetric, implying that the low-energy Hamiltonian of Eq. (2.1) is invariant under the swap of  $L$  and  $R$ . The exchange matrix has to be symmetric ( $\bar{\mathbf{J}} = \bar{\mathbf{J}}^s$ ) and the Zeeman splittings

have to be identical ( $\Delta^a = 0$ ), therefore in line with Eq. (2.10) the inversion symmetry decouples the singlet  $|S\rangle$  from the three triplets, but the  $|T_0\rangle$  state can still be coupled to the  $|T_{\pm}\rangle$  states in the Hamiltonian  $H_{(1,1)}$ .

To simplify the numerical calculation of the Coulomb integrals, the eigenstates of the left (right) QD  $|0_{L(R)}\rangle$  and  $|1_{L(R)}\rangle$  were calculated numerically using harmonic confinement,

$$V_{\text{NW}}(x, y) = \frac{\hbar^2 \gamma_1}{2m l_T^4} (x^2 + y^2), \quad (2.13)$$

for the transverse directions as well, where  $2l_T$  is the diameter of the NW. After the orthonormalization, the two-particle states were constructed in order to project the Hamiltonian of Eq. (2.7) to the lowest  $6 \times 6$  subspace. In order to take the effect of the doubly occupied singlets into account, we perform a second-order Schrieffer-Wolff transformation and obtain the coefficients of the effective Hamiltonian in Eq. (2.10) as a function of the magnetic field direction  $\varphi$ . The result [73] is presented in Fig. 2.4.

As implied by Eq. (2.6), the off-diagonal elements of the exchange matrix  $J_{xz}$  and  $J_{yz}$  and the Zeeman splittings (i.e.,  $\Delta_{x,y}$ ) corresponding to off-diagonal terms in the single-qubit Hamiltonian vanish, if  $\mathbf{B}$  is along a high-symmetry direction. The coupling between the  $|T_{\pm}\rangle$  states, i.e.,  $\langle T_- | C | T_+ \rangle = \frac{1}{4}(J_{xx} - J_{yy} + 2iJ_{xy})$  remains finite regardless of the angle  $\varphi$ . The exchange matrix element  $J_{xy}$  vanishes along the high-symmetry directions in Fig. 2.4, however, this is only due to the relative phase between the numerically calculated basis states  $|T_{\pm}\rangle$ . The  $ST_0$  splitting  $(J_{xx} + J_{yy})/2$  is approximately equal to  $J_{zz}$ , but this feature is observed only for small enough potential barriers  $v_B$ . The anisotropic exchange matrix elements and the Zeeman splittings acquire their highest value at the low-symmetry field direction  $\varphi \sim \pi/8$ , i.e., in-between high-symmetry points.

Having obtained the effective interaction between the two qubits, we are now in the position to discuss how the anisotropic corrections affect the fidelity of two-qubit gates. This will be done in the following subsection.

### **$\sqrt{\text{SWAP}}$ gate with anisotropic exchange interaction**

Isotropic exchange interaction is a well-known way to implement the  $\sqrt{\text{SWAP}}$  gate [1] from which the fundamental CNOT gate can be obtained. However, in Fig. 2.4 we have seen that anisotropic exchange

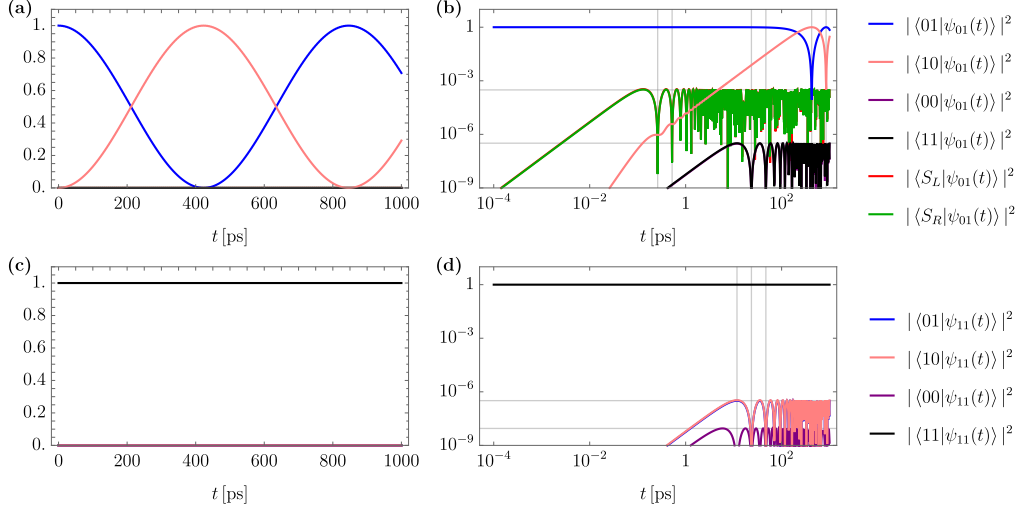


Figure 2.5: Overlaps between DQD basis states and the states  $|\psi_{01}(t)\rangle$  [(a) and (b)] and  $|\psi_{11}(t)\rangle$  [(c) and (d)] as a function of time for the low-symmetry case where  $\varphi = \pi/8$ , for a silicon NW. The time evolution is shown (a) on a liner-linear scale (b) on a log-log scale, with the horizontal lines showing the estimates for the overlaps obtained in Eqs. (2.14)-(2.16) [(c) and (d) similarly]. Horizontal lines are showing the maximal overlap as a function of time [note that the one corresponding to  $|\langle 01|\psi_{11}(t)\rangle|^2 = |\langle 11|\psi_{01}(t)\rangle|^2$  is shown on both (b) and (d)]. Overlaps with different basis states are oscillating with the half-cycle duration of  $\sim h/U$  for  $|\langle S_L|\psi_{01}(t)\rangle|^2$ ,  $\sim h/\Delta_z$  for  $|\langle 11|\psi_{01}(t)\rangle|^2$ , and  $\sim h/(2\Delta_z)$  for  $|\langle 00|\psi_{11}(t)\rangle|^2$  as illustrated by the vertical lines in (b) and (d).

matrix elements and off-diagonal Zeeman splittings (i.e.,  $\Delta_{x,y}$ ) emerge which might affect the operation of such a quantum gate for exchange coupled hole-spin qubits.

In this subsection we adopt the notation widely used in the literature of quantum computation. Instead of the two-particle states with (1, 1) charge configuration we introduce the two-qubit basis states  $|00\rangle = |T_+\rangle$ ,  $|11\rangle = |T_-\rangle$ ,  $|01\rangle = (|T_0\rangle - |S\rangle)/\sqrt{2}$ , and  $|10\rangle = (|T_0\rangle + |S\rangle)/\sqrt{2}$ . However, the discussion of the gate errors for exchange coupled QDs cannot be complete without taking into account the doubly occupied singlets  $|S_L\rangle$  and  $|S_R\rangle$  explicitly. An ideal  $\sqrt{\text{SWAP}}$  gate leaves the qubit states unchanged, if the two qubits are in the  $|00\rangle$  or  $|11\rangle$  state, while creating a maximally entangled state, if they are either in the  $|01\rangle$  or in the  $|10\rangle$  state, e.g.,  $U_{\sqrt{\text{SWAP}}} |01\rangle = |-\rangle \equiv (|01\rangle - i|10\rangle)/\sqrt{2}$ .

Since the exchange interaction is electrically tunable via the potential barrier  $v_B$  [1, 69, 74–76], we consider a case where initially the two qubits are in a (disentangled) product state e.g.,  $|01\rangle$  or  $|11\rangle$  and the interaction is switched on at  $t = 0$ . Therefore, we study the time evolution of the state  $|\psi_{01}(t)\rangle$  according to the effective low-energy  $6 \times 6$  Hamiltonian  $H_{\text{DQD}}^{6 \times 6}$  corresponding to the parameters of Sec. 2.6, such that the time evolution starts from a product state, e.g.,  $|\psi_{01}(0)\rangle = |01\rangle$ . The state  $|\psi_{01}(t)\rangle$  will have the highest overlap with the target state  $|-\rangle$ , when  $t = \tau_s = \hbar\pi (J_{xx} + J_{yy})^{-1}$ . To benchmark the accuracy of the gate corresponding to the  $|01\rangle$  input state, we define the fidelity  $\mathcal{F}_{01} = |\langle - | U_{\sqrt{\text{SWAP}}} | 01 \rangle|^2 = |\langle - | \psi_{01}(\tau_s) \rangle|^2$  and the error rate  $1 - \mathcal{F}_{01}$ .

To illustrate the role of the anisotropic corrections, we compare the performance of the gate for two different magnetic field directions, a high symmetry case ( $\varphi = 0$ ), where the system respects the twofold symmetry  $S_{2B}$ , and a low-symmetry case ( $\varphi = \pi/8$ ), where the anisotropic corrections are the largest in Fig. 2.4. Due to the relatively low potential barrier  $v_B = 3 \text{ meV}$ , fast operation times  $\tau_s \sim 210 \text{ ps}$  can be achieved, but the fidelity  $\mathcal{F}_{01}$  is limited by the tunneling to the doubly occupied states [see Figs. 2.5(a)-(b) for the low-symmetry case]. Exploiting the  $L \leftrightarrow R$  symmetry, the error rate  $1 - \mathcal{F}_{01}$  can be simply estimated by

$$1 - \mathcal{F}_{01} \sim 2 |\langle S_L | \psi_{01}(\tau_s) \rangle|^2 \sim \frac{J_{xx} + J_{yy}}{U}, \quad (2.14)$$

where  $U \sim 15 \text{ meV}$  is the charging energy. This error also sets a limit for the fidelity in the high-symmetry case, since the singlet-singlet tunneling cannot be ruled out by symmetry arguments.

Due to the anisotropic coupling terms in Hamiltonian  $H_{\text{DQD}}^{6 \times 6}$ , the  $|11\rangle$  and  $|00\rangle$  states are also affected by the operation. Introducing the state  $|\psi_{11}(t)\rangle$ , such that the time evolution starts from a product state, i.e.,  $|\psi_{11}(0)\rangle = |11\rangle$ , we define the fidelity of the gate corresponding to the  $|11\rangle$  input state as  $\mathcal{F}_{11} = |\langle 11 | U_{\sqrt{\text{SWAP}}} | 11 \rangle|^2 = |\langle 11 | \psi_{11}(\tau_s) \rangle|^2$  and the corresponding error rate  $1 - \mathcal{F}_{11}$ . In Figs. 2.5(c)-(d) the time evolution of the overlaps of the state  $|\psi_{11}(t)\rangle$  with the four two-qubit basis states are shown in the low-symmetry case ( $\varphi = \pi/8$ ). In this case, the fidelity is limited by the transition probability from the input state  $|11\rangle$  to the  $|01\rangle$  and  $|10\rangle$  states. The estimated error rate is then given by the induced Zeeman splittings as

$$1 - \mathcal{F}_{11} \sim 2 |\langle 01 | \psi_{11}(\tau_s) \rangle|^2 \sim 2 \frac{\Delta_x^2 + \Delta_y^2}{\Delta_z^2}. \quad (2.15)$$

	high symmetry	low symmetry
$\varphi$	0	$\pi/8$
$1 - \mathcal{F}_{01}$	$6.2 \cdot 10^{-4}$	$6 \cdot 10^{-4}$
$1 - \mathcal{F}_{11}$	$10^{-8}$	$6.4 \cdot 10^{-7}$

Table 2.2: Error rates of the  $\sqrt{\text{SWAP}}$  gate for the high-symmetry case ( $\varphi = 0$ ) and a low-symmetry case ( $\varphi = \pi/8$ , providing the poorest fidelities as a function of magnetic field direction) for the silicon NW setup illustrated in Fig. 2.3(a).

As pointed out in Sec. 2.5, the  $|00\rangle$  and  $|11\rangle$  states ( $|T_{\pm}\rangle$  states in the earlier notation) are coupled to each other even in the presence of a twofold symmetry. The error rate  $1 - \mathcal{F}_{11}$  in the high-symmetry case is then determined by the anisotropic correction to the exchange term  $J_{xx} - J_{yy}$  as follows

$$1 - \mathcal{F}_{11} \sim |\langle 00 | \psi_{11}(\tau_s) \rangle|^2 \sim \left( \frac{J_{xx} - J_{yy}}{4\Delta_z} \right)^2. \quad (2.16)$$

However, for the system considered in Sec. 2.6 the fidelity  $\mathcal{F}_{11}$  is significantly higher than  $\mathcal{F}_{01}$  for both the high- and low-symmetry cases (see Tab. 2.2 for the calculated values), implying that for low enough potential barriers  $v_B$  the fidelity of the  $\sqrt{\text{SWAP}}$  gate is not limited by the anisotropic corrections but by the probability of tunneling to a doubly occupied state (the opposite limit with a high potential barrier  $v_B$  is discussed in App. 2.G).

## 2.7 Discussion

*Validity of the axial limit.* In the axial limit ( $\Delta\gamma, q \rightarrow 0$ ), the symmetry of the Hamiltonian in Eq. (2.4) is higher than the actual symmetry of the system. In this case due to the continuous rotation symmetry of the Hamiltonian, the total angular momentum component  $\hbar F_B$  ( $= \hbar\alpha_{\infty}$ ) is a good quantum number regardless of the magnetic field direction. Therefore this approximation completely ignores the couplings between  $T_{\pm}$  and the  $ST_0$  sector that arise even for perfectly inversion symmetric confinement.

Since the anisotropic terms coupling states with different quantum numbers in Eqs. (2.12a) and (2.12b) are proportional to  $\Delta\gamma$  and  $q$ , they are expected to be suppressed for materials of lower anisotropy. A comparison of exchange interaction between the above studied silicon and



the Ge/Si core/shell NW presented in App. 2.H is consistent with this expectation.

*Silicon NW with different arrangements.* In Ref. [33] the authors suggested to study silicon NWs with  $\langle 100 \rangle$  growth direction, since a Rashba-type of SOI is enhanced in these directions compared to the conventionally used  $\langle 110 \rangle$  growth direction [77]. On the other hand, the  $\langle 110 \rangle$  growth direction can be advantageous for the study of the anisotropy induced SOI effects, since it is less susceptible to external electric fields.

Another interesting feature of the  $\langle 100 \rangle$  growth direction is that the NW axis coincides with a 4-fold symmetry axis. If the magnetic field is applied along the NW, the modulo-4 conservation law of the angular momentum rules out the anisotropic coupling  $J_{xx} - J_{yy}$  as well. However, in order to achieve such a symmetry in an experimental setup, the electrostatic gates would have to be arranged such that they respect the 4-fold rotation symmetry and therefore this favourable case does not seem to be within current experimental reach.

*Orientation of the spin-orbit vector.* When an electron or hole propagates along the NW axis  $z$ , an electric field along the  $x$  direction induces an effective magnetic field along the  $y$  axis on account of Rashba SOI. For holes, however, additional terms can arise such that the electric-field-induced effective magnetic field (spin-orbit vector) is not parallel to  $y$ . For example, considering a silicon NW with  $z \parallel \langle 100 \rangle$  and a square cross-section, the calculations in Ref. [33] resulted in an effective magnetic field whose component along  $x$  (parallel to the electric field) is nonzero unless  $\gamma_2 = \gamma_3$  or  $\sin(4\phi') = 0$ , where the angle  $\phi'$  depends on the orientation of the crystallographic axes with respect to the NW cross-section. We note that this result has remarkable similarities with Eq. (2.12a). The symmetry considerations in the present work provide a simple and intuitive explanation for the unusual, effective magnetic field component parallel to the electric field derived in Ref. [33].

*Further signatures for the  $T_{\pm}$  decoupling.* As discussed in Sec. 2.5, a remarkable consequence of the conserved quantum number is the vanishing exchange interaction and single-particle couplings between the  $T_{\pm}$  sector and the remaining four basis states. Besides the numerical results for the overlap  $S_{01}$  and the matrix elements in Fig. 2.4, we also studied the crossing of the  $|S_L\rangle$  and the  $|T_{-}\rangle$  energy levels as a function of detuning and the leakage current near the crossing point. These results also confirmed the decoupling of the sectors with different quantum numbers.

*Magnetic Weyl points.* In Refs. [78]- [79], the authors find that topologically protected magnetic degeneracy points (referred to as magnetic

Weyl points) can appear in DQDs for arbitrary SOI, i.e., for certain orientations of the magnetic field  $\pm \mathbf{B}_W$ , the singlet  $|S\rangle$  and the lower triplet state  $|T_-\rangle$  become degenerate: the levels cross as function of magnetic field and are protected from hybridization.

In the DQD system considered here, the decoupling of the  $T_{\pm}$  states from the  $ST_0$  states also leads to magnetic degeneracy points at fine-tuned magnetic fields. These degeneracies are protected by the two-fold (in general  $N$ -fold) symmetry of the DQD system. However, establishing a connection between the topologically and symmetry protected magnetic degeneracies requires further analysis.

*Applications in experiments.* Our results corroborate the strong anisotropy in spin-related quantities observed in recent experiments [35, 36, 80, 81]. Furthermore, many of the recent experimental setups seem to be invariant under reflection with respect to a certain plane, e.g., the plane being perpendicular to the plunger gates in Refs. [40] and [78]. Since the orientation of the magnetic field is usually tunable via a two- or three-dimensional vector magnet, the study of anisotropic effects is well within the reach of state-of-the-art experiments. *In situ* control of the confinement is usually also available by all-electrical means via tuning the confinement gate voltages [82].

## 2.8 Conclusion

We showed that an effective spin quantum number can be assigned to confined hole-states even in highly anisotropic materials if the magnetic field is applied along a twofold symmetry axis of the system. Even though in general, the isotropic Heisenberg exchange is not sufficient to describe the interaction, exchange based two-qubit gates are likely to be feasible for hole-spin qubits in NWs. Besides enabling fast single-qubit operations by purely electrical means [16], silicon and Ge/Si core/shell NWs are also promising platforms to realize fast and high fidelity two-qubit operations.

### 2.A Magnetic field along an $N$ -fold symmetry axis, generalization of Bloch's theorem

Considering a system with continuous translational symmetry and imposing periodic boundary conditions with a period of  $L$ , the eigenstates

of the Hamiltonian are characterized by the momentum  $p = \hbar n \frac{2\pi}{L}$  with  $n \in \mathbb{Z}$ . For discrete translational symmetry Bloch's theorem [83] states that only the wave number  $k = \text{mod}_G(p/\hbar)$  is a good quantum number, where  $G = \frac{2\pi}{a}$ , is the primitive reciprocal lattice vector with  $a$  being the lattice constant. Even though the wave number  $k$  is not a consequence of a continuous symmetry, it obeys the conservation law  $\text{mod}_G[\sum_i(k_i - k'_i)] = 0$  for microscopic processes involving more than one particle, where  $k_i$  and  $k'_i$  are the initial and final wave numbers of the  $i$ th particle.

An analogous conservation law holds for the angular momentum in a system with discrete rotational symmetry. The proof is very similar to that of Bloch's theorem for a one-dimensional lattice, only the translation operator  $T_a = \exp(-i\hat{p}a/\hbar)$ , with  $\hat{p}$  being the momentum operator, needs to be replaced by the rotation operator  $R_\phi = \exp(-i\phi\hat{F}_z)$ , with  $\hbar\hat{F}_z$  being the  $z$ -component of the total angular momentum operator,  $\hbar\hat{\mathbf{F}} = \hbar\hat{\mathbf{L}} + \hbar\hat{\mathbf{J}}$ , keeping in mind that for particles with half-odd-integer spin the periodic boundary condition should be imposed for  $\phi = 4\pi$ .

For a system where  $z$  is an  $N$ -fold symmetry axis the eigenstates of the Hamiltonian are characterized by the quantum number  $\alpha_N = \text{mod}_N(F_z)$ , where  $F_z$  is the associated angular momentum eigenvalue. A derivation analogous to the case of translational symmetry leads to the conservation of the quantum number  $\alpha_N$ , namely

$$\text{mod}_N \left[ \sum_i (\alpha_{Ni} - \alpha'_{Ni}) \right] = 0, \quad (2.17)$$

where  $\alpha_{Ni}$  and  $\alpha'_{Ni}$  are the initial and final quantum numbers of the  $i$ th particle. The wave function  $f_{m,j,\alpha_N}(\mathbf{r}) = \langle \mathbf{r}, j | m\alpha_N \rangle$  corresponding to the single particle eigenstate  $|m\alpha_N\rangle$  of the Hamiltonian respecting an  $N$ -fold symmetry can be written as

$$f_{m,j,\alpha_N}(r, \phi, z) = e^{i(\alpha_N - j)\phi} u_{m,j,\alpha_N}(r, \phi, z), \quad (2.18)$$

where  $j$  is the eigenvalue of  $\hat{J}_z$ , and the function  $u_{m,j,\alpha_N}(\mathbf{r})$  respects the  $N$ -fold rotation symmetry, i.e.,  $u_{m,j,\alpha_N}(r, \phi, z) = u_{m,j,\alpha_N}(r, \phi + 2\pi n/N, z)$  for every  $n \in \mathbb{Z}$ . In the  $N \rightarrow \infty$  limit  $\alpha_\infty = F_z$  is conserved in agreement with Noether's theorem and Eq. (2.18) corresponds to the ansatz of the axial limit from Refs. [30]- [32]. This finding also explains the presence or absence of "hole-spin mixing" for vertically stacked lateral QDs in Ref. [65], even without assuming cylindrical symmetry for the LK Hamiltonian.

In the case of roto-reflections  $S_{NB}$ , the derivation is very similar, however, the symmetry of the function  $u_{m,j,\alpha_N}(\mathbf{r})$  corresponds to the roto-reflection, i.e.,  $u_{m,j,\alpha_N}(r, \phi, z) = u_{m,j,\alpha_N}(r, \phi + \pi n + 2\pi n/N, (-1)^n z)$  for every  $n \in \mathbb{Z}$ .

## 2.B Lowest-energy Kramers doublet

In this appendix we show that the two lowest-energy eigenstates of a single-particle Hamiltonian  $H_{B=0}$  obeying a twofold symmetry  $\mathcal{R}_2$  have to belong to different values of the quantum number  $\alpha \equiv \alpha_2$  in the absence of a magnetic field.

According to Kramers theorem, in the absence of magnetic field each energy level should be at least twofold degenerate. Let us assume that there are no fields and the two energetically lowest eigenstates  $|\psi_1\rangle$  and  $|\psi_2\rangle = \mathcal{T}|\psi_1\rangle$  are degenerate ground states, i.e.,

$$H_{B=0} |\psi_{1,2}\rangle = \varepsilon_0 |\psi_{1,2}\rangle, \quad (2.19)$$

with  $\mathcal{T}$  being the anti-unitary time-reversal operator and  $\varepsilon_0$  is the ground state energy. Furthermore, due to the anti-unitarity of  $\mathcal{T}$  the time-reversed partner  $|\psi_2\rangle$  is necessarily orthogonal to  $|\psi_1\rangle$  [67].

If the Hamiltonian commutes with a twofold symmetry operator  $D(\mathcal{R}_2)$ , the eigenstates  $|\psi_{1,2}\rangle$  can always be chosen to be simultaneous eigenstates of  $D(\mathcal{R}_2)$  as well,

$$D(\mathcal{R}_2) |\psi_1\rangle = \pm i |\psi_1\rangle. \quad (2.20)$$

with the eigenvalue either  $+i$  or  $-i$ . Since  $\mathcal{T}$  commutes with  $D(\mathcal{R}_2)$ , one obtains

$$\begin{aligned} D(\mathcal{R}_2) |\psi_2\rangle &= D(\mathcal{R}_2) \mathcal{T} |\psi_1\rangle = \mathcal{T} D(\mathcal{R}_2) |\psi_1\rangle \\ &= \mathcal{T} (\pm i |\psi_1\rangle) = \mp i \mathcal{T} |\psi_1\rangle = \mp i |\psi_2\rangle. \end{aligned} \quad (2.21)$$

In other words, if  $|\psi_1\rangle$  belongs to the quantum number  $\alpha = +1/2$  its time reversed partner  $|\psi_2\rangle$  has to have the opposite quantum number  $\alpha = -1/2$ .

Consequently, when the doublet is split by an external magnetic field such that the twofold symmetry is preserved, the resulting eigenstates are of different quantum number (unless the Zeeman splitting exceeds the orbital splitting, in which case the lowest eigenstates of  $H_{\text{QD}}$  are not time-reversed partners of each other).

## 2.C Conservation of the effective spin

In this appendix we derive Eq. (2.6) of the main text. First we list some important relations regarding the effect of the symmetry operator  $D_2 \equiv D(\mathcal{R}_2)$  on single- and two-particle states which are eigenstates of this operator:

$$D_2 |m\alpha\rangle = e^{-i\pi\alpha} |m\alpha\rangle, \quad (2.22a)$$

$$D_2^2 |m\alpha\rangle = -|m\alpha\rangle, \quad (2.22b)$$

$$\begin{aligned} \tilde{D}_2 |m\alpha, n\beta\rangle &= \left( D_2^{(1)} \otimes D_2^{(2)} \right) |m\alpha, n\beta\rangle \\ &= (-1)^{\alpha+\beta} |m\alpha, n\beta\rangle, \end{aligned} \quad (2.22c)$$

$$\tilde{D}_2^2 |m\alpha, n\beta\rangle = |m\alpha, n\beta\rangle, \quad (2.22d)$$

where the two-particle states above,  $|m\alpha, n\beta\rangle = |m\alpha\rangle_1 \otimes |n\beta\rangle_2$ , are product states of the single-particle states  $|m\alpha\rangle_1$  and  $|n\beta\rangle_2$  for the first and second particle, respectively. The indices  $m, n, p, q \in \{0_L, 0_R, 1_L, 1_R, 2_L, \dots\}$  label the single-particle eigenstates of the left or right QD, and  $\alpha, \beta, \chi, \xi = \pm 1/2$  stand for the effective spins associated to the single-particle states. The representation of the symmetry  $\tilde{D}_2$  acts on the two-particle states as a tensor product of the corresponding single-particle representations  $D_2^{(1,2)}$ . Furthermore, we see that  $\tilde{D}_2^2$  acts on the two-particle states as the identity, in correspondence with the fact that these states are always of integer spin.

Provided that the DQD Hamiltonian  $H_{\text{DQD}}$  commutes with the symmetry operator  $\tilde{D}_2$  using the relations given above one finds

$$\begin{aligned} \langle m\alpha, n\beta | H_{\text{DQD}} | p\chi, q\xi \rangle &= \langle m\alpha, n\beta | H_{\text{DQD}} \tilde{D}_2^2 | p\chi, q\xi \rangle \\ &= \langle m\alpha, n\beta | \tilde{D}_2 H_{\text{DQD}} \tilde{D}_2 | p\chi, q\xi \rangle \\ &= (-1)^{\alpha+\beta+\chi+\xi} \langle m\alpha, n\beta | H_{\text{DQD}} | p\chi, q\xi \rangle. \end{aligned} \quad (2.23)$$

Subtracting the rightmost part of the equation from the leftmost, we obtain

$$(1 - (-1)^{\alpha+\beta+\chi+\xi}) \langle m\alpha, n\beta | H_{\text{DQD}} | p\chi, q\xi \rangle = 0, \quad (2.24)$$

which leads to Eq. (2.6) in the main text.

## 2.D Orthonormalization method

In this appendix we present a method to orthonormalize the single-particle states of the left  $|a_L\rangle$  and right dot  $|b_R\rangle$ . Even though the Gram-Schmidt procedure is a well known method for the orthonormalization, being a recursive method it can not ensure the  $L \leftrightarrow R$  symmetry for the orthonormalized states. Here we present a method that is although less straightforward, conserves the physically relevant implications of the inversion symmetry.

Assuming  $L \leftrightarrow R$  symmetry, the most general transformation connecting the single-particle states  $|a_{L(R)}\rangle$  to the orthonormalized states  $|a_{L(R)}\rangle_{\text{ON}}$  has a block-matrix structure, i.e.,

$$\begin{pmatrix} |0_L\rangle_{\text{ON}} \\ |1_L\rangle_{\text{ON}} \\ |0_R\rangle_{\text{ON}} \\ |1_R\rangle_{\text{ON}} \end{pmatrix} = \mathbf{C}^T \begin{pmatrix} |0_L\rangle \\ |1_L\rangle \\ |0_R\rangle \\ |1_R\rangle \end{pmatrix} = \begin{pmatrix} \mathbf{A} & \mathbf{B} \\ \mathbf{B} & \mathbf{A} \end{pmatrix} \begin{pmatrix} |0_L\rangle \\ |1_L\rangle \\ |0_R\rangle \\ |1_R\rangle \end{pmatrix}, \quad (2.25)$$

where  $\mathbf{A}$  and  $\mathbf{B}$  are general  $2 \times 2$  matrices.

Let us consider the state  $|i\rangle_{\text{ON}}$  which is a linear combination of the states  $|n\rangle \equiv |a_{L(R)}\rangle$ , that can have nonzero overlap  $\langle n|m\rangle$ , i.e.,

$$|i\rangle_{\text{ON}} = \sum_n (C^T)_{in} |n\rangle = \sum_n C_{ni} |n\rangle, \quad i = 1, \dots, 4, \quad (2.26)$$

where  $C_{ni}$  are coefficients. Next, we impose the orthonormality condition on these states,

$$\begin{aligned} \langle i|_{\text{ON}} |j\rangle_{\text{ON}} &= \sum_{n,m} C_{ni}^* C_{mj} \langle n|m\rangle \\ &= \sum_{n,m} C_{ni}^* S_{nm} C_{mj} \stackrel{!}{=} \delta_{ij}, \end{aligned} \quad (2.27)$$

where we defined the overlap-matrix  $S_{nm} = \langle n|m\rangle$ . Making the choice  $C_{nm} = (S^{-1/2})_{nm}$  (used e.g. in Ref. [84]), the transformation matrix is not only Hermitian but also acquires the block-matrix structure of Eq. (2.25) as will be shown below.

First the eigenvalue problem of the overlap-matrix will be solved and then the inverse square-root matrix will be calculated via its eigen-decomposition.

In the  $L \leftrightarrow R$  symmetric case the aligned overlaps  $S_{00}$  and  $S_{11}$  are real and the anti-aligned overlaps are related via conjugation  $S_{10} = S_{01}^*$ .

Therefore the overlap-matrix  $S_{nm}$  obtains a simple form

$$\mathbf{S} = \mathbb{1}_{4 \times 4} + \begin{pmatrix} 0 & 0 & S_{00} & S_{01} \\ 0 & 0 & S_{01}^* & S_{11} \\ S_{00} & S_{01} & 0 & 0 \\ S_{01}^* & S_{11} & 0 & 0 \end{pmatrix}, \quad (2.28)$$

where  $\mathbb{1}_{4 \times 4}$  is the  $4 \times 4$  identity-matrix. We recall that the states  $|0_L\rangle$  and  $|1_L\rangle$  are orthonormal and the same applies to the right QD. Since the matrix has two identical Hermitian blocks, its eigenvectors are of the following form

$$\mathbf{v}^{(1)} = \frac{1}{\sqrt{2}} \begin{pmatrix} v_1 \\ v_2 \\ v_1 \\ v_2 \end{pmatrix}, \quad \mathbf{v}^{(2)} = \frac{1}{\sqrt{2}} \begin{pmatrix} v_1 \\ v_2 \\ -v_1 \\ -v_2 \end{pmatrix}, \quad (2.29a)$$

$$\mathbf{v}^{(3)} = \frac{1}{\sqrt{2}} \begin{pmatrix} -v_2^* \\ v_1 \\ -v_2^* \\ v_1 \end{pmatrix}, \quad \mathbf{v}^{(4)} = \frac{1}{\sqrt{2}} \begin{pmatrix} -v_2^* \\ v_1 \\ v_2^* \\ -v_1 \end{pmatrix}, \quad (2.29b)$$

corresponding to the eigenvalues  $1 + \lambda_+$ ,  $1 - \lambda_+$ ,  $1 + \lambda_-$ , and  $1 - \lambda_-$ , respectively. The parameters of the eigenvectors and eigenvalues are given by

$$v_1 = \frac{1}{\mathcal{N}'} \left( \frac{S_{00} - S_{11}}{2} + |w_S| \right), \quad v_2 = \frac{S_{10}}{\mathcal{N}'}, \quad (2.30a)$$

$$\lambda_{\pm} = \frac{S_{00} + S_{11}}{2} \pm |w_S|,$$

where we used the following definitions:

$$\mathcal{N}'^2 = \left( \frac{S_{00} - S_{11}}{2} + |w_S| \right)^2 + |S_{01}|^2, \quad (2.30b)$$

$$|w_S|^2 = (S_{00} - S_{11})^2/4 + |S_{01}|^2.$$

The inverse square-root matrix  $\mathbf{C} = \mathbf{S}^{-1/2}$  is then obtained in the eigen-decomposition.

The first block  $\mathbf{A}$  of the transformation matrix  $\mathbf{C}^T$  reads as

$$\begin{aligned} \mathbf{A} = & \frac{1}{2} \begin{pmatrix} v_1^2 \left( \frac{1}{\sqrt{1-\lambda_+}} + \frac{1}{\sqrt{1+\lambda_+}} \right) + |v_2|^2 \left( \frac{1}{\sqrt{1-\lambda_-}} + \frac{1}{\sqrt{1+\lambda_-}} \right) \\ v_1 v_2^* \left( \frac{1}{\sqrt{1-\lambda_+}} + \frac{1}{\sqrt{1+\lambda_+}} - \frac{1}{\sqrt{1-\lambda_-}} - \frac{1}{\sqrt{1+\lambda_-}} \right) \\ v_1 v_2 \left( \frac{1}{\sqrt{1-\lambda_+}} + \frac{1}{\sqrt{1+\lambda_+}} - \frac{1}{\sqrt{1-\lambda_-}} - \frac{1}{\sqrt{1+\lambda_-}} \right) \\ v_1^2 \left( \frac{1}{\sqrt{1-\lambda_-}} + \frac{1}{\sqrt{1+\lambda_-}} \right) + |v_2|^2 \left( \frac{1}{\sqrt{1-\lambda_+}} + \frac{1}{\sqrt{1+\lambda_+}} \right) \end{pmatrix} \\ = & \begin{pmatrix} 1 + \frac{3}{8} (v_1^2 \lambda_+^2 + |v_2|^2 \lambda_-^2) & v_1 v_2 \frac{3}{8} (\lambda_+^2 - \lambda_-^2) \\ v_1 v_2^* \frac{3}{8} (\lambda_+^2 - \lambda_-^2) & 1 + \frac{3}{8} (v_1^2 \lambda_-^2 + |v_2|^2 \lambda_+^2) \end{pmatrix} + \mathcal{O}(S_{ab}^3), \end{aligned} \quad (2.31a)$$

where we exploited that  $v_1^2 + |v_2|^2 = 1$  and  $\lambda_{\pm} = \mathcal{O}(S_{ab})$  as implied by Eq. (2.30a). The lowest order corrections to the identity matrix are of second order in  $S_{ab} = \langle a_L | b_R \rangle$ . Similarly, one can obtain the matrix  $\mathbf{B}$  and perform the Taylor expansion in  $S_{ab}$  as

$$\begin{aligned} \mathbf{B} = & \frac{1}{2} \begin{pmatrix} v_1^2 \left( -\frac{1}{\sqrt{1-\lambda_+}} + \frac{1}{\sqrt{1+\lambda_+}} \right) + |v_2|^2 \left( -\frac{1}{\sqrt{1-\lambda_-}} + \frac{1}{\sqrt{1+\lambda_-}} \right) \\ v_1 v_2^* \left( -\frac{1}{\sqrt{1-\lambda_+}} + \frac{1}{\sqrt{1+\lambda_+}} + \frac{1}{\sqrt{1-\lambda_-}} - \frac{1}{\sqrt{1+\lambda_-}} \right) \\ v_1 v_2 \left( -\frac{1}{\sqrt{1-\lambda_+}} + \frac{1}{\sqrt{1+\lambda_+}} + \frac{1}{\sqrt{1-\lambda_-}} - \frac{1}{\sqrt{1+\lambda_-}} \right) \\ v_1^2 \left( -\frac{1}{\sqrt{1-\lambda_-}} + \frac{1}{\sqrt{1+\lambda_-}} \right) + |v_2|^2 \left( -\frac{1}{\sqrt{1-\lambda_+}} + \frac{1}{\sqrt{1+\lambda_+}} \right) \end{pmatrix} \\ = & -\frac{1}{2} \begin{pmatrix} v_1^2 \lambda_+ + |v_2|^2 \lambda_- & v_1 v_2 (\lambda_+ - \lambda_-) \\ v_1 v_2^* (\lambda_+ - \lambda_-) & v_1^2 \lambda_- + |v_2|^2 \lambda_+ \end{pmatrix} + \mathcal{O}(S_{ab}^3), \end{aligned} \quad (2.31b)$$

which turns out to be of the first order in  $S_{ab}$ .

Finally, we comment on the well-known case of electrons with separable wave functions, where  $S_{01} = 0$  and  $S_{00} = S_{11} = \mathcal{S}$ , and thus  $\lambda_{\pm} = \mathcal{S}$ . Substituting this into Eqs. (2.31a) and (2.31b) and using  $v_1^2 + |v_2|^2 = 1$ , the formula used for the orthonormalized states in Refs. [69,84] is recovered.



## 2.E Single-particle basis for the numerics

The eigenvalue problem of Eq. (2.2) was solved numerically using a finite number of basis states. The eigenstates  $|a\rangle$  of the Hamiltonian in Eq. (2.2) can be expanded on the product basis of orbital states  $|m, n, p\rangle$  and the spin-3/2 eigenstates  $|j\rangle$  as

$$|a\rangle = \sum_{m,n,p,j} c_j^{m,n,p} |m, n, p, j\rangle, \quad (2.32)$$

where  $p$  is the orbital quantum number corresponding to the wire axis,  $m$  and  $n$  are the orbital quantum numbers corresponding to the transverse direction,  $j$  is the eigenvalue of a spin-3/2 operator  $\hat{J}_z$ , and the expansion coefficients are given by  $c_j^{m,n,p} = \langle m, n, p, j | a \rangle$ .

For the analysis of the overlaps in the presence of both electric and magnetic fields we used hard-wall confinement in the transverse directions, i.e.,

$$V_{\text{NW}}(x, y) = \begin{cases} 0, & \text{if } x^2 + y^2 < R^2 \\ \infty, & \text{otherwise} \end{cases}, \quad (2.33)$$

with  $R$  being the radius. In this case, the basis states can be decomposed into a product form  $|m, n, p, j\rangle = |m, n\rangle |p, j\rangle$ . For the state corresponding to the transverse directions  $|m, n\rangle$  the wave function is given in terms of Bessel-functions of the first kind,

$$\begin{aligned} \langle r, \phi | m, n \rangle &= \frac{1}{J_{m+1}(x_{m,n})\sqrt{\pi}R} J_m\left(x_{m,n} \frac{r}{R}\right) \\ &\times \begin{cases} \sqrt{2} \cos(m\phi), & \text{for } m > 0 \\ 1, & \text{for } m = 0 \\ \sqrt{2} \sin(m\phi), & \text{for } m < 0, \end{cases} \end{aligned} \quad (2.34)$$

where  $x_{m,n}$  is the  $n$ th root of the  $m$ th Bessel function  $J_m$ . The confinement of the QD along the wire ( $z$  axis) is assumed to be harmonic, with the corresponding eigenstates given by Hermite polynomials  $H_p(z)$ . The  $z$ -resolved wave function of the second part  $|p, j\rangle$  then becomes

$$\langle z | p, j \rangle = \frac{H_p(z/l_{zj}) \exp(-\frac{z^2}{2l_{zj}^2})}{\sqrt{2^p p! l_{zj} \sqrt{\pi}}} |j\rangle, \quad (2.35)$$

where the confinement length is defined with the effective mass  $m_{zj}$  as  $l_{zj}^4 = \hbar^2 a^2 / (8v_B m_{zj})$ . The effective mass is obtained by taking the coefficient of the  $k_z^2$  term in  $\langle j | H_{\text{LK}} | j \rangle$ , and equating it with  $\hbar^2 / (2m_{zj})$ . Allowing

for different confinement lengths  $l_{zj}$  in the basis states  $\langle z|p, j\rangle$  for different  $j$ , we can reduce the off-diagonal elements in the Hamiltonian. In our calculation for Fig. 2.3, the quantum numbers can take the following values:  $m \in \{-2, -1, 0, 1, 2\}$ ,  $n \in \{1, 2, 3\}$ , and  $p \in \{0, 1, 2, 3, 4\}$ .

Calculating the coefficients of the exchange interaction in Fig. 2.4 required the numerical evaluation of the matrix elements of the Coulomb interaction  $\sim 1/|\mathbf{r}_1 - \mathbf{r}_2|$  between two-particle basis states. In the basis of Bessel-functions the solution leads to long running times and poor accuracy. However, assuming harmonic confinement in the transversal directions and using the basis of Hermite polynomials in the  $x$  and  $y$  directions analogous to Eq. (2.35) facilitates the analytical calculation of the matrix elements in the transversal directions. For Fig. 2.4 the quantum numbers of the basis states can take the following value  $m \in \{0, 1, 2\}$ ,  $n \in \{0, 1, 2\}$  and  $p \in \{0, 1, 2, 3, 4\}$ .

## 2.F $S_{01}$ as a figure of merit for the effective spin mixing

In the main text we argued that the quantity  $S_{01}$  is a good measure for the (unwanted) mixing of effective spins (qubits) in the absence of a twofold symmetry. Here we will show that  $S_{01}$  can be expressed in terms of the anisotropy terms  $\Delta_{x,y}$  of the DQD Hamiltonian as well as the off-diagonal exchange matrix elements such as  $J_{xz}$ .

To this end we focus on our particular example of a silicon NW with [001] growth direction and in the presence of a perpendicular magnetic field and perform the symmetry decomposition given in Eq. (2.11) of the corresponding single QD Hamiltonian in Eq. (2.2) according to the mirror symmetry  $S_{2B}$ . The symmetry breaking part  $H_{SO}$  contains the terms shown in Eqs. (2.12a)-(2.12c). From this decomposition we derive an effective  $2 \times 2$  Hamiltonian describing the lowest energy (or qubit) subspace. A convenient way to do this is to find the eigenstates of the high-symmetry part  $H_0$  and perform an exact Schrieffer-Wolff transformation. This leads to

$$H_{\text{QD}}^{2 \times 2} = H_0^{2 \times 2} + H_{\text{SO}}^{2 \times 2} = \frac{\Delta'_0}{2} \sigma'_z + \text{Re}(\nu) \sigma'_x + \text{Im}(\nu) \sigma'_y \quad (2.36)$$

for the lowest  $2 \times 2$  block of  $H_{\text{QD}}$ , which is decoupled from the rest of the states. The Pauli matrices above are defined as  $\sigma'_z = |0+\rangle \langle 0+| - |1-\rangle \langle 1-|$ ,

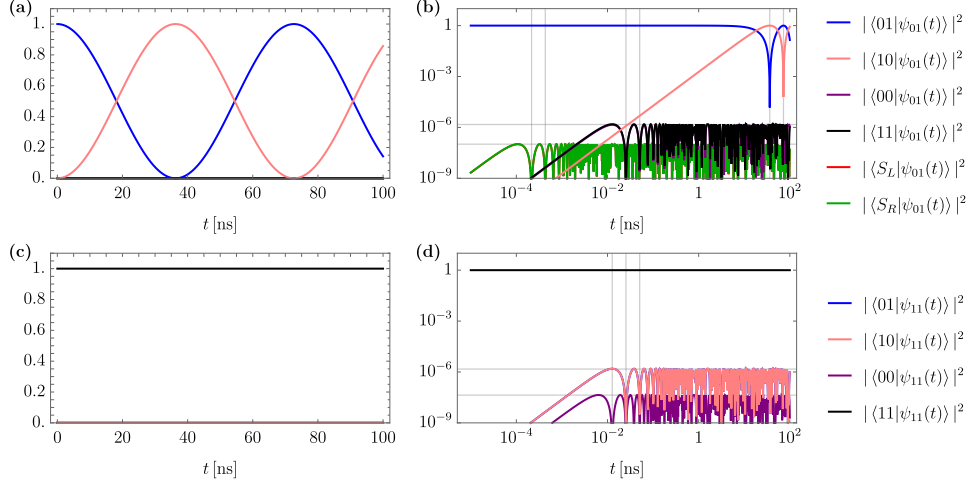


Figure 2.6: Overlaps of the  $|\psi_{01}(t)\rangle$  state [(a) and (b)], and the  $|\psi_{11}(t)\rangle$  state [(c) and (d)] as a function of time for the low symmetry case, where  $\varphi = \pi/8$  and  $v_B = 15$  meV, for a silicon NW. The time evolution is shown (a) on a liner-linear scale (b) on a log-log scale, with the horizontal lines showing the estimates for the overlaps obtained in Eqs. (2.15), (2.16), and (2.43) [(c) and (d) similarly]. Horizontal lines are showing the maximal overlap as a function of time [note that the one corresponding to  $|\langle 01|\psi_{11}(t)\rangle|^2 = |\langle 11|\psi_{01}(t)\rangle|^2$  is shown on both (b) and (d)]. Overlaps with different basis states are oscillating with the half cycle duration of  $\sim h/U$  for  $|\langle S_L|\psi_{01}(t)\rangle|^2$ ,  $\sim h/\Delta_z$  for  $|\langle 11|\psi_{01}(t)\rangle|^2$ , and  $\sim h/(2\Delta_z)$  for  $|\langle 00|\psi_{11}(t)\rangle|^2$  as illustrated by the vertical lines in (b) and (d).

with the states  $|0+\rangle$  and  $|1-\rangle$  being eigenstates of the symmetry operator  $D(S_{2B})$ . The energy splitting between the states  $|0+\rangle$  and  $|1-\rangle$  is  $\Delta'_0$  and the symmetry breaking part of the Hamiltonian  $H_{\text{SO}}^{2 \times 2}$  is proportional to  $\nu = \langle 1- | H_{\text{SO}}^{2 \times 2} | 0+ \rangle = \langle 1- | H_{\text{QD}}^{2 \times 2} | 0+ \rangle$ . Furthermore,  $\text{Re}(\nu)$  and  $\text{Im}(\nu)$  correspond to the real and imaginary parts of  $\nu$ , respectively.

Even though the coupling  $\nu$  cannot be expressed in a simple form generally, for the NW system considered in Sec. 2.6 one can simply extract relations for  $\nu$  in two special cases, without performing an explicit Schrieffer-Wolff transformation. These are:

- (i) If  $E_B = 0$ , the symmetry breaking part contains only Eqs. (2.12a) and (2.12b) and therefore  $H_{\text{SO}} \sim \sin(4\varphi)$ . Consequently, the coupling associated with the cubic anisotropy is  $\nu \sim \sin(4\varphi)$ . The values of  $\varphi$  where the coupling vanishes correspond to high-symmetry directions in the system where

$S_{2B}$  is a symmetry of the Hamiltonian  $H_{\text{QD}}$ .

(ii) If we treat the bulk Hamiltonian  $H_{\text{LK}} + H_Z$  in the axial approximation (i.e.,  $\Delta\gamma = q = 0$ ), the coupling induced by the electric field is  $\nu \sim eE_B$ , similarly to the case of Rashba SOI. Therefore, we associate this effect to DRSOI [32,33].

Diagonalizing the effective  $2 \times 2$  Hamiltonian of Eq. (2.36), we recover the eigenstates of  $H_{\text{QD}}$  as

$$|0\rangle = \frac{\Delta_0 + \Delta'_0}{2\mathcal{N}} |0+\rangle + \frac{\nu}{\mathcal{N}} |1-\rangle, \quad (2.37a)$$

$$|1\rangle = -\frac{\nu^*}{\mathcal{N}} |0+\rangle + \frac{\Delta_0 + \Delta'_0}{2\mathcal{N}} |1-\rangle, \quad (2.37b)$$

corresponding to the energies  $+\Delta_0/2 = \sqrt{\Delta_0'^2/4 + |\nu|^2}$  and  $-\Delta_0/2$ , respectively. The normalization factor is  $\mathcal{N} = \sqrt{(\Delta_0 + \Delta'_0)^2/4 + |\nu|^2}$ .

Moving on to the DQD problem, we introduce the low-energy basis  $|0_{L(R)+}\rangle$  and  $|1_{L(R)-}\rangle$  associated to the left (right) QDs and define the overlaps

$$s_0 = \langle 0_L+ | 0_R+ \rangle \quad (2.38a)$$

$$s_1 = \langle 1_L- | 1_R- \rangle, \quad (2.38b)$$

which are in general nonzero, whereas the anti-aligned overlaps vanish, i.e.,  $\langle 1_L- | 0_R+ \rangle = \langle 0_L+ | 1_R- \rangle = 0$  due to the symmetry properties of the basis states. The system we consider in Sec. 2.6 is  $L \leftrightarrow R$  symmetric, implying that the quantities  $s_0$  and  $s_1$  are real. Exploiting the relations between the basis states Eq. (2.38), we write the overlap between eigenstates  $|0_L\rangle$  and  $|1_R\rangle$  as

$$S_{01} = \langle 0_L | 1_R \rangle = \frac{\nu^*}{\mathcal{N}} \frac{\Delta_0 + \Delta'_0}{2\mathcal{N}} (s_1 - s_0). \quad (2.39)$$

Due to the cylindrical symmetry of the NW the confinement respects the symmetry  $S_{2B}$ , if the magnetic field is applied perpendicularly to the wire. The induced Zeeman splittings of the left QD reads

$$\begin{aligned} \frac{\Delta_x^L - i\Delta_y^L}{2} &= \frac{\nu^*}{\mathcal{N}} \frac{\Delta_0 + \Delta'_0}{2\mathcal{N}} \\ &\times [\langle 1_L- | \delta V_L | 1_L- \rangle - \langle 0_L+ | \delta V_L | 0_L+ \rangle], \end{aligned} \quad (2.40)$$

where  $\delta V_L = V_{\text{DQD}} - V_L$ , and the corrections due to the orthogonalization of the left and right bases are neglected. At last, we show the formula for

the coupling matrix element  $\langle T_+ | C | T_0 \rangle$  (to lowest order in the overlaps)

$$\begin{aligned} \frac{J_{xz}^s - iJ_{yz}^s}{2\sqrt{2}} &= \frac{\nu^*}{\mathcal{N}} \left( \frac{\Delta_0 + \Delta'_0}{2\mathcal{N}} \right)^3 \sqrt{2} \\ &\times \left[ \langle 0_{L+}, 1_{R-} | C | 0_{L+}, 1_{R-} \rangle \right. \\ &\quad \left. - \langle 0_{L+}, 0_{R+} | C | 0_{L+}, 0_{R+} \rangle \right]. \end{aligned} \quad (2.41)$$

Importantly, the overlap  $S_{01}$  and anisotropic couplings share the prefactor  $\nu^*/\mathcal{N}$ , which is typically a small parameter. Therefore, the simple quantity  $S_{01}$  does not only show the symmetry properties of  $H_{\text{DQD}}$  but can also be used to study the competition of the two main spin mixing effects, the cubic anisotropy and DRSOI.

## 2.G Slow $\sqrt{\text{SWAP}}$ gates and anisotropy-limited fidelity

In Sec. 2.6 we considered the time evolution of the states  $|\psi_{01}(t)\rangle$  and  $|\psi_{11}(t)\rangle$ , identified the couplings leading to the largest undesired overlaps which provided good estimates for the error rates  $1 - \mathcal{F}_{01}$  and  $1 - \mathcal{F}_{11}$  for the  $\sqrt{\text{SWAP}}$  gate. We found that the error rate  $1 - \mathcal{F}_{01}$  is orders of magnitudes higher than the one corresponding to the  $|11\rangle$  state, due to the possibility of tunneling to a doubly occupied state.

In this appendix we discuss a parameter regime for the  $\sqrt{\text{SWAP}}$  gate where the two fidelities are limited by the same transition probability that is set by the anisotropic couplings. This is the regime where the potential barrier is high enough, e.g.,  $v_B = 15$  meV in Fig. 2.6, while the rest of the parameters were set to be identical to the case of Figs. 2.4 and 2.5. The corresponding error rate for the  $\sqrt{\text{SWAP}}$  gate is obtained as

$$1 - \mathcal{F} \sim 2 |\langle 01 | \psi_{11}(\tau_s) \rangle|^2 \sim 2 \frac{\Delta_x^2 + \Delta_y^2}{\Delta_z^2} \sim 3 \cdot 10^{-6}, \quad (2.42)$$

where  $\mathcal{F} = \mathcal{F}_{01} = \mathcal{F}_{11}$  is the gate fidelity that is independent from the input state. When the potential barrier is increased, the singlet triplet splitting is reduced, increasing the  $\sqrt{\text{SWAP}}$  operation time by two orders of magnitude to  $\tau_s \sim 18$  ns.

For large enough potential barrier  $v_B$ , Eq. (2.14) loses its validity since in general the transition probability is set by the tunnel coupling  $\langle S_L | H_{\text{DQD}}^{6 \times 6} | S \rangle$ ,

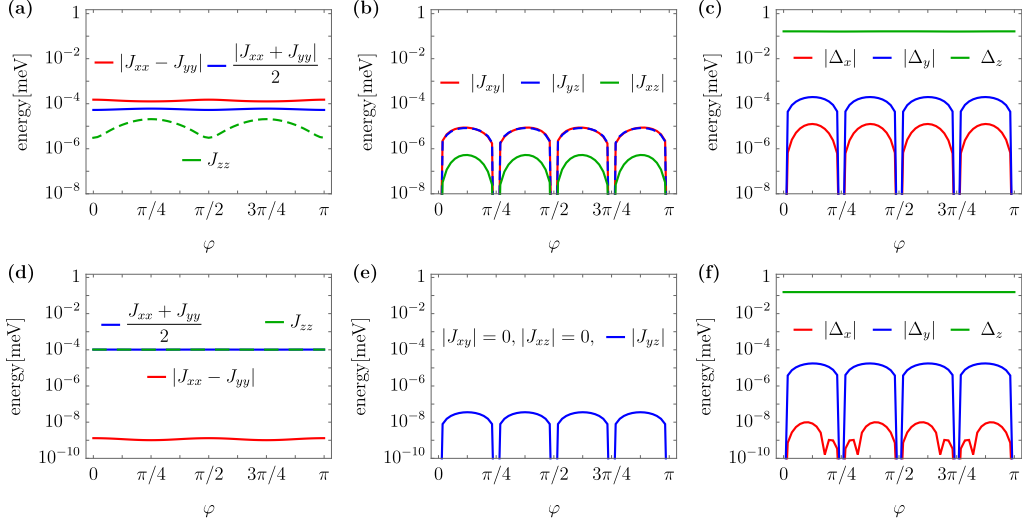


Figure 2.7: (a)-(c) Coefficients characterizing the exchange interaction and the single particle Hamiltonian as a function of the magnetic field direction  $\varphi$  for a silicon NW. For the numerical simulation the following parameters were used: double dot distance  $2a = 30$  nm; barrier height  $v_B = 15$  meV; magnetic field  $B = 1$  T; harmonic potential in the transverse directions with a confinement length of  $2l_T = 8$  nm. (d)-(f) Coefficients characterizing the exchange interaction as a function of the magnetic field direction  $\varphi$  for a Ge/Si core/shell NW. For the numerical simulation the following parameters were used: double dot distance  $2a = 60$  nm; barrier height  $v_B = 15$  meV; magnetic field  $B = 0.5$  T; relative shell thickness [85]  $(R_s - R_c)/R_c = 0.2$ ; harmonic potential in the transverse directions with a confinement length of  $2l_T = 8$  nm.

i.e.,

$$|\langle S_L | \psi_{01}(\tau_s) \rangle|^2 \sim 2 \frac{|\langle S_L | H_{\text{DQD}}^{6 \times 6} | S \rangle|^2}{U^2} \sim 10^{-7}. \quad (2.43)$$

This is an order of magnitude smaller than the leading correction to the error rate. Therefore, we conclude that the anisotropic corrections are influencing the  $\sqrt{\text{SWAP}}$  gate fidelities only for very slow gates.

## 2.H Comparison of the exchange interaction between silicon and Ge/Si core/shell NWs

In this appendix we present the role of the anisotropy parameters  $\Delta\gamma/\bar{\gamma}$  and  $q/|\kappa|$  for the exchange interaction and, in particular, compare silicon with Ge/Si NWs in the absence of electric fields, i.e.,  $\mathbf{E} = 0$ . In Fig. 2.4 we saw for the case of silicon that the cubic anisotropy renders the exchange interaction anisotropic and introduces off-diagonal terms  $J_{xz}$ ,  $J_{yz}$ , if the magnetic field is applied in a low-symmetry direction. As we have seen in App. 2.F, these anisotropic effects disappear in the axial approximation since the symmetry breaking parts of the Hamiltonian, Eqs. (2.12a) and (2.12b) are proportional to  $\Delta\gamma$  and  $q$ , respectively.

Next, given the recent experimental interest, we consider a Ge/Si core/shell NW, with [001] growth direction. The coordinate axes were chosen identically to the case of silicon ( $x, y, z$  correspond to the [100], [010] and [001] crystallographic axes, respectively) in which case the Bir-Pikus Hamiltonian becomes

$$H_{\text{BP}}^{[001]} = b(\epsilon_{zz} - \epsilon_{\perp})J_z^2, \quad (2.44)$$

where we omitted a constant part,  $b = -2.5 \text{ eV}$ , while the values of the strain ( $\epsilon_{zz}$  and  $\epsilon_{\perp}$ ) as a function of relative shell thickness  $(R_s - R_c)/R_c = 0.2$  are taken from Ref. [85].

We performed the calculation similarly to Sec. 2.6. For the case of a silicon NW in Figs. 2.7(a)-(c) we used the same parameters as in Sec. 2.6, the only difference being that we used a significantly higher potential barrier,  $v_B = 15 \text{ meV}$ . For the case of the Ge/Si core/shell NW [see Figs. 2.7(d)-(f)], the shell is taken into account via the strain term in the Hamiltonian of Eq. (2.44), and the Luttinger parameters are  $\gamma_1 = 13.38$ ,  $\gamma_2 = 4.24$ ,  $\gamma_3 = 5.69$ ,  $\kappa = 3.41$ , and  $q = 0.06$  [63]. Note that while the anisotropy parameters for silicon are  $\Delta\gamma/\bar{\gamma} = 1.1$  and  $q/|\kappa| = 0.024$ , for germanium the same quantities are significantly smaller, i.e.,  $\Delta\gamma/\bar{\gamma} = 0.28$  and  $q/|\kappa| = 0.018$ .

A remarkable reduction can be observed in the anisotropic exchange terms for a Ge/Si core/shell NW (see Fig. 2.7), compared to the case of silicon NWs. The parameters are set such that the Zeeman splitting and the diagonal exchange matrix elements are of the same order for the two materials. One can directly see that although in the case of silicon NW the off-diagonal terms can be comparable to the diagonal ones, they almost

disappear (at least they are below the accuracy of our numerics) for the strained Ge/Si core/shell NW.



# Bibliography

- [1] D. Loss and D. P. DiVincenzo, *Phys. Rev. A* **57**, 120 (1998).
- [2] C. Kloeffer and D. Loss, *Annu. Rev. Condens. Matter Phys.* **4**, 51 (2013).
- [3] V. N. Golovach, M. Borhani, and D. Loss, *Phys. Rev. B* **74**, 165319 (2006).
- [4] K. C. Nowack, F. H. L. Koppens, Yu. V. Nazarov, and L. M. K. Vandersypen, *Science* **318**, 1430 (2007).
- [5] S. Nadj-Perge, S. M. Frolov, E. P. A. M. Bakkers, and L. P. Kouwenhoven, *Nature (London)* **468**, 1084 (2010).
- [6] M. D. Schroer, K. D. Petersson, M. Jung, and J. R. Petta, *Phys. Rev. Lett.* **107**, 176811 (2011).
- [7] J. R. Petta, A. C. Johnson, J. M. Taylor, E. A. Laird, A. Yacoby, M. D. Lukin, C. M. Marcus, M. P. Hanson, and A. C. Gossard, *Science* **309**, 2180 (2005).
- [8] R. Brunner, Y.-S. Shin, T. Obata, M. Pioro-Ladriere, T. Kubo, K. Yoshida, T. Taniyama, Y. Tokura, and S. Tarucha, *Phys. Rev. Lett.* **107**, 146801 (2011).
- [9] M. Veldhorst, C. H. Yang, J. C. C. Hwang, W. Huang, J. P. Dehollain, J. T. Muhonen, S. Simmons, A. Laucht, F. E. Hudson, K. M. Itoh, A. Morello, and A. S. Dzurak, *Nature (London)* **526**, 410 (2015).
- [10] A. V. Khaetskii, D. Loss, and L. Glazman, *Phys. Rev. Lett.* **88**, 186802 (2002).
- [11] W. A. Coish and D. Loss, *Phys. Rev. B* **70**, 195340 (2004).

- [12] W. A. Coish and J. Baugh, *Physica Status Solidi B* **246**, 2203 (2009).
- [13] D. V. Bulaev and D. Loss, *Phys. Rev. Lett.* **95**, 076805 (2005).
- [14] D. V. Bulaev and D. Loss, *Phys. Rev. Lett.* **98**, 097202 (2007).
- [15] X.-J. Hao, T. Tu, G. Cao, C. Zhou, H.-O. Li, G.-C. Guo, W. Y. Fung, Z. Ji, G.-P. Guo, and W. Lu, *Nano Lett.* **10**, 2956 (2010).
- [16] C. Kloeffer, M. Trif, P. Stano, and D. Loss, *Phys. Rev. B* **88**, 241405(R) (2013).
- [17] R. Maurand, X. Jehl, D. Kotekar-Patil, A. Corna, H. Bohuslavskiy, R. Laviéville, L. Hutin, S. Barraud, M. Vinet, M. Sanquer, and S. De Franceschi, *Nat. Commun.* **7**, 13575 (2016).
- [18] R. Li, F. E. Hudson, A. S. Dzurak, and A. R. Hamilton, *Nano Lett.* **15**, 7314 (2015).
- [19] H. Watzinger, J. Kukučka, L. Vukušić, F. Gao, T. Wang, F. Schäffler, J. Zhang, and G. Katsaros, *Nat. Commun.* **9**, 3902 (2018).
- [20] L. A. Terrazos, E. Marcellina, S. N. Coppersmith, M. Friesen, A. R. Hamilton, X. Hu, B. Koiller, A. L. Saraiva, D. Culcer, and R. B. Capaz, *arXiv:1803.10320* (2018).
- [21] F. Gao, J.-H. Wang, H. Watzinger, H. Hu, M. J. Rančić, J.-Y. Zhang, T. Wang, Y. Yao, G.-L. Wang, J. Kukučka, L. Vukušić, C. Kloeffer, D. Loss, F. Liu, G. Katsaros, and J.-J. Zhang, *Adv. Mater.* **2020**, 1906523 (2020).
- [22] J. Fischer, W. A. Coish, D. V. Bulaev, and D. Loss, *Phys. Rev. B* **78**, 155329 (2008).
- [23] D. Brunner, B. D. Gerardot, P. A. Dalgarno, G. Wüst, K. Karrai, N. G. Stoltz, P. M. Petroff, and R. J. Warburton, *Science* **325**, 70 (2009).
- [24] J. Fischer and D. Loss, *Phys. Rev. Lett.* **105**, 266603 (2010).
- [25] F. Maier, C. Kloeffer, and D. Loss, *Phys. Rev. B* **87**, 161305(R) (2013).
- [26] L. Vukušić, J. Kukučka, H. Watzinger, J. M. Milem, F. Schäffler, and G. Katsaros, *Nano Lett.* **18**, 117141 (2018).

- [27] W. J. Hardy, C. T. Harris, Y. Su, Y. Chuang, J. Moussa, L. N. Maurer, J. Li, T. Lu, and D. R. Luhman, *Nanotechnology*, **30**, 215202 (2019).
- [28] A. Greilich, S. G. Carter, D. Kim, A. S. Bracker, and D. Gammon, *Nat. Photonics* **5**, 702 (2011).
- [29] N.W. Hendrickx, D.P. Franke, A. Sammak, G. Scappucci, M. Veldhorst, *Nature* **577**, 487 (2020).
- [30] P. C. Sercel and K. J. Vahala, *Phys. Rev. B* **42**, 3690 (1990).
- [31] D. Csontos, P. Brusheim, U. Zülicke, and H. Q. Xu, *Phys. Rev. B* **79**, 155323 (2009).
- [32] C. Kloeffer, M. Trif, and D. Loss, *Phys. Rev. B* **84**, 195314 (2011).
- [33] C. Kloeffer, M. J. Rančić, and D. Loss, *Phys. Rev. B* **97**, 235422 (2018).
- [34] A. P. Higginbotham, F. Kuemmeth, T. W. Larsen, M. Fitzpatrick, J. Yao, H. Yan, C. M. Lieber, and C. M. Marcus, *Phys. Rev. Lett.* **112**, 216806 (2014).
- [35] M. Brauns, J. Ridderbos, A. Li, E. P. A. M. Bakkers, and F. A. Zwanenburg, *Phys. Rev. B* **93**, 121408(R) (2016).
- [36] B. Voisin, R. Maurand, S. Barraud, M. Vinet, X. Jehl, M. Sanquer, J. Renard, and S. De Franceschi, *Nano Lett.* **16**, 88 (2016).
- [37] R. Wang, R. S. Deacon, J. Yao, C. M. Lieber, and K. Ishibashi, *Semicond. Sci. Technol.* **32**, 094002 (2017).
- [38] A. Crippa, R. Maurand, L. Bourdet, D. Kotekar-Patil, A. Amisse, X. Jehl, M. Sanquer, R. Laviéville, H. Bohuslavskiy, L. Hutin, S. Barraud, M. Vinet, Y.-M. Niquet, and S. De Franceschi, *Phys. Rev. Lett.* **120**, 137702 (2018).
- [39] J. Sun, R. S. Deacon, R. Wang, J. Yao, C. M. Lieber, and K. Ishibashi, *Nano Lett.* **18**, 6144 (2018).
- [40] F. N. M. Froning, M. K. Rehmann, J. Ridderbos, M. Brauns, F. A. Zwanenburg, A. Li, E. P. A. M. Bakkers, D. M. Zumbühl, and F. R. Braakman, *Appl. Phys. Lett.* **113**, 073102 (2018).

- [41] F. K. de Vries, J. Shen, R. J. Skolasinski, M. P. Nowak, D. Varjas, L. Wang, M. Wimmer, J. Ridderbos, F. A. Zwanenburg, A. Li, S. Koelling, M. A. Verheijen, E. P. A. M. Bakkers, and L. P. Kouwenhoven, *Nano Lett.* **18**, 6483 (2018).
- [42] Y. Jiang, N. Singh, T. Y. Liow, P. C. Lim, S. Tripathy, G. Q. Lo, D. S. H. Chan, and D.-L. Kwong, *IEEE Electron Device Lett.* **30**, 392 (2009).
- [43] A. V. Kuhlmann, V. Deshpande, L. C. Camenzind, D. M. Zumbühl, and Andreas Fuhrer, *Appl. Phys. Lett.* **113**, 122107 (2018).
- [44] A. M. Tyryshkin, S. Tojo, J. J. L. Morton, H. Riemann, N. V. Abrosimov, P. Becker, H.-J. Pohl, T. Schenkel, M. L. W. Thewalt, K. M. Itoh, and S. A. Lyon, *Nat. Mater.* **11**, 143 (2012).
- [45] M. Veldhorst, J. C. C. Hwang, C. H. Yang, A. W. Leenstra, B. de Ronde, J. P. Dehollain, J. T. Muhonen, F. E. Hudson, K. M. Itoh, A. Morello, and A. S. Dzurak, *Nat. Nanotechnol.* **9**, 981 (2014).
- [46] J. T. Muhonen, J. P. Dehollain, A. Laucht, F. E. Hudson, R. Kalra, T. Sekiguchi, K. M. Itoh, D. N. Jamieson, J. C. McCallum, A. S. Dzurak, and A. Morello, *Nat. Nanotechnol.* **9**, 986, (2014).
- [47] A. J. Sigillito, R. M. Jock, A. M. Tyryshkin, J. W. Beeman, E. E. Haller, K. M. Itoh, and S. A. Lyon, *Phys. Rev. Lett.* **115**, 247601 (2015).
- [48] L. Trifunovic, O. Dial, M. Trif, J. R. Wootton, R. Abebe, A. Yacoby, and D. Loss, *Phys. Rev. X* **2**, 011006 (2012).
- [49] S. E. Nigg, A. Fuhrer, and D. Loss, *Phys. Rev. Lett.* **118**, 147701 (2017).
- [50] S. C. Benjamin, *Phys. Rev. A* **64**, 054303 (2001).
- [51] J. Levy, *Phys. Rev. Lett.* **89**, 147902 (2002).
- [52] J. M. Taylor, H.-A. Engel, W. Dür, A. Yacoby, C. M. Marcus, P. Zoller, and M. D. Lukin, *Nature Physics* **1**, 177 (2005).
- [53] K. Ono, D. G. Austing, Y. Tokura, and S. Tarucha, *Science* **297**, 1313 (2002).

- [54] K. V. Kavokin, Phys. Rev. B **69**, 075302 (2004).
- [55] P. Wenk, M. Kammermeier, and J. Schliemann, Phys. Rev. B **93**, 115312 (2016).
- [56] B. Venitucci, L. Bourdet, D. Pouzada, and Y.-M. Niquet, Phys. Rev. B **98**, 155319 (2018).
- [57] N. O. Lipari and A. Baldereschi, Phys. Rev. Lett. **25**, 1660 (1970).
- [58]  $K(\mathbf{k}, \hat{\mathbf{J}}) = \frac{\hbar^2}{2m} \left[ -\frac{3}{2}k^2 + \frac{6}{5}(k_{x'}^2 \hat{J}_{x'}^2 + k_{y'}^2 \hat{J}_{y'}^2 + k_{z'}^2 \hat{J}_{z'}^2) - \frac{8}{5}(\{k_{x'}, k_{y'}\}\{\hat{J}_{x'}, \hat{J}_{y'}\} + \{k_{y'}, k_{z'}\}\{\hat{J}_{y'}, \hat{J}_{z'}\} + \{k_{z'}, k_{x'}\}\{\hat{J}_{z'}, \hat{J}_{x'}\}) \right]$ , where the anti-commutator is defined as  $\{A, B\} = \frac{1}{2}(AB + BA)$ .
- [59] Note that the corresponding equations (64) and (65) of Ref. [61] contain a typo in the first terms of the Hamiltonians, i.e.  $k^2 \rightarrow k^2/2$ . Furthermore, in equation (65) of Ref. [61] in the Zeeman term ( $\kappa - \bar{\gamma}/2$ ) should be replaced by  $(\kappa + \bar{\gamma}/2)$ . These corrections are then consistent with the equations (45), (69), and the rest of Ref. [61].
- [60] J. M. Luttinger and W. Kohn, Phys. Rev. **97**, 869 (1955).
- [61] J. M. Luttinger, Phys. Rev. **102**, 1030 (1956).
- [62] The anisotropic Zeeman term reads as  $2q\mu_B \mathbf{B} \cdot \hat{\mathcal{J}} = 2q\mu_B (B_{x'} \hat{J}_{x'}^3 + B_{y'} \hat{J}_{y'}^3 + B_{z'} \hat{J}_{z'}^3)$  where the axes  $x', y', z'$  are along the crystallographic axes  $\langle 100 \rangle$ .
- [63] R. Winkler, *Spin-Orbit Coupling Effects in Two-Dimensional Electron and Hole Systems* (Springer, Berlin, 2003).
- [64] D. S. Miserev and O. P. Sushkov, Phys. Rev. B **95**, 085431 (2017).
- [65] M. F. Doty, J. I. Climente, A. Greilich, M. Yakes, A. S. Bracker, and D. Gammon, Phys. Rev. B **81**, 035308 (2010).
- [66] Within the framework of this paper, we define the modulo function with shifted range, i.e.,  $\text{mod}_N(x) \in [-N/2, N/2)$ , for any  $x \in \mathbb{R}$ . This is related to the conventional definition via  $\text{mod}_N(x) = \text{mod}'_N(x + N/2) - N/2$ , where  $\text{mod}'_N(x) \in [0, N)$ .
- [67] J. Sólyom, *Fundamentals of the Physics of Solids (Vol. 1): Structure and Dynamics* (Springer, Berlin, 2007).

- [68] In our calculations we consider homogeneous electric and magnetic fields. Therefore  $H_{QD} - V_{QD}$  [see Eq. (2.2)] is identical for both QDs and Eq. (2.7) invariant under particle exchange.
- [69] G. Burkard, D. Loss, and D. P. DiVincenzo, Phys. Rev. B **59**, 2070 (1999).
- [70] G. Burkard and D. Loss, Phys. Rev. Lett. **88**, 047903 (2002).
- [71] D. Stepanenko, N. E. Bonesteel, D. P. DiVincenzo, G. Burkard, and D. Loss, Phys. Rev. B **68**, 115306 (2003).
- [72] S. Bravyi, D. DiVincenzo, and D. Loss, Ann. Phys. (New York) **326**, 2793 (2011).
- [73] Note that the matrix elements of the Hamiltonian in Eq. (2.10) are not independent of the relative phase of the basis states, and therefore only the absolute values of the off-diagonal exchange couplings and induced Zeeman splittings are shown in Figs. 2.4 and 2.7.
- [74] G. Burkard, G. Seelig, and D. Loss, Phys. Rev. B **62**, 2581, (2000).
- [75] M. D. Reed, B. M. Maune, R. W. Andrews, M. G. Borselli, K. Eng, M. P. Jura, A. A. Kiselev, T. D. Ladd, S. T. Merkel, I. Milosavljevic, E. J. Pritchett, M. T. Rakher, R. S. Ross, A. E. Schmitz, A. Smith, J. A. Wright, M. F. Gyure, and A. T. Hunter, Phys. Rev. Lett. **116**, 110402 (2016).
- [76] F. Martins, F. K. Malinowski, P. D. Nissen, E. Barnes, S. Fallahi, G. C. Gardner, M. J. Manfra, C. M. Marcus, and F. Kuemmeth, Phys. Rev. Lett. **116**, 116801 (2016).
- [77] We refer here to the direction along the NW as the growth direction.
- [78] Z. Scherübl, A. Pályi, G. Frank, I. E. Lukács, G. Fülöp, B. Fülöp, J. Nygård, K. Watanabe, T. Taniguchi, G. Zaránd, and S. Csonka, Comm. Phys. v. **2**, 108 (2019).
- [79] G. Frank, Z. Scherübl, S. Csonka, G. Zaránd, and A. Pályi, arXiv:1910.02831 (2019).

- [80] D. Q. Wang, O. Klochan, J.-T. Hung, D. Culcer, I. Farrer, D. A. Ritchie, and A. R. Hamilton, *Nano Lett.* **16**, 7685 (2016).
- [81] J.-T. Hung, E. Marcellina, B. Wang, A. R. Hamilton, and D. Culcer, *Phys. Rev. B* **95**, 195316 (2017).
- [82] L. C. Camenzind, L. Yu, P. Stano, J. D. Zimmerman, A. C. Gossard, D. Loss, and D. M. Zumbühl, *Phys. Rev. Lett.* **122**, 207701 (2019).
- [83] F. Bloch, *Z. Phys.* **52**, 555–600 (1929).
- [84] S. Bosco and D. P. DiVincenzo, *Phys. Rev. B* **100**, 035416 (2019).
- [85] C. Kloeffer, M. Trif, and D. Loss, *Phys. Rev. B* **90**, 115419 (2014).

# CHAPTER 3

## Zero-field splitting in Si and Ge quantum dots

*Adapted from:*

Bence Hetényi, Stefano Bosco, and Daniel Loss

*“Anomalous zero-field splitting for hole spin qubits in Si and Ge quantum dots”,*

arXiv:2205.02582 (2022)

An anomalous energy splitting of spin triplet states at zero magnetic field has recently been measured in germanium quantum dots. This zero-field splitting could crucially alter the coupling between tunnel-coupled quantum dots, the basic building blocks of state-of-the-art spin-based quantum processors, with profound implications for semiconducting quantum computers. We develop an analytical model linking the zero-field splitting to spin-orbit interactions that are cubic in momentum. Such interactions naturally emerge in hole nanostructures, where they can also be tuned by external electric fields, and we find them to be particularly large in silicon and germanium, resulting in a significant zero-field splitting in the  $\mu\text{eV}$  range. We confirm our analytical theory by numerical simulations of different quantum dots, also including other possible sources of zero-field splitting. Our findings are applicable to a broad range of current architectures encoding spin qubits and provide a deeper understanding of these materials, paving the way towards the next generation of semiconducting quantum processors.



### 3.1 Introduction

The compatibility of localized spins in semiconducting quantum dots (QDs) [1] with the well-developed CMOS technology is pushing these architectures to the front of the race towards the implementation of scalable quantum computers [2, 4, 11, 16, 18]. Spin qubits based on hole states in silicon (Si) and germanium (Ge), in particular, are gaining increasing attention in the community [11, 16] because of their large spin-orbit interaction (SOI) [7–10], enabling fast and power-efficient all-electric gates [11–13] and strong transversal and longitudinal coupling to microwave resonators [14–18]. Also, significant steps forward in material engineering [19, 20] as well as fast spin read-out and qubit initialization protocols [21–24] facilitated the implementation of high-fidelity two-qubit gates [6, 25] and of a four-qubit quantum processor with controllable qubit-qubit couplings [27].

In contrast to electrons, the properties of hole QDs depend on the mixing of two bands, the heavy-hole (HH) and light-hole (LH) bands, resulting in several unique features that are beneficial for quantum computing applications [28–35]. In addition to the large and externally controllable SOI [7, 28, 33], that can be conveniently engineered to be linear or cubic in momentum [8, 29, 36–39], hole spin qubits also feature highly anisotropic and electrically tunable  $g$ -factors [40–44], hyperfine interactions [35], and anisotropies of exchange interaction at finite magnetic fields [31]. Because HHs and LHs are strongly mixed in quasi one-dimensional (1D) systems, these effects are significantly enhanced in long QDs.

Recent experiments in Ge QDs with even hole occupation have also detected a large anomalous lifting of the threefold degeneracy of triplet states at zero magnetic field [45], yielding another striking difference between electrons and holes. A similar zero-field splitting (ZFS) has been reported in other quantum systems e.g., divacancies in silicon carbide [46], nitrogen-vacancies in diamond [47, 48], and carbon nanotubes [49], where it is associated to the anisotropy of the two-particle exchange interaction. In this letter, we discuss the microscopic origin of this anisotropy in hole QDs and we propose a general theory modelling the ZFS in a wide range of devices. Our theory helps to develop a fundamental understanding of ZFS, essential to account for its effect in quantum computing applications. For example, the exchange anisotropy could enable the encoding of hole singlet-triplet qubits [50–53] at zero magnetic field, and when combined with a Zeeman field, it can lift the Pauli spin-blockade,

with critical implications in read-out protocols [54]. Furthermore, ZFS can introduce systematic errors in two-qubit gates based on isotropic interactions between tunnel-coupled QDs [1, 31, 55].

We associate the large ZFS emerging in hole QDs to a SOI cubic in momentum. The SOI is a natural candidate to explain exchange anisotropies, however, its dominant contribution –linear in momentum– can be gauged away in quasi 1D systems [56–58] and cannot lift the triplet degeneracy without magnetic fields. While in electronic systems only the linear SOI is sizeable, in hole nanostructures the large mixing of HHs and LHs induces a large cubic SOI [29, 30] yielding a significant ZFS in Si and Ge QDs. Strikingly, this ZFS is tunable by external electric fields and can be engineered by the QD design.

We develop a theory for the cubic-SOI induced ZFS that relies exclusively on single-particle properties of the QD and the Bohr radius, providing an accurate estimate of the ZFS in a wide range of common architectures. In realistic systems, this ZFS is in the  $\mu\text{eV}$  range, orders of magnitude larger than alternative mechanisms. For example, we find that ZFS of a few neV can also be induced by short-range corrections of the Coulomb interaction arising from the  $p$ -type orbital wavefunctions of the valence band [34, 59]. In addition, our theory relates the axis of the exchange anisotropy to the direction of the SOI, and corroborates the observed response of the QDs to small magnetic fields [45]. Importantly, because in long QDs comprising two holes the Coulomb repulsion of the two particles forms a double QD [60–63], our theory describes the exchange anisotropy also in tunnel-coupled QDs, the prototypical building blocks of current spin-based quantum processors [31, 55, 64], and thus our findings have profound implications in the growing research field of quantum computing with holes.

## 3.2 Analytical theory

Large SOI emerges naturally in hole spin qubits encoded in long quantum dots, where the confinement potential in two directions is stronger than in the third one. Such nanostructures include a wide range of common spin qubit architectures, such as Si FinFETs [12, 23, 28, 33], squeezed QDs in planar Ge [37], and Si and Ge NWs [7, 9, 62, 68]. Their response is well-described by an effective 1D low-energy Hamiltonian acting only on a few subbands.

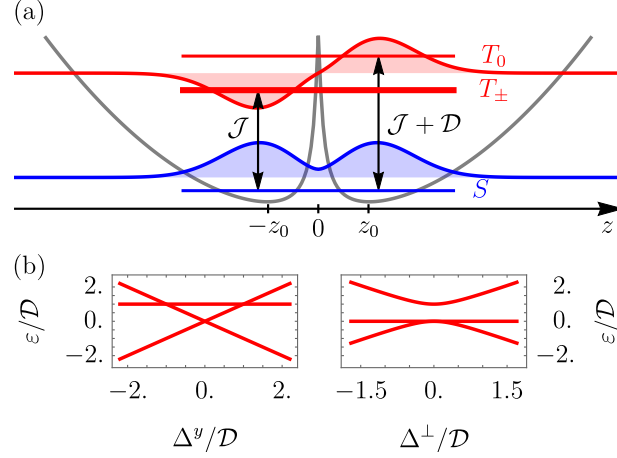


Figure 3.1: Exchange interaction in long quantum dots. (a) The effective 1D potential  $V_c(z_1 - z_2)$  is shown in gray (without units) as a function of relative coordinate  $z = z_1 - z_2$ , where  $\pm z_0$  are the minima of the potential. The energy levels corresponding to the lowest singlet and triplet states, and the corresponding orbital wavefunctions are overlaid with blue and red, respectively. Vertical arrows show the definition of the exchange splitting and ZFS,  $\mathcal{J}$  and  $\mathcal{D}$ , respectively. Note that the energy scale of the singlet-triplet energy levels is only schematic, not matched with that of the effective potential. (b) Splitting  $\epsilon$  of the three triplet states when the Zeeman field is aligned with the SOI ( $\Delta^y$ , left panel), and when it is perpendicular to it ( $\Delta^\perp$ , right panel).

We now focus on a QD defined in a NW with a square cross-section of side  $L$ . By resorting to Schrieffer-Wolff perturbation theory [69] discussed in detail in Sec. 3.A of [66], we find the effective Hamiltonian acting on the lowest pair of subbands as

$$H_1 = \frac{p_z^2}{2m^*} + vp_z\sigma^y + v_3p_z^3\sigma^y + \frac{\hbar^2\gamma_1}{2m^*l_z^4}z^2, \quad (3.1)$$

up to third order in the momentum  $p_z$  in the long-direction. Here,  $m^*$  is the effective mass,  $v$  and  $v_3$  are the linear and cubic SOI, respectively, and  $\sigma^y$  is a Pauli matrix. The QD is defined by a harmonic potential parametrized by the length  $l_z$  and modelling the smooth electrostatic confinement produced by metallic gates. Eq. (3.1) is valid when  $l_z \gtrsim L/\pi$ . Two holes confined in the same QD are described by the Hamiltonian  $H_2 = H_1^{(1)} + H_1^{(2)} + V_c^{(1,2)}$ , where  $V_c^{(1,2)}$  is the effective Coulomb potential in the lowest subband sector. Coulomb interactions with higher sub-

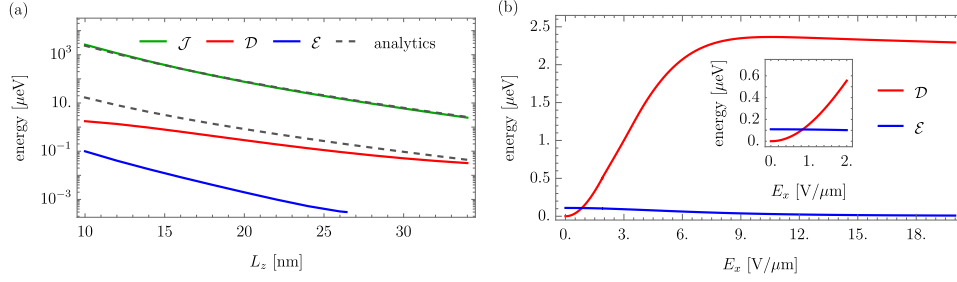


Figure 3.2: Anisotropic exchange interactions in Ge. (a) Exchange splitting  $\mathcal{J}$  and ZFSs  $\mathcal{D}$  and  $\mathcal{E}$  in a Ge square NW with side length  $L = 10$  nm and compressive strain  $\epsilon_{zz} = -0.5\%$ , as a function of QD length  $L_z$  for  $E_x = 5$  V/ $\mu\text{m}$ ; the analytical results of the corresponding quantities are shown in dashed lines. Here the QD length is defined as  $L_z = (m^*\gamma_1/m_e)^{1/4}l_z \approx l_z$ , where  $m_e/\gamma_1$  is the averaged hole mass with  $m_e$  being the electron mass and  $\gamma_1$  is a Luttinger parameter [65, 66]. (b) ZFSs as a function of electric field  $E_x$  for  $L_z = 12$  nm; inset: zoom at small electric fields, where the main anisotropy axis changes from the wire axis ( $z$ ) to the SOI axis ( $y$ ).

bands are negligible when  $L/\pi < a_B$ , where  $a_B = 4\pi\epsilon_r\hbar^2/m^*e^2$  is the effective Bohr radius with  $\epsilon_r$  being the dielectric constant of the material. The Coulomb potential  $V_c^{(1,2)}$  is sketched in Fig. 3.1(a), and is discussed in [66].

The linear SOI  $v$  in Eq. (3.1) can be eliminated exactly by a spin-dependent shift of momentum that leaves the potential unchanged, and only negligibly renormalizes the effective mass  $m^*$  [66]. The two-particle Hamiltonian is then given by

$$H_2 = \frac{1}{4m^*}P^2 + \frac{\hbar^2}{m^*l_z^4}Z^2 + \frac{1}{m^*}p^2 + \frac{\hbar^2}{4m^*l_z^4}z^2 + V_c(z) + \mathcal{P}_3^+(\sigma_1^y + \sigma_2^y) + \mathcal{P}_3^-(\sigma_1^y - \sigma_2^y), \quad (3.2)$$

where  $Z = (z_1 + z_2)/2$  is the center-of-mass (COM) coordinate with conjugate momentum  $P = p_{z_1} + p_{z_2}$ , and  $z = z_1 - z_2$  is the relative coordinate with momentum  $p = (p_{z_1} - p_{z_2})/2$ . The cubic SOI yields the perturbative corrections  $\mathcal{P}_3^+ = v_3 (\frac{1}{8}P^3 + \frac{3}{2}Pp^2)$ , and  $\mathcal{P}_3^- = v_3 (\frac{3}{4}P^2p + p^3)$  in the second line of Eq. (3.2); these terms mix relative and COM coordinates and are crucial for the ZFS.

At  $v_3 = 0$ , the Hamiltonian of the COM coordinates is a harmonic oscillator with an orbital energy  $\Delta_o = \hbar^2/m^*l_z^2$ , while the Hamiltonian of

the relative coordinates is  $H_{\text{rel}} = p^2/m^* + \hbar^2 z^2/4m^*l_z^4 + V_c(z)$ . In a NW with a square cross-section and when  $l_z \gtrsim a_B$ , the effective 1D Coulomb interaction is well-approximated by  $V_c(z) \approx \Delta_o[z^2 + (L/4)^2]^{-1/2}l_z^2/a_B$ , where  $L/4$  is a short-range cutoff of the potential derived in Sec. 3.A of [66]. In this case, the system is fully described by two relative length scales  $l_z/a_B$  and  $L/a_B$ . Because the effective potential in  $H_{\text{rel}}$  is an even function of  $z$ , the corresponding eigenfunctions have either even or odd parity, enabling the distinction between singlets (even) and triplets (odd) states.

While in this work we focus on a single QD occupied by two holes, we emphasize that our theory is also valid for two tunnel-coupled QDs, the basic components of current spin-based quantum processors [6, 27]. In fact, as sketched in Fig. 3.1(a), in a doubly occupied long QD, with  $l_z \gtrsim a_B$ , the Coulomb repulsion forces the two particles towards opposite ends of the dot [60–62], effectively resulting in two coupled dots. We also remark that because  $a_B \sim 12$  nm ( $a_B \sim 3$  nm) in Ge (Si), the condition  $l_z \gtrsim a_B$  of long QDs is typically respected in current experimental setups [13, 45, 70].

By a second order Schrieffer-Wolff transformation [69] and projecting the two-particle Hamiltonian onto the lowest energy singlet and triplet states, we find that the exchange Hamiltonian is

$$H_{\text{eff}} = \frac{1}{4}(\mathcal{J} + \mathcal{D})\boldsymbol{\sigma}_1 \cdot \boldsymbol{\sigma}_2 - \frac{1}{2}\mathcal{D}\sigma_1^y\sigma_2^y + \frac{1}{2}\boldsymbol{\Delta}^\perp \cdot (\boldsymbol{\sigma}_1^\perp + \boldsymbol{\sigma}_2^\perp) + \frac{1}{2}\Delta^y(\sigma_1^y + \sigma_2^y), \quad (3.3)$$

where  $\Delta^y$  is the Zeeman field parallel to the SOI, while  $\boldsymbol{\Delta}^\perp = (\Delta^x, \Delta^z)$  are components perpendicular to it. The exchange splitting  $\mathcal{J} = \varepsilon_{T_\pm} - \varepsilon_S > 0$  only weakly depends on  $v_3$  and it is well approximated by  $\mathcal{J}_0 = \zeta \hbar^2 a_B^2/m^*l_z^4$ , the energy gap between the lowest odd and even eigenstates of the relative coordinate Hamiltonian. We introduce the dimensionless coefficient  $\zeta \sim 0.3 - 1$  for  $0.8 < L/a_B < 2$  and  $a_B \lesssim l_z$  [66].

Without magnetic fields,  $\Delta^i = 0$  and Eq. (3.3) corresponds to an exchange Hamiltonian with a uni-axial anisotropy, i.e.,  $J_{xx} = J_{zz} = \mathcal{J}$  and the anisotropy axis is aligned to the SOI (i.e.,  $y$ -direction) with  $J_{yy} = \mathcal{J} + \mathcal{D}$ . As sketched in Fig. 3.1(a), the ZFS  $\mathcal{D}$  lifts the degeneracy of the triplets  $T_\pm$  and  $T_0$ , where the three triplets  $T_{\pm,0}$  are defined with quantization axis along  $y$ -direction. From perturbation theory, we obtain [66]

$$\mathcal{D} = m^*v_3^2 \frac{\hbar^4}{l_z^4} \eta. \quad (3.4)$$

Here the dimensionless coefficient  $\eta \sim 0.4 - 0.8$  includes various combinations of dimensionless momentum matrix elements. The exact functional dependence of  $\eta$  and  $\zeta$  on  $L$  and  $l_z$  is discussed in detail in Sec. 3.A of [66]. Because  $\eta$  depends only weakly on the relative length scales  $l_z/a_B$  and  $L/a_B$  in long QDs, to good approximation we find that  $\mathcal{D} \propto l_z^{-4}$ . We also emphasize that this ZFS is strongly dependent on the cubic SOI and it requires a sizeable value of  $v_3$ , achievable only in hole QDs. The relative anisotropy of the exchange interactions is

$$\frac{\mathcal{D}}{\mathcal{J}} = \frac{m^* v_3^2 \hbar^2 \eta}{a_B^2 \zeta}, \quad (3.5)$$

where  $\eta/\zeta \sim 1 - 5$  depends weakly on  $a_B$  and therefore, the anisotropy scales as  $\mathcal{D}/\mathcal{J} \propto (m^*)^4$ .

The magnetic field dependence of the triplet states can also be deduced straightforwardly from Eq. (3.3) and it is sketched in Fig 3.1(b). If the magnetic field is applied parallel to the SOI (i.e. the anisotropy axis) the non-degenerate triplet  $T_0$  is unaffected by the field and  $\varepsilon_{T_0} = \mathcal{J} + \mathcal{D}$ , whereas the degenerate triplets  $T_{\pm}$  split linearly with the Zeeman field as  $\varepsilon_{T_{\pm}} = \mathcal{J} \pm \Delta^y$ . In contrast, if the field is applied perpendicular to the SOI, one of the degenerate triplets, e.g.,  $T'_0$ , stays at the same energy  $\varepsilon_{T'_0} = \mathcal{J}$ , while the remaining triplets  $T'_{\pm}$  split quadratically as  $\varepsilon_{T'_{\pm}} = \mathcal{J} + \mathcal{D}/2 \pm \sqrt{\mathcal{D}^2/4 + |\Delta^{\perp}|^2}$  at small Zeeman fields. This signature of the exchange anisotropy is consistent with recent experimental observations in Ref. [45], supporting our theory of ZFS in Ge hut wires.

### 3.3 Numerics

We confirm our analytical results by comparing them with a numerical simulation of long QDs in square Ge and Si NWs with side length  $L$  based on the 6-band Kane model [65]. By imposing hard-wall boundary conditions at the edge of the NW cross-section, we obtain an effective 1D model including several transversal subbands. With a third order Schrieffer-Wolff transformation, we then fold the higher energy subbands down to the lowest four subbands, also accounting for terms that are cubic in momentum. We emphasize that in contrast to our analytical treatment, where we only account for a single pair of subbands, see Eq. (3.1), our numerical treatment also includes a pair of higher-energy subbands [66]. Furthermore, we include Coulomb interaction matrix elements that couple different subbands, as well as short-range interband

corrections to the Coulomb interaction [34], that we identify as an alternative source of ZFS. In our simulation, we also consider a compressive strain along the wire, with  $\epsilon_{zz} = -0.5\%$ , ensuring that the lowest band has a positive effective mass [7, 28]. More details on the numerical simulation are provided in Sec. 3.B of [66], where we also confirm the validity of our four subband model by comparing it to a full three-dimensional simulation.

In Fig. 3.2(a), we compare the numerical simulation of a Ge NW with  $L = 10$  nm with the analytical formulas of the exchange splitting  $\mathcal{J}$  and the ZFS in Eq. (3.4) as a function of QD length  $L_z$ . In this calculation, the  $\{x, y, z\}$  axes coincide with the  $\langle 100 \rangle$  crystallographic directions. Strikingly, the numerical exchange splitting  $\mathcal{J}$  is in excellent agreement with the analytical formula, and also  $\mathcal{D}$  is reasonably well captured by the simple Eq. (3.4) in a wide range of QD sizes. We emphasize that due to the weak dependence of the coefficient  $\eta$  on the side length  $L$  in long QDs ( $L, a_B < l_z$ ) Eq. (3.4) can accurately estimate the ZFS in general architectures.

The numerical solution in Fig. 3.2(a) also reveals an additional ZFS of the remaining two triplet states, that emerges because of the short-range corrections to the Coulomb interaction [34]. These corrections stem from the atomistic interactions of the  $p$ -type Bloch functions and induce mixing between the different bulk hole bands. The contribution of the short-range corrections to the effective Hamiltonian of Eq. (3.3) can be written as

$$H_{\text{eff, s-r}} = \frac{1}{2} \mathcal{E} \sigma_1^z \sigma_2^z, \quad (3.6)$$

where  $\mathcal{E}$  is the exchange anisotropy along the NW ( $z$ -direction). This ZFS induces an energy gap  $\mathcal{E}$  between the triplets  $|T_0\rangle$ ,  $|T_a\rangle = (|T_+\rangle + |T_-\rangle)/\sqrt{2}$ , and the remaining states [the singlet  $|S\rangle$  and the third triplet  $|T_b\rangle = (|T_+\rangle - |T_-\rangle)/\sqrt{2}$ ], thereby lifting the remaining triplet degeneracy at zero magnetic field.

The exchange anisotropy  $\mathcal{E}$  induced by the short-range Coulomb interaction is also present without external electric fields, where the SOI vanishes [see Fig. 3.2(b)]. In this special case because of the fourfold symmetry of the system, the anisotropy axis is aligned to the wire [66, 71, 72]. If an electric field is applied perpendicular to the wire, the symmetry is reduced and the remaining degeneracy is also lifted. (For a detailed symmetry analysis of different wire geometries see Sec. 3.C of [66].) At small  $E_x$ , the ZFS  $\mathcal{D}$  increases quadratically with the electric field, be-

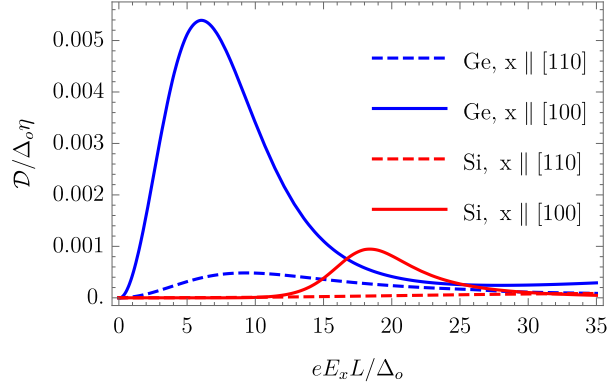


Figure 3.3: Dependence of the ZFS  $\mathcal{D}$  in Eq. (3.4) on the electric field  $E_x$ . With blue (red) lines, we show Ge (Si) for two different growth directions and split-off gap  $\Delta_{SO} \sim 150\Delta_o$  ( $\Delta_{SO} \sim 4\Delta_o$ ). Here, we consider  $l_z = L = 2a_B$ ,  $z \parallel [001]$ , and we use the strain  $\epsilon_{zz} = -0.5\%$ . The orbital energy is  $\Delta_o = \hbar^2/m^*l_z^2$ .

cause  $v_3 \sim E_x$ , and eventually overcomes  $\mathcal{E}$  [see the inset in Fig. 3.2(b)], aligning the main anisotropy axis to the SOI. For higher electric fields,  $v_3$  (and thus  $\mathcal{D}$ ) reaches a maximum value and starts to decrease, in analogy to the linear SOI  $v$  in various NW geometries [28,33].

The electric field dependence of the ZFS in Eq. (3.4) is dominated by  $v_3^2$  and therefore  $\mathcal{D}$  is highly tunable by the external gate potentials and by the QD design. In particular, in Fig. 3.3 we show  $\mathcal{D}$  as a function of electric field in Ge and Si NWs for different growth directions. For both growth directions, the ZFS –relative to the orbital splitting– is significantly smaller in Si than in Ge. This reduction is a result of the hybridization of HHs and LHs with the spin-orbit split-off band that is much closer in Si ( $\Delta_{SO} = 44$  meV) than in Ge ( $\Delta_{SO} = 296$  meV) [65], effectively decreasing the HH-LH mixing and the SOI [33].

The ZFS also varies substantially between different growth directions for both materials as shown in Fig. 3.3. The strong dependence of the SOI on the growth direction is well-known in Si nanowires [28,33], and it is also significant in Ge. Strikingly, the linear SOI  $v$  changes only slightly in Ge between the two growth directions [28,37], but the cubic SOI  $v_3$  is strongly altered between the two cases, yielding an order of magnitude larger ZFS when  $x \parallel [110]$ . This enhancement can be explained by considering that the cubic SOI is a higher order correction that involves more subbands, making  $v_3$  more sensitive to the growth direction and to the



design of the QD. This finding stresses once again that the ZFS in hole QDs is induced by the cubic SOI  $v_3$  and that there is no direct relation between the ZFS and the linear SOI  $v$ .

### 3.4 Conclusions

We presented a simple analytical model explaining the large anomalous triplet splitting at zero magnetic field, emerging in QDs occupied by two holes and shedding some light on recent experimental findings [45]. We related the ZFS to a cubic SOI that is externally tunable by electric fields and can be engineered by the design of the QD. In striking contrast to linear SOI effects, the ZFS is found to depend significantly on the growth direction not only in Si but also in Ge QDs, where such anisotropic effects are typically small [7, 28]. The SOI induced ZFS is also found to be orders of magnitude larger than short-range corrections to the Coulomb interaction, an alternative mechanisms for the ZFS of triplet states. While our analytical model focuses on doubly occupied long QDs, our findings are also valid in two tunnel-coupled QDs, the main building blocks of current spin-based quantum processors, and thus our work has deep implications for the design of future scalable quantum computing architectures with hole spin qubits.

We thank A. Pályi, D. Miserev, and G. Katsaros for the fruitful discussions. This work was supported as a part of NCCR SPIN funded by the Swiss National Science Foundation (grant number 51NF40-180604).

#### 3.A Zero-field splitting induced by cubic spin-orbit interaction

Here, we discuss in more detail the effective model of the zero-field splitting introduced in the main text. When the QD is elongated in the  $z$  direction, the low-energy behaviour of the system can be described by an effective model where only the lowest subbands of a quasi-1D system are taken into account. Here we present a two-band minimal model that is sufficient to explain the mechanism. This model gives a rather accurate estimate of the zero-field splitting in a wide range of cases. We consider the Hamiltonian up to third order in momentum including a harmonic

confinement

$$H_1 = \frac{p_z^2}{2m} + vp_z\sigma^y + v_3p_z^3\sigma^y + \frac{\hbar^2\gamma_1}{2m_eL_z^4}z^2, \quad (3.7)$$

where  $m$  is the effective mass,  $v$  is the spin-orbit velocity,  $v_3$  is the coefficient of the SOI cubic in momentum  $p_z$ , and  $L_z$  the harmonic confinement length of the QD. Note that the linear and the cubic SOI terms need to be aligned to the same SOI axis (here  $\sigma^y$ ), otherwise one could construct second order terms at  $B = 0$  such as  $\langle p^3 \rangle_{mn} \langle p \rangle_{nm} \sigma^x \sigma^y \sim p^4 \sigma^z$  that would break time-reversal symmetry.

We apply a unitary transformation  $U(p_0) = \exp(-ip_0z\sigma^y/\hbar)$  on the Hamiltonian in Eq. (3.7) that shifts the momentum as  $p_z \rightarrow p_z - p_0\sigma^y$ . By choosing the momentum shift  $p_0 = (1 - \sqrt{1 - 12m^2v_3v})/6mv_3$  such that the terms linear in  $p_z$  vanish, we obtain the Hamiltonian

$$\begin{aligned} \tilde{H}_1 = U^\dagger(p_0)H_1U(p_0) &= \frac{p_z^2}{2m^*} + v_3p_z^3\sigma^y + \frac{\hbar^2\gamma_1}{2m_eL_z^4}z^2 \\ \text{with } \frac{1}{m^*} &= \frac{1}{m}\sqrt{1 - 12m^2v_3v}, \end{aligned} \quad (3.8)$$

where  $12m^2v_3v \ll 1$  even for strong electric fields and we introduce the renormalized harmonic confinement length as  $l_z = (m_e/m^*\gamma_1)^{1/4}L_z$ . In the followings we omit the tilde from the transformed Hamiltonian  $\tilde{H}_1$  (as in the main text).

We now consider two-particle systems and we include Coulomb interaction in the 1D Hamiltonian of Eq. (3.8). Then the two-particle Hamiltonian reads

$$H_2 = H_1^{(1)} + H_1^{(2)} + \frac{\hbar^2}{2m^*l_z^4}(z_1^2 + z_2^2) + V_c(z_1 - z_2). \quad (3.9)$$

Here,  $V_c(z_1 - z_2)$  is the effective 1D Coulomb interaction obtained by projecting the Coulomb interaction onto the lowest subband with the corresponding lowest eigenstates of the full 3D Hamiltonian at  $p_z = 0$ . Due to this projection, the singularity of the Coulomb interaction is cut off in  $V_c(z_1 - z_2)$  at a distance  $|z_1 - z_2| \sim L \ll l_z$  determined by the transversal confinement (see Sec. 3.A for a fitting formula at square cross section). Moving to the center-of-mass (COM) frame one obtains,

$$\begin{aligned} H_2 &= \frac{1}{4m^*}P^2 + \frac{\hbar^2}{m^*l_z^4}Z^2 + \frac{p^2}{m^*} + \frac{\hbar^2}{4m^*l_z^4}z^2 + V_c(z) \\ &+ v_3 \left( \frac{1}{8}P^3 + \frac{3}{2}Pp^2 \right) (\sigma_1^y + \sigma_2^y) + v_3 \left( \frac{3}{4}P^2p + p^3 \right) (\sigma_1^y - \sigma_2^y), \end{aligned} \quad (3.10)$$

where the position and the conjugate momentum for the COM and the relative coordinates read

$$Z = (z_1 + z_2)/2, \quad P = p_{z_1} + p_{z_2}, \quad (3.11a)$$

$$z = z_1 - z_2, \quad p = (p_{z_1} - p_{z_2})/2, \quad (3.11b)$$

respectively. Since the cubic SOI term  $\propto v_3$  is obtained by a third order Schrieffer-Wolff (SW) transformation, it is suppressed by the subband gap compared to other terms of the Hamiltonian. If the subband gap is large compared to  $v_3 \hbar^3 / l_z^3$ , the cubic SOI term can be treated as a small perturbation that couples both the COM and relative coordinates with the spin degree of freedom. We divide Eq. (3.10) into three terms

$$H_2^{\text{COM}} = \frac{1}{4m^*} P^2 + \frac{\hbar^2}{m^* l_z^4} Z^2, \quad (3.12a)$$

$$H_2^{\text{rel}} = \frac{p^2}{m^*} + \frac{\hbar^2}{4m^* l_z^4} z^2 + V_c(z), \quad (3.12b)$$

$$\begin{aligned} V &= v_3 \left( \frac{1}{8} P^3 + \frac{3}{2} P p^2 \right) (\sigma_1^y + \sigma_2^y) + v_3 \left( \frac{3}{4} P^2 p + p^3 \right) (\sigma_1^y - \sigma_2^y) \\ &\equiv \mathcal{P}_3^+ (\sigma_1^y + \sigma_2^y) + \mathcal{P}_3^- (\sigma_1^y - \sigma_2^y). \end{aligned} \quad (3.12c)$$

The COM Hamiltonian of Eq. (3.12a) can be rewritten using the harmonic oscillator ladder operators defined as  $P = i(a^\dagger - a)\hbar/l_z$  and  $Z = (a^\dagger + a)l_z/2$  such that  $H_2^{\text{COM}} = \Delta_o a^\dagger a$ , where  $\Delta_o = \hbar^2/m^* l_z^2$  is the energy splitting of the COM mode. In contrast to  $H^{\text{COM}}$  the Hamiltonian  $H^{\text{rel}}$  cannot be diagonalized exactly. Nevertheless exploiting the  $z \leftrightarrow -z$  symmetry of the Hamiltonian, we can denote the lowest even (odd) eigenstate with  $S$  ( $T$ ) referring to their singlet-like (triplet-like) behaviour under particle exchange. Even though the 1D two-particle problem of a harmonic potential in the long QD limit ( $l_z \gg a_B$ ) can be treated analytically in the Hund-Mulliken approximation [60, 62], here we resort to the numerical solution of this problem because we are interested in the  $l_z \gtrsim a_B$  regime where this approximation is not accurate.

By using a second order Schrieffer-Wolff transformation, we project the Hamiltonian to the ground state of the COM Hamiltonian and the two energetically lowest eigenstates of the relative coordinate Hamiltonian (i.e., one singlet-like and one triplet-like state). Thereby, an effective low-energy Hamiltonian is obtained, from which the anisotropy axis can

be deduced and the magnetic field dependence can be straightforwardly discussed. The effective low-energy Hamiltonian reads

$$H_{\text{eff}} = -\mathcal{J}_0 |\chi_S\rangle \langle \chi_S| + W_{\text{eff}}, \quad (3.13)$$

where  $\mathcal{J}_0$  is the energy splitting between the lowest-energy eigenstates of (3.12b) and  $|\chi_S\rangle = (|\uparrow\rangle_1 |\downarrow\rangle_2 - |\downarrow\rangle_1 |\uparrow\rangle_2)/\sqrt{2}$  is the spin part of the singlet wavefunction, and where we choose the spin quantization axis along  $y$ -direction, i.e.  $\sigma_i^y |\uparrow\rangle (\downarrow)\rangle_i = \pm |\uparrow\rangle (\downarrow)\rangle_i$ . In the following we also need the three triplet-like states, denoted by  $|\chi_{T_0}\rangle = (|\uparrow\rangle_1 |\downarrow\rangle_2 + |\downarrow\rangle_1 |\uparrow\rangle_2)/\sqrt{2}$ ,  $|\chi_{T_+}\rangle = |\uparrow\rangle_1 |\uparrow\rangle_2$ , and  $|\chi_{T_-}\rangle = |\downarrow\rangle_1 |\downarrow\rangle_2$ . The effective coupling

$$\begin{aligned} W_{\text{eff}} &= -\frac{i}{2\hbar} \lim_{\eta \rightarrow 0^+} \int_0^\infty dt e^{-\eta t} \langle [V(t), V] \rangle \\ &= -\frac{i}{\hbar} \lim_{\eta \rightarrow 0^+} \int_0^\infty dt e^{-\eta t} \left\{ \langle [\mathcal{P}_3^+(t), \mathcal{P}_3^+] \rangle (1 + \sigma_1^y \sigma_2^y) \right. \\ &\quad \left. + \langle [\mathcal{P}_3^-(t), \mathcal{P}_3^-] \rangle (1 - \sigma_1^y \sigma_2^y) \right\}, \end{aligned} \quad (3.14)$$

stems from the cubic SOI terms of Eq. (3.12c), where  $V(t) = e^{iH_0 t/\hbar} V e^{-iH_0 t/\hbar}$  is the perturbation in the interaction picture, with the unperturbed Hamiltonian  $H_0 = H_2^{\text{COM}} + H_2^{\text{rel}}$ . Also, the expectation values in Eq. (3.14) project the effective Hamiltonian onto the low-energy singlet-triplet subspace, and in the second equation we exploited the fact that  $(\sigma_1^y + \sigma_2^y)(\sigma_1^y - \sigma_2^y) = 0$ .

To include Pauli's principle, we restrict the Hilbert space to the anti-symmetric 2-particle solutions by projecting Eq. (3.14) onto the lowest-energy singlet and triplet basis. The respective spin matrices projected onto the triplet sector can be written as

$$(1 + \sigma_1^y \sigma_2^y)_T = 2(|\chi_{T_+}\rangle \langle \chi_{T_+}| + |\chi_{T_-}\rangle \langle \chi_{T_-}|) = 1 + \sigma_1^y \sigma_2^y, \quad (3.15a)$$

$$(1 - \sigma_1^y \sigma_2^y)_T = 2|\chi_{T_0}\rangle \langle \chi_{T_0}| = \frac{1}{2} - \sigma_1^y \sigma_2^y + \frac{1}{2} \boldsymbol{\sigma}_1 \cdot \boldsymbol{\sigma}_2, \quad (3.15b)$$

while the corresponding projection of the singlets reads

$$(1 + \sigma_1^y \sigma_2^y)_S = 0, \quad (3.15c)$$

$$(1 - \sigma_1^y \sigma_2^y)_S = 2|\chi_S\rangle \langle \chi_S| = \frac{1}{2} - \frac{1}{2} \boldsymbol{\sigma}_1 \cdot \boldsymbol{\sigma}_2. \quad (3.15d)$$

Exploiting that the spin parts of the effective low-energy Hamiltonian do not couple the singlet with the triplet sectors one may write the perturbation as

$$W_{\text{eff}} = W_T^+(1 + \sigma_1^y \sigma_2^y) + W_T^- \left( \frac{1}{2} - \sigma_1^y \sigma_2^y + \frac{1}{2} \boldsymbol{\sigma}_1 \cdot \boldsymbol{\sigma}_2 \right) + W_S^- \left( \frac{1}{2} - \frac{1}{2} \boldsymbol{\sigma}_1 \cdot \boldsymbol{\sigma}_2 \right), \quad (3.16)$$

where the prefactors, in analogy with Eq. (3.14) are given by

$$W_{S(T)}^\pm = -\frac{i}{\hbar} \lim_{\eta \rightarrow 0^+} \int_0^\infty dt e^{-\eta t} \langle [\mathcal{P}_3^\pm(t), \mathcal{P}_3^\pm] \rangle_{S(T)}. \quad (3.17)$$

Here,  $\langle \dots \rangle_{S(T)}$  is the expectation value taken with respect to the state  $|0, \psi_{S(T)}\rangle = |0\rangle |\psi_{S(T)}\rangle$ , where  $|0\rangle$  is the ground state of the COM Hamiltonian and  $|\psi_{S(T)}\rangle$  is the lowest-energy singlet-like (triplet-like) eigenstate of the relative coordinate Hamiltonian in Eq. (3.12b).

Substituting the effective coupling (3.16) into (3.13), the effective Hamiltonian can be written in the following form

$$H_{\text{eff}} = \frac{1}{4}(\mathcal{J} + \mathcal{D})\boldsymbol{\sigma}_1 \cdot \boldsymbol{\sigma}_2 - \frac{1}{2}\mathcal{D}\sigma_1^y \sigma_2^y, \quad (3.18)$$

where  $\mathcal{D} = 2(W_T^- - W_T^+)$  is the exchange anisotropy responsible for the zero-field splitting and  $\mathcal{J} = \mathcal{J}_0 + 2(W_T^+ - W_S^-)$  is the exchange splitting between the singlet and the  $T_\pm$  doublet. In order to determine the zero-field splitting  $\mathcal{D}$  we need to calculate the quantities  $W_{S(T)}^\pm$ . To this aim, we first write the time-evolution of the COM momentum as

$$P(t) = i\frac{\hbar}{l_z} (a^\dagger e^{i\Delta_\sigma t/\hbar} - a e^{-i\Delta_\sigma t/\hbar}), \quad (3.19)$$

while higher powers of the momentum can be expressed straightforwardly by using the creation and annihilation operators  $a^\dagger$  and  $a$ . For the matrix elements of the relative momentum we can only exploit the even/odd parity of the basis states to write the matrix elements of  $p$  and  $p^3$  between  $|\psi_{S(T)}\rangle$  and an arbitrary state  $|\psi_n\rangle$  as

$$\langle \psi_S | p^{1,3}(t) | \psi_n \rangle = \sum_i \delta_{n,T_i} \langle p^{1,3} \rangle_{S,T_i} e^{-i(\varepsilon_{T_i} - \varepsilon_S)t/\hbar}, \quad (3.20a)$$

$$\langle \psi_T | p^{1,3}(t) | \psi_n \rangle = \sum_i \delta_{n,S_i} \langle p^{1,3} \rangle_{T,S_i} e^{-i(\varepsilon_{S_i} - \varepsilon_T)t/\hbar}, \quad (3.20b)$$

where  $S_i$  ( $T_i$ ) denote the higher energy even (odd) states for  $i = 1, 2, 3 \dots$ . The matrix elements of  $p^2(t)$  can be written analogously and only couple even (odd) states to higher even (odd) states. In the next step the projected commutators in Eq. (3.17) are obtained using Eqs. (3.19)-(3.20b), resulting in

$$\begin{aligned} \langle [\mathcal{P}_3^+(t), \mathcal{P}_3^+] \rangle_T &= \frac{9}{64} v_3^2 \frac{\hbar^6}{l_z^6} e^{-i\Delta_o t/\hbar} + \frac{6}{64} v_3^2 \frac{\hbar^6}{l_z^6} e^{-3i\Delta_o t/\hbar} \\ &+ \frac{9}{8} v_3^2 \frac{\hbar^4}{l_z^4} \langle p^2 \rangle_{TT} e^{-i\Delta_o t/\hbar} \\ &+ \frac{9}{4} v_3^2 \frac{\hbar^2}{l_z^2} \sum_i |\langle p^2 \rangle_{TT_i}|^2 e^{-i(\Delta_o + \varepsilon_{T_i} - \varepsilon_T)t/\hbar} - h.c., \end{aligned} \quad (3.21a)$$

$$\begin{aligned} \langle [\mathcal{P}_3^-(t), \mathcal{P}_3^-] \rangle_T &= \frac{3}{2} v_3^2 \frac{\hbar^2}{l_z^2} \sum_i \text{Re}[\langle p^3 \rangle_{TS_i} \langle p \rangle_{S_i T}] e^{-i(\varepsilon_{S_i} - \varepsilon_T)t/\hbar} \\ &+ v_3^2 \sum_i |\langle p^3 \rangle_{TS_i}|^2 e^{-i(\varepsilon_{S_i} - \varepsilon_T)t/\hbar} \\ &+ \frac{9}{16} v_3^2 \frac{\hbar^4}{l_z^4} \sum_i |\langle p \rangle_{TS_i}|^2 e^{-i(\varepsilon_{S_i} - \varepsilon_T)t/\hbar} \\ &+ \frac{9}{8} v_3^2 \frac{\hbar^4}{l_z^4} \sum_i |\langle p \rangle_{TS_i}|^2 e^{-i(2\Delta_o + \varepsilon_{S_i} - \varepsilon_T)t/\hbar} - h.c., \end{aligned} \quad (3.21b)$$

$$\begin{aligned} \langle [\mathcal{P}_3^-(t), \mathcal{P}_3^-] \rangle_S &= \frac{3}{2} v_3^2 \frac{\hbar^2}{l_z^2} \sum_i \text{Re}[\langle p^3 \rangle_{ST_i} \langle p \rangle_{T_i S}] e^{-i(\varepsilon_{T_i} - \varepsilon_S)t/\hbar} \\ &+ v_3^2 \sum_i |\langle p^3 \rangle_{ST_i}|^2 e^{-i(\varepsilon_{T_i} - \varepsilon_S)t/\hbar} \\ &+ \frac{9}{16} v_3^2 \frac{\hbar^4}{l_z^4} \sum_i |\langle p \rangle_{ST_i}|^2 e^{-i(\varepsilon_{T_i} - \varepsilon_S)t/\hbar} \\ &+ \frac{9}{8} v_3^2 \frac{\hbar^4}{l_z^4} \sum_i |\langle p \rangle_{ST_i}|^2 e^{-i(2\Delta_o + \varepsilon_{T_i} - \varepsilon_S)t/\hbar} - h.c., \end{aligned} \quad (3.21c)$$

where the commutator in  $W_S^+$  is not listed since it does not contribute to the effective coupling in Eq. (3.16). The time integrals in Eq. (3.17) can be evaluated using  $\int_0^\infty e^{i\omega t - 0^+ t} = -i/(\omega - i0^+)$ .

Finally, the zero-field splitting  $\mathcal{D}$  is expressed in terms of momentum matrix elements as

$$\begin{aligned} \mathcal{D} = & \frac{11}{16} v_3^2 \frac{\hbar^6}{l_z^6} \frac{1}{\Delta_o} + \frac{9}{2} v_3^2 \frac{\hbar^4}{l_z^4} \frac{\langle p^2 \rangle_{TT}}{\Delta_o} + 9 v_3^2 \frac{\hbar^2}{l_z^2} \sum_i \frac{|\langle p^2 \rangle_{TT_i}|^2}{\Delta_o + \varepsilon_{T_i} - \varepsilon_T} \\ & - 6 v_3^2 \frac{\hbar^2}{l_z^2} \sum_i \frac{\text{Re}[\langle p^3 \rangle_{TS_i} \langle p \rangle_{S_i T}]}{\varepsilon_{S_i} - \varepsilon_T} - 4 v_3^2 \sum_i \frac{|\langle p^3 \rangle_{TS_i}|^2}{\varepsilon_{S_i} - \varepsilon_T} \\ & - \frac{9}{4} v_3^2 \frac{\hbar^4}{l_z^4} \sum_i \frac{|\langle p \rangle_{TS_i}|^2}{\varepsilon_{S_i} - \varepsilon_T} - \frac{9}{2} v_3^2 \frac{\hbar^4}{l_z^4} \sum_i \frac{|\langle p \rangle_{TS_i}|^2}{2\Delta_o + \varepsilon_{S_i} - \varepsilon_T} \equiv m^* v_3^2 \frac{\hbar^4}{l_z^4} \eta, \end{aligned} \quad (3.22)$$

where we defined the dimensionless prefactor  $\eta$  as in Eq. (3.4) of the main text. We show its functional dependence in Sec. 3.A. Moreover, the exchange splitting is given by

$$\begin{aligned} \mathcal{J} = & \mathcal{J}_0 - \frac{11}{16} v_3^2 \frac{\hbar^6}{l_z^6} \frac{1}{\Delta_o} - \frac{9}{2} v_3^2 \frac{\hbar^4}{l_z^4} \frac{\langle p^2 \rangle_{TT}}{\Delta_o} - 9 v_3^2 \frac{\hbar^2}{l_z^2} \sum_i \frac{|\langle p^2 \rangle_{TT_i}|^2}{\Delta_o + \varepsilon_{T_i} - \varepsilon_T} \\ & + 6 v_3^2 \frac{\hbar^2}{l_z^2} \sum_i \frac{\text{Re}[\langle p^3 \rangle_{ST_i} \langle p \rangle_{T_i S}]}{\varepsilon_{T_i} - \varepsilon_S} + 4 v_3^2 \sum_i \frac{|\langle p^3 \rangle_{ST_i}|^2}{\varepsilon_{T_i} - \varepsilon_S} \\ & + \frac{9}{4} v_3^2 \frac{\hbar^4}{l_z^4} \sum_i \frac{|\langle p \rangle_{ST_i}|^2}{\varepsilon_{T_i} - \varepsilon_S} + \frac{9}{2} v_3^2 \frac{\hbar^4}{l_z^4} \sum_i \frac{|\langle p \rangle_{ST_i}|^2}{2\Delta_o + \varepsilon_{T_i} - \varepsilon_S} \approx \mathcal{J}_0, \end{aligned} \quad (3.23)$$

where  $\mathcal{J}_0 = \varepsilon_T - \varepsilon_S$  is the triplet-singlet splitting of the unperturbed Hamiltonian. These equations correspond to the ones reported in the main text.

### Momentum matrix elements of the relative coordinate

We now provide more details on the magnitude of the exchange  $\mathcal{J}$  and of the zero-field splitting  $\mathcal{D}$ . The analytical result of the ZFS in Eq. (3.22) involves a number of matrix elements of different powers of momentum between the eigenstates of the Hamiltonian  $H_2^{\text{rel}}$  of the relative coordinate in Eq. (3.12b). Since the Hamiltonian contains the effective 1D potential  $V_c(z_1 - z_2)$ , it is difficult to estimate this matrix elements in general.

Here we restrict our attention to nanowires with square cross section and side length of  $L$  and calculate the effective 1D Coulomb potential numerically as discussed in Sec. 3.B. We find that the relevant momentum matrix elements are very well reproduced by using the following

effective potential

$$V_c(z) \approx \frac{e^2}{4\pi\epsilon_r} \frac{1}{\sqrt{z^2 + (L/4)^2}}, \quad (3.24)$$

where  $\epsilon_r$  is the dielectric constant of the material. The dimensionless Hamiltonian with the approximating formula used for the effective 1D Coulomb interaction reads as

$$\frac{H_2^{\text{rel}}}{\Delta_o} = -\partial_x^2 + \frac{1}{4}x^2 + \frac{l_z}{a_B} \frac{1}{\sqrt{x^2 + (L/4l_z)^2}}, \quad (3.25)$$

where  $x = z/l_z$ . The Hamiltonian depends on two dimensionless parameters  $l_z/a_B$  and  $L/l_z$  (or equivalently  $l_z/a_B$  and  $L/a_B$ ). Therefore all the matrix elements in Eq. (3.22) can be expressed as a function of these quantities leading to  $\mathcal{D} = \eta m^* v_3^2 \hbar^4 / l_z^4$ . The dimensionless coefficient  $\eta$  depends on the relative length scales through the eigenstates of  $H_2^{\text{rel}}$  and can be written as

$$\eta = \frac{11}{16} - \frac{9}{2} \langle \partial_x^2 \rangle_{o_1 o_1} + \sum_i \left\{ 9 \frac{|\langle \partial_x^2 \rangle_{o_1 o_i}|^2}{1 + \tilde{\epsilon}_{o_i} - \tilde{\epsilon}_{o_1}} - 6 \frac{\text{Re}[\langle \partial_x^3 \rangle_{o_1 e_i} \langle \partial_x \rangle_{e_i o_1}]}{\tilde{\epsilon}_{e_i} - \tilde{\epsilon}_{o_1}} - 4 \frac{|\langle \partial_x^3 \rangle_{o_1 e_i}|^2}{\tilde{\epsilon}_{e_i} - \tilde{\epsilon}_{o_1}} - \frac{9}{4} \frac{|\langle \partial_x \rangle_{o_1 e_i}|^2}{\tilde{\epsilon}_{e_i} - \tilde{\epsilon}_{o_1}} - \frac{9}{2} \frac{|\langle \partial_x \rangle_{o_1 e_i}|^2}{2 + \tilde{\epsilon}_{e_i} - \tilde{\epsilon}_{o_1}} \right\}, \quad (3.26)$$

where  $H_2^{\text{rel}}/\Delta_o |e_i\rangle = \tilde{\epsilon}_{e_i} |e_i\rangle$  for the even,  $H_2^{\text{rel}}/\Delta_o |o_i\rangle = \tilde{\epsilon}_{o_i} |o_i\rangle$  for the odd eigenstates with respect to  $x$ , and  $-i \langle \partial_x \rangle_{nm} = -i \langle \psi_n | \partial_x | \psi_m \rangle$  is the matrix element of the dimensionless momentum. The coefficient  $\eta$  is shown as a function of the two relative length scales  $l_z/a_B$  and  $L/a_B$  in Fig. 3.4(a). Importantly, the dependence on the 1D cutoff  $L/4$  is rather weak for  $l_z \gtrsim a_B$  and therefore we expect the analytical formula provided in the main text, see Eq. (3.4), to be valid for a wide range of cross sections.

The (unperturbed) exchange splitting  $\mathcal{J}_0 = \Delta_o(\tilde{\epsilon}_{o_1} - \tilde{\epsilon}_{e_1})$  can also be expressed in terms of the two relative length scales  $l_z/a_B$  and  $L/a_B$ , as  $\mathcal{J}_0 = \zeta \hbar^2 a_B^2 / m^* l_z^4$ , where  $\zeta$  is a dimensionless coefficient. Combining  $\mathcal{J}_0$  with  $\mathcal{D}$ , we find that the anisotropy can be expressed as

$$\frac{\mathcal{D}}{\mathcal{J}} = \frac{m^* v_3^2 \hbar^2}{a_B^2} \frac{\eta}{\zeta} + \mathcal{O}(v_3^4). \quad (3.27)$$

This equation shows that the anisotropy depends strongly on both  $v_3$  and on the effective mass, i.e.,  $\mathcal{D}/\mathcal{J} \sim (m^*)^4$ . The mass dependence can be understood by considering that  $a_B \propto 1/m^*$  and that  $\eta/\zeta$  depends weakly on  $a_B$ , and therefore on the mass as well [see Fig. 3.4(b)].



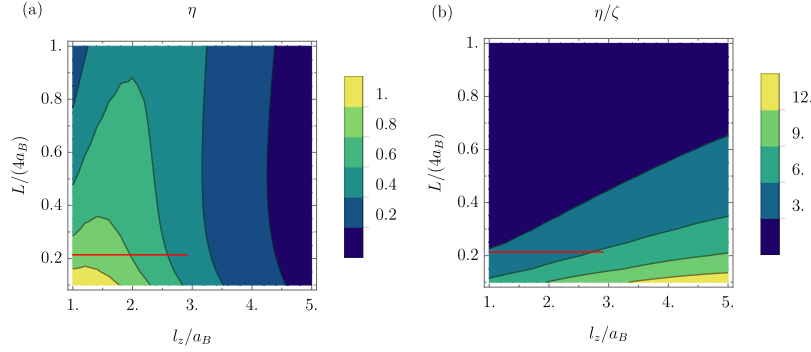


Figure 3.4: (a) Coefficient  $\eta$  of the zero-field splitting  $\mathcal{D}$  as a function of QD length  $l_z$  and NW width  $L$ . (b) Ratio  $\eta/\zeta$  of the anisotropy  $\mathcal{D}/\mathcal{J}$  as a function of QD length and NW width. The thin red line corresponds to the region plotted in Fig. 3.2(a) of the main text. For reference  $a_B \approx 11.7$  nm in Ge and  $a_B \approx 2.7$  nm in Si.

### 3.B Details of the numerical calculation

Here, we discuss in detail the numerical calculations introduced in the main text. We start the numerical analysis by considering a single QD with two holes, and assume harmonic confinement along the wire ( $z$  direction) as

$$H = H_{K,1}(\mathbf{p}_1) + H_{K,2}(\mathbf{p}_2) + \frac{\hbar^2 \gamma_1}{2m_e L_z^4} (z_1^2 + z_2^2) + C(\mathbf{r}_1 - \mathbf{r}_2), \quad (3.28)$$

where  $\mathbf{p}_i$  and  $\mathbf{r}_i$  are the momentum and spatial coordinate of the  $i$ th particle,  $C(\mathbf{r}_1 - \mathbf{r}_2)$  is the Coulomb interaction, and hard-wall boundary conditions in the  $x$ - $y$  directions are implied. The  $n \times n$  Kane model describing  $n = 4$  or  $n = 6$  valence bands in inversion symmetric semiconductors close to the  $\Gamma$  point is [65]

$$H_K^{n \times n}(\mathbf{p}) = \sum_{\alpha=1}^n E_{\alpha} |\alpha\rangle \langle \alpha| + \frac{\gamma_1}{2m_e} p^2 - \left( \frac{\gamma_2}{m_e} p_x^2 + \frac{2}{3} D_u \epsilon_{xx} \right) A_{xx} - \left( 2 \frac{\gamma_3}{m_e} \{p_x, p_y\} + \frac{4}{3} D'_u \epsilon_{xy} \right) A_{xy} + c.p., \quad (3.29)$$

where  $E_{\alpha}$  is the energy of the band  $\alpha$  at  $\mathbf{p} = 0$ , the coefficients  $\gamma_1$ ,  $\gamma_2$ , and  $\gamma_3$  are the Luttinger parameters determined by the band structure of the material,  $D_u$  and  $D'_u$  are the deformational potentials, and  $A_{ij}$  are

$n \times n$  matrices acting on the band degree of freedom. Moreover, the anticommutator between two operators  $O_1$  and  $O_2$  is defined as  $\{O_1, O_2\} = (O_1 O_2 + O_2 O_1)/2$ . For example in the 4-band Luttinger-Kohn model describing the top of the HH and LH bands,  $E_\alpha = 0$  and  $A_{ij} = \{J_i, J_j\}$  where  $J_i$  are the spin-3/2 matrices. For the 6-band model –obtained by considering the third pair of valence bands– the splitt-off holes are shifted by  $\Delta_{SO}$  from the HH and LH bands, and the  $A_{ij}$  matrices are given in Ref. [65]. Throughout this work, we assume compressive strain with strain tensor  $\epsilon_{ij} \propto \epsilon_{ii} \delta_{ij}$ .

### Long-QD calculation

Here we study the long QD case, where the Coulomb interaction is weak compared to the transversal confinement energy but stronger than the longitudinal confinement energy, i.e.,  $L/\pi \lesssim a_B \lesssim L_z$ . We start by deriving an effective 1D model (in  $z$  direction) accounting for a few NW subbands. To this goal, we add the electric field term  $H_E = -e\mathbf{E} \cdot \mathbf{r}$  to the Hamiltonian of Eq. (3.29), impose the hard-wall boundary conditions in the  $x - y$  directions, and expand the full Hamiltonian in powers of momentum  $p_z$ . The operator multiplying  $p_z^j$  reads as  $H_K^{(j)} = \frac{1}{j!} \partial_{p_z}^j H_K(\mathbf{p})|_{p_z=0}$  for  $j \in \{0, 1, 2\}$  [35]. Then, we find the eigensystem of the Hamiltonian  $H_K^{(0)}$  as

$$H_K^{(0)} \phi_n(x, y, s) = \varepsilon_n \phi_n(x, y, s), \quad (3.30)$$

where  $s$  is the band index of the Kane model. The eigenstates  $\phi_n(x, y, s)$  include the effects of electric field and strain and are used to project the full Hamiltonian onto the 1D subspace as

$$[H_K(p_z)]_{nm} = \varepsilon_n \delta_{nm} + [H_K^{(1)}]_{nm} p_z + [H_K^{(2)}]_{nm} p_z^2, \quad (3.31)$$

where the indices  $m$  and  $n$  label the NW subbands. We include a large number of NW subbands ( $N_{xy} = 200$  in the present work) and we derive the effective wire model

$$[\tilde{H}_K(p_z)]_{nm} = \varepsilon_n \delta_{nm} + [H_K^{(1)}]_{nm} p_z + [\tilde{H}_K^{(2)}]_{nm} p_z^2 + [\tilde{H}_K^{(3)}]_{nm} p_z^3 + \mathcal{O}(p_z^4), \quad (3.32)$$

by third order SW transformation. By using this effective Hamiltonian instead of Eq. (3.31), we can restrict ourselves to a few number of bands, greatly simplifying the two-body problem.

In our numerical analysis we applied an additional transformation that helps to improve the convergence of the ZFSs for large linear SOI.

For this, we divide the Hamiltonian in Eq (3.32) into  $2 \times 2$  blocks according to the Kramers partners. Due to time reversal symmetry, each diagonal block has to be of the form of Eq. (3.8), therefore for each subband one can apply a spin dependent momentum shift analogous to the one in Eq. (3.7).

Using the NW subbands, the two particle Hamiltonian of Eq. (3.28) reads

$$H_{m_1, m_2}^{n_1, n_2}(z_1, z_2) = [H_K(p_{z_1})]_{n_1 m_1} + [H_K(p_{z_2})]_{n_2 m_2} + \frac{\hbar^2 \gamma_1}{2m_e L_z^4} (z_1^2 + z_2^2) + C_{m_1, m_2}^{n_1, n_2}(z_1 - z_2), \quad (3.33)$$

where the Coulomb matrix elements are defined as

$C_{m_1, m_2}^{n_1, n_2} = \langle \phi_{n_1}, \phi_{n_2} | C | \phi_{m_1}, \phi_{m_2} \rangle$ . For example the Coulomb matrix element in the lowest subbands is  $C_{m_1, m_2}^{n_1, n_2}(z_1 - z_2) = \delta_{m_1, n_1} \delta_{m_2, n_2} V_c(z_1 - z_2)$ , (where  $m_{1,2}, n_{1,2} \in \{1, 2\}$ ) that has no singularity at  $z_1 = z_2$ , and is well approximated by using a simple cutoff determined by the transversal confinement length as shown in Eq. (3.24).

To diagonalize Eq. (3.33), we move to the COM frame, using the relation in Eq. (3.11), and we define the orthonormal basis states

$$\psi_{u, w, s_1, s_2}^{n_1, n_2}(\mathbf{r}_1, \mathbf{r}_2) = \phi_{n_1}(x_1, y_1, s_1) \phi_{n_2}(x_2, y_2, s_2) \times \phi_{n_1, n_2, u}^{\text{COM}} \left[ \frac{1}{2}(z_1 + z_2) \right] \phi_{n_1, n_2, w}^{\text{rel}}(z_1 - z_2). \quad (3.34)$$

The COM basis state  $\phi^{\text{COM}}$  satisfy the eigenvalue equation  $H^{\text{COM}}(n_1, n_2) \phi_{n_1, n_2, u}^{\text{COM}}(Z) = \varepsilon_u^{\text{COM}} \phi_{n_1, n_2, u}^{\text{COM}}(Z)$ , with the Hamiltonian

$$H^{\text{COM}}(n_1, n_2) = \frac{1}{4} \left( [\tilde{H}_K^{(2)}]_{n_1 n_1} + [\tilde{H}_K^{(2)}]_{n_2 n_2} \right) k_Z^2 + \frac{\hbar^2 \gamma_1}{m_e L_z^4} Z^2. \quad (3.35)$$

We note that the COM basis states are harmonic oscillator eigenstates with subband dependent mass  $1/m_{n_1, n_2} = \left( [\tilde{H}_K^{(2)}]_{n_1 n_1} + [\tilde{H}_K^{(2)}]_{n_2 n_2} \right) / 2\hbar^2$ . In contrast, the basis states of the relative coordinate depend also on the Coulomb potential. We use  $\phi^{\text{rel}}$  as basis states, i.e., the eigenfunctions satisfying the eigenvalue equation  $H^{\text{rel}}(n_1, n_2) \phi_{n_1, n_2, w}^{\text{rel}}(z) = \varepsilon_w^{\text{rel}} \phi_{n_1, n_2, w}^{\text{rel}}(z)$ , with Hamiltonian

$$H^{\text{rel}}(n_1, n_2) = \left( [\tilde{H}_K^{(2)}]_{n_1 n_1} + [\tilde{H}_K^{(2)}]_{n_2 n_2} \right) k_z^2 + \frac{\hbar^2 \gamma_1}{4m_e L_z^4} z^2 + C_{n_1, n_2}^{n_1, n_2}(z). \quad (3.36)$$

### Short-QD calculation

Using a few NW subbands as a basis for the numerical calculation is only justified if the longitudinal confinement length is large compared to the width of the NW, i.e.,  $l_z > L/\pi$ . However, in short QDs, where the ZFS is expected to be stronger, several subbands may be required. In this case, instead of effective wire bands, we use multiple basis states in the  $x$ - $y$  direction that satisfy the appropriate boundary conditions. In the present work, we start from the  $4 \times 4$  Kane model and use the particle in a box basis states

$$\phi_{n,m}(x, y) |3/2, s\rangle = \frac{2}{L} \cos(n\pi x/L) \cos(m\pi y/L) |3/2, s\rangle, \quad (3.37)$$

where the spin part is  $|3/2, s\rangle \equiv |j = 3/2, j_z = s\rangle$ . Along the  $z$  direction, the COM and relative coordinate basis states are chosen as eigenstates of the Hamiltonians

$$H_{s_1, s_2}^{\text{COM}} = \frac{\hbar^2}{2m_s} k_z^2 + \frac{\hbar^2 \gamma_1}{m_e L_z^4} Z^2, \quad (3.38)$$

$$H_{s_1, s_2}^{\text{rel}} = \frac{2\hbar^2}{m_s} k_z^2 + \frac{\hbar^2 \gamma_1}{4m_e L_z^4} z^2 + C_{n_1, m_1, n_2, m_2}^{m_1, m_1, n_2, m_2}(z), \quad (3.39)$$

respectively, where the mass is

$$\frac{1}{m_s} = \frac{1}{m_e} \begin{cases} (\gamma_1 - 2\gamma_2), & \text{if } |s_1| = |s_2| = 3/2 \\ (\gamma_1 + 2\gamma_2), & \text{if } |s_1| = |s_2| = 1/2 \\ \gamma_1, & \text{if } |s_1| \neq |s_2| \end{cases}. \quad (3.40)$$

Finally, the resulting the two-particle basis states used to diagonalize the complete 2-body Hamiltonian are

$$\begin{aligned} \psi_{u, w, s_2, s_2}^{n_1, m_1, n_2, m_2}(\mathbf{r}_1, \mathbf{r}_2) = & \phi_{n_1, m_1}(x_1, y_1) \phi_{n_2, m_2}(x_2, y_2) \\ & \times \phi_{s_1, s_2, u}^{\text{COM}} \left[ \frac{1}{2}(z_1 + z_2) \right] [\phi^{\text{rel}}]_{s_1, s_2, w}^{n_1, m_1, n_2, m_2}(z_1 - z_2). \end{aligned} \quad (3.41)$$

### Anisotropic short-range corrections to the Coulomb interaction

In Ref. [34] it is shown that the Coulomb interaction can acquire anisotropic corrections at short distances that couple the band degrees of freedom,

i.e., the HH, LH, and the spin-orbit split-off bands. This effect is a consequence of the finite orbital angular momentum of the  $p$ -type wavefunctions corresponding to the valence bands.

Three different type of corrections were identified in Ref. [34]: intraband, partially intraband, and interband corrections. The intraband and partially intraband terms contain both short-range ( $r < a/4$ , where  $a$  is the lattice constant) and long-range ( $a/4 < r \lesssim 2a$ ) contributions, while the interband corrections are exclusively short-ranged. Here we omit the long-ranged contributions as their contribution is negligible compared to the short-range terms [34]. The form of the short-range Coulomb corrections used in our work is

$$\begin{aligned} \delta C_{s-r} = & \frac{F_2}{25} g_d(\mathbf{r}_1 - \mathbf{r}_2) [P_{HH}(1)P_{HH}(2) + P_{LH}(1)P_{LH}(2) \\ & - P_{LH}(1)P_{HH}(2) - P_{HH}(1)P_{LH}(2)] \\ & + \sqrt{2} \frac{F_2}{25} g_d(\mathbf{r}_1 - \mathbf{r}_2) [J_{\text{part,d}}(1)J_{\text{part,od}}(2) + J_{\text{part,od}}(1)J_{\text{part,d}}(2)] \quad (3.42) \\ & + \frac{F_2}{25} g_d(\mathbf{r}_1 - \mathbf{r}_2) \left[ J_{\text{part,od}}(1)J_{\text{part,od}}(2) + 3J_{\text{int,Y}}J_{\text{int,Y}}^\dagger + 3J_{\text{int,Y}}^\dagger J_{\text{int,Y}} \right. \\ & \left. + 6J_{\text{int,X}}J_{\text{int,X}}^\dagger + 6J_{\text{int,X}}^\dagger J_{\text{int,X}} \right], \end{aligned}$$

where the first term is the intraband, the second term is the partially interband, the third term is the interband correction, and  $F_2 = F_2(4p, 4p) = 4.235$  eV is the relevant Slater-Condon parameter for Ge as provided in Ref. [59]. The functional form of  $g_d(\mathbf{r})$  has been derived for the continuum representation of the atomistic model in Ref. [34]. Here we provide only the simplest approximation for this short-ranged function, i.e.,

$$g_d(\mathbf{r}) \propto \left(\frac{a}{2}\right)^3 \delta(\mathbf{r}). \quad (3.43)$$

Since  $g_d(\mathbf{r})$  is cut at the boundary of a cube with an edge of  $a/2$  (where  $a = 0.56$  nm is the lattice constant for Ge), the spatial dependence is well approximated by a Dirac delta within the envelope function approximation (i.e.,  $L, l_z \gg a$ ).

In order to simplify the formulas of Ref. [34] to the case of the  $6 \times 6$  Kane model in Eq. (3.42), we introduced the following operators

$$P_{HH} = \left| \frac{3}{2}, \frac{3}{2} \right\rangle \left\langle \frac{3}{2}, \frac{3}{2} \right| + \left| \frac{3}{2}, -\frac{3}{2} \right\rangle \left\langle \frac{3}{2}, -\frac{3}{2} \right|, \quad (3.44a)$$

$$P_{LH} = \left| \frac{3}{2}, \frac{1}{2} \right\rangle \left\langle \frac{3}{2}, \frac{1}{2} \right| + \left| \frac{3}{2}, -\frac{1}{2} \right\rangle \left\langle \frac{3}{2}, -\frac{1}{2} \right|, \quad (3.44b)$$

$$J_{\text{part,d}} = P_{\text{HH}} - P_{\text{LH}}, \quad (3.44\text{c})$$

$$J_{\text{part,od}} = \left| \frac{3}{2}, \frac{1}{2} \right\rangle \left\langle \frac{1}{2}, \frac{1}{2} \right| + \left| \frac{3}{2}, -\frac{1}{2} \right\rangle \left\langle \frac{1}{2}, -\frac{1}{2} \right| + h.c., \quad (3.44\text{d})$$

$$\begin{aligned} J_{\text{int,X}} = & -\frac{1}{\sqrt{3}} \left| \frac{3}{2}, \frac{3}{2} \right\rangle \left\langle \frac{3}{2}, -\frac{1}{2} \right| - \sqrt{\frac{2}{3}} \left| \frac{3}{2}, \frac{3}{2} \right\rangle \left\langle \frac{1}{2}, -\frac{1}{2} \right| \\ & + \frac{1}{\sqrt{3}} \left| \frac{3}{2}, \frac{1}{2} \right\rangle \left\langle \frac{3}{2}, -\frac{3}{2} \right| + \sqrt{\frac{2}{3}} \left| \frac{1}{2}, \frac{1}{2} \right\rangle \left\langle \frac{3}{2}, -\frac{3}{2} \right|, \end{aligned} \quad (3.44\text{e})$$

$$\begin{aligned} J_{\text{int,Y}} = & -\sqrt{\frac{2}{3}} \left| \frac{3}{2}, \frac{3}{2} \right\rangle \left\langle \frac{3}{2}, \frac{1}{2} \right| + \frac{1}{\sqrt{3}} \left| \frac{3}{2}, \frac{3}{2} \right\rangle \left\langle \frac{1}{2}, \frac{1}{2} \right| \\ & - \sqrt{\frac{2}{3}} \left| \frac{3}{2}, -\frac{1}{2} \right\rangle \left\langle \frac{3}{2}, -\frac{3}{2} \right| + \frac{1}{\sqrt{3}} \left| \frac{1}{2}, -\frac{1}{2} \right\rangle \left\langle \frac{3}{2}, -\frac{3}{2} \right| \\ & + \left| \frac{3}{2}, \frac{1}{2} \right\rangle \left\langle \frac{1}{2}, -\frac{1}{2} \right| - \left| \frac{1}{2}, \frac{1}{2} \right\rangle \left\langle \frac{3}{2}, -\frac{1}{2} \right|, \end{aligned} \quad (3.44\text{f})$$

where the states  $|j, j_z\rangle$  are eigenstates of the total angular momentum operators  $\hbar^2 \hat{J}^2$  and  $\hbar \hat{J}_z$  with eigenvalues  $\hbar^2 j(j+1)$  and  $\hbar j_z$ , respectively.

### Comparison between short and long QDs

In this section we compare the two numerical approaches described in Secs. 3.B and 3.B to calculate the exchange- and zero-field splittings. The first approach well describes long quantum dots, with  $L_z > a_B, L$ . In this approach we account for 4 NW subbands, and 30 states for the COM and 30 states for the relative coordinates. The second approach works for short QDs, with  $L_z L < a_B$ , and uses basis states adapted to the confinement in each spatial directions (3-3 particle in a box eigenstates in  $x-y$  and 8 harmonic oscillator eigenstates in  $z$  directions) and therefore describe the short QD limit, i.e.,  $L_z \sim L < a_B$ . Since the numerical analysis in short QDs requires a large number of basis states to converge, in these calculations we omit the spin-orbit split-off bands (reducing the size of the two-particle Hilbert space to 82'944 in the short QD case). The effect of the split-off holes is fully accounted for in the main text.

The results of the two numerical solutions are compared in Fig. 3.5 for a Ge wire with square cross-section with side length  $L = 10$  nm, compressive strain  $\epsilon_{zz} = -2.5\%$ , and electric field  $E_x = 2$  V/ $\mu\text{m}$ . The  $\{x, y, z\}$  axes of the wire correspond to the  $\langle 100 \rangle$  crystallographic directions. The simulation of the exchange shows a good quantitative agreement in the

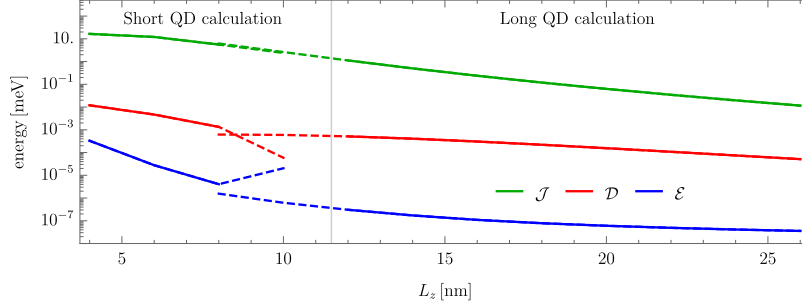


Figure 3.5: Exchange splitting  $\mathcal{J}$  and zero-field splittings  $\mathcal{D}$  and  $\mathcal{E}$  as a function of  $L_z$  in a Ge quantum dot. We consider a square wire with side length  $L = 10$  nm, compressive strain  $\epsilon_{zz} = -2.5\%$ , and electric field  $E_x = 2$  V/ $\mu$ m. The  $\{x, y, z\}$  axes of the wire correspond to the  $\langle 100 \rangle$  crystallographic directions. The first set of curves starting from  $L_z = 4$  nm to  $L_z = 10$  nm are calculated in the short QD assumption discussed in Sec. 3.B, while the second set from  $L_z = 8$  nm to  $L_z = 26$  nm is calculated using the long QD calculation discussed in Sec. 3.B and also used in the main text. The vertical line corresponds to  $L_z = a_B$  in Ge.

two cases. The ZFSs computed in these cases are also in qualitative agreement, however, at  $L \sim 10$  nm the numerical precision used for short QDs is not sufficient and the results of the short QD simulation are not reliable for larger QD lengths. We expect that the ZFS interpolates smoothly between the two limits.

From this comparison we conclude that the results obtained with the long quantum dot procedure remain reasonably accurate even at rather small values of  $L_z$ , confirming also the numerical and analytical theory discussed in the main text.

### 3.C Symmetry analysis of the triplet degeneracy

In this section we use group theoretical tools to study the degree of degeneracy of the two-particle eigenstates that is allowed by the irreducible representations of the two-particle point groups (i.e., double groups). Starting from the case with cubic symmetry, we consider the compatibility table of the cubic point group and we show how the degeneracy is resolved if certain symmetries are broken by e.g., the interface, electric

$O_h$	$\Gamma_1^+(1)$	$\Gamma_2^+(1)$	$\Gamma_3^+(2)$	$\Gamma_4^+(3)$	$\Gamma_5^+(3)$
$D_{4h}$	$\Gamma_1^+(1)$	$\Gamma_3^+(1)$	$\Gamma_1^+(1)+\Gamma_3^+(1)$	$\Gamma_2^+(1)+\Gamma_5^+(2)$	$\Gamma_4^+(1)+\Gamma_5^+(2)$
$D_{2h}$	$\Gamma_1^+(1)$	$\Gamma_1^+(1)$	$2\Gamma_1^+(1)$	$\Gamma_2^+(1)+\Gamma_3^+(1)+\Gamma_4^+(1)$	$\Gamma_2^+(1)+\Gamma_3^+(1)+\Gamma_4^+(1)$
$C_{2v}$	$\Gamma_1(1)$	$\Gamma_2(1)$	$\Gamma_1(1)+\Gamma_2(1)$	$\Gamma_2(1)+\Gamma_3(1)+\Gamma_4(1)$	$\Gamma_1(1)+\Gamma_3(1)+\Gamma_4(1)$

Table 3.1: Compatibility table of the cubic point group [72]. For NW QDs the symmetry groups  $D_{4h}$ ,  $D_{2h}$ , and  $C_{2v}$  correspond to square, rectangular cross section, and the hut wire, respectively. Assuming that the confinement along the wire is symmetric, the coordinate axes  $x, y, z$  correspond to  $\langle 100 \rangle$  crystallographic axes, and no additional fields are applied.

field, or strain.

In the following discussion, we restrict our attention to the HH and LH bands. These bands at  $\mathbf{k} = 0$  are described by the irreducible representation  $\Gamma_8^+(4)$ , where " + " indicates even parity with respect to inversion and the number in parentheses is the dimension of the representation i.e., the degree of degeneracy [71]. By assuming the most general form of the interaction –e.g., accounting for the short-range interband Coulomb interaction– the two-particle representation can be decomposed into irreducible representations as follows

$$\Gamma_8^+(4) \times \Gamma_8^+(4) = \Gamma_1^+(1) + \Gamma_2^+(1) + \Gamma_3^+(2) + 2\Gamma_4^+(3) + 2\Gamma_5^+(3), \quad (3.45)$$

where one obtains 1-, 2-, and 3-dimensional irreducible representations. This decomposition implies that the full 3-fold degeneracy of the triplet states is maintained if the QD confinement respects every symmetry of the cubic point group. In experiments this is usually not the case, therefore we consider the few nontrivial point groups that are of practical relevance:

- (i) a NW with square cross section and  $E_x = 0$  as in Figs. 3.2 and 3.3 of the main text, described by the  $D_{4h}$  tetragonal point group that contains one fourfold and two twofold rotation axes as well as inversion symmetry. The triplet degeneracy is indeed lifted as predicted by the first line of Tab. 3.1.
- (ii) a rectangular NW in the absence of electric field, or a square wire with compressive strain along the  $x$  or  $y$  directions, described by the  $D_{2h}$  orthorhombic point group that contains three twofold rotation axes as well as inversion symmetry. In this case each of the three



triplets are non-degenerate (see second line of Tab. 3.1). This case has been confirmed in our numerical calculation (not shown).

- (iii) a rectangular or square NW with electric field applied perpendicular to either of the sides of the cross section, or a NW with an equilateral triangle cross section. These cases are both described by the  $C_{2v}$  orthorhombic point group that contains two reflection planes and one twofold rotation axis. In this case each of the three triplets are non-degenerate (see third line of Tab. 3.1). This case has been confirmed as well by our numerical calculation (see Figs. 3.2 and 3.3 of the main text).

Finally, we note that including only the spin-independent Coulomb interaction is not enough to lift all the triplet degeneracies as predicted by symmetries. To obtain the lowest possible degeneracy, short-range interband corrections to the Coulomb interaction also need to be considered. However, in the main text, we show that these effects are significantly smaller than the cubic spin-orbit induced lifting of triplet degeneracy.

# Bibliography

- [1] D. Loss and D. P. DiVincenzo. Quantum computation with quantum dots. *Phys. Rev. A*, 57:120–126, Jan 1998.
- [2] M. A. Eriksson, M. Friesen, S. N. Coppersmith, R. Joynt, L. J. Klein, K. Slinker, C. Tahan, P. M. Mooney, J. O. Chu, and S. J. Koester. Spin-based quantum dot quantum computing in silicon. *Quantum Information Processing*, 3(1):133–146, 2004.
- [3] G. Burkard, T. D. Ladd, J. M. Nichol, A. Pan, and J. R. Petta. Semiconductor spin qubits. *arXiv:2112.08863*, 2021.
- [4] L. Bellentani, M. Bina, S. Bonen, A. Secchi, A. Bertoni, S. P. Voinigescu, A. Padovani, L. Larcher, and F. Troiani. Toward hole-spin qubits in Si *p*-mosfets within a planar cmos foundry technology. *Phys. Rev. Applied*, 16:054034, Nov 2021.
- [5] C. Kloeffer and D. Loss. Prospects for spin-based quantum computing in quantum dots. *Annu. Rev. Condens. Matter Phys.*, 4(1):51–81, 2013.
- [6] G. Scappucci, C. Kloeffer, F. A. Zwanenburg, D. Loss, M. Myronov, J.-J. Zhang, S. De Franceschi, G. Katsaros, and M. Veldhorst. The germanium quantum information route. *Nature Reviews Materials*, pages 1–18, 2020.
- [7] C. Kloeffer, M. Trif, and D. Loss. Strong spin-orbit interaction and helical hole states in ge/si nanowires. *Phys. Rev. B*, 84:195314, Nov 2011.
- [8] L. A. Terrazos, E. Marcellina, Y. Wang, S. N. Coppersmith, M. Friesen, A. R. Hamilton, X. Hu, B. Koiller, A. L. Saraiva, D. Culcer, and R. B. Capaz. Theory of hole-spin qubits in strained germanium quantum dots. *Phys. Rev. B*, 103:125201, Mar 2021.

- [9] F. N. M. Froning, M. J. Rančić, B. Hetényi, S. Bosco, M. K. Rehmann, A. Li, E. P. A. M. Bakkers, F. A. Zwanenburg, D. Loss, D. M. Zumbühl, and F. R. Braakman. Strong spin-orbit interaction and g-factor renormalization of hole spins in Ge/Si nanowire quantum dots. *Physical Review Research*, 3(1):013081, 2021.
- [10] H. Liu, T. Zhang, K. Wang, F. Gao, G. Xu, X. Zhang, S.-X. Li, G. Cao, T. Wang, J. Zhang, X. Hu, H.-O. Li, and G.-P. Guo. Gate-tunable spin-orbit coupling in a germanium hole double quantum dot. *Phys. Rev. Applied*, 17:044052, Apr 2022.
- [11] F. N. M. Froning, L. C. Camenzind, O. A. H. van der Molen, A. Li, E. P. A. M. Bakkers, D. M. Zumbühl, and F. R. Braakman. Ultrafast hole spin qubit with gate-tunable spin-orbit switch functionality. *Nature Nanotechnology*, pages 1–5, 2021.
- [12] L. C. Camenzind, S. Geyer, A. Fuhrer, R. J. Warburton, D. M. Zumbühl, and A. V. Kuhlmann. A hole spin qubit in a fin field-effect transistor above 4 kelvin. *Nature Electronics*, 5(3):178–183, 2022.
- [13] K. Wang, G. Xu, F. Gao, H. Liu, R.-L. Ma, X. Zhang, Z. Wang, G. Cao, T. Wang, J.-J. Zhang, D. Culcer, X. Hu, H.-W. Jiang, H.-O. Li, G.-C. Guo, and G.-P. Guo. Ultrafast coherent control of a hole spin qubit in a germanium quantum dot. *Nature Communications*, 13(1):206, 2022.
- [14] C. Kloeffel, M. Trif, P. Stano, and D. Loss. Circuit qed with hole-spin qubits in ge/si nanowire quantum dots. *Phys. Rev. B*, 88:241405, Dec 2013.
- [15] P. M. Mutter and G. Burkard. Natural heavy-hole flopping mode qubit in germanium. *Phys. Rev. Research*, 3:013194, Feb 2021.
- [16] V. P. Michal, J. C. Abadillo-Uriel, S. Zihlmann, R. Maurand, Y.-M. Niquet, and M. Filippone. Tunable hole spin-photon interaction based on g-matrix modulation. *arXiv:2204.00404*, 2022.
- [17] S. Bosco, P. Scarlino, J. Klinovaja, and D. Loss. Fully tunable longitudinal spin-photon interactions in si and ge quantum dots. *arXiv:2203.17163*, 2022.
- [18] S. Bosco and D. Loss. Hole spin qubits in thin curved quantum wells. *arXiv:2204.08212*, 2022.

- [19] N. W. Hendrickx, D. P. Franke, A. Sammak, M. Kouwenhoven, D. Sabbagh, L. Yeoh, R. Li, M. L. V. Tagliaferri, M. Virgilio, G. Capellini, G. Scappucci, and M. Veldhorst. Gate-controlled quantum dots and superconductivity in planar germanium. *Nature Communications*, 9(1):2835, 2018.
- [20] G. Scappucci, P. J. Taylor, J. R. Williams, T. Ginley, and S. Law. Crystalline materials for quantum computing: Semiconductor heterostructures and topological insulators exemplars. *MRS Bulletin*, 46(7):596–606, 2021.
- [21] L. Vukušić, J. Kukučka, H. Watzinger, Joshua M. Milem, F. Schäffler, and G. Katsaros. Single-shot readout of hole spins in ge. *Nano letters*, 18(11):7141–7145, 2018.
- [22] H. Watzinger, J. Kukučka, L. Vukušić, F. Gao, T. Wang, F. Schäffler, J.-J. Zhang, and G. Katsaros. A germanium hole spin qubit. *Nature communications*, 9(1):1–6, 2018.
- [23] M. Urdampilleta, D. J. Niegemann, E. Chanrion, B. Jadot, C. Spence, P.-A. Mortemousque, C. Bäuerle, L. Hutin, B. Bertrand, S. Barraud, R. Maurand, M. Sanquer, X. Jehl, S. De Franceschi, M. Vinet, and T. Meunier. Gate-based high fidelity spin readout in a cmos device. *Nature Nanotechnology*, 14(8):737–741, 2019.
- [24] N. W. Hendrickx, W. I. L. Lawrie, L. Petit, A. Sammak, G. Scappucci, and M. Veldhorst. A single-hole spin qubit. *Nature Communications*, 11(1):3478, 2020.
- [25] A. Greilich, S. G Carter, D. Kim, A. S. Bracker, and D. Gammon. Optical control of one and two hole spins in interacting quantum dots. *Nature Photonics*, 5(11):702, 2011.
- [26] N. W. Hendrickx, D. P. Franke, A. Sammak, G. Scappucci, and M. Veldhorst. Fast two-qubit logic with holes in germanium. *Nature*, 577(7791):487–491, 2020.
- [27] N. W. Hendrickx, W. I. L. Lawrie, M. Russ, F. van Riggelen, S. L. de Snoo, R. N. Schouten, A. Sammak, G. Scappucci, and M. Veldhorst. A four-qubit germanium quantum processor. *Nature*, 591(7851):580–585, 2021.

- [28] C. Kloeffel, M. J. Rančić, and D. Loss. Direct rashba spin-orbit interaction in si and ge nanowires with different growth directions. *Phys. Rev. B*, 97:235422, Jun 2018.
- [29] R. Winkler, D. Culcer, S. J. Papadakis, B. Habib, and M. Shayegan. Spin orientation of holes in quantum wells. *Semiconductor Science and Technology*, 23(11):114017, oct 2008.
- [30] R. Moriya, K. Sawano, Y. Hoshi, S. Masubuchi, Y. Shiraki, A. Wild, C. Neumann, G. Abstreiter, D. Bougeard, T. Koga, and T. Machida. Cubic rashba spin-orbit interaction of a two-dimensional hole gas in a strained-Ge/SiGe quantum well. *Phys. Rev. Lett.*, 113:086601, Aug 2014.
- [31] B. Hetényi, C. Kloeffel, and D. Loss. Exchange interaction of hole-spin qubits in double quantum dots in highly anisotropic semiconductors. *Phys. Rev. Research*, 2:033036, Jul 2020.
- [32] J. Li, B. Venitucci, and Y.-M. Niquet. Hole-phonon interactions in quantum dots: Effects of phonon confinement and encapsulation materials on spin-orbit qubits. *Phys. Rev. B*, 102:075415, Aug 2020.
- [33] S. Bosco, B. Hetényi, and D. Loss. Hole spin qubits in Si finfets with fully tunable spin-orbit coupling and sweet spots for charge noise. *PRX Quantum*, 2:010348, Mar 2021.
- [34] A. Secchi, L. Bellentani, A. Bertoni, and F. Troiani. Inter- and intra-band coulomb interactions between holes in silicon nanostructures. *Phys. Rev. B*, 104:205409, Nov 2021.
- [35] S. Bosco and D. Loss. Fully tunable hyperfine interactions of hole spin qubits in si and ge quantum dots. *Phys. Rev. Lett.*, 127:190501, Nov 2021.
- [36] D. V. Bulaev and D. Loss. Electric dipole spin resonance for heavy holes in quantum dots. *Phys. Rev. Lett.*, 98:097202, Feb 2007.
- [37] S. Bosco, M. Benito, C. Adelsberger, and D. Loss. Squeezed hole spin qubits in ge quantum dots with ultrafast gates at low power. *Phys. Rev. B*, 104:115425, Sep 2021.
- [38] Z. Wang, E. Marcellina, A. R. Hamilton, J. H. Cullen, S. Rogge, J. Salfi, and D. Culcer. Optimal operation points for ultrafast, highly

- coherent ge hole spin-orbit qubits. *npj Quantum Information*, 7(1):54, 2021.
- [39] N. Piot, B. Brun, V. Schmitt, S. Zihlmann, V. P. Michal, A. Apra, J. C. Abadillo-Uriel, X. Jehl, B. Bertrand, H. Niebojewski, L. Hutin, M. Vinet, M. Urdampilleta, T. Meunier, Y.-M. Niquet, R. Maurand, and S. De Franceschi. A single hole spin with enhanced coherence in natural silicon. *arXiv:2201.08637*, 2022.
- [40] F. Maier, C. Kloeffel, and D. Loss. Tunable  $g$  factor and phonon-mediated hole spin relaxation in Ge/Si nanowire quantum dots. *Phys. Rev. B*, 87:161305, Apr 2013.
- [41] A. Crippa, R. Maurand, L. Bourdet, D. Kotekar-Patil, A. Amisse, X. Jehl, M. Sanquer, R. Laviéville, H. Bohuslavskyi, L. Hutin, S. Barraud, M. Vinet, Y.-M. Niquet, and S. De Franceschi. Electrical spin driving by  $g$ -matrix modulation in spin-orbit qubits. *Phys. Rev. Lett.*, 120:137702, Mar 2018.
- [42] B. Venitucci, L. Bourdet, D. Pouzada, and Y.-M. Niquet. Electrical manipulation of semiconductor spin qubits within the  $g$ -matrix formalism. *Phys. Rev. B*, 98:155319, Oct 2018.
- [43] S. Studenikin, M. Korkusinski, M. Takahashi, J. Ducatel, A. Padawer-Blatt, A. Bogan, D. G. Austing, L. Gaudreau, P. Zawadzki, An Sachrajda, Y. Hirayama, L. Tracy, J. Reno, and T. Hargett. Electrically tunable effective  $g$ -factor of a single hole in a lateral gaas/algaas quantum dot. *Communications Physics*, 2(1):1–8, 2019.
- [44] J. H. Qvist and J. Danon. Anisotropic  $g$ -tensors in hole quantum dots: Role of transverse confinement direction. *Phys. Rev. B*, 105:075303, Feb 2022.
- [45] G. Katsaros, J. Kukučka, L. Vukušić, H. Watzinger, F. Gao, T. Wang, J.-J. Zhang, and K. Held. Zero field splitting of heavy-hole states in quantum dots. *Nano Letters*, 20(7):5201–5206, 2020.
- [46] J. Davidsson, V. Ivády, R. Armiento, N. T. Son, A. Gali, and I. A. Abrikosov. First principles predictions of magneto-optical data for semiconductor point defect identification: the case of divacancy defects in 4H-SiC. *New Journal of Physics*, 20(2):023035, 2018.

- [47] A. Lenef and S. C. Rand. Electronic structure of the n-v center in diamond: Theory. *Phys. Rev. B*, 53:13441–13455, May 1996.
- [48] J. R. Maze, A. Gali, E. Togan, Y. Chu, A. Trifonov, E. Kaxiras, and M. D. Lukin. Properties of nitrogen-vacancy centers in diamond: the group theoretic approach. *New Journal of Physics*, 13(2):025025, feb 2011.
- [49] P. Szakács, Á. Szabados, and P. R. Surján. Zero-field-splitting in triplet-state nanotubes. *Chemical Physics Letters*, 498(4-6):292–295, 2010.
- [50] D. Jirovec, A. Hofmann, A. Ballabio, P. M. Mutter, G. Tavani, M. Bortifoll, A. Crippa, J. Kukucka, O. Sagi, F. Martins, J. Saez-Mollejo, I. Prieto, M. Borovkov, J. Arbiol, D. Chrastina, G. Isella, and G. Katsaros. A singlet-triplet hole spin qubit in planar ge. *Nature Materials*, 20(8):1106–1112, 2021.
- [51] D. Jirovec, P. M. Mutter, A. Hofmann, A. Crippa, M. Rychetsky, D. L. Craig, J. Kukucka, F. Martins, A. Ballabio, N. Ares, D. Chrastina, G. Isella, G. Burkard, and G. Katsaros. Dynamics of hole singlet-triplet qubits with large  $g$ -factor differences. *Phys. Rev. Lett.*, 128:126803, Mar 2022.
- [52] P. M. Mutter and G. Burkard. All-electrical control of hole singlet-triplet spin qubits at low-leakage points. *Phys. Rev. B*, 104:195421, Nov 2021.
- [53] D. Fernandez-Fernandez, Y. Ban, and G. Platero. Quantum control of hole spin qubits in double quantum dots. *arXiv:2204.07453*, 2022.
- [54] K. Ono, D. G. Austing, Y. Tokura, and S. Tarucha. Current rectification by pauli exclusion in a weakly coupled double quantum dot system. *Science*, 297(5585):1313–1317, 2002.
- [55] G. Burkard, D. Loss, and D. P. DiVincenzo. Coupled quantum dots as quantum gates. *Phys. Rev. B*, 59:2070–2078, Jan 1999.
- [56] H.-B. Braun and D. Loss. Berry’s phase and quantum dynamics of ferromagnetic solitons. *Phys. Rev. B*, 53:3237–3255, Feb 1996.
- [57] L. S. Levitov and E. I. Rashba. Dynamical spin-electric coupling in a quantum dot. *Phys. Rev. B*, 67:115324, Mar 2003.

- [58] D. Stepanenko, M. Rudner, B. I. Halperin, and D. Loss. Singlet-triplet splitting in double quantum dots due to spin-orbit and hyperfine interactions. *Phys. Rev. B*, 85:075416, Feb 2012.
- [59] C. Satoko. Calculated tables of atomic energies and slater-condon parameters. *Bulletin of the Institute of Natural Sciences*, (25):p97–123, 1990.
- [60] M. Taut. Two electrons in an external oscillator potential: Particular analytic solutions of a coulomb correlation problem. *Phys. Rev. A*, 48:3561–3566, Nov 1993.
- [61] J. C. Abadillo-Uriel, B. Martinez, M. Filippone, and Y.-M. Niquet. Two-body wigner molecularization in asymmetric quantum dot spin qubits. *Phys. Rev. B*, 104:195305, Nov 2021.
- [62] F. Gao, J.-H. Wang, H. Watzinger, H. Hu, M. J. Rančić, J.-Y. Zhang, T. Wang, Y. Yao, G.-L. Wang, J. Kukučka, L. Vukušić, C. Kloeffer, D. Loss, F. Liu, G. Katsaros, and J.-J. Zhang. Site-Controlled Uniform Ge/Si Hut Wires with Electrically Tunable Spin–Orbit Coupling. *Advanced Materials*, 32(16):1906523, 2020.
- [63] H. E. Ercan, S. N. Coppersmith, and M. Friesen. Strong electron-electron interactions in si/sige quantum dots. *Phys. Rev. B*, 104:235302, Dec 2021.
- [64] A. Secchi, L. Bellentani, A. Bertoni, and F. Troiani. Interacting holes in si and ge double quantum dots: From a multiband approach to an effective-spin picture. *Phys. Rev. B*, 104:035302, Jul 2021.
- [65] R. Winkler. *Spin-orbit coupling effects in two-dimensional electron and hole systems*, volume 191. Springer, 2003.
- [66] See Supplemental Material for an explicit derivation of the ZFS and further details of the numerical calculation. the symmetry analysis of the triplet degeneracy is also provided, as well as the exact form of the interband Coulomb corrections. furthermore we compare the numerical calculation for long QDs with a different numerical approach relying on a short QD assumption.
- [67] R. Maurand, X. Jehl, D. Kotekar-Patil, A. Corna, H. Bohuslavskyi, R. Laviéville, L. Hutin, S. Barraud, M. Vinet, M. Sanquer, and S. De Franceschi. A cmos silicon spin qubit. *Nature Communications*, 7(1):13575, 2016.



- [68] C. Adelsberger, M. Benito, S. Bosco, J. Klinovaja, and D. Loss. Hole-spin qubits in ge nanowire quantum dots: Interplay of orbital magnetic field, strain, and growth direction. *Phys. Rev. B*, 105:075308, Feb 2022.
- [69] S. Bravyi, D. P. DiVincenzo, and D. Loss. Schrieffer–wolff transformation for quantum many-body systems. *Annals of Physics*, 326(10):2793–2826, 2011.
- [70] F. N. M. Froning, M. K. Rehmann, J. Ridderbos, M. Brauns, F. A. Zwanenburg, A. Li, E. P. A. M. Bakkers, D. M. Zumbühl, and F. R. Braakman. Single, double, and triple quantum dots in ge/si nanowires. *Applied Physics Letters*, 113(7):073102, 2018.
- [71] J. Sólyom. *Fundamentals of the Physics of Solids: Volume 1: Structure and Dynamics*, volume 1. Springer Science & Business Media, 2007.
- [72] G. F. Koster, J. O. Dimmock, and R. G. Wheeler. *Properties of the thirty-two point groups*, volume 24. MIT press, 1963.

## Strong spin-orbit interaction and $g$ -factor renormalization

*Adapted from:*

F. N. M. Froning, M. J. Rančić, B. Hetényi, S. Bosco, M. K. Rehmann, A. Li, E. P. A. M. Bakkers, F. A. Zwanenburg, D. Loss, D. M. Zumbühl, and F. R. Braakman  
*“Strong spin-orbit interaction and  $g$ -factor renormalization of hole spins in Ge/Si nanowire quantum dots”,*  
Phys. Rev. Research **3**, 013081 (2021)

The spin-orbit interaction lies at the heart of quantum computation with spin qubits, research on topologically non-trivial states, and various applications in spintronics. Hole spins in Ge/Si core/shell nanowires experience a spin-orbit interaction that has been predicted to be both strong and electrically tunable, making them a particularly promising platform for research in these fields. We experimentally determine the strength of spin-orbit interaction of hole spins confined to a double quantum dot in a Ge/Si nanowire by measuring spin-mixing transitions inside a regime of spin-blockaded transport. We find a remarkably short spin-orbit length of  $\sim 65$  nm, comparable to the quantum dot length and the interdot distance. We additionally observe a large orbital effect of the applied magnetic field on the hole states, resulting in a large magnetic field dependence of the spin-mixing transition energies. Strikingly, together with these orbital effects, the strong spin-orbit interaction causes a significant enhancement of the  $g$ -factor with magnetic field. The large spin-orbit interaction strength demonstrated is consistent with the predicted direct

Rashba spin-orbit interaction in this material system and is expected to enable ultrafast Rabi oscillations of spin qubits and efficient qubit-qubit interactions, as well as provide a platform suitable for studying Majorana zero modes.

## 4.1 Introduction

The spins of single electrons or holes can be coupled to orbital degrees of freedom through the spin-orbit interaction. In a solid-state environment, this interaction arises from the motion of electrons or holes in electric fields associated with the host lattice atoms, structural or bulk inversion fields, or externally applied electric fields, and its strength can range from a typically small perturbation in the conduction band to a significant effect in the valence band [1]. Spin-orbit interaction is particularly useful for fundamental applications in spintronics and quantum information processing with spin qubits [2–4], as it can be employed to realize fast manipulation of spin states purely through electrical means [5, 6]. For example, Rabi oscillations with frequencies of  $\sim 100$  MHz have been obtained for electron spins confined in group III-IV semiconductor nanowires, where the spin-orbit interaction was used to mediate a coupling of the spins to an electrical driving field [7, 8]. Furthermore, spin-orbit interaction provides a promising path towards implementing entangling operations between distant spin qubits, by mediating the coupling of spins to electromagnetic cavity modes [9, 10] or floating gate architectures [11]. An important advantage of using spin-orbit interaction for these purposes is that it requires no additional on-chip components such as micromagnets.

The emergence of Majorana zero modes in semiconductor nanowires relies on the presence of a strong spin-orbit interaction [12–15]. When combined with conventional bulk s-wave superconductivity, induced in the nanowire through proximitization, and with a Zeeman field, sufficiently strong spin-orbit interaction results in an effective 1D p-wave superconductor supporting Majorana zero modes. Such Majorana zero modes are of fundamental interest since they exhibit exotic non-Abelian statistics and hold great promise to realize quantum computation with topological protection from decoherence [16]. The strength of the spin-orbit interaction sets the range of Zeeman energies in which a topologically non-trivial phase exists together with a sufficiently large supercon-

ducting gap, making a strong spin-orbit interaction essential for experimental studies [17].

Hole spins in semiconductor nanostructures can experience a spin-orbit interaction many times stronger than for electron spins [1, 18, 19]. In particular, a strong and electrically tunable direct Rashba spin-orbit interaction arises for holes confined in one-dimensional Ge- or Si-based nanostructures [20, 21]. The direct Rashba spin-orbit interaction results from direct dipolar coupling of holes to an external electric field, in combination with mixing of heavy and light hole states due to confinement to one dimension. This interaction is estimated to be 10-100 times stronger than the conventional Rashba-type spin-orbit interaction for electrons or holes.

Such a strong spin-orbit interaction would enable pushing spin qubit Rabi frequencies into the GHz regime [9], an order of magnitude higher than recently demonstrated with hole spin qubits [14, 22, 23], and state-of-the-art electron-based spin qubits [8, 25, 32]. Moreover, a large electrical tunability of spin-orbit interaction strength promises exquisite control over qubit coherence and manipulation speeds, providing a gate-controlled *ON/OFF* switch of the coupling to electrical environmental degrees of freedom, which could be used to, on the one hand, maximize the coupling to microwave drive fields and, on the other hand, minimize the coupling to charge noise. Such controllable coupling would make it possible to combine ultrafast qubit operations with long coherence times. Furthermore, such electrical tunability can be used to control the localization length of Majorana zero-modes confined to each end of a nanowire [17], creating the possibility of electrically performing topologically non-protected operations on Majorana zero-modes.

Due to the tunable nature of the spin-orbit interaction, the magnitude of the  $g$ -factor of hole spins in Ge/Si nanowires can be modulated over a large range using applied electric fields [27, 28]. This feature enables local control over the Zeeman energy and allows to tune the energy of a qubit relative to a spin resonance driving field, or to a microwave cavity mode, making it possible to selectively address individual qubits in a multi-qubit device. Furthermore, in addition to strong and tunable spin-orbit interaction, hole spins in Ge/Si nanowires combine several other features that make them amenable for implementation of high-quality qubits. Hyperfine-induced decoherence is expected to be strongly suppressed, since holes have a p-type Bloch function, which has zero overlap with lattice nuclear spins [29]. Furthermore, both Ge and Si have a low natural abundance of isotopes with non-zero nuclear spins ( $^{29}\text{Si} < 5\%$ ,

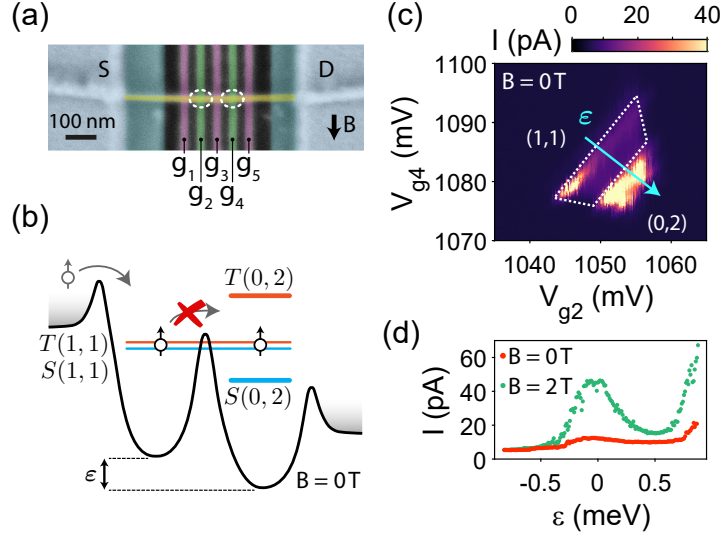


Figure 4.1: Device and Pauli spin blockade. (a) False-colour scanning electron micrograph of the device, used for all the measurements of this work. The finger gates  $g_{1-5}$  (red: barrier gates, green: plunger gates) are biased with positive voltages  $V_{g1-5}$  in order to create a double quantum dot in the Ge/Si core/shell nanowire (yellow). The source (S) and drain (D) contacts are defined on either side of the nanowire. Dashed ellipses indicate the approximate locations of the two quantum dots. (b) Schematic illustration of Pauli spin blockade, with zero magnetic field. When the double dot is occupied by holes in a triplet  $(1, 1)$  state, the current is blocked until mixing with a singlet state takes place. The double dot detuning is indicated by  $\epsilon$ . (c) Bias triangles taken at  $V_{SD} = 2$  mV showing signatures of Pauli spin blockade, through a suppression of current, in the area delineated by the dashed white lines. The blue arrow indicates the direction of the detuning axis. (d) Current as a function of detuning, swept along the arrow in (c), without (red) and with (green) applied magnetic field.

$^{29}\text{Ge} < 8\%$ ), which can be made vanishingly small through isotopic purification. Finally, in contrast to electrons, holes in Ge and Si do not experience valley degeneracy, which for electron spins in Si-based devices can have a detrimental effect on qubit relaxation times [30].

Here, we investigate the spin-orbit interaction of hole spins confined in a double quantum dot defined electrostatically in a Ge/Si core/shell nanowire [31, 32]. We use mixing of singlet and triplet spin states de-

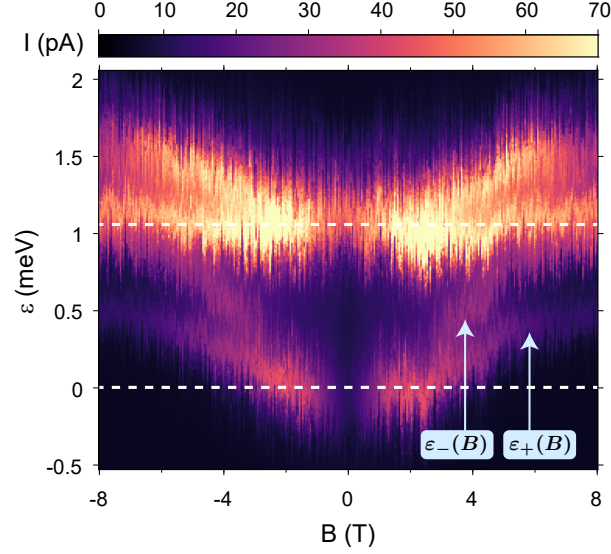


Figure 4.2: Measured leakage current as a function of magnetic field for detunings covering the entire bias triangle, as shown by the arrow in Fig. 4.1(c). The dashed white lines delineate the spin-blockaded region also shown in Fig. 4.1(c). Here,  $V_{g3} = 3820$  mV.

tected through lifting of Pauli spin blockade [33–37] to perform spectroscopy on the effectively doubly occupied double dot. Notably, we also find a large orbital effect of the magnetic field. We have developed a spectroscopic model, which fully takes into account these orbital effects, allowing to independently determine the Landé  $g$ -factor, the inter-dot tunnel coupling strength, and the strength of the spin-orbit interaction in this device. We find a particularly strong spin-orbit interaction, with a spin-orbit length of the same order as the dot size. Such a regime of strong spin-orbit interaction is expected to exhibit effects [38, 39] typically not observed in experiments with quantum dots. Specifically, it causes a renormalization of the  $g$ -factor, which we find here to lead to a Zeeman energy that is a non-linear function of the applied magnetic field.

## 4.2 Device and measurement setup

The device we use consists of a single Ge/Si core/shell nanowire deterministically placed on top of five finger gates, which are equally spaced with a pitch of 50 nm (see Fig. 4.1(a)). The nanowire has an overall ra-

dus of  $11 \text{ nm} \pm 2 \text{ nm}$ , as determined through atomic force microscopy, and a nominal Si shell thickness of  $2.5 \text{ nm}$ . A  $20 \text{ nm}$  thick layer of  $\text{Al}_2\text{O}_3$  in between gates and nanowire serves as electrical insulation. Electrical contact to the nanowire is made through two Ti/Pd contact pads, defined on either side of the nanowire. For more details of the device, see Froning et al. [31]. Previously, we have shown a large degree of control over the formation of quantum dots in such devices, which can be tuned over hundreds of charge transitions down to the few-holes occupation regime [31, 32]. Here, we form a tunnel-coupled double quantum dot by applying positive voltages to the finger gates  $g_1 - g_5$  that locally deplete the nanowire hole gas [40]. We use the contact pads to apply a source-drain voltage bias of  $V_{\text{SD}} = 2 \text{ mV}$  across the nanowire and to measure the current flowing through the double dot. An external magnetic field is applied in the sample plane, perpendicular to the major axis of the nanowire, as indicated in Fig. 4.1(a). All measurements were taken at a temperature of  $1.4 \text{ K}$ .

### 4.3 Double quantum dot and Pauli spin blockade

We tune the double dot to an effective occupation of two holes and study the transport cycle  $(0, 1) \rightarrow (1, 1) \rightarrow (0, 2) \rightarrow (0, 1)$  in a Pauli spin blockade [3, 33] configuration (see Fig. 4.1(b)). Here the first and second numbers refer to the effective hole occupation of the left and right dot, respectively. Transport in this regime is subject to a spin selection rule imposed by the Pauli exclusion principle: interdot transitions  $(1, 1) \rightarrow (0, 2)$  are blocked for spin triplet states ( $|T_{\downarrow\downarrow}\rangle, |T_0\rangle, |T_{\uparrow\uparrow}\rangle$ , with spin quantum numbers  $s = 1$  and  $m_s = -1, 0, +1$ ), since the  $|T(0, 2)\rangle$  states are energetically inaccessible. In contrast, interdot transitions are energetically allowed for holes in a spin singlet state ( $|S\rangle, s = m_s = 0$ ). Therefore, when a triplet  $(1, 1)$  state gets occupied, current through the double dot is blocked, until mixing with a singlet state takes place.

We exploit such spin-selective transport as a read-out method allowing us to distinguish spin states [33]. Fig. 4.1(c) shows a measurement of the current through the double dot as a function of the voltage on gates  $g_2$  and  $g_4$ , taken at zero magnetic field. We identify the area of reduced current, enclosed by the dashed line in Fig. 4.1(c), as a signature of spin blockade. Consistently, for opposite  $V_{\text{SD}}$ , we obtain a larger current

(not shown). Furthermore, as can be seen in the traces of Fig. 4.1(d), the blockade is lifted at a finite magnetic field, resulting in an increased current. Even when in a triplet state, transport can become unblocked [33] through various spin-mixing mechanisms that coherently or incoherently couple triplet and singlet states. Possible spin-mixing mechanisms are based on hyperfine interactions with the nuclear spin bath of the host lattice [34, 35, 41], spin-flip cotunneling [36, 42–44],  $g$ -factor differences in the double quantum dot, and spin-orbit interaction [13, 35–37, 41]. The dominant spin-mixing mechanism can be investigated by leakage currents in Pauli spin blockade.

## 4.4 Lifting of Pauli Spin Blockade

We study the lifting of spin blockade in more detail, focussing on the dependence of the resulting leakage current on double-dot detuning  $\varepsilon$ , magnetic field  $B$ , and interdot tunnel coupling strength  $t_c$ . Fig. 4.2 shows a measurement of the current through the double dot as a function of magnetic field  $B$  and detuning  $\varepsilon$ . The latter is swept over the entire bias triangle, by changing  $V_{g2}$  and  $V_{g4}$  following the arrow in Fig. 4.1(c). The white dashed lines in Fig. 4.2 indicate the spin-blockaded regime  $0 < \varepsilon < \varepsilon_\Delta$ , with  $\varepsilon_\Delta \approx 1$  meV the detuning for which states with one hole in the first orbital excited state becomes energetically available. For detunings exceeding  $\varepsilon_\Delta$ , we observe features with a significantly increased current. We attribute these features to spin-flip transitions involving a higher orbital state, i.e. either  $|T_{\uparrow\uparrow,\downarrow\downarrow}(1, 1)\rangle - |S_\Delta(0, 2)\rangle$ , or  $|S(1, 1)\rangle - |T_{\uparrow\uparrow,\downarrow\downarrow}(0, 2)\rangle$  transitions, where  $|S_\Delta\rangle$  refers to a singlet state with one hole in the orbital ground state and one hole in the first orbital excited state. Note that also spin-conserving  $|T(1, 1)\rangle - |T(0, 2)\rangle$  transitions can take place for these detunings, but these transitions would not exhibit multiple peaks at finite magnetic field, since they do not exhibit a Zeeman splitting. Remarkably, we find that in our experiment transitions that do not conserve spin have a higher amplitude than transitions that do conserve spin, as discussed later.

Here we are interested in the spin-blockaded region and in the remaining part we focus on the features between the white lines in Fig. 4.2. In this range of detuning, we see a markedly increased current that correspond to lifting of Pauli spin blockade. These leakage current features form the main topic of this work. We can make two important obser-



variations: 1) for a given sign of  $B$ , the leakage current is maximum along two curves as a function of  $\varepsilon$  and  $B$ , marked  $\varepsilon_{\pm}(B)$  in Fig. 4.2; 2) around zero magnetic field the leakage current is suppressed. These observations form the starting point in identifying the triplet-singlet transitions underlying the leakage current along  $\varepsilon_{\pm}(B)$ , as well as the spin-mixing mechanism.

As explained in more detail in Section 4.6, the position of the two curves as a function of detuning and magnetic field allows us to assign them to  $|T_{\uparrow\downarrow}(1, 1)\rangle - |S(0, 2)\rangle$  transitions. These transitions occur at different detuning depending on the magnetic field, due to an increase in Zeeman splitting, as well as orbital effects of the magnetic field. As shown in the next section, we identify spin-orbit interaction as the dominant spin-mixing mechanism by evaluating the magnetic field-dependent intensity of these transitions.

## 4.5 Possible Spin-mixing mechanisms

We now discuss the origin of the spin mixing leading to the observed lifting of spin blockade by considering the dependence of possible spin-mixing mechanisms on the magnetic field and detuning. In particular, the zero-field gap can be attributed to spin-orbit interaction, which is not effective at  $B = 0$  T due to time-reversal invariance [41, 46], but becomes important at finite  $B$  [47, 48]. Furthermore, for  $\varepsilon = 0$  and  $|B|$  smaller than a characteristic field  $\tilde{B}$ , the triplet  $(1, 1)$  states lie within the  $|S(1, 1)\rangle - |S(0, 2)\rangle$  avoided crossing, at which point spin-orbit interaction does not couple them efficiently to the singlet states.

Spin-flip cotunneling can also lead to dips or peaks in the leakage current around  $B = 0$  T. Such spin-flip cotunneling involves the exchange of a hole spin with one of the lead reservoirs through a process involving a virtual intermediate state, which can lead to decay of the triplet  $(1, 1)$  to a singlet state. Such cotunneling can result in a leakage current peak at  $B = 0$  T that exists for  $\varepsilon = 0$ , as well as for values of  $\varepsilon$  up to  $\varepsilon_{\Delta}$ . A shallow zero-field dip can also result from cotunneling, when the temperature  $T$  is small compared to  $t_c$  [42, 43]. However, the data presented in Fig. 4.2 shows a deep zero-field gap and our operating temperature of 1.4 K is, as will be shown later, comparable to  $t_c$ . We therefore rule out spin-flip cotunneling as the dominant spin-mixing mechanism in our measurements.

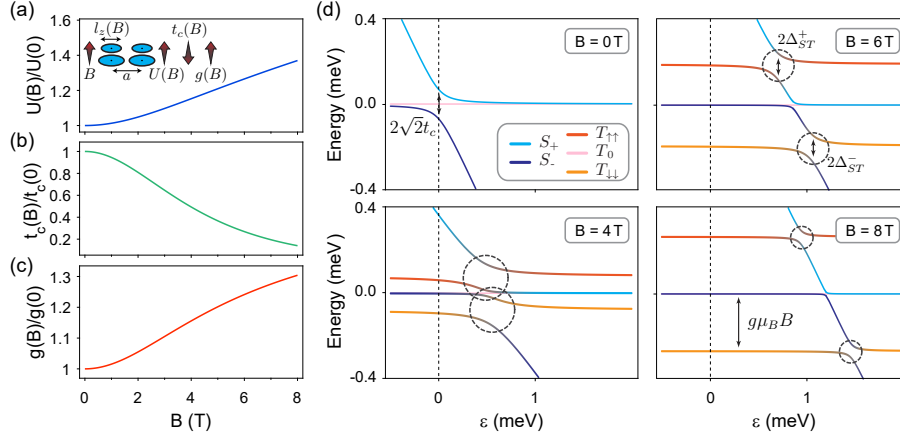


Figure 4.3: Magnetic-field dependencies. (a) Calculated magnetic field dependence of the addition energy  $U$  (See Eq. (4.35) of Appendix 4.B). Inset: Schematic illustration of the effect of increasing magnetic field  $B$  on dot size and separation leading to the observed changes in  $U$ ,  $t_c$  and  $g$ . Quantities change qualitatively with  $B$  as indicated by the arrows. (b) Calculated magnetic field dependence of the spin-conserving tunnel coupling  $t_c$  (see Eq. (4.30a) of Appendix 4.B). (c) Calculated magnetic field dependence of the  $g$ -factor (see Eq. (4.2)). For the plots in (a)-(c), the relevant parameters correspond to those of the measurement of Fig. 4.2. (d) Double dot energy level diagrams for different values of the magnetic field. For  $B = 0$  T, the spin-conserving tunnel coupling  $t_c$  is maximum and there is no singlet-triplet mixing due to spin-orbit interaction. For large enough magnetic fields ( $B > \tilde{B}$ ), avoided crossings (highlighted by dashed circles) appear when the triplet (1, 1) states cross a singlet state with (0, 2) component, corresponding to spin-flip tunneling due to spin-orbit interaction. The size of all avoided crossings becomes smaller with increasing magnetic field, as can be understood from (b) and Eq. (4.4). Moreover, due to the magnetic field dependence of the addition energy  $U$  (see (a)), as well as the Zeeman energy, all avoided crossings move to higher detuning with magnetic field. Parameters used to plot the diagrams were extracted from the data set shown in Fig. 4.2, using the model described in the text.

Furthermore, fluctuating polarizations of the nuclear spin bath in the double dot can result in triplet-singlet mixing [34, 35, 49]. However, as mentioned in the introduction, hyperfine interaction is expected to be very small for hole spins in Ge- and Si-based devices. Moreover, this

mechanism is only effective for values of  $B$  up to the root mean square value of nuclear field fluctuations, which we estimate to be  $< 1$  mT in our system [34]. Most notably, in contrast to what we observe, this spin-mixing mechanism should result in a leakage current peak [34,35] around  $B = 0$  T for  $\varepsilon$  up to  $\varepsilon_\Delta$ .

Finally, differences in  $g$ -factor between the two dots need to be considered. The effective  $g$ -factor for holes in Ge/Si nanowires can depend sensitively on the electric field [27], confinement potential [38,39], and hole occupation number. At finite field, such a  $g$ -factor difference will mix the  $|T_0(1, 1)\rangle$  and  $|S(1, 1)\rangle$  states, thus leading to an additional resonance of the leakage current. However, such  $|T_0(1, 1)\rangle - |S(1, 1)\rangle$  mixing would not result in the two separated curves of increased current that we observe, but instead provide a background leakage current in the detuning range considered, with no magnetic field dependence. Note further that such mixing is suppressed as  $|T_0(1, 1)\rangle$  is split off from the singlet by the exchange energy.

In conclusion, we identify spin-orbit interaction as the dominant spin-mixing mechanism responsible for the observed leakage current. In a double quantum dot, spin-orbit interaction can flip the spin of a hole tunneling between the quantum dots. This enables triplet-singlet mixing, when these states are aligned in energy, which can effectively lift Pauli spin blockade. As shown in the next section, we can explain the spectroscopy of the observed leakage current using this mechanism.

## 4.6 Model of the two transitions

Here, we present an analytical model that takes into account non-spin-conserving interdot tunneling and its dependence on magnetic field and detuning. Our model agrees very well with the data and accurately reproduces the field-dependence of the two observed transitions shown in Fig. 4.2, allowing us to identify them as  $|T_{\uparrow\downarrow, \downarrow\downarrow}\rangle - |S\rangle$  transitions.

As mentioned before, we assume that the spin-blockade and its lifting can be understood in terms of an effectively doubly-occupied double dot. When the spin-conserving interdot tunnel coupling  $t_c$  is finite, the singlet states  $|S(0, 2)\rangle$  and  $|S(1, 1)\rangle$  are coupled, giving rise to two new eigenstates we refer to as the lower and higher hybridized singlet states,  $|S_-\rangle$  and  $|S_+\rangle$ , respectively [50]. These hybridized singlets are defined as  $|S_-\rangle = \sin(\theta/2)|S(1, 1)\rangle - \cos(\theta/2)|S(0, 2)\rangle$  and  $|S_+\rangle = \cos(\theta/2)|S(1, 1)\rangle + \sin(\theta/2)|S(0, 2)\rangle$ , with the mixing angle  $\theta$  being a function of detuning

$\varepsilon$  and  $t_c$  (see Eq. (4.37) for the full expression of  $\theta$ ). The  $|S_{\pm}\rangle$  states exhibit an avoided crossing around  $\varepsilon = 0$  with a gap of  $2\sqrt{2}t_c$ , as shown in Fig. 4.3(d). Importantly, the proportion of  $|S(0, 2)\rangle$  and  $|S(1, 1)\rangle$  present in each of the  $|S_{\pm}\rangle$  states depends on the detuning.

In the presence of spin-orbit interaction, spin-flip tunneling couples the  $|T_{\uparrow\uparrow,\downarrow\downarrow}(1, 1)\rangle$  states with the two hybridized  $|S_{\pm}\rangle$  states, due to the  $|S(0, 2)\rangle$  content of the latter. The coupling strength of this spin-flip tunneling is given by the strength of the spin-conserving tunnel coupling as well as the strength of the spin-orbit interaction and can be written as  $t_{so} = t_c \tan(a/\lambda_{so})$  (see Appendix 4.B for derivation), with  $a$  the interdot distance and  $\lambda_{so}$  the spin-orbit length (defined by  $\pi\lambda_{so}/2$  being the distance a hole has to travel for spin-orbit interaction to induce a  $\pi$ -rotation of its spin state).

This coupling leads to avoided crossings when the energies of the  $|T_{\uparrow\uparrow,\downarrow\downarrow}\rangle$  states exactly match the energies of the  $|S_{\pm}\rangle$  states, as illustrated in the energy level diagrams in Fig. 4.3(d). The leakage current is maximum for those values of the detuning where the triplet-singlet avoided crossings occur, which can be written as:

$$\varepsilon_{\pm}(B) = U(B) - U(0) \pm \left( \frac{2t_c^2(B)}{g(B)\mu_B B} - g(B)\mu_B B \right). \quad (4.1)$$

Here the indices  $+$  and  $-$  correspond to the  $|T_{\uparrow\uparrow}\rangle - |S_{+}\rangle$  and  $|T_{\downarrow\downarrow}\rangle - |S_{-}\rangle$  transitions, respectively. Furthermore,  $\mu_B$  is the Bohr magneton,  $g$  the  $g$ -factor in the dot, and  $U$  the single dot addition energy. Eq. (4.1) describes the evolution of spin-blockade leakage current with magnetic field shown in Fig. 4.2 between the white dashed lines, with  $\varepsilon_{\pm}(B)$  giving the detunings of the resonant peaks of the two features as a function of magnetic field.

In order to explain the precise magnetic field dependence of  $\varepsilon_{\pm}(B)$ , we need to take into account effects that rely on the magnetic field changing the size of the hole orbitals. In the experiment, the magnetic field is oriented perpendicular to the principal nanowire axis and is varied over a wide range of amplitudes ( $-8 \text{ T} \leq B \leq 8 \text{ T}$ ), making such orbital effects significant in this system.

Remarkably, this turns the spin-conserving tunnel coupling  $t_c$ , the addition energy  $U$  and the  $g$ -factor into quantities that all depend on the magnetic field (see inset Fig. 4.3(a)). Such effects are usually dealt with only qualitatively, even though their relative magnitude can be quite

large. Here, we take these effects fully into account in our spectroscopic model, enabling us to quantify the  $g$ -factor and the spin-orbit length in our device.

To derive the functional dependence of these quantities on  $B$ , we start from the Hund-Mulliken theory of atomic orbitals and we assume harmonic confinement in all three directions. By considering an anisotropic 3-dimensional oscillator, we model the effects of a confinement potential that is smoother (sharper) in the direction along (perpendicular to) the nanowire as well as the strain-induced anisotropy of the effective mass [21]. The hole wavefunctions in each dot are squeezed by the magnetic field and as a result the spin-conserving tunneling  $t_c(B)$  is reduced at large fields while the single-dot addition energy  $U(B)$  is enhanced, as shown schematically in the inset of Fig. 4.3(a). The explicit dependencies of  $t_c(B)$  and  $U(B)$  on magnetic field are given in Eqs. (4.30a) and (4.35) of Appendix 4.B, and are plotted in Fig. 4.3(a), (b).

The detunings at which the  $|T_{\uparrow\downarrow}\rangle - |S_{\pm}\rangle$  avoided crossings appear also depend on the Zeeman splitting  $E_Z$  of the  $|T_{\uparrow\downarrow}\rangle$  states with respect to the singlets. Usually, the Zeeman splitting is a linear function of the magnetic field, which can be written in terms of the  $g$ -factor as  $E_Z = g\mu_B|B|$ . However, strong spin-orbit interaction can renormalize the  $g$ -factor [38,39] when the size of the quantum dot is changed. In our case, the magnetic field changes the dot size through orbital effects, leading to a dependence of the  $g$ -factor on the magnetic field and turning the Zeeman energy into a non-linear function of the magnetic field.

The shrinking of the dot with increasing magnetic field causes the  $g$ -factor to be enhanced at large values of the magnetic field and we can write [38,39]

$$g(B) = g_0 e^{-\frac{l_{\parallel}^2}{\lambda_{so}^2} \left(1 + \frac{B^2}{B_0^2}\right)^{-1/2}}, \quad (4.2)$$

where  $g_0$  is the  $g$ -factor without the spin-orbit-induced renormalization. Furthermore,  $l_{\parallel}$  is the field-independent harmonic length of the hole wavefunction ( $l_{\parallel} = l_z(B = 0)$ , with  $l_z$  being the dot confinement length along the wire) and  $B_0$  is a characteristic magnetic field that depends on the average confinement strength in the directions perpendicular to the field. See Appendix 4.A for the precise definition of these quantities. Fig. 4.3(c) shows a plot of Eq. (4.2), using the values of  $l_{\parallel}$  and  $B_0$  extracted from the measurement of Fig. 4.2. We stress that the magnetic-field dependence of

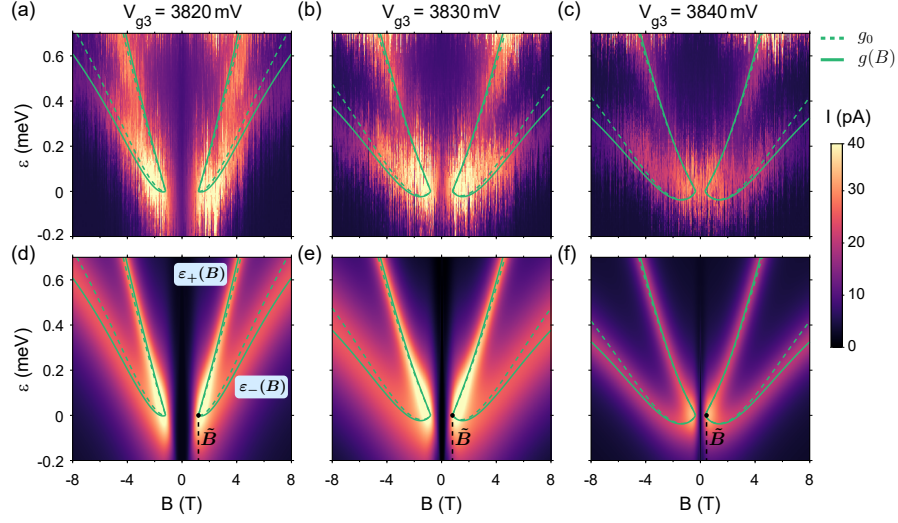


Figure 4.4: Spectroscopy measurements and modelling. (a)-(c) Measured leakage current as a function of magnetic field and detuning  $\varepsilon < \varepsilon_\Delta$ , for  $V_{g3} = 3820, 3830$ , and  $3840$  mV. The green curves are fits of each data set to Eq. (4.1), with (solid) and without (dashed) taking into account  $g$ -factor renormalization with magnetic field. (d)-(f), Simulated leakage current as a function of magnetic field and detuning. Here, we used the model discussed in Sections 4.6-4.8 of the main text, with relevant parameters determined from fits of the data shown in (a)-(c). The green curves are identical to the curves in (a)-(c).

the  $g$ -factor in Eq. (4.2) is a direct consequence of the strong spin-orbit interaction in the nanowire and it vanishes when the spin-orbit length  $\lambda_{so}$  is much larger than the dot size, which is typically the case for quantum dot systems that have been experimentally realized thus far.

As will be shown in the next section, when taking into account the magnetic field dependence of  $U$ ,  $t_c$ , and  $g$ , the resonant positions  $\varepsilon_\pm(B)$  of the  $|T_{\uparrow\uparrow,\downarrow\downarrow}\rangle - |S_\pm\rangle$  transitions given by Eq. (4.1) closely reproduce the evolution of the two features of spin blockade leakage current of Fig. 4.2 as a function of magnetic field and detuning.

## 4.7 Varying the strength of interdot tunnel coupling

To demonstrate the versatility of our model we now explore the influence of varying the voltage  $V_{g3}$  on the middle gate on the leakage current. The main expected effects are a change in the interdot tunnel coupling  $t_c$  and a change in the dot confinement. Figs. 4.4(a)-(c) show measurements similar to that of Fig. 4.2, for three values of  $V_{g3}$  (see the Supplemental Material for extended data sets). Comparing the three data sets, we see that an increase of  $V_{g3}$  leads to a closing of the zero-field gap. As discussed before, Pauli spin blockade only becomes lifted through spin-orbit interaction for magnetic fields above a critical value. This critical field  $\tilde{B}$  can be written as

$$\tilde{B} = \frac{\sqrt{2} t_c(\tilde{B})}{\mu_B g(\tilde{B})}, \quad (4.3)$$

where we include the magnetic field dependence of  $t_c$  and  $g$ . When  $|B| = \tilde{B}$ , the Zeeman energy matches the size of half of the avoided crossing given by  $t_c$ . At this point,  $\varepsilon_-(B) = \varepsilon_+(B)$  (see Eq. (4.1)) and both  $|T_{\uparrow\downarrow}(1, 1)\rangle - |S_{\pm}\rangle$  transitions become possible at  $\varepsilon \approx 0$  (see Fig. 4.3(d) and Fig. 4.4(a)). For  $|B| < \tilde{B}$ , each of the singlet-triplet avoided crossings occur at detunings where the involved  $|S_{\pm}\rangle$  states are mostly composed of  $|S(1, 1)\rangle$ , which does not couple to  $|T_{\uparrow\downarrow}(1, 1)\rangle$  through spin-orbit interaction, leading to a gap in leakage current with characteristic width  $\tilde{B}$  around zero magnetic field.

By increasing  $V_{g3}$ , we reduce  $t_c$  and from Eq. (4.3) it follows that spin blockade can be lifted at smaller magnetic fields. This moves the points of emergence of  $\varepsilon_{\pm}(B)$  for both magnetic field polarities closer together and effectively reduces the width of the zero-field gap of leakage current, in accordance with the observations. In Fig. 4.4(a)-(c), we can clearly see this reduction of the zero-field gap (indicated with  $\tilde{B}$ ) when the middle gate voltage  $V_{g3}$  is increased. Using Eq. (4.3), we extract the ratio  $t_c/g$  at the critical field  $\tilde{B}$  for each data set. When the magnetic field is not much larger than  $\tilde{B}$ , we neglect as a first approximation the variation of  $t_c(B)$  and  $g(B)$  from their value at  $\tilde{B}$ , see Figs. 4.3(a) and (c), and so using Eq. (4.1) we deduce  $t_c(\tilde{B})$  and  $g(\tilde{B})$  from the relative position of the resonant peaks. Values of  $\tilde{B}$ ,  $t_c(\tilde{B})$ , and  $g(\tilde{B})$  extracted in this way for the three data sets of Fig. 4.4 are listed in Table 4.1.

By taking into account the orbital effects, our model allows us to explain the main features of the resonances at low magnetic fields. By linearly expanding the single-dot addition energy in the vicinity of the critical field,  $U(B) \approx U(\tilde{B}) + U'(\tilde{B})(B - \tilde{B})$ , we can approximate  $\varepsilon_-(B) \approx \varepsilon(\tilde{B}) + (U'(\tilde{B}) + g(\tilde{B})\mu_B)(B - \tilde{B})$ , reproducing the approximately linear dependence of the upper resonance on magnetic field seen in Fig. 4.4. On the other hand, in the expression of the  $\varepsilon_+(B)$  resonant peak the term linear in  $B$  is smaller and the  $1/B$  term gives a significant contribution, leading to a less pronounced shift in detuning, especially at low magnetic field. Although the  $1/B$  term is proportional to the tunneling energy, its effect is counter-intuitively more pronounced in Fig. 4.4(c), because here Pauli spin blockade is lifted at lower magnetic fields.

To characterize the overall magnetic field dependence of the leakage current, we now find  $\varepsilon_{\pm}(B)$  for each data set by fitting to Eq. (4.1). The green curves in Fig. 4.4 are plots of  $\varepsilon_{\pm}(B)$  with (solid) and without (dashed) taking into account the renormalization of the  $g$ -factor given by Eq. (4.2). The additional features at larger magnetic fields, such as the bending of the  $\varepsilon_+(B)$  curve, are captured by the model by considering the function  $U(B)$  beyond the linear approximation, as well as the renormalization of the  $g$ -factor due to spin-orbit interaction. We see that the enhancement of the  $g$ -factor captured by Eq. (4.2) is quite important for large magnetic fields (see also the Supplementary Material), where it causes a sizeable bending of the resonant peaks. Including the renormalized  $g$ -factor gives much better agreement with the measurements over the whole range of magnetic field values.

In order to calculate the renormalized  $g$ -factor using Eq. (4.2), we estimate the dot confinement length  $l_{\parallel} = \sqrt{\hbar/(m_{\parallel}\omega_{\parallel})}$ , which depends on the confinement energy  $\omega_{\parallel}$  and on the effective mass  $m_{\parallel}$  along the nanowire. We determine  $\hbar\omega_{\parallel} \sim 1$  meV from measurements of the double dot charge stability diagram and assume  $m_{\parallel} \sim 0.05 m_0$  (here  $m_0$  is the bare electron mass). This choice of  $m_{\parallel}$  is justified by the fact that we still measure a non-zero current even at  $|B| = 8$  T. If the effective mass along the nanowire growth direction would be smaller, the orbital effects would shrink the wavefunction to the extent that the interdot tunnel coupling would vanish at 8 T. For our experiment, we determine  $l_{\parallel} \approx 39 - 45$  nm for the range of  $V_{g3}$  used here. All the parameters extracted from our analysis for the three datasets are reported in Table 4.1. These values capture the qualitative trend expected: when the voltage  $V_{g3}$  is increased, the hole wavefunctions become more separated and squeezed, causing a



reduction of the tunneling energy  $t_c$  and an enhancement of the  $g$ -factor because of the strong spin-orbit interaction, as described by Eq. (4.2). As shown in the next section, our model allows us to extract the spin-orbit length for each measurement. The model color plots shown in Fig. 4.4(d)-(f) take into account the extracted values of the spin-orbit length, allowing a full reconstruction of the leakage current in very good agreement with the measurements.

## 4.8 Spin-orbit length

We now turn to the evaluation of the strength of the spin-orbit interaction from the measurements shown in Fig. 4.4. The model developed in the previous sections facilitates the extraction of this strength from the width of the two leakage current features as a function of detuning in Fig. 4.4(a)-(c). This width is given by the sizes  $2\Delta_{\text{ST}}^{\pm}$  of the avoided crossings (see Fig. 4.3d) induced by the spin-orbit interaction. Here, the spin-flip tunneling energies  $\Delta_{\text{ST}}^{\pm}$  are functions of the spin-orbit length  $\lambda_{so}$  and furthermore depend on the overlap of the wave functions of the  $|T_{\uparrow\downarrow}(1,1)\rangle$  states with those of the  $|S_{\pm}\rangle$  states, as well as on the dot size. The spin-flip tunneling energy can be written as (see Appendix 4.C for the complete derivation)

$$\Delta_{\text{ST}}^{\pm} = t_c \tan\left(\frac{a}{\lambda_{so}}\right) \sqrt{\frac{1 \pm \cos(\theta)}{2}}, \quad (4.4)$$

with  $\theta$  the mixing angle of the  $|S_{\pm}\rangle$  states.

The leakage current  $I_{\pm}(B)$  corresponding to the resonances around  $\varepsilon = \varepsilon_{\pm}(B)$  can be written as [13, 51–53]

$$I_{\pm} = I_0 + e\Gamma \frac{(\Delta_{\text{ST}}^{\pm})^2}{(\varepsilon - \varepsilon_{\pm})^2 + 3(\Delta_{\text{ST}}^{\pm})^2 + h^2\Gamma^2/4}. \quad (4.5)$$

Here, the lead-to-dot relaxation rate  $\Gamma \sim 0.45$  GHz is taken to be symmetric for both of the leads and is estimated by adjusting the formula in Eq. (4.5) for the  $|S(0,2)\rangle \rightarrow |S(1,1)\rangle$  transition, and fitting it to the current measured for opposite  $V_{\text{SD}}$ . The offset current term  $I_0$  contains all incoherent relaxation mechanisms, as well as  $|S\rangle - |T_0\rangle$  mixing. Discussing this term in detail is beyond the scope of this paper and we refer the interested reader to Ref. [41]. Additionally, we note that since we operate

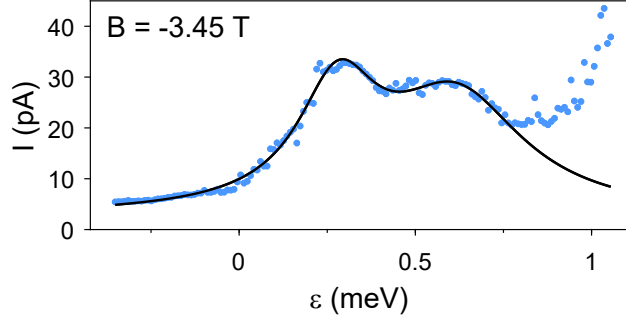


Figure 4.5: Measured leakage current as a function of detuning, for  $V_{g3} = 3820$  mV and  $B = -3.45$  T. The black curve is a fit of Eq. (4.5) to the data.

at relatively high temperature, it might be expected that the transitions are thermally broadened. However, the temperature of 1.4 K is still low compared to the orbital level splitting of 1 meV, making such broadening negligible. The dot-lead tunneling rate  $\Gamma$  is influenced by temperature, but the value of  $\Gamma$  that we determine independently from the measurements already includes this effect.

We therefore conclude that the width of the two leakage current features is given by the spin-flip tunneling energies  $\Delta_{ST}^{\pm}$ , which are then deduced by fitting the Lorentzians in Eq. (4.5) to the data sets of Fig. 4.4(a)-(c). An example of this is shown in Fig. 4.5. The color plots of Fig. 4.4(d)-(f) are constructed from the Lorentzians found in this way for different values of the magnetic field. It can be seen that the model plots accurately reproduce the leakage current observed in the corresponding experimental data.

Importantly, the determined  $\Delta_{ST}^{\pm}$  allow to extract the spin-orbit length  $\lambda_{so}$ . Using Eq. (4.4), we obtain the ratio  $\lambda_{so}/a$  directly from the ratio  $\Delta_{ST}/t_c$  of the average spin-flip tunneling  $\Delta_{ST} = [(\Delta_{ST}^+)^2 + (\Delta_{ST}^-)^2]^{1/2}$  and the spin-conserving tunneling  $t_c$ . This yields ratios of  $\lambda_{so}/a$  as shown in Table 4.1 for the different configurations of our double quantum dot. The precise value of the interdot distance  $a$  cannot be exactly determined from the measurements, but we can roughly estimate  $a \sim 90$  nm by considering the distance between the gates  $g_2$  and  $g_4$  (see Fig. 4.1(a)). Using this value, we obtain an average estimated value  $\lambda_{so} \sim 65$  nm for the spin-orbit length, with small variation between the measurements of Fig. 4.4(a)-(c).

	$V_{g3}$ (mV)	$\tilde{B}$ (T)	$B_0$ (T)	$t_c(\tilde{B})$ ( $\mu\text{eV}$ )	$g(\tilde{B})$	$l_{\parallel}$ (nm)	$\lambda_{so}/a$
Fig. 4.4(a)	3820	1.2	3.8	44	0.9	45	0.78
Fig. 4.4(b)	3830	0.8	4.8	33	1.0	41	0.72
Fig. 4.4(c)	3840	0.35	5.0	16	1.1	39	0.71

Table 4.1: Extracted hole spin parameters, obtained for the three datasets shown in Fig. 4.4 by fitting the model to the data as described in the main text.

Together with the orbital effects of the magnetic field, this notably small  $\lambda_{so}$  leads to a dependence of the  $g$ -factor on the magnetic field, as described by Eq. (4.2). This effect is large, since the spin-orbit length  $\lambda_{so}$  and the confinement length along the wire  $l_{\parallel}$  are of the same order of magnitude. In our measurements, this manifests itself in the additional bending of the transitions  $\varepsilon_{\pm}(B)$  at high values of the magnetic field.

## 4.9 Conclusions and outlook

Summarizing, we have characterized the strength of spin-orbit interaction for hole spins confined in a double quantum dot in a Ge/Si nanowire, using spectroscopy measurements in Pauli spin blockade. We found the spin-orbit length to be of the same order of magnitude as the dot length and interdot distance. This has the remarkable consequence that the  $g$ -factor exhibits a non-linear dependence on magnetic field, which we observe experimentally at high values of the magnetic field.

The observation of this strong spin-orbit interaction in Ge/Si nanowires forms the starting point of various subsequent experiments in this material system. From the value of  $\lambda_{so}$  we can estimate the Rabi frequency for electric dipole induced spin resonance [5, 19] mediated through spin-orbit interaction to be in the range of  $\sim 0.1 - 1$  GHz, for realistic values of microwave amplitudes. Such Rabi frequencies form an excellent basis for the implementation of fast hole spin qubits in this system.

Further characterization studies of the spin-orbit interaction in this platform are of interest, in particular because here a quantitative comparison to relevant theoretical works [9, 17, 20, 21, 27] is challenging, due to the relatively high dot occupation number. For instance, direct Rashba

spin-orbit interaction is predicted to lead to a profound dependence of the spin-orbit interaction as well as the  $g$ -factor on electric fields. While we observe a dependence of the  $g$ -factor on a gate voltage (see Table 4.1), a more complete investigation of these effects would include measurements of the strength of the spin-orbit interaction as function of electric field amplitude or orientation of magnetic field. Such tunability of  $g$ -factor and spin-orbit strength could enable individual addressability of spin qubits in coupling them to microwave fields, as well as provide a way to limit the impact of charge noise on spin coherence.

## 4.A Model Hamiltonian

Here, we provide a more detailed analysis of the theoretical model used in the main text. The relevant physics of a single hole confined in a quantum dot can be captured by the effective 2-dimensional Hamiltonian

$$H = H_o + H_{so} + H_Z , \quad (4.6)$$

with

$$H_o = \frac{\pi_x^2}{2m_\perp} + \frac{\pi_y^2}{2m_\perp} + \frac{\pi_z^2}{2m_\parallel} + \frac{m_\parallel \omega_\parallel^2}{2} z^2 + \frac{m_\perp \omega_\perp^2}{2} (x^2 + y^2) , \quad (4.7a)$$

$$H_{so} = \alpha \pi_z \sigma_y , \quad (4.7b)$$

$$H_Z = \frac{g_0 \mu_B}{2} \mathbf{B} \cdot \boldsymbol{\sigma} . \quad (4.7c)$$

Here, we define the dynamical momentum  $\boldsymbol{\pi} = -i\hbar\nabla - e\mathbf{A}$ , where  $\mathbf{A}$  is the vector potential accounting for an externally applied magnetic field  $\mathbf{B}$ . These operators satisfy the commutation relations  $[\pi_i, \pi_j] = i\epsilon_{ijk}\hbar e B_k$ ,  $[\pi_i, x_j] = -i\hbar\delta_{ij}$ . We model the confinement potential by an anisotropic harmonic oscillator, with confinement frequencies  $\omega_\perp$  and  $\omega_\parallel$ , and effective masses  $m_\perp$  and  $m_\parallel$  in the direction perpendicular and parallel to the nanowire growth direction, respectively. In the following, we assume  $\omega_\perp > \omega_\parallel$ . Because of the magnetic field, the spin states are split in energy by the Zeeman energy; here  $g_0$  is the  $g$ -factor of the system and the field  $\mathbf{B}$  is assumed to be homogeneous. The interaction between different spin states is captured by a Rashba-like spin-orbit interaction  $H_{so}$  [20, 21].

Our final goal is to extract from the measurements the spin-orbit interaction parameter  $\alpha$ . It is convenient to introduce the spin-orbit length

$$\lambda_{so} = \frac{\hbar}{m_{\parallel}\alpha} , \quad (4.8)$$

and to perform the unitary spin-dependent displacement of states [54]

$$S = e^{i\sigma_y z/\lambda_{so}} , \quad (4.9)$$

that diagonalizes the spin-orbit interaction in spin-space

$$S(H_o + H_{so})S^\dagger = H_o - \frac{\hbar^2}{2m_{\parallel}\lambda_{so}^2} , \quad (4.10)$$

converting the Zeeman term to a position-dependent quantity. We now focus on the case where the magnetic field points in the  $x$ -direction, i.e.  $\mathbf{B} = B\mathbf{e}_x$ , and we obtain

$$SH_ZS^\dagger = \frac{g_0\mu_B}{2}B \left[ \sigma_x \cos\left(\frac{2z}{\lambda_{so}}\right) + \sigma_z \sin\left(\frac{2z}{\lambda_{so}}\right) \right] . \quad (4.11)$$

In the harmonic confinement approximation, the orbital Hamiltonian  $H_o$  can always be diagonalized exactly. Assuming  $B > 0$ , we can introduce the vector of gauge-independent canonical positions  $\mathbf{Q}$  and momenta  $\mathbf{P}$

$$\mathbf{Q} = \begin{pmatrix} \frac{z}{l_B} - \frac{l_B}{\hbar}\pi_y \\ \frac{l_B}{\hbar}\pi_y \\ x \end{pmatrix} \quad \text{and} \quad \mathbf{P} = \begin{pmatrix} \frac{y}{l_B} + \frac{l_B}{\hbar}\pi_z \\ \frac{l_B}{\hbar}\pi_z \\ -i\partial_x \end{pmatrix} , \quad (4.12)$$

satisfying  $[Q_i, P_j] = i\delta_{ij}$ ; here  $l_B = \sqrt{\hbar/(e|B|)}$  is the magnetic length. When  $B < 0$ , the first two positions and momenta are swapped. The coupled harmonic oscillators can be decoupled by the symplectic Bogoliubov transformation

$$\begin{pmatrix} \mathbf{Q} \\ \mathbf{P} \end{pmatrix} = \begin{pmatrix} \mathcal{A}(r) & 0 \\ 0 & \mathcal{A}(-r)^T \end{pmatrix} \begin{pmatrix} \mathbf{q} \\ \mathbf{p} \end{pmatrix} , \quad (4.13)$$

where 3-dimensional matrix  $\mathcal{A}(r)$  is defined by

$$\mathcal{A}(r) = \begin{pmatrix} \cosh(r) & -\frac{\omega_{\perp}}{\omega_{\parallel}} \sinh(r) & 0 \\ -\frac{\omega_{\parallel}}{\omega_{\perp}} \sinh(r) & \cosh(r) & 0 \\ 0 & 0 & 1 \end{pmatrix} , \quad (4.14)$$

with squeezing parameter

$$r = \frac{1}{2} \operatorname{arccoth} \left( \frac{\frac{e^2 B^2}{m_\perp m_\parallel} + \omega_\perp^2 + \omega_\parallel^2}{2\omega_\perp \omega_\parallel} \right). \quad (4.15)$$

In the new coordinate system with positions  $\mathbf{q}$  and momenta  $\mathbf{p}$ , we obtain three independent harmonic oscillators with frequencies  $\omega_\perp$  and  $\omega_1 < \omega_2$ , where the Fock-Darwin frequencies are

$$\begin{aligned} \omega_1 &= \omega_2 \tanh(r) \\ &= \frac{\sqrt{m_\parallel m_\perp}}{eB} \omega_\parallel \omega_\perp \sqrt{\left(1 - \frac{\omega_\parallel}{\omega_\perp} \tanh(r)\right) \left(1 - \frac{\omega_\perp}{\omega_\parallel} \tanh(r)\right)}. \end{aligned} \quad (4.16)$$

We point out that when  $B \rightarrow 0$ , Eq. (4.16) is still valid and it leads to the expected result  $\omega_1 = \omega_\parallel$  and  $\omega_2 = \omega_\perp$ .

The groundstate  $|0\rangle$  is the state simultaneously annihilated by the annihilation operators in this coordinate system

$$a_j = \frac{1}{\sqrt{2}} \left( \beta_j q_j + \frac{i}{\beta_j} p_j \right), \quad (4.17)$$

where

$$\beta_j = \left[ \left( \frac{\omega_\parallel m_\parallel}{\omega_\perp m_\perp} \gamma \right)^{1/4}, \left( \frac{\omega_\parallel m_\parallel}{\omega_\perp m_\perp} \frac{1}{\gamma} \right)^{1/4}, \sqrt{m_\perp \omega_\perp / \hbar} \right]_j, \quad (4.18)$$

and  $\gamma = \frac{\omega_\parallel}{\omega_\perp} \frac{\omega_\parallel / \omega_\perp - \coth(r)}{\omega_\perp / \omega_\parallel - \coth(r)}$ . To determine the groundstate wavefunction in real-space, we need to specify a gauge. In the symmetric gauge  $\mathbf{A} = \mathbf{B} \times \mathbf{r}/2$ , and combining Eqs. (4.12), (4.13) and (4.17), we obtain

$$\psi_0(\mathbf{r}) = \frac{1}{\pi^{3/4} \sqrt{l_x l_y l_z}} e^{-\frac{1}{2} \left( \frac{x^2}{l_x^2} + \frac{y^2}{l_y^2} + \frac{z^2}{l_z^2} \right) + i \frac{yz}{2l_B^2} \left( \frac{\omega_\parallel - \omega_\perp}{\omega_\parallel + \omega_\perp} \right)}, \quad (4.19)$$

where we defined the magnetic field-dependent lengths

$$l_y = l_\perp \left( 1 + \frac{B^2}{B_0^2} \right)^{-1/4} \quad \text{and} \quad l_z = l_\parallel \left( 1 + \frac{B^2}{B_0^2} \right)^{-1/4}, \quad (4.20)$$

and the usual harmonic lengths

$$l_x = l_\perp = \sqrt{\frac{\hbar}{m_\perp \omega_\perp}} \quad \text{and} \quad l_\parallel = \sqrt{\frac{\hbar}{m_\parallel \omega_\parallel}} . \quad (4.21)$$

The characteristic magnetic field  $B_0$  in Eq. (4.20) determines the relevant field at which the orbital effects start to become significant and it is defined by

$$B_0 = \frac{\sqrt{m_\parallel m_\perp}}{e} (\omega_\parallel + \omega_\perp) . \quad (4.22)$$

Projecting the Hamiltonian in Eq. (4.6) onto the groundstate subspace and subtracting a constant energy term, we obtain the effective low energy Hamiltonian

$$H_{GS} = \frac{g\mu_B B}{2} \sigma_x , \quad (4.23)$$

where we introduce the effective  $g$ -factor

$$g = g_0 e^{-l_z^2/\lambda_{so}^2} . \quad (4.24)$$

We emphasize that the  $g$ -factor is renormalized by the spin-orbit interaction, and it acquires a magnetic field dependence via  $l_z$ , see Eq. (4.20).

We remark that because of the transformation in Eq. (4.9), we are now treating spin-orbit interaction exactly, and the perturbation coupling different orbital states comes from the space-dependent magnetic field in the Zeeman energy, see Eq. (4.11). This approach is the most convenient to describe the results of this experiment, where a strong spin-orbit interaction is measured. Because of this term, the orbital ground state is coupled to the first excited orbital state  $|1\rangle$  with energy  $\hbar\omega_1$ . In particular, the interaction is

$$\langle 0|H|1\rangle = \frac{l_B}{\sqrt{2}\lambda_{so}\beta_1} \left( \cosh(r) - \frac{\omega_\parallel}{\omega_\perp} \sinh(r) \right) g\mu_B B \sigma_z . \quad (4.25)$$

Using the values extracted in the main text, see Table 4.1, we find that the amplitude of this interaction term is  $\sim 20\%$  of the energy gap  $\sim \hbar\omega_1$  at the maximal field measured  $B = 8$  T. Consequently, in the following we focus on the ground state subspace only.

## 4.B Double-dot Hamiltonian

We now construct the double-dot effective Hamiltonian by using the Hund-Mulliken method. To do so, we create an orthonormal basis of harmonic eigenfunctions whose center of mass is at the positions  $z = \pm a/2$ . Here,  $a$  is the interdot distance. Following the conventional procedure, we find the overlap matrix between the orbital ground states of the two dots:  $\mathcal{P}_{ij} = \langle \Psi_i | \Psi_j \rangle$ , where  $\Psi = (T_z(-a/2)S^\dagger\psi_0, T_z(+a/2)S^\dagger\psi_0)$ . The magnetic translation operators are defined as  $T_z(X) = e^{iX(\pi_z/\hbar + y/l_B^2)}$  and  $\psi_0$  is the ground state wavefunction in Eq. (4.19). Here  $|\Psi\rangle$  is defined as:

$$|\Psi\rangle = (T_z(-a/2)S^\dagger|\psi_0 \uparrow\rangle, T_z(-a/2)S^\dagger|\psi_0 \downarrow\rangle, T_z(+a/2)S^\dagger|\psi_0 \uparrow\rangle, T_z(+a/2)S^\dagger|\psi_0 \downarrow\rangle) \quad (4.26)$$

Importantly, because the unitary  $S^\dagger$  in Eq. (4.9) is spin-dependent, here  $\mathcal{P}$  is a  $4 \times 4$  matrix. Explicitly, we find

$$\mathcal{P} = \tau_0\sigma_0 + s \cos\left(\frac{a}{\lambda_{so}}\right) \tau_x\sigma_0 + s \sin\left(\frac{a}{\lambda_{so}}\right) \tau_y\sigma_y, \quad (4.27)$$

where  $\tau_i$  are Pauli matrices acting on the different dots,  $\sigma_i$  are acting on spins and we define the small parameter

$$s = e^{-\frac{a^2}{4l_z^2} \left( 1 + \frac{(\omega_\perp - \omega_\parallel)^2}{4\omega_\perp\omega_\parallel} \frac{B^2}{B^2 + B_0^2} \right)}. \quad (4.28)$$

Orthogonal and symmetric states  $|O\rangle$  are constructed from the non-orthogonal states  $|NO\rangle$  by the linear map  $|O\rangle = |NO\rangle\mathcal{P}^{-1/2}$  and single-particle operators  $H$  transform as  $H_O = \mathcal{P}^{-1/2}H_{NO}\mathcal{P}^{-1/2}$ . The generalization to two-body operators is straightforward.

For rather general double-dot confinement potentials, we find that the orbital Hamiltonian in the orthonormal basis has the form

$$H_o = t_c\tau_x\sigma_0 + t_{so}\tau_y\sigma_y + \frac{\varepsilon}{2}\tau_z\sigma_0. \quad (4.29)$$

Here,  $\varepsilon$  is the detuning between the two dots typically caused by an electric field along the wire,  $t_c$  is the spin-conserving tunneling energy and



$t_{so}$  is the spin-flip tunneling energy caused by the spin-orbit interaction. In particular, we find that

$$t_c = \frac{s}{1-s^2} t_0 \cos\left(\frac{a}{\lambda_{so}}\right) \quad \text{and} \quad (4.30a)$$

$$t_{so} = \frac{s}{1-s^2} t_0 \sin\left(\frac{a}{\lambda_{so}}\right) = t_c \tan\left(\frac{a}{\lambda_{so}}\right). \quad (4.30b)$$

where  $t_0$  is a characteristic energy dependent on the details of the confinement potential and the leading magnetic field dependence of the tunneling energy is caused by the exponential dependence of the overlap  $s$  on  $B$ , see Eq. (4.28).

Also, the Zeeman energy in the orthogonal basis is

$$H_Z = \frac{g\mu_B B}{2} \left( g_1 \tau_0 \sigma_x + g_2 \tau_x \sigma_x + g_3 \tau_z \sigma_z \right), \quad (4.31)$$

where we introduce the dimensionless prefactors

$$\begin{aligned} g_1 &= \frac{1 + \sqrt{1-s^2} - 2s^2 \cos\left(\frac{a}{\lambda_{so}}\right)}{2 - 2s^2} \\ &\quad + \frac{(1 - \sqrt{1-s^2}) \cos\left(\frac{2a}{\lambda_{so}}\right)}{2 - 2s^2} \\ &= 1 + \mathcal{O}(s^2), \end{aligned} \quad (4.32)$$

$$g_2 = \frac{1 - \cos\left(\frac{a}{\lambda_{so}}\right)}{1 - s^2} s, \quad (4.33)$$

$$g_3 = \frac{s^2 - (1 - \sqrt{1-s^2}) \cos\left(\frac{a}{\lambda_{so}}\right)}{1 - s^2} \sin\left(\frac{a}{\lambda_{so}}\right) = \mathcal{O}(s^2). \quad (4.34)$$

Neglecting corrections of order  $s^2$ , we can discard the term proportional to  $g_3$ , that couple the triplet states  $T_{\uparrow\downarrow}(1, 1)$  to the singlet state  $S(1, 1)$ . The term proportional to  $g_2$  arise when the spin-orbit interaction is large and cause interactions between the triplet  $T_0(1, 1)$  and the doubly-occupied singlet states  $S(2, 0)$  and  $S(0, 2)$ . This term causes an extra resonant peak of the leakage current, however, in the present experiment the energy of this interaction is of a few microelectronvolts, much smaller than the contribution due to the spin-flip tunneling. Consequently, in the following,

we will ignore it and consider only  $H_Z \approx g\mu_B B\tau_0\sigma_x/2$ .

Coulomb interactions are also required to understand the physics of the system. In particular, the most relevant electrostatic interaction element for the current experiment is the addition energy,

$$\begin{aligned} U &= \langle \Psi_i \Psi_i | \frac{e^2}{4\pi\epsilon_s \mathbf{r}} | \Psi_i \Psi_i \rangle \\ &= \frac{e^2}{4\pi\epsilon_s} \sqrt{\frac{2}{\pi}} \frac{F\left(\cos^{-1}\left(\frac{l_z}{l_x}\right) \middle| \frac{l_x^2 - l_y^2}{l_x^2 - l_z^2}\right)}{\sqrt{l_x^2 - l_z^2}}, \end{aligned} \quad (4.35)$$

where  $F(a|b)$  is the elliptic  $F$  function and  $\epsilon_s = 16\epsilon_0$  is the dielectric constant of the Germanium times the vacuum permittivity  $\epsilon_0$ . Eq. (4.35) holds for general values of lengths  $l_i$  provided that the appropriate limit is taken carefully. The next largest Coulomb interaction elements are the Hartree and Fock terms  $U_H = \langle \Psi_i \Psi_{j \neq i} | \frac{e^2}{4\pi\epsilon_s \mathbf{r}} | \Psi_{j \neq i} \Psi_i \rangle$  and  $U_F = \langle \Psi_i \Psi_{j \neq i} | \frac{e^2}{4\pi\epsilon_s \mathbf{r}} | \Psi_i \Psi_{j \neq i} \rangle$ , respectively. In the present experiment, the overlap  $s$  between wave functions of different dots is expected to be small, and so we discard the corrections of order  $\mathcal{O}(s^2)$  and we ignore the exchange interaction  $U_F \approx 0$ .

## 4.C Singlet-Triplet basis

We can now rewrite the Hamiltonian in the singlet-triplet basis. Neglecting higher orbital states, the relevant triplet states are

$$\begin{aligned} |T_{\uparrow\uparrow, \downarrow\downarrow}(1, 1)\rangle &= c_{-, \uparrow(\downarrow)}^\dagger c_{+, \uparrow(\downarrow)}^\dagger |0\rangle \quad \text{and} \\ |T_0(1, 1)\rangle &= \frac{c_{-, \uparrow}^\dagger c_{+, \downarrow}^\dagger + c_{-, \downarrow}^\dagger c_{+, \uparrow}^\dagger}{\sqrt{2}} |0\rangle, \end{aligned}$$

and the singlets are

$$\begin{aligned} |S(0, 2)\rangle &= c_{+, \uparrow}^\dagger c_{+, \downarrow}^\dagger |0\rangle \quad \text{and} \\ |S_0(1, 1)\rangle &= \frac{c_{-, \uparrow}^\dagger c_{+, \downarrow}^\dagger - c_{-, \downarrow}^\dagger c_{+, \uparrow}^\dagger}{\sqrt{2}} |0\rangle, \end{aligned}$$

where we introduce the fermionic ladder operators  $c_{i,\sigma}^\dagger$  creating an electron at the  $i$ th dot with spin  $\sigma$ . We do not consider here the singlet state

$S(2, 0)$  because it is far detuned in energy, and so the interactions of these states with it are suppressed by the large energy difference.

By aligning the spin quantization axis to the direction of the magnetic field, we find in the singlet-triplet basis  $(S(0, 2), S(1, 1), T_{\uparrow} \uparrow (1, 1), T_{\downarrow} \downarrow (1, 1), T_0(1, 1))^T$

$$H = \begin{pmatrix} U - \varepsilon & \sqrt{2}t_c & t_{so} & -t_{so} & 0 \\ \sqrt{2}t_c & U_H & 0 & 0 & 0 \\ t_{so} & 0 & U_H + g\mu_B B & 0 & 0 \\ -t_{so} & 0 & 0 & U_H - g\mu_B B & 0 \\ 0 & 0 & 0 & 0 & U_H \end{pmatrix}, \quad (4.36)$$

where  $t_c$ ,  $t_{so}$  and  $g$  and  $U$  are defined in Eqs. (4.30a), (4.24) and (4.35), respectively. The singlet sector is hybridized by the spin-conserving tunneling energy. By introducing the hybridized singlet states  $S_{\pm}$  obtained by rotating the singlet sector by  $\theta/2$ , where  $\theta$  is

$$\theta = \arctan \left( \frac{2\sqrt{2}t_c}{U - U_H - \varepsilon} \right), \quad (4.37)$$

we can rewrite the Hamiltonian in the convenient form

$$H = \begin{pmatrix} E_+ & 0 & \Delta_{ST}^+ & -\Delta_{ST}^+ & 0 \\ 0 & E_- & -\Delta_{ST}^- & \Delta_{ST}^- & 0 \\ \Delta_{ST}^+ & -\Delta_{ST}^- & U_H + g\mu_B B & 0 & 0 \\ -\Delta_{ST}^+ & \Delta_{ST}^- & 0 & U_H - g\mu_B B & 0 \\ 0 & 0 & 0 & 0 & U_H \end{pmatrix}, \quad (4.38)$$

where we defined the hybridized singlet energies  $E_{\pm}$  and the spin-orbit interaction  $\Delta_{ST}^{\pm}$  via

$$E_{\pm} = \frac{1}{2} (U + U_H - \varepsilon) \pm \sqrt{2t_c^2 + \frac{1}{4} (U - U_H - \varepsilon)^2}, \quad (4.39a)$$

$$\Delta_{ST}^{\pm} = t_{so} \sqrt{\frac{1 \pm \cos(\theta)}{2}}. \quad (4.39b)$$

Note that in the limit of weak spin orbit coupling, i.e.,  $a/\lambda_{so} \ll 1$ , we recover the result obtained previously for the ST splitting [50].

The leakage current is related to the matrix elements  $\Delta_{\text{ST}}^{\pm}$  between singlet and triplet states via [13, 51–53]

$$I_{\pm} = e\Gamma_L \frac{(\Delta_{\text{ST}}^{\pm})^2}{(\varepsilon - \varepsilon_{\pm})^2 + (\Delta_{\text{ST}}^{\pm})^2 \left( \frac{\Gamma_L}{\Gamma_R} + 2 \right) + \hbar^2 \Gamma_L^2 / 4} . \quad (4.40)$$

where  $\Gamma_{R(L)}$  is the coupling between the right, occupied (left, unoccupied) dot to the metallic lead and  $\varepsilon_{\pm}$  is the position of the triplet  $T_{\uparrow\uparrow,\downarrow\downarrow}(1, 1)$  and the singlet  $S_{\pm}$  anticrossing. In particular, by using Eq. (4.39a), we find

$$\varepsilon_{\pm} = U - U_H \pm \left( \frac{2t_c^2}{g\mu_B B} - g\mu_B B \right) . \quad (4.41)$$

Neglecting the corrections due to the Hartree energy  $U_H$ , small compared to the addition energy  $U$ , and assuming symmetric dot-lead coupling  $\Gamma_L \approx \Gamma_R = \Gamma$ , we obtain Eqs. (4.1) and (4.5) of the main text. Note that in the main text the detuning is measured from the singlet-singlet anticrossing, therefore Eq. (4.1) contains a constant energy shift.

# Bibliography

- [1] R. Winkler, *Spin–Orbit Coupling Effects in Two-Dimensional Electron and Hole Systems*, vol. 191 of *Springer Tracts in Modern Physics*. Berlin, Heidelberg: Springer Berlin Heidelberg, 2003.
- [2] D. Loss and D. P. DiVincenzo, “Quantum computation with quantum dots,” *Phys. Rev. A*, vol. 57, pp. 120–126, Jan. 1998.
- [3] R. Hanson, L. P. Kouwenhoven, J. R. Petta, S. Tarucha, and L. M. K. Vandersypen, “Spins in few-electron quantum dots,” *Rev. Mod. Phys.*, vol. 79, pp. 1217–1265, Oct. 2007.
- [4] G. Scappucci, C. Kloeffel, F. A. Zwanenburg, D. Loss, M. Myronov, J.-J. Zhang, S. De Franceschi, G. Katsaros, and M. Veldhorst, “The germanium quantum information route,” *ArXiv200408133 Cond-Mat Physicsquant-Ph*, Apr. 2020.
- [5] V. N. Golovach, M. Borhani, and D. Loss, “Electric-dipole-induced spin resonance in quantum dots,” *Phys. Rev. B*, vol. 74, p. 165319, Oct. 2006.
- [6] K. C. Nowack, F. H. L. Koppens, Y. V. Nazarov, and L. M. K. Vandersypen, “Coherent Control of a Single Electron Spin with Electric Fields,” *Science*, vol. 318, pp. 1430–1433, Nov. 2007.
- [7] S. Nadj-Perge, S. M. Frolov, E. P. a. M. Bakkers, and L. P. Kouwenhoven, “Spin-orbit qubit in a semiconductor nanowire,” *Nature*, vol. 468, pp. 1084–1087, Dec. 2010.
- [8] J. W. G. van den Berg, S. Nadj-Perge, V. S. Pribiag, S. R. Plissard, E. P. A. M. Bakkers, S. M. Frolov, and L. P. Kouwenhoven, “Fast Spin-Orbit Qubit in an Indium Antimonide Nanowire,” *Phys. Rev. Lett.*, vol. 110, p. 066806, Feb. 2013.

- [9] C. Kloeffer, M. Trif, P. Stano, and D. Loss, "Circuit QED with hole-spin qubits in Ge/Si nanowire quantum dots," *Phys. Rev. B*, vol. 88, p. 241405, Dec. 2013.
- [10] G. Burkard, M. J. Gullans, X. Mi, and J. R. Petta, "Superconductor–semiconductor hybrid-circuit quantum electrodynamics," *Nat. Rev. Phys.*, vol. 2, pp. 129–140, Mar. 2020.
- [11] L. Trifunovic, O. Dial, M. Trif, J. R. Wootton, R. Abebe, A. Yacoby, and D. Loss, "Long-Distance Spin-Spin Coupling via Floating Gates," *Phys. Rev. X*, vol. 2, p. 011006, Jan. 2012.
- [12] R. M. Lutchyn, J. D. Sau, and S. Das Sarma, "Majorana Fermions and a Topological Phase Transition in Semiconductor-Superconductor Heterostructures," *Phys. Rev. Lett.*, vol. 105, p. 077001, Aug. 2010.
- [13] Y. Oreg, G. Refael, and F. von Oppen, "Helical Liquids and Majorana Bound States in Quantum Wires," *Phys. Rev. Lett.*, vol. 105, p. 177002, Oct. 2010.
- [14] J. Alicea, "Majorana fermions in a tunable semiconductor device," *Phys. Rev. B*, vol. 81, p. 125318, Mar. 2010.
- [15] J. Klinovaja and D. Loss, "Composite Majorana fermion wave functions in nanowires," *Phys. Rev. B*, vol. 86, p. 085408, Aug. 2012.
- [16] A. Y. Kitaev, "Fault-tolerant quantum computation by anyons," *Annals of Physics*, vol. 303, pp. 2–30, Jan. 2003.
- [17] F. Maier, J. Klinovaja, and D. Loss, "Majorana fermions in Ge/Si hole nanowires," *Phys. Rev. B*, vol. 90, p. 195421, Nov. 2014.
- [18] D. V. Bulaev and D. Loss, "Spin Relaxation and Decoherence of Holes in Quantum Dots," *Phys. Rev. Lett.*, vol. 95, p. 076805, Aug. 2005.
- [19] D. V. Bulaev and D. Loss, "Electric Dipole Spin Resonance for Heavy Holes in Quantum Dots," *Phys. Rev. Lett.*, vol. 98, p. 097202, Feb. 2007.
- [20] C. Kloeffer, M. Trif, and D. Loss, "Strong spin-orbit interaction and helical hole states in Ge/Si nanowires," *Phys. Rev. B*, vol. 84, p. 195314, Nov. 2011.

- [21] C. Kloeffel, M. J. Rančić, and D. Loss, "Direct Rashba spin-orbit interaction in Si and Ge nanowires with different growth directions," *Phys. Rev. B*, vol. 97, p. 235422, June 2018.
- [22] H. Watzinger, J. Kukučka, L. Vukušić, F. Gao, T. Wang, F. Schäffler, J.-J. Zhang, and G. Katsaros, "A germanium hole spin qubit," *Nat. Commun.*, vol. 9, p. 3902, Sept. 2018.
- [23] N. W. Hendrickx, D. P. Franke, A. Sammak, G. Scappucci, and M. Veldhorst, "Fast two-qubit logic with holes in germanium," *Nature*, vol. 577, pp. 487–491, Jan. 2020.
- [24] N. W. Hendrickx, W. I. L. Lawrie, L. Petit, A. Sammak, G. Scappucci, and M. Veldhorst, "A single-hole spin qubit," *ArXiv191210426 Cond-Mat*, Dec. 2019.
- [25] J. Yoneda, T. Otsuka, T. Nakajima, T. Takakura, T. Obata, M. Pioro-Ladrière, H. Lu, C. J. Palmstrøm, A. C. Gossard, and S. Tarucha, "Fast Electrical Control of Single Electron Spins in Quantum Dots with Vanishing Influence from Nuclear Spins," *Phys. Rev. Lett.*, vol. 113, p. 267601, Dec. 2014.
- [26] J. Yoneda, K. Takeda, T. Otsuka, T. Nakajima, M. R. Delbecq, G. Allison, T. Honda, T. Koder, S. Oda, Y. Hoshi, N. Usami, K. M. Itoh, and S. Tarucha, "A quantum-dot spin qubit with coherence limited by charge noise and fidelity higher than 99.9%," *Nat. Nanotechnol.*, vol. 13, p. 102, Feb. 2018.
- [27] F. Maier, C. Kloeffel, and D. Loss, "Tunable  $g$  factor and phonon-mediated hole spin relaxation in Ge/Si nanowire quantum dots," *Phys. Rev. B*, vol. 87, p. 161305, Apr. 2013.
- [28] M. Brauns, J. Ridderbos, A. Li, E. P. A. M. Bakkers, and F. A. Zwanenburg, "Electric-field dependent  $g$ -factor anisotropy in Ge-Si core-shell nanowire quantum dots," *Phys. Rev. B*, vol. 93, p. 121408, Mar. 2016.
- [29] J. Fischer, W. A. Coish, D. V. Bulaev, and D. Loss, "Spin decoherence of a heavy hole coupled to nuclear spins in a quantum dot," *Phys. Rev. B*, vol. 78, p. 155329, Oct. 2008.
- [30] C. H. Yang, A. Rossi, R. Ruskov, N. S. Lai, F. A. Mohiyaddin, S. Lee, C. Tahan, G. Klimeck, A. Morello, and A. S. Dzurak, "Spin-valley

- lifetimes in a silicon quantum dot with tunable valley splitting," *Nat. Commun.*, vol. 4, pp. 1–8, June 2013.
- [31] F. N. M. Froning, M. K. Rehmann, J. Ridderbos, M. Brauns, F. A. Zwanenburg, A. Li, E. P. a. M. Bakkers, D. M. Zumbühl, and F. R. Braakman, "Single, double, and triple quantum dots in Ge/Si nanowires," *Appl. Phys. Lett.*, vol. 113, p. 073102, Aug. 2018.
  - [32] M. Brauns, J. Ridderbos, A. Li, W. G. van der Wiel, E. P. A. M. Bakkers, and F. A. Zwanenburg, "Highly tuneable hole quantum dots in Ge-Si core-shell nanowires," *Appl. Phys. Lett.*, vol. 109, p. 143113, Oct. 2016.
  - [33] K. Ono, D. G. Austing, Y. Tokura, and S. Tarucha, "Current Rectification by Pauli Exclusion in a Weakly Coupled Double Quantum Dot System," *Science*, vol. 297, pp. 1313–1317, Aug. 2002.
  - [34] F. H. L. Koppens, J. A. Folk, J. M. Elzerman, R. Hanson, L. H. W. van Beveren, I. T. Vink, H. P. Tranitz, W. Wegscheider, L. P. Kouwenhoven, and L. M. K. Vandersypen, "Control and Detection of Singlet-Triplet Mixing in a Random Nuclear Field," *Science*, vol. 309, pp. 1346–1350, Aug. 2005.
  - [35] S. Nadj-Perge, S. M. Frolov, J. W. W. van Tilburg, J. Danon, Y. V. Nazarov, R. Algra, E. P. A. M. Bakkers, and L. P. Kouwenhoven, "Disentangling the effects of spin-orbit and hyperfine interactions on spin blockade," *Phys. Rev. B*, vol. 81, p. 201305, May 2010.
  - [36] M. Brauns, J. Ridderbos, A. Li, E. P. A. M. Bakkers, W. G. van der Wiel, and F. A. Zwanenburg, "Anisotropic Pauli spin blockade in hole quantum dots," *Phys. Rev. B*, vol. 94, p. 041411, July 2016.
  - [37] A. Zarassi, Z. Su, J. Danon, J. Schwenderling, M. Hocevar, B. M. Nguyen, J. Yoo, S. A. Dayeh, and S. M. Frolov, "Magnetic field evolution of spin blockade in Ge/Si nanowire double quantum dots," *Phys. Rev. B*, vol. 95, p. 155416, Apr. 2017.
  - [38] M. Trif, V. N. Golovach, and D. Loss, "Spin dynamics in InAs nanowire quantum dots coupled to a transmission line," *Phys. Rev. B*, vol. 77, p. 045434, Jan. 2008.
  - [39] O. Dmytruk, D. Chevallier, D. Loss, and J. Klinovaja, "Renormalization of the quantum dot  $g$ -factor in superconducting Rashba nanowires," *Phys. Rev. B*, vol. 98, p. 165403, Oct. 2018.



- [40] W. Lu, J. Xiang, B. P. Timko, Y. Wu, and C. M. Lieber, "One-dimensional hole gas in germanium/silicon nanowire heterostructures," *PNAS*, vol. 102, pp. 10046–10051, July 2005.
- [41] J. Danon and Y. V. Nazarov, "Pauli spin blockade in the presence of strong spin-orbit coupling," *Phys. Rev. B*, vol. 80, p. 041301, July 2009.
- [42] F. Qassemi, W. A. Coish, and F. K. Wilhelm, "Stationary and Transient Leakage Current in the Pauli Spin Blockade," *Phys. Rev. Lett.*, vol. 102, p. 176806, Apr. 2009.
- [43] W. A. Coish and F. Qassemi, "Leakage-current line shapes from inelastic cotunneling in the Pauli spin blockade regime," *Phys. Rev. B*, vol. 84, p. 245407, Dec. 2011.
- [44] D. E. F. Biesinger, C. P. Scheller, B. Braunecker, J. Zimmerman, A. C. Gossard, and D. M. Zumbühl, "Intrinsic Metastabilities in the Charge Configuration of a Double Quantum Dot," *Phys. Rev. Lett.*, vol. 115, p. 106804, Sept. 2015.
- [45] R. Li, F. E. Hudson, A. S. Dzurak, and A. R. Hamilton, "Pauli Spin Blockade of Heavy Holes in a Silicon Double Quantum Dot," *Nano Lett.*, vol. 15, pp. 7314–7318, Nov. 2015.
- [46] V. N. Golovach, A. Khaetskii, and D. Loss, "Spin relaxation at the singlet-triplet crossing in a quantum dot," *Phys. Rev. B*, vol. 77, p. 045328, Jan. 2008.
- [47] L. R. Schreiber, F. R. Braakman, T. Meunier, V. Calado, J. Danon, J. M. Taylor, W. Wegscheider, and L. M. K. Vandersypen, "Coupling artificial molecular spin states by photon-assisted tunnelling," *Nat. Commun.*, vol. 2, p. 556, Nov. 2011.
- [48] F. R. Braakman, J. Danon, L. R. Schreiber, W. Wegscheider, and L. M. K. Vandersypen, "Dynamics of spin-flip photon-assisted tunneling," *Phys. Rev. B*, vol. 89, p. 075417, Feb. 2014.
- [49] O. N. Jouravlev and Y. V. Nazarov, "Electron Transport in a Double Quantum Dot Governed by a Nuclear Magnetic Field," *Phys. Rev. Lett.*, vol. 96, p. 176804, May 2006.

- [50] D. Stepanenko, M. Rudner, B. I. Halperin, and D. Loss, "Singlet-triplet splitting in double quantum dots due to spin-orbit and hyperfine interactions," *Phys. Rev. B*, vol. 85, p. 075416, Feb. 2012.
- [51] W. G. van der Wiel, S. De Franceschi, J. M. Elzerman, T. Fujisawa, S. Tarucha, and L. P. Kouwenhoven, "Electron transport through double quantum dots," *Rev. Mod. Phys.*, vol. 75, pp. 1–22, Dec. 2002.
- [52] Y. V. Nazarov, "Quantum interference, tunnel junctions and resonant tunneling interferometer," *Physica B: Condensed Matter*, vol. 189, pp. 57–69, June 1993.
- [53] T. H. Stoof and Y. V. Nazarov, "Time-dependent resonant tunneling via two discrete states," *Phys. Rev. B*, vol. 53, pp. 1050–1053, Jan. 1996.
- [54] L. S. Levitov and E. I. Rashba, "Dynamical spin-electric coupling in a quantum dot," *Phys. Rev. B*, vol. 67, p. 115324, Mar. 2003.

# CHAPTER 5

## Fully tunable spin-orbit interaction in Si FinFETs

*Adapted from:*

Stefano Bosco, Bence Hetényi, and Daniel Loss

*“Hole Spin Qubits in Si FinFETs With Fully Tunable Spin-Orbit Coupling and Sweet Spots for Charge Noise”,*

PRX Quantum 2, 010348 (2021)

The strong spin-orbit coupling in hole spin qubits enables fast and electrically tunable gates, but at the same time enhances the susceptibility of the qubit to charge noise. Suppressing this noise is a significant challenge in semiconductor quantum computing. Here, we show theoretically that hole Si FinFETs are not only very compatible with modern CMOS technology, but they present operational sweet spots where the charge noise is completely removed. The presence of these sweet spots is a result of the interplay between the anisotropy of the material and the triangular shape of the FinFET cross-section, and it does not require an extreme fine-tuning of the electrostatics of the device. We present how the sweet spots appear in FinFETs grown along different crystallographic axes and we study in detail how the behaviour of these devices change when the cross-section area and aspect ratio are varied. We identify designs that maximize the qubit performance and could pave the way towards a scalable spin-based quantum computer.

## 5.1 Introduction

Strong spin-orbit coupling [1] is a desirable ingredient to build a scalable spin-based quantum computer [2,3], enabling fast and fully electrical manipulations of quantum bits [4–6]. Promising platforms to reach large values of spin-orbit interactions are  $p$ -doped semiconductor nanowires, where the charge carriers are holes rather than electrons [7–14]. When holes are strongly confined in two directions, an externally tunable electric field generates a large effective spin-orbit field [15, 16] that results in ultrafast Rabi frequencies, larger than 400 MHz [17, 18], and in spin-orbit lengths of tens of nanometers [19–25], shorter than typical interdot distances. The regime of strong coupling between spins and photons in microwave resonators [26, 27] has been predicted in these systems [28], which could enable long-range coupling between distant qubits. Because of the large spin-orbit interaction, hole-superconductor heterostructures have attracted also much interest as platforms to detect and manipulate Majorana bound states [29–31].

On the other hand, large interactions between spin and charge degrees of freedom render the system strongly susceptible to charge noise, reducing the qubit lifetime [17, 32–34]. Efforts to find operational sweet spots where charge noise is reduced have been focusing on planar Ge qubits [35] or considering single atoms [36], as well as artificial spin-orbit fields [37]. The appearance of sweet spots depending on the direction of the applied magnetic field has also been analyzed [38, 39]. At the working points identified in these studies, the spin-orbit interaction is not susceptible to small fluctuations of the electric field, but remains finite. However, in electrostatically defined quantum dots in hole nanowires, there are additional noise channels that are not suppressed at these working points. For example, because of the large value of the spin-orbit coupling, the fluctuations of the size of the dot strongly couple to the spin and lead to decoherence. To remove charge noise in these systems, one needs the ability to on-demand fully switch *ON* and *OFF* the spin-orbit interactions depending on whether the qubit is operational or idle.

We find that such a spin-orbit switch naturally occurs in  $p$ -doped Silicon Fin Field Effect Transistors (FinFETs) [40–43], thus making these devices ideal candidates to reliably store quantum information. Silicon is highly compatible with modern semiconductor industry and is one of the frontrunner materials for scalable large scale quantum computers. State-of-the-art electron Si qubits can operate reliably at temperatures higher

than 1 K [44, 45], and high fidelity two-qubit gates [46–50], as well as singlet-triplet qubit operations [51], control over higher spin states [52] and scalable readout schemes [53–57] have been demonstrated in Si. In addition, Si offers the unique possibility to drastically reduce the hyperfine noise [58–64] by isotopic purification [65, 66], resulting in spin qubits whose performances are essentially limited only by the charge noise [32].

The tunability of the spin-orbit coupling by varying the electric field is a well-known feature of semiconductor nanowires [9, 11], but in many typical geometries, such as wires with rectangular [16, 67, 68] or circular cross-sections [15, 17, 24, 28], the spin-orbit interaction is only fully removed when there is no external electric field. While working without a DC electric field can be possible for etched [69] or self-assembled [70] quantum dots, in electrostatically defined nanostructures, an external gate potential is required to delimit the dot. Consequently, the electric field cannot be easily set to zero, resulting in a residual spin-orbit interaction, which degrades the qubit performance. In contrast, a crucial feature of the Si FinFETs studied here is their nearly triangular cross-section, which results in sweet spots where the spin-orbit coupling can be switched off at finite values of the electric field, thus removing the charge noise. In fact, we show that holes confined in triangular wires present a large spin-orbit coupling even without electric fields and, depending on the design of the fin, an external gate potential can suppress this intrinsic coupling.

The present paper is organized as follows. In Sec. 5.2, we introduce different state-of-the-art FinFET designs [40–43], including Silicon-on-Insulator (SOI) FinFETs and bulk Si FinFETs, and we discuss the theoretical model used in our analysis.

In Sec. 5.3, we consider an ideal fin with an equilateral triangular cross-section and study the long wavelength dynamics of the holes confined there. Because Si is an anisotropic semiconductor [1], we pay particular attention to how different growth directions affect the effective spin-orbit interactions [16, 71–73]. By using a simple theoretical model, which only includes heavy and light holes, and by considering realistic inhomogeneous electric field profiles, we identify qualitatively distinct mechanisms that remove the spin-orbit coupling and that are suitable for different device designs. Here, we also comment on the effect of a possible moderate strain on the spin-orbit switch.

In Sec. 5.4, we extend the theoretical model of the FinFET by including the spin-orbit split-off hole band (SOHs). This band is energetically separated from heavy and light holes by the bulk Si spin-orbit gap [1],

but it strongly influences the hole behaviour in small wires and we find that it can even remove the spin-orbit sweet spot in wires with a triangular cross-section of side shorter than 35 nm. Fortunately, we find that a more careful device design can counteract the action of the SOHs and we discuss a possible way of recovering the sweet spot.

Finally, in Sec. 5.5, we study the charge noise of spin 1/2 qubits [2] in Si FinFETs. We find that working close to the spin-orbit sweet spot drastically suppresses the influence of charge noise on the qubit lifetime, and strongly improves the dephasing time. By including in our analysis the fluctuations of the  $g$ -factor as a function of the electric field, a charge noise mechanism that is not directly related to the effective spin-orbit coupling of the wire, the exact position of the sweet spot is slightly shifted, but the charge noise can still be exactly cancelled, resulting in a system fully resilient against small charge fluctuations.

## 5.2 Theoretical Model

In this paper, we analyze the hole Si FinFET sketched in Fig. 5.1. The fin extends in the  $z$ -direction and it defines a nanowire with an isosceles triangular cross-section with equal sides  $L_y$  and base  $L_x$ . We study two different FinFET designs: Silicon-on-Insulator and bulk FinFETs. In SOI FinFETs, the triangular fin lies on top of a dielectric material, while in bulk FinFETs, it lies on top of a Si substrate. The apex of the fin is covered by a dielectric with an ideal metallic gate placed on top. The top gate is fixed at a potential  $V_g$  measured with respect to a back-gate at a distance  $d_B$  from the bottom of the wire. In bulk FinFET, a negative gate potential  $V_g$  is required to localize the hole wavefunction inside the fin, while in SOI FinFETs, the holes are confined in the wire by the dielectric and  $V_g$  can attain positive values, too.

The dynamics of this system is accurately described by the Hamiltonian

$$H = H_{\text{LK}} + V_{\text{HW}}(x, y) + V_E(x, y) , \quad (5.1)$$

which comprises the hole kinetic energy  $H_{\text{LK}}$  and two distinct potential energies  $V_{\text{HW}}$  and  $V_E$ .

The potential  $V_{\text{HW}}$  captures the abrupt interfaces between the semiconductor and the dielectric and because of the large energy gap between the materials, we model it by requiring the wavefunction to vanish at the edges of the system (hard-wall boundary conditions). In contrast,  $V_E$  describes the smoother and externally tunable electrostatic po-

tential generated by  $V_g$ . In the cross-section of the wire, this term is well-approximated by the multipole expansion

$$V_E(x, y) = -e\mathbf{E} \cdot \mathbf{r} - \frac{e}{2}\mathbf{r} \cdot \underline{\delta E} \cdot \mathbf{r}, \quad (5.2)$$

that includes a homogeneous electric field vector  $\mathbf{E} = (E_x, E_y)$  and a tensor modelling the inhomogeneous component of the electric field  $(\underline{\delta E})_{ij}$ . The coordinate system  $\mathbf{r} = (x, y)$  is centred in the center of mass of the wire. Importantly, both the homogeneous and inhomogeneous components of the electric field depend linearly on the external gate potential  $V_g$  and their strength can be tuned by the gate design. More details on this approximation and a thorough discussion on the values of  $E_i$  and  $\delta E_{ij}$  in the FinFETs analyzed in this paper can be found in App. 5.A.

A precise description of the kinetic energy of the holes in the valence bands of semiconductors is provided by the  $4 \times 4$  Luttinger-Kohn (LK) Hamiltonian [1, 74]

$$H'_{\text{LK}} = \left( \gamma_1 + \frac{5}{2}\gamma_2 \right) \frac{p'^2}{2m} - \frac{\gamma_2}{m} \mathbf{p}'^2 \cdot \mathbf{J}'^2 - \frac{2\gamma_3}{m} p'_i p'_j \{J'_i, J'_j\} + \text{cp}, \quad (5.3)$$

which describes the mixing of heavy holes (HHs) and light holes (LHs) with spin  $3/2$  and  $1/2$ , respectively. Here,  $m$  is the bare electron mass, we use the anticommutator  $\{A, B\} = (AB + BA)/2$ , and cp stands for cyclic permutations. Also, we defined  $p'^2 = p_x'^2 + p_y'^2 + p_z'^2$  and the vectors  $\mathbf{p}'^2 = (p_x'^2, p_y'^2, p_z'^2)$  and  $\mathbf{J}'^2 = (J_x'^2, J_y'^2, J_z'^2)$ , where  $p'_i = -i\hbar\partial_{i'}$  are canonical momenta and the four-dimensional matrices  $J'_i$  are spin  $3/2$  matrices. The primed coordinate system is aligned to the main crystallographic axes, i.e.  $x' \parallel [100]$ ,  $y' \parallel [010]$  and  $z' \parallel [001]$ .

The LK Hamiltonian is parametrized by three material-dependent dimensionless quantities:  $\gamma_{1,2,3}$ . Here, we use the values of  $\gamma_i$  given in Ref. [1]. Si is an anisotropic semiconductor because the parameters  $\gamma_2$  and  $\gamma_3$  are quite different. As a consequence, the low-energy description of the system strongly depends on the orientation of the nanowire with respect to the crystallographic axes [16, 71–73]. In our convention, the nanowire always extends along the  $z$ -direction, and to conveniently account for different growth directions, we transform the LK Hamiltonian as  $H'_{\text{LK}} \rightarrow H_{\text{LK}}$  by performing a rotation of an angle  $\theta$  around the  $y' \parallel [010]$  crystallographic axis and a subsequent rotation of an angle  $\varphi$  around the rotated  $z'$  axis, see Fig. 5.1. This transformation aligns the coordinate system and the spin-matrices to the axes  $(x, y, z)$  in the figure;

the Hamiltonian  $H_{\text{LK}}$  and the relation between the primed and unprimed coordinates are given explicitly in Eqs. (5.30) and (5.31), respectively.

The most relevant orientations of the wire for this paper are summarized in Fig. 5.1b). In particular, it is instructive to study the behaviour of wires where the coordinate system is aligned to the crystallographic axes, and of wires grown along the  $[110]$  direction, as standardly done in experiments [22, 41–43, 67]. We also consider the growth direction that maximizes the direct Rashba spin-orbit interactions in inversion symmetric Silicon nanowires [16] and quantum dots [71]. We will refer to these orientations as to Crystallographic Axes (CA), Standard Axes (SA), and Direct Rashba Axes (DRA), respectively.

The  $4 \times 4$  LK Hamiltonian in Eq. (5.3) captures accurately the physics of Si nanowires with large cross-sections, however, to describe smaller wires one needs to include the contribution of the spin  $1/2$  spin-orbit split-off holes (SOHs), that are gapped from the HHs and LHs by a material-dependent spin-orbit energy  $\Delta_0$ . The SOHs are negligible only when  $\Delta_0$  is much larger than the confinement energy, such that the HH-LH subspace is well-separated in energy from the subspace of the SOHs. In Silicon, the gap  $\Delta_0 \approx 44.1$  meV [1], is comparable to the confinement energy in narrow wires, leading to a strong influence of the SOHs on the response, especially in the presence of an electric field. To take the SOHs fully into account, we compare our results obtained with the  $4 \times 4$  Hamiltonian (5.3) to more accurate results obtained with the  $6 \times 6$  extension of the LK Hamiltonian, the complete form of which can be found for example in Appendix C of Ref. [1]. The conduction electrons are separated by a much larger gap from the holes, and so their contribution is always neglected in the present analysis.

Without magnetic field, the eigenvalues of the Hamiltonian in Eq. (5.1) are doubly-degenerate Kramers partners. When the wavelength of the hole wavefunction along the nanowire is larger than the confinement length in the cross-section, the low-energy physics of the system is well described by an effective nanowire Hamiltonian  $H_{\text{NW}}$  that only acts on the lowest pair of eigenstates. To second order in the momentum  $p_z$  along the wire, we obtain

$$H_{\text{NW}} = \frac{p_z^2}{2m^*} + \mathbf{v} \cdot \boldsymbol{\sigma} p_z, \quad (5.4)$$

where  $\boldsymbol{\sigma}$  is a vector of Pauli matrices acting on the subspace of the lowest Kramers partners. The nanowire Hamiltonian is parametrized by an effective mass  $m^*$  and a spin-orbit velocity vector  $\mathbf{v}$  that can be found



in perturbation theory. In particular, one can decompose  $H$  into powers of  $p_z$  as  $H = H_0 + H_1 p_z + H_2 p_z^2$ , with  $H_0 = H_{\text{LK}}(p_z = 0) + V_{\text{HW}}(x, y) + V_E(x, y)$ , and introduce the unitary matrix  $M_E$  that diagonalizes  $H_0$ , i.e.  $(M_E^\dagger H_0 M_E)_{nm} = \epsilon_E^n \delta_{nm}$ . To obtain accurate results, we compute the eigenvectors  $M_E$  and the eigenenergies  $\epsilon_E$  numerically by discretizing the Hamiltonian  $H_0$ . By standard perturbation theory, it is straightforward to find

$$(\mathbf{v} \cdot \boldsymbol{\sigma})_{ij} = (M_E^\dagger H_1 M_E)_{ij}, \quad (5.5)$$

where  $i, j$  only act on the lowest pair of Kramers partners; a similar perturbative expression for the effective mass is given in Eq. (5.36). The subscript  $E$  in the eigensystem  $M_E$  and  $\epsilon_E$  emphasizes the dependence on the electric field. For this reason, the effective parameters of the wire Hamiltonian are externally tunable by the gate potential  $V_g$ , which controls the electrostatic potential  $V_E(x, y)$ . We also introduce the spin-orbit length

$$l_{so} = \frac{\hbar}{m^* |\mathbf{v}|}, \quad (5.6)$$

that characterizes the spin-orbit interactions relative to the inertia of the particle.

To define a spin qubit, we include an external, homogeneous magnetic field  $\mathbf{B}$ . For weak values of the magnetic field, typically below one Tesla, we can safely neglect the orbital contribution of the magnetic field and only focus on the coupling of the magnetic field to the spin-degree of freedom via the Zeeman energy, which in the  $4 \times 4$  Luttinger-Kohn Hamiltonian is  $H_Z = 2\mathbf{B} \cdot (\kappa \mathbf{J} + q \mathbf{J}^3)$ . Here,  $\kappa$  and  $q$  are material-dependent parameters for the magnetic interactions. The magnetic interactions when SOHs are included, as well as the precise value of  $\kappa$  and  $q$  for Si, can be found in Ref. [1]. Projecting the Zeeman Hamiltonian onto the groundstate of the wire, to linear order in  $B$ , the effective Hamiltonian in Eq. (5.4) acquires the correction

$$H_{\text{NW}}^Z = \frac{1}{2} \boldsymbol{\Delta} \cdot \boldsymbol{\sigma}, \quad (5.7)$$

where we introduce the vector  $\boldsymbol{\Delta} = \mu_B \underline{g} \cdot \mathbf{B}$ . Here,  $\mu_B$  is the Bohr magneton and  $\underline{g}$  is a dimensionless  $3 \times 3$  matrix of  $g$ -factors. From perturbation theory, we obtain the electric field dependent Zeeman interactions

$$(\boldsymbol{\Delta} \cdot \boldsymbol{\sigma})_{ij} = 2 (M_E^\dagger H_Z M_E)_{ij}. \quad (5.8)$$

### 5.3 Equilateral FinFETs

To have a simple model of FinFETs, we consider first a nanowire with a triangular cross-section and we require that the hole wavefunction vanishes at the boundaries of the triangle, see Fig. 5.1. This model provides an accurate description of SOI FinFETs, but it is questionable in bulk Si FinFETs, where there is no sharp interface at the bottom of the fin and the wavefunction can leak into the bulk. In this case, however, the hard-wall approximation still provides a good qualitative understanding of the system, especially when the hole wavefunction is strongly confined inside the fin by a large negative gate potential  $V_g$ . The effect of the substrate in a bulk Si FinFET is discussed in App. 5.F.

The choice of a triangular fin is crucial in our analysis. In fact, compared to rectangular or circular nanowires, a triangular cross-section lacks inversion symmetry in the  $(x, y)$  plane, i.e.  $V_{\text{HW}}(x, y) \neq V_{\text{HW}}(-x, -y)$ , and consequently the triangular nanowire can present large intrinsic spin-orbit interactions without external homogeneous electric fields, i.e.  $v_0 \equiv v(\mathbf{E} = 0) \neq 0$ <sup>1</sup>.

In this section, we examine how the spin-orbit interaction varies as a function of the gate potential and of the growth direction in an ideal case, where the cross-section is an equilateral triangle of side  $L$ . In Si FinFETs, the triangular cross-section can be made rather equilateral, see e.g. [42, 43], however it is often the case that the fin is a more narrow [41] or wide [22] isosceles triangle. The spin-orbit coupling in isosceles triangles with different aspect ratios is analyzed in Sec. 5.4.

A convenient orthonormal basis to describe this system comprises the eigenfunctions of the two-dimensional Laplace operator  $p_x^2 + p_y^2$  vanishing at the boundary of an equilateral triangle. Because of the highly symmetric geometry, the eigenfunctions can be expressed in terms of trigonometric functions, see App. 5.B [in particular Eq. (5.27)] and Ref. [75] for more

<sup>1</sup>If  $\mathbf{E} = 0$  and the cross-section is inversion symmetric, then  $V(x, y) \equiv V_{\text{HW}}(x, y) + V_E(x, y) = \mathcal{I}V(x, y)\mathcal{I}^\dagger = V(-x, -y)$ , where  $\mathcal{I} = e^{-i\pi F_z}$  is the inversion operator in the  $(x, y)$  plane;  $F_z$  is the component parallel to the wire of the total angular momentum. It follows that the ground subspace of  $H_{\text{LK}}(p_z = 0) + V(x, y)$  can be labelled by  $|i, \uparrow\downarrow\rangle$  and is composed of a degenerate Kramers doublet  $|\uparrow\downarrow\rangle$  that is also an eigenstate of  $\mathcal{I}$  to eigenvalue  $i$ . Let us consider the correction to the LK Hamiltonian  $H_1 p_z$  to linear order in  $p_z$ , such that the states  $|i, \uparrow\downarrow\rangle$  are still approximate eigenstates. Because  $H_1$  anticommutes with  $\mathcal{I}$ , i.e.  $\mathcal{I}H_1\mathcal{I}^\dagger = -H_1$ ,  $H_1$  is a block off-diagonal matrix in the basis of the eigenstates of  $\mathcal{I}$ . Consequently, in the groundstate subspace there cannot be spin-orbit interactions linear in  $p_z$  and because time-reversal symmetry prohibits different masses for the Kramers partners, the first possible spin-orbit interactions are  $\propto p_z^3$ .

details. A natural energy scale for this problem is the confinement energy

$$\epsilon_c = \frac{16\hbar^2\pi^2}{3mL^2}\gamma_1, \quad (5.9)$$

which characterizes the energy gap between different orbital states, see Eq. (5.29). This energy is quite large, for example in a Silicon wire with side  $L = 35$  nm, the quantization energy is  $\epsilon_c \approx 14$  meV, approximately 30% of the gap to the split-off band  $\Delta_0 \approx 44.1$  meV [1]. While for  $L \gtrsim 35$  nm, the  $4 \times 4$  LK Hamiltonian in Eq. (5.3) is valid, in smaller wires such a strong quantization results in a large contribution of the SOHs, which demands a more detailed analysis that fully includes these states. In the following, we will refer to small (large) wires when the side  $L$  is smaller (larger) than 35 nm. To gain a qualitative understanding of the system, we begin our analysis by studying large nanowires by using the  $4 \times 4$  LK Hamiltonian; a detailed analysis of the effect of the SOHs is postponed to Sec. 5.4.

We first compute the intrinsic spin-orbit velocity  $\mathbf{v}_0$  in the absence of electric fields, focusing on its dependence on the growth direction. Then, we separately describe the effect of homogeneous and inhomogeneous electric fields. We discuss when the electric field-induced spin-orbit coupling compensates for the intrinsic spin-orbit interactions, yielding convenient operational sweet spots where spin-orbit effects vanish.

### Intrinsic spin-orbit velocity

Without external fields, a simple yet satisfactory description of the system is provided by a reduced 12 dimensional Hamiltonian  $H_{12}$  that includes only the lowest three orbital states in Eq. (5.27).  $H_{12}$  parametrically depends on the growth orientation via the angles  $\varphi$  and  $\theta$ , see Fig. 5.1, and its general expression can be obtained by combining Eqs. (5.34) and (5.33); when  $\theta = 0$ ,  $H_{12}$  is explicitly given in Eq. (5.39). By using a second order Schrieffer-Wolff transformation [1,76] on  $H_{12}$ , the intrinsic spin-orbit velocity  $\mathbf{v}_0$  can be written as

$$\mathbf{v}_0 = \frac{\hbar}{mL}(\gamma_3 - \gamma_2) \boldsymbol{\alpha}_0(\theta, \varphi), \quad (5.10)$$

where  $\boldsymbol{\alpha}_0(\theta, \varphi)$  is a dimensionless three-dimensional vector that characterizes strength and direction of the spin-orbit field and depends on the growth direction and on the Luttinger parameters. Importantly, for an

$a_1$	$a_2$	$a_3$	$b_1$	$b_2$
2.468	0.683	0.013	0.298	0.011

Table 5.1: Parameters of the intrinsic spin-orbit vector  $\mathbf{v}_0$  in Eq. (5.11b) when  $\theta = -\pi/2$ . These parameters describe the SA (CA) when  $\varphi = -3\pi/4$  ( $\varphi = 0$ ).

equilateral triangle, the intrinsic spin-orbit interaction is a result of the anisotropy of the semiconductor and it vanishes when  $\gamma_2 = \gamma_3$ . For this reason, materials such as Silicon, where the anisotropy is large, are a convenient choice to study this effect.

The general dependence of these quantities on the growth directions in Silicon is discussed in App. 5.C, see, in particular, Fig. 5.12. From the analysis, we observe that the maximal value of  $|\mathbf{v}_0| \approx 2.91\hbar/(mL)$  is reached when the wire extends along one of the crystallographic axes, i.e. when  $z \parallel [100]$ ,  $[010]$ , or  $[001]$ . In this case, there is no spin-orbit coupling in the direction of the wire, i.e.  $(\mathbf{v}_0)_z = 0$ , and we define the complex quantity  $\alpha_0(\theta) = (\boldsymbol{\alpha}_0)_x(\theta, \varphi) + i(\boldsymbol{\alpha}_0)_y(\theta, \varphi)$ , where to simplify the notation we suppress the explicit dependence of  $\alpha_0(\theta)$  on  $\varphi$ . In particular, we find

$$\alpha_0(0) = 9.34 \frac{\gamma_3}{\gamma_1 + (5/2)\gamma_2} e^{-4i\varphi} \approx 2.631 e^{-4i\varphi}, \quad (5.11a)$$

$$\alpha_0\left(\frac{\pi}{2}\right) = \frac{a_1 - a_2 \cos(4\varphi) + a_3 (\gamma_3 - \gamma_2) \cos(8\varphi)}{1 - b_1 (\gamma_3 - \gamma_2) \cos(4\varphi) + b_2 (\gamma_3 - \gamma_2)^2 \cos(8\varphi)}, \quad (5.11b)$$

where  $a_i$  and  $b_i$  are real functions of the Luttinger parameters, whose values for Silicon are shown in Table 5.1. The numerical value 2.631 in Eq. (5.11a) is obtained by using the Luttinger parameters of Si and describes the CA and the DRA. From Eq. (5.11b), we estimate  $\alpha_0(\frac{\pi}{2}) \approx 2.354$  at  $\varphi = -3\pi/4$ , corresponding to the SA.

A comparison between the perturbative results in Eq. (5.10) and the exact spin-orbit velocity computed numerically by using Eq. (5.5) and a larger number  $N = 200$  of the orbital basis states in Eq. (5.27) is shown in Fig. 5.2. When the elevation angle is  $\theta = 0$ , the wire extends along the  $[001]$  direction, and the spin-orbit vector has a roughly constant amplitude, but as a consequence of the four-fold rotational symmetry of the Luttinger-Kohn Hamiltonian, its direction oscillates as a function of the azimuthal angle  $\varphi$  with period  $\pi/2$ . In contrast, when  $\theta = \pm\pi/2$ , the intrinsic spin-orbit vector has a constant direction ( $\mathbf{v} \parallel \mathbf{e}_x$ ) and an oscillating amplitude that reaches its maximum when the wire is aligned to

the main crystallographic axes  $[100]$  or  $[010]$ . The minimal spin-orbit coupling occurs when the wire extends along the  $[110]$  direction, which corresponds to the standard experimental growth direction (SA), see Fig. 5.1b). We note that while Eq. (5.11a) agrees well with the numerically computed spin-orbit coupling, Eq. (5.11b) captures the periodic oscillations but overestimates absolute value of the intrinsic coupling at the SA.

The dependence of the effective mass and of the spin-orbit length on the growth direction can also be straightforwardly obtained, and a detailed analysis of these quantities is given in App. 5.C. Importantly, the spin-orbit length defined in Eq. (5.6) is of the order of the side  $L$  of the triangle, which is typically much smaller than the lateral size of the dot, and it reaches the minimal value  $l_{so} \approx 0.83L$  when  $z \parallel [001]$ . Consequently, we expect hole Si FinFETs to show effects due to large spin-orbit interaction such as renormalization of the  $g$ -factor [10, 21, 24, 25, 67, 68] and ultrafast Rabi oscillations [17].

## Homogeneous electric field

We now analyze the effect of the electrostatic potential  $V_E$  in Eq. (5.2) on the spin-orbit velocity. For Si wires, there are two distinct mechanisms that suppress the spin-orbit interactions and eventually remove them entirely. These mechanisms are the application of a homogeneous electric field  $E_y$  pointing along the  $y$  direction and the application of inhomogeneous electric fields  $\delta E_{xx}$  and  $\delta E_{yy}$  that harmonically confine the wavefunction inside the fin. Both these fields are controllable by the external potential, and their strengths strongly depend on the gate design, see App. 5.A for a more detailed analysis.

Let us first consider the effect of homogeneous electric fields, which models setups where the non-linearities of the fields are suppressed. In realistic devices the top gate covers the wire rather symmetrically with respect to the  $y$ -direction. For this reason, the homogeneous electric field  $E_x$  in the  $x$ -direction is zero and we will neglect it in the present analysis<sup>2</sup>.

In Fig. 5.3, we show the results of a numerical analysis showing the dependence of the spin-orbit velocity on the dipole energy  $eE_y L$  for the

---

<sup>2</sup>The results presented in Sec. 5.3 are qualitatively valid even in the presence of asymmetries that lead to a finite  $E_x$ . In particular, we find that the value of the spin-orbit velocity at  $E_y = 0$  is increased by  $E_x$  and consequently the spin-orbit switch is pushed to higher values of  $E_y$ .

growth directions given in Fig. 5.1b). These results are obtained by projecting the Hamiltonian (5.1) onto the first 200 orbital states in Eq. (5.27) and using Eq. (5.5). We observe that the electric field strongly influences the spin-orbit field and it can increase it or decrease it depending on the orientation of the wire. In particular, for the DRA and the SA, the spin-orbit field can be exactly switched off when the dipole energy  $eE_yL$  becomes comparable to the confinement energy  $\epsilon_c$ . More precisely, the spin-orbit switch occurs at

$$E_{\text{DRA}}^{\text{SW}} \approx 1.13 \frac{\epsilon_c}{eL} \approx 19.42 \times \frac{10^3 \text{nm}^3}{L^3} \text{V}/\mu\text{m} , \quad (5.12a)$$

$$E_{\text{SA}}^{\text{SW}} \approx -4.3 \frac{\epsilon_c}{eL} \approx -73.9 \times \frac{10^3 \text{nm}^3}{L^3} \text{V}/\mu\text{m} . \quad (5.12b)$$

for the DRA and SA case, respectively. For realistic cross-section with sides of a few tens of nanometers, these electric fields are of the order  $\text{V}/\mu\text{m}$ , easily reachable in state-of-the-art devices. For the DRA, the spin-orbit coupling is removed when the electric field is positive and the holes are pushed to the apex of the fin, while for the SA growth direction, a negative field is required and the holes are pushed to the bottom of the triangle. Consequently, the SA is convenient in SOI FinFETs, where the wire is separated from the substrate by an oxide and the hard-wall boundary condition is a good approximation also at the bottom of the fin. In contrast, the DRA can also be suitable in bulk FinFETs because the large positive electric field confines the hole wavefunction in the fin and suppresses the leakage of the wavefunction into the substrate.

The suppression of the spin-orbit interaction comes from an interplay between the anisotropy of Si and the reduced symmetry of the cross-section. For simplicity, we focus on wires where  $z \parallel [001]$ , i.e.  $\theta = 0$ , and examine the dependence of  $\mathbf{v}$  on  $\varphi$ . In this limit, a reasonable description of the system is provided by the reduced Hamiltonian  $H_{12}$  in Eq. (5.39), which includes the lowest three orbital states given in Eq. (5.27). By applying a fourth order Schrieffer-Wolff transformation to  $H_{12}$ , we find that  $v_z = 0$ , and we can write the complex off-diagonal matrix element of the spin-orbit velocity  $v = (\mathbf{v})_x + i(\mathbf{v})_y$  as the sum of an anisotropic term  $\alpha_A$  and an isotropic direct Rashba-like term  $\alpha_I$ , i.e.

$$v = \frac{\hbar}{mL} \left[ (\gamma_3 - \gamma_2) \alpha_A(\varphi) + (\gamma_3 + \gamma_2) \alpha_I \right] . \quad (5.13)$$

Importantly,  $\alpha_I$  is a real function of  $eE_yL$  and it does not depend on the azimuthal growth angle  $\varphi$ , while  $\alpha_A$  is a complex function of  $eE_yL$  and

oscillates as a function of  $\varphi$ . In particular, for small electric fields and in Silicon we find

$$\alpha_A(\varphi) \approx \alpha_0 - 0.367e^{-4i\varphi} (eE_y L/\epsilon_c)^2, \quad (5.14a)$$

$$\alpha_I \approx 0.35 (eE_y L/\epsilon_c) + 0.246 (eE_y L/\epsilon_c)^2, \quad (5.14b)$$

where  $\alpha_0$  is the zero field result in Eq. (5.11a) and in  $\alpha_A$  we also neglected quantitatively small corrections linear in  $eE_y L/\epsilon_c$  and proportional to different powers of  $e^{-4i\varphi}$ . For the general dependence of these parameters on the Luttinger parameters, see Eq. (5.41). To better convey the importance of the shape of the cross-section, in App. 5.C, we highlight the main differences in the spin-orbit coupling of triangular and square Si wires.

The spin-orbit interaction is fully switched off when  $|\mathbf{v}| = 0$ . From Eq. (5.14), it follows that this cancellation can only occur at the growth angles  $\varphi = \pi(2n + 1)/4$  where  $\alpha_A$  is a real-valued function, and where  $\alpha_0$  has a sign opposite to all the electric field-dependent terms. From Eqs. (5.13) and (5.14), we estimate that the switch in Silicon occurs at  $E_{\text{DRA}}^{\text{SW}} \approx 1.52\epsilon_c/(eL)$ . Note that our perturbative analysis provides good qualitative insights into the switching mechanism, and in addition, the numerical prefactor 1.52 is reasonably close to the prefactor 1.13, derived from the detailed numerical analysis including higher orbital states.

## Inhomogeneous electric field

The electric field profile in a triangular FinFET comprises a large inhomogeneous component that significantly alters the spin-orbit velocity. In this section, we restrict ourselves to the analysis of Si FinFETs where a negative gate potential  $V_g$  is applied, such that the hole wavefunction is pushed to the apex of the triangle.

When the back gate is far from the wire, the inhomogeneous component of the electric field in the cross-section can be well-approximated by a linearly varying electric field parametrized by the tensor  $\delta E_{ij}$ , see Eq. (5.2). As discussed in App. 5.A, in typical devices, the cross-terms  $\delta E_{xy}$  are very small. In contrast, the diagonal components  $\delta E_{xx}$  and the  $\delta E_{yy}$  are large and they vary linearly with the top gate potential  $V_g$ , with slopes that are comparable in absolute value, but have opposite signs. In particular, we estimate  $\delta E_{xx}/\delta E_{yy} \approx -1.01$ , and thus the saddle potential energy

$$V_E(x, y) = e\delta E(y^2 - x^2)/2, \quad (5.15)$$

accurately describes the inhomogeneity of the electric field. Negative values of  $V_g$  correspond to positive values of the parameter  $\delta E$  and so  $V_E(x, y)$  harmonically confines the holes in the  $y$ -direction and pushes their wavefunction to the sides of the triangle in the  $x$ -direction.

We first study separately the effect of the inhomogeneous coupling by setting the homogeneous electric field to zero, i.e.  $E_y = 0$ . We remark that for inversion symmetric cross-sections such as cylindrical or rectangular wires, the potential in Eq. (5.15) does not induce any spin-orbit interactions because  $V_E(x, y) = V_E(-x, -y)$ , and the results obtained in this section are specific for triangular wires.

In Fig. 5.4a), we show the spin-orbit interactions as a function of  $\delta E$  and for the orientations in Fig. 5.1b). We observe a qualitatively similar picture as discussed in Sec. 5.3 for the homogeneous electric field: depending on the growth direction, the spin-orbit velocity varies with  $\delta E$ , and while it increases in the CA and SA, it decreases for the DRA, resulting in an operational sweet spot at

$$\delta E^{SW} \approx 20.5 \frac{\epsilon_c}{eL^2} \approx 35 \times 10^3 \times \frac{10^4 \text{nm}^4}{L^4} \text{V}/\mu\text{m}^2, \quad (5.16)$$

where  $|\mathbf{v}|$  vanishes.

This spin-orbit sweet spot remains present also when non-idealities of the electric fields are included. In App. 5.D, we show that the spin-orbit switch persists in rather general FinFET design, where  $\delta E_{xx} \neq -\delta E_{yy}$ . Also, possible asymmetries of the gate design can lead to a small cross-coupling  $\delta E_{xy}$ . The effect of  $\delta E_{xy}$  on the spin-orbit velocity is shown in the inset of Fig. 5.4a). We find that the spin-orbit switch is removed by including  $\delta E_{xy}$ . However, we expect that in most setups,  $\delta E_{xy}$  remains a few orders of magnitude smaller than  $\delta E$  and thus, at the switch, the spin-orbit velocity is orders of magnitude smaller than the intrinsic velocity  $|\mathbf{v}_0|$ , still providing a good working point where charge noise is strongly reduced.

In realistic devices, the effects of homogeneous and linearly varying electric fields cannot be easily decoupled and thus we now examine how their interplay affects the spin-orbit switch. In App. 5.A, we estimate that in the FinFET shown in Fig. 5.1

$$E_y \approx -0.3 \frac{V_g}{d_B} \approx 0.25 L \delta E. \quad (5.17)$$

While this constraint is strictly valid only for setups with top and back gates, we now explore a much larger parameter space where  $E_y$  and  $\delta E$



are varied independently. Consequently, our results are valid for a broad range of device designs, including for example Si FinFETs with gates placed sequentially along the wire.

In Fig. 5.4b), we show the spin-orbit velocity in a FinFET grown along the DRA as a function of both  $E_y$  and  $\delta E$ . We observe that  $|\mathbf{v}|$  vanishes along a (blue) curve that intersects the (purple) line defining the constraint (5.17) at the point  $(e\delta EL^2, eE_y L) = (7.8\epsilon_c, 1.95\epsilon_c)$ .

The switching-off of the spin-orbit velocity is mostly driven by the homogeneous electric field  $E_y$  and the inhomogeneous potential  $\delta E$  only renormalizes the value of  $E_y$  required to compensate for the intrinsic spin-orbit interaction. Combining with Eq. (5.17), this point corresponds to the potential  $V_g^{SW} = -111.7 \times \text{nm}^2 (d_B/L^3) \text{ V}$  and when  $L = 20 \text{ nm}$  and  $d_B = 100 \text{ nm}$ , one obtains the working point  $V_g^{SW} = -1.4 \text{ V}$ . Perturbative expressions of  $|\mathbf{v}|$  as a function of  $E_y$  and  $\delta E$  can be found by generalizing the treatment discussed in Sec. 5.3 and are given in App. 5.C, see Eq. (5.41).

Another important feature of the spin-orbit switch is its robustness against moderate strain. In semiconductor nanostructures, strain can play a relevant role by renormalizing the response of the system to external fields [77]. In Si wires, strain could be induced for example by nearby metallic gates [78], or by incoherent interfaces between  $\text{SiO}_2$  and Si [79, 80]. The precise strain profile is strongly device dependent and it can be engineered by a careful fabrication process, where details such as choice of the materials [81] and dielectric thickness matter. Instead of focusing on a specific device realization, here we consider a simple strain model where the elements of the strain tensor  $\epsilon_{ij}$  are homogeneous in the fin. By using the Bir-Pikus Hamiltonian [1, 82], we estimate that the analysis provided above is qualitatively valid as long as

$$\epsilon_{xx} + \epsilon_{yy} - 2\epsilon_{zz} \in [0.54\%, -1.6\%] \times (L/10 \text{ nm})^{-2}, \quad (5.18a)$$

$$|\epsilon_{xx} - \epsilon_{yy}| < 0.12\% \times (L/10 \text{ nm})^{-2}, \quad (5.18b)$$

$$|\epsilon_{xz}|, |\epsilon_{yz}| < 0.08\% \times (L/10 \text{ nm})^{-2}, \quad (5.18c)$$

$$|\epsilon_{xy}| < 0.9\% \times (L/10 \text{ nm})^{-2}. \quad (5.18d)$$

Consequently, for typical cross-sections where  $L$  is a few tens of nanometers, reasonable values of the strain parameters  $\epsilon_{ij} \sim 0.1\%$  can still preserve the spin-orbit switch. A detailed analysis of the effect of strain as well as a justification for the homogeneous model is provided in App. 5.E.

## 5.4 Effect of the SOHs

In Sec. 5.3, the effective spin-orbit velocity is computed by using the  $4 \times 4$  LK Hamiltonian in Eq. (5.3), which describes the mixing of heavy and light holes. In this case, nanowires with equilateral triangular cross-sections having different sides  $L$  show the same qualitative behaviour, and  $L$  only sets the scale of the spin-orbit velocity  $v \propto \hbar/(mL)$  and of the confinement energy  $\epsilon_c \propto \hbar^2/(mL^2)$ , see Eqs. (5.13) and (5.9), respectively. This model is valid for wires with a large cross-section, where  $\epsilon_c$  is the smallest energy scale and one can neglect the coupling to the split-off holes, gapped by a large energy  $\Delta_0$ . In contrast, for small Si wires,  $\Delta_0$  is comparable with  $\epsilon_c$  and because of the influence of the SOHs, the ground-state dynamics of the wire depends non-trivially on the side  $L$  of the cross-section [83]. As anticipated in Sec. 5.2, to study this dependence we use the  $6 \times 6$  LK Hamiltonian [1], fully accounting for the SOHs.

In Fig. 5.5, we show how the intrinsic spin-orbit velocity  $|v_0|$  is modified by the SOHs in wires with different cross-section sides  $L$ . For large wires, with  $L \gtrsim 35$  nm, the contribution of the SOHs is small and  $|v_0|$  approaches the value in Eq. (5.10) obtained with the  $4 \times 4$  LK Hamiltonian (dashed lines). In contrast, for very small wires, with  $L \lesssim 10$  nm, the SOHs strongly suppress  $|v_0|$ . For moderately small wires, because of the anisotropy of Si, the effect of the SOHs strongly depends on the growth direction. In fact, while for the SA  $|v_0|$  decreases monotonically, when  $\theta = 0$ , the spin-orbit velocity overshoots and reaches a maximum at  $L \sim 20$  nm, where  $|v_0|$  is larger than the value obtained for the  $4 \times 4$  LK Hamiltonian. In addition, at  $L \sim 10$  nm we observe that for the DRA, the intrinsic spin-orbit interaction can be exactly cancelled, restoring the usual direct Rashba spin-orbit coupling typical of inversion symmetric cross-sections [15, 16].

The SOHs strongly affect the response of the system to external electric fields. For example, we analyze here the spin-orbit velocity in wires with the DRA, where in Sec. 5.3, we predict that the intrinsic spin-orbit interaction can be exactly cancelled by a positive homogeneous electric field  $E_y$  and by an inhomogeneous field  $\delta E$ . In Fig. 5.6, we show how the spin-orbit switch-off mechanism discussed in Sec. 5.3 and Sec. 5.3 are modified by the SOHs. In particular, in Fig. 5.6a) we show the combined effect of  $E_y$  and  $\delta E$  on the spin-orbit velocity  $v$  when the SOHs are accounted for. We study here an equilateral triangle of side  $L = 20$  nm, which maximises the intrinsic spin-orbit coupling, see Fig. 5.5, and is eas-

ily achievable in state-of-the-art devices [41–43]. Comparing to Fig. 5.4b), where  $v$  is obtained by using the  $4 \times 4$  LK Hamiltonian, we observe that the SOHs drastically alter the response of the wire and they remove the charge noise sweet spot produced by the homogeneous electric field  $E_y$ , while maintaining the sweet spot resulting from the inhomogeneous field  $\delta E$ . This latter sweet spot persists also when a strong homogeneous electric field  $E_y$  is present and  $E_y$  only pushes the switch-off field  $\delta E^{SW}$  to larger values. In the plot, we show with a dashed line the curve along which the spin-orbit vanishes when the SOHs are neglected. Importantly, for the simple gate design studied here, where  $E_y$  and  $\delta E$  are constrained along the purple line in the figure, the charge noise sweet spot is removed by the SOHs.

To have a better understanding of the system, we show in Figs. 5.6b) and 5.6c) the effect of  $E_y$  and  $\delta E$  in wires grown along the DRA and having different cross-section side  $L$ . We observe that when  $L \lesssim 35$  nm, the spin-orbit switch at  $E_{\text{DRA}}^{SW}$  is removed by the SOHs. In contrast, the SOHs enhance the effect of  $\delta E$  and the spin-orbit switch at  $\delta E^{SW}$  persists in small wires and is pushed to lower values. A more detailed analysis of the inhomogeneous electric field response, including the general dependence on  $\delta E_{xx}$  and  $\delta E_{yy}$  for different growth directions is given in App. 5.D.

A more careful device design can minimize the effect of the SOHs. For example, in wires grown along the DRA, the spin-orbit switch is restored in wide isosceles FinFETs. To understand this result, we analyze the spin-orbit coupling in isosceles triangular wires with equal sides  $L_y$  and base  $L_x$ , see Fig. 5.1. The aspect ratio is

$$r \equiv L_x/L_y = 2 \sin(\Theta/2) \in (0, 2) . \quad (5.19)$$

The FinFET is equilateral when  $r = 1$ , and we call wide and narrow FinFETs the devices with  $r > 1$  and  $r < 1$ , respectively [ $\Theta$  is the apex angle of the fin]. For convenience, we also define an effective length  $\tilde{L} = L_y \sqrt{\sin(\Theta)/\sin(\pi/3)}$ , that is the side of an ideal equilateral triangle with the same area of the isosceles triangle. We redefine the confinement energy  $\epsilon_c$  in Eq. (5.9) by the substitution  $L \rightarrow \tilde{L}$ .

In Fig. 5.7a), we focus on cross-sections with  $\tilde{L} = 20$  nm and we examine the dependence of  $|v|$  on  $\delta E$  when  $E_y = 0$  and when different values of  $r$  are considered. These numerical results are obtained by using Eq. (5.5) and by discretizing the  $6 \times 6$  LK Hamiltonian in isosceles triangular cross-sections. Here, we use the approximate potential in Eq. (5.15); the limits

of this approximation in isosceles fins are discussed in App. 5.D. Importantly, we observe that  $\delta E$  can remove the spin-orbit interactions for a broad range of  $r$  and that  $\delta E^{SW}$  is significantly reduced when the fin is wide.

This enhancement of the inhomogeneous field is crucial to restore the spin-orbit sweet spot. In fact, in Fig. 5.7b), we show the simultaneous effect of  $\delta E$  and  $E_y$  when  $r = 1.2$  and  $\tilde{L} = 20$  nm, i.e.  $L_x = 22.8$  nm and  $L_y = 19$  nm. In the FinFET design shown in Fig. 5.1, where  $\delta E$  and  $E_y$  are constrained on the (purple) line defined by Eq. (5.17), we find that the spin-orbit coupling can be switched off by the inhomogeneous electric field at the gate potential  $V_g^{SW} \approx -249 \times \text{nm}^2 d_B / \tilde{L}^3$  V. This value corresponds to  $V_g^{SW} \approx -3.12$  V when  $\tilde{L} = 20$  nm and the back gate is  $d_B = 100$  nm apart from the center of mass of the wire. This gate potential is rather large, but it can be reduced by placing a back gate closer to the fin. We believe that an optimized electrostatic design of the device can also reduce  $V_g^{SW}$ , but we do not investigate this aspect further. Interestingly, in this setup, we recover also the spin-orbit sweet spot  $E_{\text{DRA}}^{SW}$  driven by the homogeneous field  $E_y$ , see the dashed line in the figure. In addition, in the inset of Fig. 5.7b), we show the total hole density  $|\psi|^2$  at  $V_g^{SW}$ . Because the wavefunction is strongly confined in the fin and has no support close to the bottom boundary, we expect the results presented here to be valid for both SOI and bulk FinFETs.

Finally, we estimate that in the range of parameters considered, the spin-orbit length in this setup can be pushed down to a minimal value of  $l_{so}^{\min} \approx 1.5\tilde{L}$  by reducing the amplitude of the gate potential. While still rather short, this length is longer than in the equilateral triangle, resulting in a smaller maximal spin-orbit coupling. Other possible SOI and bulk FinFETs designs where the spin-orbit switch is restored are discussed in App. 5.F. Amongst the setups analyzed, we chose to focus on the wide DRA FinFET because it guarantees the largest spin-orbit coupling when the interaction is turned on.

## 5.5 Suppressing charge noise in FinFET Qubits

We now study the susceptibility to charge noise of an elongated quantum dot that defines a spin 1/2 qubit [2]. All the results discussed in this section take fully into account the SOHs. To define the dot, we include a confining potential in the direction of the wire  $e\delta E_{zz}z^2/2$ , which is assumed to be much smoother than the cross-section side  $L$ ; in this way, the

effective wire Hamiltonian in Eq. (5.4) accurately describes the system. We emphasize that while here we discuss only elongated quantum dots, where  $l \gg L$ , our results apply also to FinFET-based spin qubits where  $l \approx L$ <sup>3</sup>, such as the ones in [42, 43]. A potential  $e\delta E_{zz}z^2/2$  is typically generated by terminating the top gate above the FinFET such that it has a finite extension in the direction along the wire ( $z$ -direction). The precise value of  $\delta E_{zz}$  depends on the size of the gate along  $z$ , on the distance  $d_B$  of the back gate; also  $\delta E_{zz}$  varies linearly with the top gate potential  $V_g$ .

Without an external magnetic field  $\mathbf{B}$ , one can exactly gauge the spin-orbit coupling away by the unitary transformation  $S = e^{-i\mathbf{n}_v \cdot \boldsymbol{\sigma} z/l_{so}}$  [84], where  $\mathbf{n}_v$  is the direction of the spin-orbit vector  $\mathbf{v}$ , and the Hamiltonian reduces to a harmonic oscillator with frequency  $\omega_z = \sqrt{e|\delta E_{zz}|/m^*}$ , whose ground state wavefunction is a gaussian with standard deviation

$$l = \sqrt{\frac{\hbar}{m^*\omega_z}} = \sqrt[4]{\frac{\hbar^2}{em^*|\delta E_{zz}|}}. \quad (5.20)$$

Because  $\delta E_{zz} \propto V_g$ , the harmonic length  $l$  depends on the gate potential as  $l \propto |V_g|^{-1/4}$ ; the divergence of  $l$  for  $V_g \rightarrow 0$  is a consequence of the fact that in electrostatically defined quantum dots a finite value of the gate potential  $V_g$  is required to confine the particles.

At finite values of  $\mathbf{B}$ , the unitary  $S$  leads to an effective magnetic field that oscillates as a function of the position along the wire. When projected onto the groundstate of the dot, these oscillations cause a spin-orbit coupling dependent renormalization of the  $g$ -tensor in the direction perpendicular to  $\mathbf{n}_v$  [21, 24, 25]. In particular, decomposing the vector  $\Delta$  defined in Eq. (5.8) into the sum of the two vectors  $\Delta_{\parallel}$  and  $\Delta_{\perp}$  that are parallel and perpendicular to the spin-orbit vector  $\mathbf{n}_v$ , respectively, we obtain the qubit Hamiltonian

$$H_q = \frac{1}{2} \left( \Delta_{\parallel} + e^{-\frac{l^2}{l_{so}^2}} \Delta_{\perp} \right) \cdot \boldsymbol{\sigma}. \quad (5.21)$$

---

<sup>3</sup>A more precise condition for the validity of the nanowire Hamiltonian in Eq. (5.4) is that the harmonic frequency  $\hbar\omega_z = \hbar^2/(m^*l^2)$  is much smaller than the energy gap  $\Delta E$  between the ground-state and the first excited state of the nanowire. For the devices considered and in the range of parameters shown the minimal energy gap is  $\Delta E \sim 0.05\epsilon_c$  at the switching field, and so we obtain the condition  $1 \gg \hbar\omega_z/\Delta E \sim 3L^2/(0.05 \times 16\pi^2\gamma_1 m^*l^2) \sim L^2/(\gamma_1 l^2)$ , where we used the effective mass in Eq. (5.35). Because of the prefactor  $1/\gamma_1 \sim 0.22$ , the nanowire Hamiltonian works reasonably well when  $L \approx l_{so} \approx l$ .

To study the effect of charge noise, we consider small fluctuations  $\delta V$  of the gate potential around the fixed working point  $V_g$ . To linear order in  $\delta V$  the parameters of  $H_q$  modify as  $\Delta \rightarrow \Delta + \Delta' \delta V$ ,  $l \rightarrow l + l' \delta V$  and  $l_{so} \rightarrow l_{so} + l'_{so} \delta V$ , leading to

$$H_q \rightarrow H_q + \frac{\delta V}{2} \mathbf{Q} \cdot \boldsymbol{\sigma}, \quad (5.22)$$

where we define the vector with the units of charge

$$\mathbf{Q} = \Delta'_{\parallel} + e^{-\frac{l^2}{l_{so}^2}} \Delta'_{\perp} + 2 \frac{l^2}{l_{so}^2} e^{-\frac{l^2}{l_{so}^2}} \left( \frac{l'_{so}}{l_{so}} - \frac{l'}{l} \right) \Delta_{\perp}. \quad (5.23)$$

Unless the device is operated at the sweet spot, in elongated hole quantum dots,  $l$  is comparable with the spin-orbit length  $l_{so}$ , and the last term in Eq. (5.23) dominates. In addition, we stress that in these systems the requirement of a vanishing first derivative  $|v|'$  of the spin-orbit velocity  $|v|$  at the sweet spot is not sufficient to remove spin-orbit-caused charge noise [35, 36], because there is an additional large contribution coming from the variation of the dot size  $l$ . In contrast, at the spin-orbit switch point, where  $l_{so} \rightarrow \infty$ , the last term in Eq. (5.23) vanishes exactly and charge noise only affects the qubit by the fluctuations of the  $g$ -factor.

We now restrict ourselves to the analysis of the wide FinFET grown along the DRA that is discussed in Sec. 5.4. Because of the symmetries of this device, the principal axes of the  $g$ -tensor are aligned to the coordinate system chosen in Fig. 5.1 [73], and the  $i$ th component of the Zeeman energy is  $\Delta_i = g_{ii} \mu_B B_i$ . Here, we consider a magnetic field pointing in the  $y$ -direction, i.e.  $\mathbf{B} = B_y \mathbf{e}_y$ . This choice maximizes the Rabi frequency in electric spin dipole resonance experiments [85] because the spin-orbit vector points in the  $x$ -direction, see Eq. (5.13). In addition, this magnetic field direction minimizes the noise and provides the largest Zeeman energy gap. The dependence of the elements of the  $g$ -factor matrix on the gate potential  $V_g$  for this device design is shown in Fig. 5.8a). The value of the  $g$ -factors computed here and the strong anisotropy of the Zeeman energy depending on the direction of the magnetic field is in reasonable agreement with experiments [12, 42, 43, 67].

In general, the vector  $\mathbf{Q}$  can have a component pointing along the vector  $\Delta$  and a component perpendicular to it; these components cause the dephasing and the relaxation of the qubit, respectively. However, when the matrix of  $g$ -factors is diagonal and  $\mathbf{B} = B_y \mathbf{e}_y$ , the vector  $\mathbf{Q}$

is aligned to  $\Delta$  and the qubit is only subjected to dephasing. From a Bloch-Redfield analysis and for  $1/f$ -type noise with spectrum  $\mathcal{S}(\omega) = \langle \delta V^2 \rangle / |\omega|$ , the dephasing rate  $1/T_2^*$  is given by [86, 87]

$$\frac{1}{T_2^*} = \frac{1}{\hbar} |\mathbf{Q}| \sqrt{\langle \delta V^2 \rangle} \sqrt{\frac{1}{2\pi} \log \left( \frac{|\mathbf{Q}| \sqrt{\langle \delta V^2 \rangle}}{\hbar \omega_{\text{ir}}} \right)}, \quad (5.24)$$

where  $\omega_{\text{ir}} \sim 1$  Hz is a cut-off frequency depending on the experiment. Here, we only consider free induction decay, and do not account for echo pulses that can further improve the qubit lifetime.

The dependence of the dephasing rates due to charge noise on the gate potential for a wide FinFET qubit with  $\tilde{L} = 20$  nm and  $r = 1.2$  is shown in Fig. 5.8b). For the plot, we consider a magnetic field  $B_y = 100$  mT, which leads to a Zeeman energy of tens of  $\mu\text{eV}$ , comparable to the values measured in [17]. Also, we consider dots with a fixed value of  $\delta E_{zz}/V_g$ , chosen such that the lateral size of the dot is  $l = 30$  nm at the spin-orbit switching point  $V_g = V_g^{SW} = -3.12$  V. In addition, at  $V_g = V_g^{SW}$ , the longitudinal confinement energy is  $\hbar\omega_z = 0.14$  meV, an order of magnitude larger than the Zeeman gap  $\Delta_y = 11$   $\mu\text{eV}$  and an order of magnitude smaller than the transverse subband gap  $\Delta E = 1.7$  meV; we then conclude that our approach is valid in this regime. To estimate the fluctuations of the gate potential, we consider that the typical fluctuations of the energy levels are  $\sqrt{\langle \hbar^2 \omega_z^2 \rangle} \sim 5$   $\mu\text{eV}$  [88] and are connected to the fluctuations of the gate potential by the dimensionless lever arm  $\alpha \equiv |\hbar \partial \omega_z / (e \partial V_g)|$ , i.e.  $\sqrt{\langle \delta V^2 \rangle} = \alpha \sqrt{\langle \hbar^2 \omega_z^2 \rangle} / e$ . At  $V_g = V_g^{SW}$ , choosing  $l = 30$  nm, we obtain  $\alpha \approx 65$ , and we estimate  $\sqrt{\langle \delta V^2 \rangle} \approx 0.3$  mV. We note that if  $l = 15$  nm at  $V_g = V_g^{SW}$ , the lever arm is  $\alpha \approx 16$ , in reasonable agreement with recent experiments where the lever arm is about 20 [89].

The black solid line in Fig. 5.8b) represents the total dephasing rate of the FinFET qubit. We observe that charge noise leads to dephasing times  $T_2^*$  of hundreds of nanoseconds, in agreement with recent experimental data [89], that can be pushed to infinity when the devices are tuned to work at the sweet spots. Importantly, the sweet spot is close to the spin-orbit switching point  $V_g^{SW} = -3.12$  V, but it does not exactly coincide with it. To have a better understanding of this shift, we show with dashed red and gray lines the dephasing rates  $1/T_2^*$  obtained by considering only the terms of the vector  $\mathbf{Q}$  in Eq. (5.23) that are related respectively to the fluctuations of the  $g$ -factor, i.e.  $\propto \Delta'$ , and to the spin-orbit coupling, i.e.  $\propto l^2/l_{so}^2$ . Because these different contributions

in Eq. (5.23) can have a different sign depending on whether the  $g$ -factor and the spin-orbit coupling increases or decreases as a function of  $V_g$ , the small shift of the sweet spot is a result of the interference between the  $g$ -factor fluctuations and the spin-orbit coupling contribution to dephasing. In the wide DRA FinFET, where the spin-orbit length is very short, the spin-orbit coupling contribution to dephasing is dominating and the  $g$ -factor fluctuations are relevant only very close to the spin-orbit switch. Working at the sweet spot leads to a clear practical advantage, completely removing the charge noise when the qubit is idle.

## 5.6 Conclusion

In this work, we present ways of suppressing charge noise in hole Si FinFET qubits. The advantage of these structures compared to other nanowires is their triangular cross-section, which by symmetry permits large intrinsic spin-orbit interactions without external electric fields. When the device has a simple equilateral triangular cross-section, we find this effect to be a result of the interplay between the low symmetry of the cross-section and the anisotropy of Si. When an external gate potential is applied an extra tunable contribution to the spin-orbit coupling arises and depending on the growth direction of the wire, it can enhance or suppress the total spin-orbit interactions. This suppression leads to points where the spin-orbit velocity can be tuned exactly to zero, dramatically boosting up the coherence times of spin-1/2 qubits.

We study in detail the dependence of spin-orbit coupling on the gate potential by considering an inhomogeneous electric field profile, which matches numerical simulations of the electrostatics of realistic FinFET devices. We distinguish between different mechanisms that drive the switching-off of the spin-orbit coupling and that have a different behaviour as the cross-section area becomes smaller as a result of the spin-orbit split-off hole band. These states generally degrade the performance of the FinFET and can even remove the spin-orbit switch. We present more involved designs, e.g. wide FinFETs, that reduce their effect and restore the spin-orbit switch.

When a small external magnetic field is applied, hole nanowire qubits become susceptible also to fluctuations of the Zeeman energy caused by an electrically tunable  $g$ -factor. By analyzing the response of FinFET devices to small magnetic fields, we find sweet spots where the charge noise can be completely removed to linear order in the fluctuations of the gate



potential, providing an ideal working point where quantum information can be reliably stored in charge noise resilient spin qubits.

## 5.A Electric field simulation

We present the model of the electric field profile in Si FinFETs and compare the approximate potential in Eq. (5.2) to the electrostatic potential obtained by solving the Laplace equation in the FinFET sketched in Fig. 5.1. We study a fin with an equilateral triangular cross-section with side  $L$ . For simplicity, we neglect the effect of the dielectric on the electric field lines. This approximation describes well devices that use thin high-k dielectric materials, with a dielectric constant similar to Si, but we expect our results to be at least qualitatively correct for a wider range of devices, including devices made with SiO<sub>2</sub>. In addition, we assume that the top and back gates extend to infinity along the wire (in the  $z$ -direction), such that we can restrict our analysis to a cross-section of the FinFET in the  $(x, y)$  plane. We solve the Laplace equation considering that the top gate fixes the electrostatic potential of Si to  $V_g$  and that the back gate is grounded to zero potential. To model the lateral sides of the substrate, we consider a wide substrate, that extends symmetrically up to  $x = \pm 15L$  from the position of the fin at  $x = 0$ , and we set the potential at the sides below the top gate to ground. This approximation describes well the potential in the fin as long as the distance  $d_B$  of the back gate from the fin is  $\lesssim 30L$ . In Fig. 5.9, we show the potential energy  $V_E^N$  simulated in this setup when the back gate is at  $d_B = 15L$  from the bottom of the fin. Note that the potential in this simple design varies linearly with  $V_g$  and that the lengths are normalized against the side  $L$  of the fin.

We compare the numerical solution  $V_E^N$  of the Laplace equation to the approximate potential in Eq. (5.2); in this section, we call the approximate potential  $V_E^A$  to distinguish it from the numerical solution  $V_E^N$ . To find the parameters  $E_i$  and  $\delta E_{ij}$ , we compute the appropriate derivatives of the potential and find their average in the fin. For example,  $\delta E_{xx} = -(1/A_{\text{fin}}) \int_{\text{fin}} d\mathbf{r} \partial_{xx} V_E^N(x, y)$ , with  $A_{\text{fin}}$  being the area of the triangle, where the averaging is performed. Because the device is symmetric around  $x = 0$ , the homogeneous electric field in the  $x$ -direction vanishes and  $E_x = 0$ . Simulating devices with different substrate thickness  $d_B$ , we find that the homogeneous and inhomogeneous components of the

electric field can be written to good approximation as

$$E_y = \frac{c_y V_g}{d_B} \text{ and } \delta E_{ij} = \frac{c_{ij} V_g}{d_B L}, \quad (5.25)$$

where the dimensionless coefficients  $c$  are of order one. By fitting these formulas against the results of the simulation, we find a good fit when

$$c_y = -0.3, \quad c_{xx} = -1.21, \quad c_{yy} = 1.2, \quad (5.26)$$

see Fig. 5.10a). Note that  $\delta E_{xx} \approx -\delta E_{yy}$ , justifying the approximation in Eq. (5.2). We also find that  $c_{xy} = 0$  in this geometry. When accounting for the finite size of the top gate,  $c_{xy}$  acquires a finite value, however, it is reasonable to assume that  $|c_{xy}| \ll |c_{ii}|$  as long as the top electrode fully covers the fin. A comparison between the approximate potential  $V_E^A$  and  $V_E^N$  simulated from the Laplace equation for  $d_B = 15L$  is shown in Fig. 5.10b) and c). We observe that the electrostatic potential in the fin  $V_E^N$  is reasonably well approximated by  $V_E^A$ . We remark that the precise values of the coefficients  $c$  can change for different devices, e.g. by including dielectric materials, changing the aspect ratio of the fin or including additional gates. While we do not expect drastic changes of our model, we do not investigate these effects in detail here.

## 5.B Orbital eigenstates

A convenient basis to analyze wires with triangular cross-sections comprises the eigenstates of the two-dimensional Laplace operator  $p_x^2 + p_y^2$  vanishing at the boundary of an equilateral triangle of side  $L$  [75]. These solutions can be chosen to be even ( $e$ ) or odd ( $o$ ) with respect to the height of the triangle at  $x = 0$  and they are written compactly as

$$\psi_\lambda(x, y) = c_\lambda \mathbf{f}_\lambda(x/L) \cdot \mathbf{g}(y/L) \quad (5.27)$$

where where  $\lambda = e, o$  indicates the parity and  $c_\lambda$  is a normalization constant. We define the vectors

$$\mathbf{f}_e(x) = \left( \cos \left[ \frac{2\pi(3m+l)}{3} x \right], \cos \left[ \frac{2\pi(3m+2l)}{3} x \right], -\cos \left[ \frac{2\pi l x}{3} \right] \right), \quad (5.28a)$$

$$\mathbf{f}_o(x) = \left( -\sin \left[ \frac{2\pi(3m+l)}{3} x \right], \sin \left[ \frac{2\pi(3m+2l)}{3} x \right], \sin \left[ \frac{2\pi l x}{3} \right] \right), \quad (5.28b)$$

$$\mathbf{g}(y) = \left( \sin \left[ \frac{2\pi(m+l)}{3} (\sqrt{3}y - 1) \right], \sin \left[ \frac{2\pi m}{3} (\sqrt{3}y - 1) \right], \sin \left[ \frac{2\pi(2m+l)}{3} (\sqrt{3}y - 1) \right] \right). \quad (5.28c)$$

The quantum numbers  $m, l$  are integers satisfying the conditions  $m \geq 1$ ,  $l \geq 0$  and  $m \geq 1$ ,  $l \geq 1$  for the even and odd solutions, respectively. These quantum numbers label the eigenvalues of the Laplace operator according to

$$(p_x^2 + p_y^2) \psi_\lambda = \frac{\hbar^2}{L^2} \frac{16\pi^2}{3} \left( m^2 + lm + \frac{l^2}{3} \right) \psi_\lambda. \quad (5.29)$$

The states characterized by  $l = 0$  are three-fold rotationally symmetric and even with respect to the height of the triangle; no odd solutions with  $l = 0$  are allowed. The remaining even and odd solutions labelled by the same quantum numbers  $m$  and  $l \neq 0$  are degenerate. The lowest three normalized eigenfunctions are shown in Fig. 5.11. These three states are used in App. 5.C to find an effective analytical model for the triangular FinFET.

## 5.C Spin-orbit interaction in perturbation theory

### Intrinsic spin-orbit velocity and length

In this section, we show the general dependence of the intrinsic spin-orbit vector  $\mathbf{v}_0$  in Eq. (5.10) and of the spin-orbit length  $l_{so}$  in Eq. (5.6) on the orientation of the wire. To account for the different growth directions,

we rotate the  $4 \times 4$  LK Hamiltonian  $H'_{\text{LK}}$  in Eq. (5.3) by the unitary operator  $U = e^{i\theta F_{y'}} e^{i\varphi F_{z'}}$ , i.e.  $H'_{\text{LK}} \rightarrow H_{\text{LK}} = U^\dagger H'_{\text{LK}} U$ , where  $\mathbf{F} = \mathbf{J}' + \mathbf{x}' \times \mathbf{p}'$  [with  $\mathbf{x}' = (x', y', z')$  and  $\mathbf{J}' = (J'_x, J'_y, J'_z)$ ] is the total angular momentum, and  $\theta$  and  $\varphi$  are the angles between the crystallographic axes and the final coordinate system, see Fig. 5.1. This unitary rotation aligns the coordinate system and the direction of the spin-matrices to the axes  $x, y$  and  $z$ . More explicitly, the Hamiltonian in the rotated coordinate system is given by

$$H_{\text{LK}} = \left( \gamma_1 + \frac{5}{2}\gamma_2 \right) \frac{p^2}{2m} - \frac{\gamma_2}{m} \mathbf{p}^2 \cdot \mathbf{J}^2 - \frac{2\gamma_3}{m} p_i p_j \{J_i, J_j\} + \text{cp} , \quad (5.30)$$

where the rotated momenta are

$$\mathbf{p} = \begin{pmatrix} \cos(\theta) \cos(\varphi) p'_x + \cos(\theta) \sin(\varphi) p'_y - \sin(\theta) p'_z \\ \cos(\varphi) p'_y - \sin(\varphi) p'_x \\ \sin(\theta) (\cos(\varphi) p'_x + \sin(\varphi) p'_y) + \cos(\theta) p'_z \end{pmatrix} , \quad (5.31)$$

and  $\mathbf{p}^2 = (p_x^2, p_y^2, p_z^2)$ ,  $\mathbf{J}^2 = (J_x^2, J_y^2, J_z^2)$ ,  $p^2 = p_x^2 + p_y^2 + p_z^2$ . The spin 3/2 matrices  $\mathbf{J}$  are rotated in the same way.

We do not include electric or magnetic fields at the moment and we focus on the intrinsic spin-orbit coupling. To obtain simple equations, we restrict the orbital space to the space spanned by the lowest three eigenstates of the Laplace equation in an equilateral triangle, see Fig. 5.11. By projecting  $H_{\text{LK}}$  onto this subspace, we obtain a  $12 \times 12$  reduced Hamiltonian  $H_{12}$  that parametrically depends on the angles  $\varphi$  and  $\theta$  and on the momentum  $p_z$ .

Specifically,  $H_{12}$  is found from  $H_{\text{LK}}$  in Eq. (5.30) by separating the different powers of  $p_i p_j$ , i.e.

$$H_{\text{LK}} \equiv \sum_{i,j} p_i p_j H_{ij} , \quad (5.32)$$

and using the matrix representation of the momenta operators in the basis  $(|1, 0, e\rangle, |1, 1, e\rangle, |1, 1, o\rangle)$ , where the eigenstates  $|m, l, \lambda\rangle$  are defined by Eqs. (5.27) and (5.28). Denoting the matrix representation of the momentum operators in this basis by a under bar  $\underline{p_i p_j}$ ,  $H_{12}$  is given by

$$H_{12} = \sum_{i,j} \underline{p_i p_j} \otimes H_{ij} , \quad (5.33)$$

The expressions of the matrix elements of  $H_{12}$  as a function of  $\theta$  and  $\varphi$  can be straightforwardly derived from Eq. (5.30) and we do not give them

here. We report instead the matrices of the momenta:

$$\underline{p}_x^2 = \frac{\hbar^2}{L^2} \begin{pmatrix} \frac{8\pi^2}{3} & \frac{k}{\sqrt{2}} & 0 \\ \frac{k}{\sqrt{2}} & \frac{56\pi^2}{9} - \frac{21}{25}k & 0 \\ 0 & 0 & \frac{56\pi^2}{9} + \frac{21}{25}k \end{pmatrix}, \quad (5.34a)$$

$$\underline{p}_x \underline{p}_y = \frac{\hbar^2}{L^2} \begin{pmatrix} 0 & 0 & -\frac{k}{\sqrt{2}} \\ 0 & 0 & -\frac{21}{25}k \\ -\frac{k}{\sqrt{2}} & -\frac{21}{25}k & 0 \end{pmatrix}, \quad (5.34b)$$

$$\underline{p}_x \underline{p}_z = \frac{9\hbar k p_z}{10\sqrt{2}\pi L} \begin{pmatrix} 0 & 0 & i \\ 0 & 0 & 0 \\ -i & 0 & 0 \end{pmatrix}, \quad (5.34c)$$

$$\underline{p}_y \underline{p}_z = \frac{9\hbar k p_z}{10\sqrt{2}\pi L} \begin{pmatrix} 0 & -i & 0 \\ i & 0 & 0 \\ 0 & 0 & 0 \end{pmatrix}, \quad (5.34d)$$

and  $\underline{p}_y^2 = \underline{p}_x^2|_{k \rightarrow -k}$ ,  $\underline{p}_z^2 = p_z^2 \mathcal{I}_3$ ; also  $k = 2187/112 \approx 19.53$  and  $\mathcal{I}_3$  is the 3-dimensional identity matrix. In the simple case  $\theta = 0$ , the  $12 \times 12$  Hamiltonian, also including electric fields, is explicitly given in Eq. (5.39).

We resort to perturbation theory on  $H_{12}$  to derive a low-energy description of the system. With a second order Schrieffer-Wolff transformation, see e.g. Appendix B of [1] or [76], we obtain a  $2 \times 2$  effective Hamiltonian that acts on the ground state subspace of the wire. Expanding the matrix elements of this Hamiltonian up to second order in  $p_z$ , we find an effective wire Hamiltonian as in Eq. (5.4). The terms linear in  $p_z$  are related to the spin-orbit velocity  $\mathbf{v}$ , while the effective mass  $m^*$  is twice of the inverse of the diagonal term quadratic in  $p_z$ .

For a Si wire, the dependence of the components of the intrinsic spin-orbit velocity vector  $\mathbf{v}_0$  on the growth angles obtained in this way is shown in Fig. 5.12. Importantly, we find that the  $\mathbf{v}_0$  is in general proportional to the anisotropy of the material  $\gamma_3 - \gamma_2$  and to the velocity  $\hbar/mL$ , and thus it can be written as in Eq. (5.10). In addition, there is no spin-orbit coupling in the direction along the wire when  $\theta = 0$  and  $\theta = \pm\pi/2$  (red and blue lines, respectively), and in these cases  $(\mathbf{v}_0)_z = 0$ . While these results were found by perturbation theory, we find numerically that they hold generally. Interestingly, the off-diagonal components of the spin-orbit velocity  $(\mathbf{v}_0)_{x,y}$  vanish e.g. when  $\varphi = \pi/4$  and  $\theta = -\arctan \sqrt{2 + \sqrt{3}}$ , where the diagonal spin-orbit  $(\mathbf{v}_0)_z$  is maximal.

This orientation corresponds to  $z \parallel [111]$ , along which the Si lattice has a three-fold rotational symmetry, and is marked with black circles in the figures.

By taking the limits  $\theta = 0$  and  $\theta = \pm\pi/2$ , the expressions of the spin-orbit vector simplify notably and are given in Eqs. (5.11). When  $\theta = \pm\pi/2$ , the spin-orbit vector points along the  $x$ -direction and it has an oscillating amplitude, while when  $\theta = 0$ , the direction is oscillating as a function of  $\varphi$ . A plot of the absolute values of  $v_0$  in these cases and a comparison between the perturbation theory and a more detailed numerical solution comprising 200 orbital states in Eq. (5.27) is shown in Fig. 5.2.

With this approach, we also find the effective mass  $m^*$  from the diagonal elements of the effective Hamiltonian. Along the  $\theta = 0$  and  $\theta = \pm\pi/2$  directions,  $m^*$  can be compactly written as

$$\frac{m}{m^*(\theta = 0)} = \gamma_1 + 2\gamma_2 - \frac{5.35\gamma_1\gamma_3^2 + 1.86\gamma_2^3 + 15.23\gamma_2\gamma_3^2}{(\gamma_1 + 5\gamma_2/2)^2} \approx 2.73, \quad (5.35a)$$

$$\frac{m}{m^*(\theta = \pm\pi/2)} \approx \frac{5.12 - 5.57 \cos(4\varphi) + 1.14 \cos(8\varphi) - 0.09 \cos(12\varphi)}{1 - 0.91 \cos(4\varphi) + 0.13 \cos(8\varphi)}. \quad (5.35b)$$

where in the second equation we discarded higher harmonic components oscillating with a small amplitude and a fast period in  $\varphi$ ;  $m$  is the bare electron mass. In Fig. 5.13a), we show the effective mass as a function of  $\varphi$ , comparing the approximate Eq. (5.35) with a more precise numerical result. This numerical result is obtained by extending the general perturbation theory developed in Sec. 5.2 [see in particular Eq. (5.5)]. By considering  $H_{LK} = H_0 + H_1 p_z + H_2 p_z^2$  and defining the matrix  $M_E$  of column eigenvectors of  $H_0$ , the effective mass is given by

$$\frac{1}{2m^*} = \left( M_E^\dagger H_2 M_E \right)_{ii} + \sum_{k \neq i,j} \frac{\left| \left( M_E^\dagger H_1 M_E \right)_{ik} \right|^2}{\epsilon_E^i - \epsilon_E^k}; \quad (5.36)$$

the indexes  $i, j$  label the ground state Kramers partners and, on the left-hand side of the equation, we omitted them because  $m_i^* = m_j^* \equiv m^*$ . In analogy to above,  $M_E$  is computed numerically by accommodating 200 orbital states given in Eq. (5.27).

We observe that the simple analytical results capture well the oscillating behaviour of the mass as a function of  $\varphi$ , but they underestimate the

amplitude of the oscillations, leading to a smaller mass, especially when the wire extends along a crystallographic axis, e.g when  $\theta = 0$  or when  $\theta = -\pi/2$  and  $\varphi = 0$ . For the SA, where  $\theta = -\pi/2$  and  $\varphi = -3\pi/4$ , Eq. (5.35b) works well and gives an effective mass  $m_{\text{SA}}^* \approx 0.17m$ , while for the CA and DRA, the numerical analysis is more precise and it gives an effective mass  $m_{\text{CA}}^* \approx m_{\text{DRA}}^* \approx 0.41m$ .

Analytical expressions for the intrinsic spin-orbit length  $l_{so}$  defined in Eq. (5.6) can be obtained when  $\theta = 0$  and  $\theta = \pi/2$  by combining Eqs. (5.10), (5.11) and (5.35). A comparison between these expressions and the numerically computed values of  $l_{so}$  is shown in Fig. 5.13b). Because of the underestimation of the effective mass, the spin-orbit length predicted by perturbation theory is larger than the numerical values when the wire extends along a crystallographic axis. In contrast, for the SA, the perturbative result is smaller than the numerical result because of the overestimation of the spin-orbit velocity, see Fig. 5.2. From the numerical analysis, we find that

$$l_{so}(\theta = 0) \approx 0.83L, \quad (5.37a)$$

$$l_{so}(\theta = \pm\pi/2) \in [0.83L, 2.89L]. \quad (5.37b)$$

Importantly, the intrinsic spin-orbit length is always of the order of the side of the triangle, typically much shorter than the confinement length of the quantum dot along the wire, leading to large spin-orbit interactions.

Finally, we point out that while our quantitative analysis here is limited to Si, our results can apply also to other semiconductors. For example, in [22], the spin-orbit interaction in hole Ge hut-wires is studied and an intrinsic spin-orbit field of  $\hbar|v_0| \sim 10 \text{ meV} \cdot \text{nm}$  was measured for a triangular device with width  $L_x = 80 \text{ nm}$  and height  $H = 4 \text{ nm}$ . An estimate of the amplitude of the intrinsic spin-orbit interaction related to the triangular cross-section can be found by using the equilateral triangle equation for the crystallographic growth direction,

$$|v_0| = 9.34 \frac{\hbar}{m\tilde{L}} \frac{\gamma_3(\gamma_3 - \gamma_2)}{\gamma_1 + (5/2)\gamma_2}, \quad (5.38)$$

obtained by combining Eqs. (5.10) and (5.11a). To better compare with the experiment, we consider a fictitious equilateral triangle of side  $\tilde{L}$  having the same area of the cross-section of the hut-wire; from the condition

$\sqrt{3}\tilde{L}^2/4 = L_x H/2$ , we find that the effective side of the fictitious equilateral triangle is  $\tilde{L} \approx 19$  nm. Using the Luttinger parameters of Ge [1], we estimate an intrinsic spin-orbit field  $\hbar|v_0| \approx 12.65$  meV · nm, in very good agreement with the experiment [22].

## Electric field dependence

Here, we focus on wires with  $\theta = 0$ , i.e. wires grown along the [001] crystallographic direction, and we study the dependence of the spin-orbit velocity on the electric field. In this case, the spin-orbit velocity vector has no component along the  $z$ -direction and is off-diagonal. We define then the complex off-diagonal component of the spin-orbit velocity  $v = (v)_x + i(v)_y$ . This quantity can be decomposed into the sum of an isotropic direct Rashba-like component that vanishes when the external electrostatic potential in Eq. (5.2) is turned off, and an anisotropic component that varies as a function of the angle  $\varphi$ , see Eq. (5.13). At finite values of the electrostatic potential,  $v$  depends on the homogeneous electric field  $E_y$  and on the inhomogeneous fields  $\delta E_{xx}$  and  $\delta E_{yy}$ . Here, we do not account for the effect of the terms  $E_x$  and  $\delta E_{xy}$  and we introduce the sum and difference of the inhomogeneous fields  $\delta E = (\delta E_{xx} - \delta E_{yy})/2$  and  $\Sigma E = (\delta E_{xx} + \delta E_{yy})/2$ . For simplicity of notation, we rescale the electric field by the confinement energy to obtain dimensionless quantities, i.e.  $eE_y L/\epsilon_c \rightarrow E_y$ ,  $e\delta E L^2/\epsilon_c \rightarrow \delta E$  and  $e\Sigma E L^2/\epsilon_c \rightarrow \Sigma E$ , and we define the vector  $\epsilon = (E_y, \delta E, \Sigma E)$ .

We neglect the SOHs and in analogy to the treatment in Sec. 5.C, we study the  $12 \times 12$  Hamiltonian obtained from the  $4 \times 4$  total Hamiltonian in Eq. (5.1) rotated by the angle  $\varphi$  and projected onto the subspace spanned by the lowest three orbital states in Eq. (5.27). Explicitly,

$$H_{12} = \frac{\hbar^2}{mL^2} \begin{pmatrix} H_{00} & H_{0e} & H_{0o} \\ H_{0e}^\dagger & H_{ee} & H_{eo} \\ H_{0o}^\dagger & H_{eo}^\dagger & H_{oo} \end{pmatrix}. \quad (5.39)$$

By introducing the quantities  $\gamma_\perp^\pm = \gamma_1 \pm \gamma_2$ ,  $\gamma_\parallel^\mp = \gamma_1 \mp 2\gamma_2$ ,  $C_\pm = \frac{\sqrt{3}}{2}k [e^{4i\varphi} (\gamma_3 - \gamma_2) \pm (\gamma_3 + \gamma_2)]$ ,  $a_E = \frac{59049}{4480\pi}\gamma_1 \approx 4.186\gamma_1$ ,  $a_\delta = \left(\frac{3969}{2000\pi} - \frac{7\sqrt{3}}{25}\right)a_E \approx 0.616\gamma_1$ ,  $b_\delta = \left(\frac{1107}{280\sqrt{2}\pi} - \sqrt{\frac{2}{3}}\right)a_E \approx 0.308\gamma_1$ ,  $K = \frac{9}{10\pi}\sqrt{\frac{3}{2}}k\gamma_3 \approx 6.851\gamma_3$ , [ $k \approx 19.53$ , see Eq. (5.34)], we can write



the dimensionless blocks as

$$H_{00} = \text{diag} \left( \frac{8\pi^2}{3}\gamma_{\perp}^+ + \frac{p_z^2}{2}\gamma_{\parallel}^-, \frac{8\pi^2}{3}\gamma_{\perp}^- + \frac{p_z^2}{2}\gamma_{\parallel}^+, \right. \quad (5.40a)$$

$$\left. \frac{8\pi^2}{3}\gamma_{\perp}^- + \frac{p_z^2}{2}\gamma_{\parallel}^+, \frac{8\pi^2}{3}\gamma_{\perp}^+ + \frac{p_z^2}{2}\gamma_{\parallel}^- \right), \quad (5.40b)$$

$$H_{ee} = \begin{pmatrix} \frac{56\pi^2}{9}\gamma_{\perp}^+ + \frac{p_z^2}{2}\gamma_{\parallel}^- & 0 & -\frac{21}{25}C_- & 0 \\ 0 & \frac{56\pi^2}{9}\gamma_{\perp}^- + \frac{p_z^2}{2}\gamma_{\parallel}^+ & 0 & -\frac{21}{25}C_- \\ -\frac{21}{25}C_-^* & 0 & \frac{56\pi^2}{9}\gamma_{\perp}^- + \frac{p_z^2}{2}\gamma_{\parallel}^+ & 0 \\ 0 & -\frac{21}{25}C_-^* & 0 & \frac{56\pi^2}{9}\gamma_{\perp}^+ + \frac{p_z^2}{2}\gamma_{\parallel}^- \end{pmatrix} - \mathcal{I}_4 \left( \frac{21}{25}a_E E_y - a_{\delta}\delta E + \frac{16}{27}\gamma_1 \Sigma E \right), \quad (5.40c)$$

$$H_{0e} = \begin{pmatrix} 0 & Kp_z & \frac{1}{\sqrt{2}}C_- & 0 \\ -Kp_z & 0 & 0 & \frac{1}{\sqrt{2}}C_- \\ \frac{1}{\sqrt{2}}C_-^* & 0 & 0 & -Kp_z \\ 0 & \frac{1}{\sqrt{2}}C_-^* & Kp_z & 0 \end{pmatrix} - \mathcal{I}_4 \left( \sqrt{2}a_E E_y - b_{\delta}\delta E \right), \quad (5.40d)$$

$$H_{eo} = \begin{pmatrix} 0 & 0 & -\frac{21}{25}iC_+ & 0 \\ 0 & 0 & 0 & -\frac{21}{25}iC_+ \\ \frac{21}{25}iC_+^* & 0 & 0 & 0 \\ 0 & \frac{21}{25}iC_+^* & 0 & 0 \end{pmatrix}. \quad (5.40e)$$

Also,  $H_{oo} = H_{ee}|_{C_- \rightarrow -C_-, \delta E \rightarrow -\delta E, E_y \rightarrow -E_y}$ ,  $H_{0o} = H_{0e}|_{C_- \rightarrow -iC_+, K \rightarrow -iK, \delta E \rightarrow 0, E_y \rightarrow 0}$ , and  $\mathcal{I}_4$  is a  $4 \times 4$  identity matrix. Here,  $p_z$  is given in units of  $\hbar/L$ .

In contrast to Sec. 5.C, a second-order Schrieffer-Wolff transformation does not capture accurately the dependence of the spin-orbit coupling on the electric field and thus we increase the accuracy of our calculation by using a fourth-order order transformation. To obtain compact equations, we also Taylor expand the spin-orbit velocity to second order in

the vector  $\epsilon$ , leading to

$$\alpha_I \approx \frac{\gamma_3}{\gamma_1 + 5\gamma_2/2} \left( \frac{\gamma_1}{\gamma_1 + 5\gamma_2/2} \alpha_I^{(1)} \cdot \epsilon \right. \quad (5.41a)$$

$$\left. + \frac{\gamma_1^2}{(\gamma_1 + 5\gamma_2/2)(\gamma_1 - \gamma_2)} \epsilon \cdot \underline{\alpha}_I^{(2)} \cdot \epsilon \right), \quad (5.41b)$$

$$\alpha_A(\varphi) \approx \frac{\gamma_3}{\gamma_1 + 5\gamma_2/2} e^{-4i\varphi} \left( \alpha_A^{(0)} + \frac{\gamma_1}{\gamma_1 + 5\gamma_2/2} \alpha_A^{(1)} \cdot \epsilon \right. \quad (5.41c)$$

$$\left. + \frac{\gamma_1^2}{(\gamma_1 + 5\gamma_2/2)(\gamma_1 - \gamma_2)} \epsilon \cdot \underline{\alpha}_A^{(2)} \cdot \epsilon \right), \quad (5.41d)$$

$$\alpha_I^{(1)} \approx \left( \frac{0.928(\gamma_1 + 6\gamma_2)}{\gamma_1 - \gamma_2}, \frac{0.066\gamma_1 - 0.407\gamma_2}{\gamma_1 - \gamma_2}, 0 \right), \quad (5.41e)$$

$$\underline{\alpha}_I^{(2)} \approx \begin{pmatrix} \frac{0.811\gamma_1 + 0.938\gamma_2}{\gamma_1 - \gamma_2} & -\frac{0.107\gamma_1 + 0.155\gamma_2}{\gamma_1 - \gamma_2} \\ 0 & \frac{0.0034\gamma_1 + 0.0055\gamma_2}{\gamma_1 - \gamma_2} \\ 0 & \frac{0.0317\gamma_1^2 + 0.2692\gamma_2\gamma_1 + 0.0871\gamma_2^2}{(\gamma_1 - \gamma_2)(\gamma_1 + 5\gamma_2/2)} \\ & \frac{0.0022\gamma_1^2 - 0.0217\gamma_2\gamma_1 - 0.0006\gamma_2^2}{(\gamma_1 - \gamma_2)(\gamma_1 + 5\gamma_2/2)} \\ & 0 \end{pmatrix}, \quad (5.41f)$$

$$\alpha_A^{(0)} = \frac{14}{45} \left( \frac{k}{2\pi} \right)^3 \approx 9.338, \quad (5.41g)$$

$$\alpha_A^{(1)} \approx (0., 0., 0.158), \quad (5.41h)$$

$$\underline{\alpha}_A^{(2)} \approx \begin{pmatrix} -\frac{1.251\gamma_1^2 + 4.231\gamma_2\gamma_1 + 1.604\gamma_2^2}{(\gamma_1 - \gamma_2)(\gamma_1 + 5\gamma_2/2)} & \frac{0.13\gamma_1^2 + 0.52\gamma_2\gamma_1 + 0.0855\gamma_2^2}{(\gamma_1 - \gamma_2)(\gamma_1 + 5\gamma_2/2)} \\ 0 & -\frac{0.0019\gamma_1^2 + 0.0185\gamma_2\gamma_1 - 0.0013\gamma_2^2}{(\gamma_1 - \gamma_2)(\gamma_1 + 5\gamma_2/2)} \\ 0 & 0 \\ & 0. \\ & 0. \\ & 0.0027 \frac{\gamma_1 - \gamma_2}{\gamma_1 + 5\gamma_2/2} \end{pmatrix}. \quad (5.41i)$$

To simplify further the expressions, we kept only the terms with the lowest possible power in  $1/\gamma_1$ . This approximation allows for a good qualitative understanding of the system while keeping the equations short. As a result of this approximation, the  $\alpha$  parameters are independent of  $\gamma_3$  and we discard small terms -at least one order of magnitude smaller than the dominant terms- in  $\alpha_A$  that do not oscillate as  $e^{-4i\varphi}$ , i.e. terms proportional to  $e^{+4i\varphi}$  and to  $(\gamma_3 - \gamma_2)e^{-8i\varphi}$ . To specify where these terms have been neglected in Eq. (5.41), we use the notation 0. and 0 to distin-

guish between terms that are negligibly small but finite (0.) from terms that are exactly zero (0). For Si, Eq. (5.41) reduces to

$$\alpha_I \approx 0.35E_y + 0.246E_y^2 + 0.0086\delta E + 0.0011\delta E^2 - 0.0331E_y\delta E + 0.0124E_y\Sigma E + 0.00011\delta E\Sigma E, \quad (5.42a)$$

$$\alpha_A(\varphi) \approx e^{-4i\varphi} (2.631 - 0.367E_y^2 - 0.00078\delta E^2 + 0.0372\Sigma E + 0.00053\Sigma E^2 + 0.0398\delta E E_y) . \quad (5.42b)$$

These expressions give valuable insights into the dependence of the spin-orbit coupling on the external fields and allow for a qualitative understanding of the numerical results presented in Sec. 5.3 and 5.3. For example, let us take the limit  $\Sigma E = 0$  as in the main text. To obtain  $v = 0$ , the intrinsic and electric field dependent spin-orbit couplings need to have opposite signs. By looking at Eq. (5.42), it is clear that the DRA, with  $\varphi = \pi/4$ , can drive the switch because in this case all the terms varying with the electric field have the opposite sign with respect to the intrinsic coupling. In this case, when  $\delta E = 0$ , we find that  $v = 0$  at  $E_{\text{DRA}}^{\text{SW}} \approx 1.52$  and when  $E_y = 0$ ,  $v = 0$  at  $\delta E^{\text{SW}} \approx 29.5$ . Quantitatively, the values of these critical fields are only accurate up to prefactors of order one, see Eqs. (5.12a) and (5.16).

The spin-orbit coupling vanishes also when the fields  $E_y$  and  $\delta E$  are both present. The precise shape of the curve along which this occurs strongly depends on the numerical values of the  $\alpha$  parameters. Using Eq. (5.42), one predicts  $v = 0$  along two separate lines that do not intersect, while numerically we observe that the two lines merge together, see the blue curve in Fig. 5.4b). This discrepancy is a consequence of the numerical inaccuracy of the approximation used: slight variations of the cross-coupling terms  $\propto E_y\delta E$  can drastically change the behaviour of the switching curve. We note that the correct qualitative behaviour of  $v$  is restored by including higher powers of  $\epsilon$  in the expansion in Eq. (5.41), but we do not give explicit expressions for these terms here.

## Comparison with square cross-section

We summarize now the key qualitative differences between Si FinFETs with equilateral triangular cross-section and Si wires with an inversion symmetric cross-section. In particular, here we focus on wires with a square cross-section; a detailed analysis of the direct Rashba spin-orbit coupling in these wires can be found in Ref. [16]. The first key difference is that without external fields, the inversion symmetry of a square

cross-section prohibits the presence of an intrinsic spin-orbit coupling, and  $\mathbf{v}_0^{\text{sq}} = 0$ . Another important difference between the two systems is that the amplitude of the spin-orbit velocity in a square wire is a symmetric function of the homogeneous electric field, and  $|\mathbf{v}^{\text{sq}}(E_y)| = |\mathbf{v}^{\text{sq}}(-E_y)|$ . In contrast, in a triangular wire, the spin-orbit coupling does not need to be symmetric and the spin-orbit velocity  $v$  is modified in different ways when the hole wavefunction is pushed to the bottom or to the apex of the triangle, see Fig. 5.3. We notice, however, that the amplitude of the spin-orbit velocity in triangular wires is still a symmetric function of the homogeneous field  $E_x$ .

To make a more quantitative comparison, we consider a Si wire with side  $L$  grown along the  $z \parallel [001]$  direction. To linear order in the electric field, the direct Rashba spin-orbit coupling can be written as [16]

$$v^{\text{sq}} \approx \frac{\hbar}{mL} [-0.41 (\gamma_3 - \gamma_2) e^{-4i\varphi} + 0.38 (\gamma_3 + \gamma_2)] \frac{eE_y L}{\epsilon_c^{\text{sq}}}, \quad (5.43)$$

where  $\epsilon_c^{\text{sq}} = \hbar^2 \pi^2 \gamma_1 / mL^2$  is the characteristic confinement energy for a particle in a square cross-section. To obtain this expression, we combined Eqs. (77), (78), (79), and (80) in Ref. [16] and used the Luttinger parameter of Si. To facilitate the comparison with our Eqs. (5.13) and (5.14) obtained for an equilateral triangle, we also introduced the imaginary spin-orbit velocity  $v^{\text{sq}} = \mathbf{v}_x^{\text{sq}} + i\mathbf{v}_y^{\text{sq}}$ , we expanded the function  $\chi(\varphi) = 0.36 / (1 + 0.16(\gamma_3 - \gamma_2) \cos(4\varphi))$  [directly related to the function in Eq. (79) of [16]] to linear order in  $(\gamma_3 - \gamma_2) \cos(4\varphi)$ , and we discarded the small terms oscillating as  $e^{4i\varphi}$  and  $e^{-8i\varphi}$ . The overall minus sign of the spin-orbit velocity here compared to Eq. (80) in Ref. [16] is a result of the field being applied in the  $y$ -direction instead of the  $x$ -direction.

Comparing Eqs. (5.13) and (5.43), we observe that in square and triangular wires the spin-orbit coupling is a sum of an isotropic term and an anisotropic term, proportional to  $\gamma_3 + \gamma_2$  and to  $\gamma_3 - \gamma_2$ , respectively. To linear order in  $E_y$ , the isotropic contributions in both cross-sections are in good quantitative agreement, but the anisotropic terms are qualitatively different, see Eq. (5.14). In fact, while in square wires the anisotropic term varies linearly with  $E_y$  and its contribution to the overall direct Rashba spin-orbit velocity is roughly equal to the isotropic contribution, in a triangular wire  $\alpha_A(\varphi)$  comprises a constant intrinsic term and has a negligible linear dependence on  $E_y$ .

Including higher powers in the electric field, we find an additional qualitative difference between the spin-orbit coupling in the two differ-

ent cross-sections. In fact, in a square wire, the spin-orbit velocity has no corrections quadratic in  $E_y$  and the next order corrections are proportional to  $E_y^3$ . In contrast, in a triangular FinFET, both  $\alpha_I$  and  $\alpha_A$  present quadratic terms proportional to  $E_y^2$ , that make  $v$  asymmetric in  $E_y$ , see Eq. (5.14).

These qualitative differences are crucial here because, as discussed in Sec. 5.3, in triangular wires the presence of a spin-orbit switch at a finite value of the electric field is a result of the competition between the intrinsic spin-orbit coupling and the direct Rashba-like spin-orbit interaction dependent on the electric field. In a square Si wire there is no intrinsic spin-orbit velocity and the spin-orbit coupling only vanishes when  $E_{x,y} = 0$  (or when  $E_{x,y} \rightarrow \infty$ , see Eq. (86) in Ref. [16]), a much inconvenient working point for electrostatically defined quantum dots.

Finally, another difference between triangular and square cross-sections comes from the sensitivity of the spin-orbit coupling to the quadratic potential  $\delta E_{ij} r_i r_j / 2$ , see Eq. (5.2). Without an homogeneous electric field, such a potential is inversion symmetric and does not produce spin-orbit coupling in square wires. In contrast, in Sec. 5.3, we show that this potential can produce another spin-orbit switch in triangular FinFETs, where the inversion symmetry is broken by the cross-section.

## 5.D Spin-orbit coupling against $\delta E_{ii}$

In the main text, we assume that the inhomogeneous electric field tensor is diagonal and  $\delta E_{xx} \approx -\delta E_{yy} \equiv \delta E$ . Here, we show that the presence of the spin-orbit switch is not related to this approximation by examining separately the effect of the fields  $\delta E_{xx}$  and  $\delta E_{yy}$  on the spin-orbit velocity. We restrict ourselves to the analysis of FinFETs grown along the [001] direction, with  $\theta = 0$ . In this section, we consider  $E_y = 0$ .

In Fig. 5.14, we study the spin-orbit velocity in equilateral triangles. In the top Figs. 5.14a) and 5.14b), we show the results obtained for large wires neglecting the SOHs and using the  $4 \times 4$  LK Hamiltonian. The two figures correspond to the DRA and CA, respectively. The purple line marks the approximation  $\delta E_{xx} = -\delta E_{yy}$  used in the main text. We observe that in the DRA,  $|v| = 0$  also by considering a more general relation between the inhomogeneous fields  $\delta E_{yy} = c_{yy} \delta E_{xx} / c_{xx}$ , see Eq. (5.25). The spin-orbit coupling is not suppressed only when  $|c_{yy} / c_{xx}| \ll 1$ . We remark that the parameters  $c_{yy}$  and  $c_{xx}$  can vary depending on the device design. In the same regime of parameters, we do not find a comparable

sweet spots for the CA. In the bottom Figs. 5.14c) and 5.14d), we show the results obtained by including the SOHs for an equilateral triangular cross-section of side  $L = 20$  nm. For the DRA, the spin-orbit coupling vanishes for any value of the ratio  $|c_{yy}/c_{xx}|$  and interestingly also when  $|c_{yy}/c_{xx}| \ll 1$ , in contrast to when the SOHs are neglected. In addition, the SOHs modify the response when the wire is grown along the crystallographic orientation. In fact, in Fig. 5.14d) we observe that the spin-orbit velocity vanishes along the vertical line  $\delta E_{xx} \approx 30\epsilon_c/(eL^2)$ . While this result shows that also this orientation might present suitable working points where charge noise is suppressed, we do not investigate this possibility further.

We now study how these results change when we consider wires with an isosceles triangular cross-section as the ones studied in Sec. 5.4. We consider a FinFET in the DRA and in Fig. 5.15, we compare the spin-orbit velocity in isosceles triangles with the same area  $\sqrt{3}\tilde{L}^2/4$  and different aspect ratios  $r = L_x/L_y$ . Here, we fully account for the SOHs and we use an effective side length of  $\tilde{L} = 20$  nm. In the top Figs. 5.15a) and 5.15b), we show the spin-orbit velocity when the triangle is narrow. When  $r = 0.8$ , the spin-orbit coupling is still suppressed when  $\delta E_{yy} = c_{yy}\delta E_{xx}/c_{xx} = -\delta E_{xx}$  (purple line), but when the ratio  $|c_{yy}/c_{xx}| \lesssim 1$ , the spin-orbit coupling does not vanish and the charge noise sweet spot is removed. Even worse, when  $r = 0.7$ , the spin-orbit coupling vanishes only when the ratio  $|c_{yy}/c_{xx}| \gg 1$ , away from the limit studied in the main text. In the bottom Figs. 5.15c) and 5.15d), we show the spin-orbit velocity when the triangle is wide. In contrast to the narrow triangle, here the spin-orbit coupling vanishes for any values of the ratio  $|c_{yy}/c_{xx}|$ . By increasing  $r$ , we observe that the line where  $|v| = 0$  is pushed towards lower values of  $\delta E$  and when  $r = 1.5$ , an additional line where the spin-orbit coupling vanishes appears. However, we also note that the maximal spin-orbit velocity in these devices decreases compared to the equilateral FinFET, see Fig. 5.14c).

## 5.E Effect of strain

Here, we examine in detail how strain modifies the spin-orbit coupling. In particular, we extract the maximal strain that the system can support before the spin-orbit switch is removed. We restrict ourselves to the analysis of heavy and light holes of a fin grown along the DRA, where the

effect of the strain tensor elements  $\epsilon_{ij}$  is well-described by the Bir-Pikus Hamiltonian [1, 82]

$$H_{\text{BP}}^{\text{DRA}} = \epsilon_0^S J_z^2 + \begin{pmatrix} 0 & \epsilon_1^S & \epsilon_2^S & 0 \\ (\epsilon_1^S)^* & 0 & 0 & \epsilon_2^S \\ (\epsilon_2^S)^* & 0 & 0 & -\epsilon_1^S \\ 0 & (\epsilon_2^S)^* & -(\epsilon_1^S)^* & 0 \end{pmatrix}, \quad (5.44)$$

with

$$\epsilon_0^S = -2b(\epsilon_{xx} + \epsilon_{yy} - 2\epsilon_{zz}), \quad (5.45a)$$

$$\epsilon_1^S = d(\epsilon_{xz} - i\epsilon_{yz}), \quad (5.45b)$$

$$\epsilon_2^S = \frac{\sqrt{3}}{2}b(\epsilon_{xx} - \epsilon_{yy}) + id\epsilon_{xy}. \quad (5.45c)$$

For Si, the parameters  $b = -2.2$  eV and  $d = -5.1$  eV can be found e.g. in Ref. [1].

In general, the strain elements  $\epsilon_{ij}$  are functions of position, resulting in a complicated spin-dependent potential. We estimate the strain profile in the Si FinFET shown in Fig. 5.1, when a pressure of 100 MPa is applied pushing the top interface downwards in the  $y$ -direction. For the simulation, we used the Structural Mechanics module of COMSOL Multiphysics® [90], and considered an equilateral triangular cross-section of side  $L = 20$  nm, and a substrate thickness of  $d_B = 20$  nm. We imposed free boundary condition on the substrate in the  $x$ -direction, while the bottom interface is kept fixed. The total width of the substrate in the  $x$  direction is 50 nm, with the fin being placed in the middle.

The relevant combination of the strain tensors are shown in Fig. 5.16. With this simple model, we observe that most terms are rather homogeneous in the cross-section, and thus we study the effect of constant values of the  $\epsilon_i^S$  energies. The homogeneous approximation is reasonable for the diagonal elements  $\epsilon_{ii}$ , but it is more debatable for the cross-terms  $\epsilon_{ij \neq i}$ . In particular, the term  $\epsilon_{xy}$  has also a component that varies linearly in the  $x$ -direction, and so we extend our analysis by using  $\text{Im}[\epsilon_2^S(x)] \approx \text{Im}(\epsilon_2^S) + x\partial_x \text{Im}(\epsilon_2^S)$ . Note however that in our simulation we are applying the pressure directly on the top of the Si structure. Applying the pressure on the electrode could potentially reduce the strain close to the boundaries of the Si triangle, due to the effect of the gate oxide. We also point out that the terms  $\epsilon_{zz}$  and  $\epsilon_{iz}$  are likely to have a  $z$ -dependence when qubits are defined and the top gate is terminated along the  $z$ -direction.

However, we expect the strain field to be strongly peaked in a narrow region close to the edges of the electrodes, where the hole density is small, and, in the following, we neglect these inhomogeneities.

By studying the effect of each term independently, we find a reasonable estimation of the strain that the system can support. The results of this analysis are given in Fig. 5.17, where we show how the spin-orbit velocity dependence on  $E_y$  and  $\delta E$  is affected by the strain energies  $\epsilon_i^S$  given in Eq. (5.45). Here, we express the energies  $\epsilon_i^S$  in terms of the confinement energy  $\epsilon_c \approx 17.2/L^2 \text{ eV} \times \text{nm}^2$ . A positive and negative diagonal strain  $\epsilon_0^S$  is examined in Figs. 5.17a) and 5.17b), respectively. The spin-orbit switch is robust against  $\epsilon_0^S$ , but the shape of the curve along which  $|v| = 0$  changes and, in particular, negative (positive) values of the strain narrow (widen) the curve. We extract bounds on the maximal strain allowed by considering that when  $\epsilon_0^S/\epsilon_c \gtrsim 0.1$ , the  $|v| = 0$  curve is too wide and the inhomogeneous switch  $\delta E^{SW}$  disappears from the range of parameters considered. In contrast, when  $\epsilon_0^S/\epsilon_c \lesssim -0.035$ , the curve becomes too narrow and results in a finite spin-orbit coupling in the whole parameter space.

Similar physics appears when the contribution of  $\text{Re}(\epsilon_2^S) \propto \epsilon_{xx} - \epsilon_{yy}$  is examined, see Figs. 5.17c) and 5.17d) for positive and negative values of  $\text{Re}(\epsilon_2^S)$ , respectively. In fact, the spin-orbit switch persists, but the  $|v| = 0$  curve is modified by the strain. In particular, when  $\text{Re}(\epsilon_2^S) < 0$  the inhomogeneous field  $\delta E$  is strongly enhanced and the switching field  $\delta E^{SW}$  is pushed towards lower values. For this reason, a moderate negative strain might be helpful to compensate for the SOHs, in analogy to the wide FinFET discussed in Sec. 5.4. We do not explore this intriguing possibility in more detail. In analogy to before, we extract the bounds  $\text{Re}(\epsilon_2^S)/\epsilon_c \in [-0.1, 0.1]$  by verifying when the switch is pushed outside the range of parameters studied.

In contrast, the homogeneous components of the cross-couplings  $\epsilon_{ij}$  remove the spin-orbit switch, but the shape of the curve where  $|v|$  is minimal does not change. In Figs. 5.17e) and 5.17f), we show how the terms  $\text{Im}(\epsilon_2^S) \propto \epsilon_{xy}$  and  $\text{Im}(\epsilon_1^S) \propto \epsilon_{yz}$  influence  $|v|$ . The effect of  $\text{Re}(\epsilon_1^S) \propto \epsilon_{xz}$  is analogous to the effect of  $\epsilon_{yz}$  and is not reported here. To find bounds on the maximal strain allowed, we estimate that when  $|\text{Im}(\epsilon_1^S)|/\epsilon_c < 0.025$  and  $|\text{Im}(\epsilon_2^S)|/\epsilon_c < 0.025$ , the minimal value of the spin-orbit coupling is lower than 10% of the maximal coupling. We report the limiting values of the tensor elements  $\epsilon_{ij}$  in Eq. (5.18).

Finally, in Figs. 5.17g) and 5.17h), we show how the largest inhomogeneous strain component  $x\partial_x \text{Im}(\epsilon_2^S)$  alters  $|v|$ . In analogy to  $\epsilon_0^S$  and  $\text{Re}(\epsilon_2^S)$ ,



the spin-orbit coupling vanishes along a curve that is rescaled by strain. We estimate that the physics described in the main text remains qualitatively valid when  $L\partial_x \text{Im}(\epsilon_2^S)/\epsilon_c \in [-0.15, 0.5]$ , from which it follows that  $L\partial_x \epsilon_{xy} \in [-1.7\%, 0.5\%] \times (L/10 \text{ nm})^{-2}$ .

From Fig. 5.16, we see that when  $L = 20 \text{ nm}$ , the cross-term  $\epsilon_{xy} \in [-0.06\%, 0.06\%]$ , resulting in  $|L\partial_x \epsilon_{xy}| \sim 0.1\%$ . This value is smaller but still comparable to the estimated bound. However, we observe that most of the inhomogeneity of the strain comes from hotspots at the boundary of the triangle, where the wavefunction has no support, and thus the effective value of  $|L\partial_x \epsilon_{xy}|$  is even smaller in more realistic scenarios. In addition, while the homogeneous part of the cross-terms  $\epsilon_{ij \neq i}$  remove the spin-orbit switch, from the simple simulations shown in Fig. 5.16, we expect those terms to be rather small. Thus, we believe that the conditions on the homogeneous part of the diagonal elements  $\epsilon_{ii}$  are the most stringent ones.

## 5.F Compensating for the SOHs

In Sec. 5.4, we show that the SOHs can remove the spin-orbit switch in small wires and wide DRA FinFETs are proposed to restore the sweet spot. Here, we discuss other possible design concepts valid for both SOI and bulk Si FinFETs that can compensate for the SOHs. In particular, in equilateral SOI FinFETs the spin-orbit can be switched-off in wires grown along the  $[110]$  direction (SA) by pushing the hole wavefunction at the bottom of the triangles, while in bulk FinFETs, the spin orbit switch is naturally recovered by considering the leakage of the hole wavefunction into the Si substrate; a summary of the different designs considered is given in Table 5.2.

In small equilateral SOI FinFETs, the spin-orbit velocity can also be suppressed by pushing the hole wavefunction towards the bottom of the fin by a positive gate potential. As discussed in Sec. 5.3, in a wire grown along the  $[110]$  direction (SA) with an equilateral triangular cross-section, the spin-orbit velocity vanishes by the effect of a negative homogeneous electric field  $E_{SA}^{SW} < 0$ , see Eq. (5.12). In Fig. 5.18a), we show the dependence of this switching field on the size of the equilateral cross-section. In this case, the SOHs do not remove the sweet spot, but they push it to lower values of the homogeneous electric field, that can be reached by a smaller gate potential. In Fig. 5.18b), we study the spin-orbit coupling in an equilateral wire with side  $L = 20 \text{ nm}$  when also  $\delta E$  is included. In this

FinFET	Orientation	Aspect ratio	$l_{so}^{\min}$	$V_g^{SW}$
SOI/Bulk	DRA	$r = 1.2$	$1.5\tilde{L}$	$-3.12$ V
SOI	SA	$r = 1$	$4L$	$+0.72$ V
Bulk	DRA	$r = 1$	$10L$	$-0.28$ V

Table 5.2: Examples of FinFETs designs where the spin-orbit sweet spot is restored in the small cross-section limit. To estimate the values of minimal spin-orbit length we consider devices with  $L = \tilde{L} = 20$  nm. For the first two designs, we consider a back gate at  $d_B = 100$  nm, while for the last FinFET, we consider a cross-section 120 nm wide and 60 nm high.  $V_g^{SW}$  increases by increasing  $d_B$  or by decreasing  $L$ .

case, we observe that, along the purple line defined by Eq. (5.17),  $|v|$  vanishes at the gate potential  $V_g^{SW} \approx +57.3 \times \text{nm}^2 d_B / \tilde{L}^3$  V, corresponding to  $V_g^{SW} \approx +0.72$  V when  $\tilde{L} = 20$  nm and  $d_B = 100$  nm, easily achievable in state-of-the-art devices. The total hole density  $|\psi|^2$  at the switching potential  $V_g^{SW}$  is shown in the inset of Fig. 5.18b). Comparing to the wide DRA FinFET, we find that in the regime of parameters examined, the SA device has a larger minimal spin-orbit length  $l_{so}^{\min} \approx 4L$ , leading to smaller spin-orbit interactions when the qubit is operational.

So far, we focused on FinFETs, where the triangular fin is well-separated from the bulk and we modelled these systems by using hard-wall boundary conditions at the edges of the triangle. This approximation is valid as long as the hole wavefunction is well-confined inside the fin, such that the substrate can be neglected. In bulk Si FinFETs, there is a thick substrate that is strongly coupled to the holes in the wire and the confinement potential that localizes the holes in the fin is provided by the negative potential  $V_g$  applied to the top gate. By fully simulating this cross-section, in Fig. 5.19, we show that a convenient working point where the spin-orbit velocity can be completely removed at smaller values of the gate potential [see Table 5.2] emerges naturally also in these systems when the wire is grown in the DRA. To obtain this result, we simulate a cross-section composed of an equilateral triangular fin with side  $L = 20$  nm symmetrically placed on top of a rectangular substrate 120 nm wide and 60 nm high. For this simulation, we used the  $6 \times 6$  LK Hamiltonian and the electrostatic potential generated by the top gate is calculated by solving the Laplace equation with the boundary conditions described in App. 5.A. When  $|V_g| \gtrsim 0.1$  V, the holes are confined in the fin and the

spin-orbit velocity shows a behaviour that is in qualitative agreement with our treatment, see e.g. Fig. 5.3. The results obtained for lower values of the gate potential  $|V_g| < 0.1$  V, where the hole wavefunction is largely spread in the substrate are inaccurate and have been removed from the figure. In this system,  $|v| = 0$  at  $V_g^{SW} = -0.28$  V, where the wavefunction is strongly localized into the fin, see the inset of the figure; in larger devices, we expect again that the potential will scale roughly as  $V_g^{SW} \propto d_B/L^3$ . While the spin-orbit coupling can be conveniently switched off in this setup, we also estimate that the minimal spin-orbit length  $l_{so}^{\min} \sim 10L$  is larger than in the other designs.

Finally, in App. 5.E, it is shown that strain can enhance the effect of the inhomogeneous electric field  $\delta E$  on the spin-orbit velocity. Consequently, we expect that one could recover the spin-orbit switch also by appropriately engineering the strain field in the device. However, here we do not analyze this possibility more quantitatively.

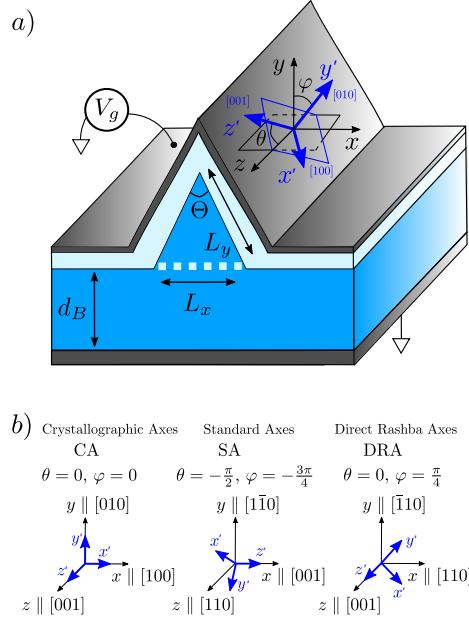


Figure 5.1: Sketch of a Si FinFET. In a), the blue and lightblue areas represent the semiconductor and the dielectric, respectively, while the gray areas are the metallic gates. The orientation of the Si FinFET with respect to the crystallographic axes (blue axes) depends on the angles  $\theta$  and  $\varphi$ . The wire extends along the  $z$ -direction and the fin has an isosceles triangular shape with base  $L_x$ , equal sides  $L_y$  and height parallel to the  $y$ -direction. The apex angle of the triangle is  $\Theta$ . We call wide and narrow FinFETs the  $\Theta > \frac{\pi}{3}$  and  $\Theta < \frac{\pi}{3}$  devices, respectively; the FinFET is equilateral when  $\Theta = \frac{\pi}{3}$ . The dashed line at the bottom of the fin indicates the lower boundary of the fin. In a SOI FinFET there is a clear physical separation between the Si substrate and the wire, which is provided by a thick dielectric layer at the position of the dashed line. In contrast, in bulk Si FinFET, there is no physical separation between substrate and the fin. In this case, the holes are localized in the fin by negative values of the gate potential  $V_g$  applied with respect to a grounded back gate at a distance  $d_B$  from the bottom of the triangle. In b), we show the main orientations of the axes of confinement with respect to the crystallographic axes.

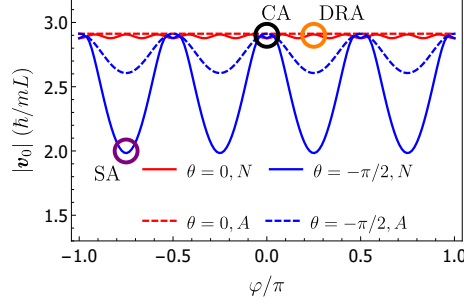


Figure 5.2: Intrinsic spin-orbit velocity  $|v_0|$  without external electric fields in an equilateral FinFET. We compute  $|v_0|$  as a function of the angle  $\varphi$  at  $\theta = 0$  (red lines) and  $\theta = -\pi/2$  (blue lines). The dashed lines are obtained by the approximate Eqs. (5.10) and (5.11), while the solid lines are obtained numerically by using Eq. (5.5) and including 200 orbital states in Eq. (5.27). We mark with black, orange, and purple circles the results obtained for the relevant orientations of axes CA, DRA, and SA, respectively, see Fig. 5.1b).

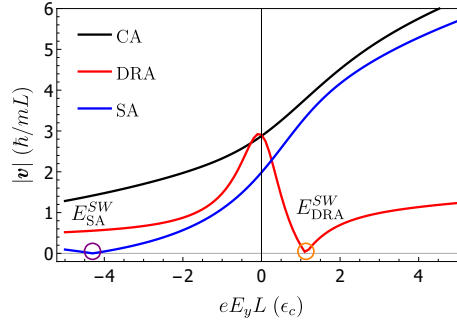


Figure 5.3: Spin-orbit velocity  $|v|$  as a function of the homogeneous electric field  $E_y$  in an equilateral FinFET. We neglect the inhomogeneous contribution to the electric field profile and we compute  $|v|$  for the growth directions in Fig. 5.1b). At negative (positive) electric fields, i.e. when the hole wavefunction is pushed to the bottom (apex) of the triangle,  $|v|$  can be zero when the wire is grown along the SA (DRA). We show the sweet spot  $E_{SA}^{SW}$  ( $E_{DRA}^{SW}$ ) see Eq. (5.12), with a purple (orange) circle.

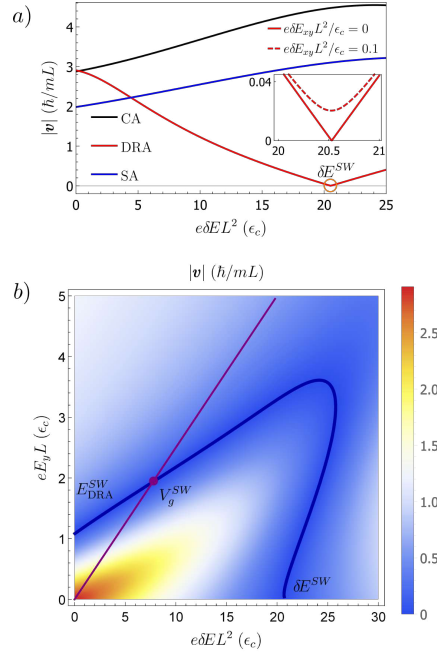


Figure 5.4: Spin-orbit velocity  $|v|$  as a function of the inhomogeneous electric field  $\delta E$  in an equilateral FinFET. In a) we use the confinement potential in Eq. (5.15) without the homogeneous field  $E_y$  and study how  $|v|$  varies for the wire orientations in Fig. 5.1b); for the DRA device,  $|v|$  vanishes at the field  $\delta E^{SW}$  given in Eq. (5.16). In the inset, we show the effect of  $\delta E_{xy}$  for the DRA close to the switching field  $\delta E^{SW}$ . In b) we show how  $|v|$  varies for the DRA device when  $\delta E$  and  $E_y$  are tuned independently. Here,  $|v|$  vanishes along the blue curve that connects  $E_{DRA}^{SW}$  and  $\delta E^{SW}$ . In the device studied here,  $E_y$  and  $\delta E$  are constrained on the purple line defined by Eq. (5.17). From the intersection of the purple and blue lines, one finds the gate potential  $V_g^{SW}$  of the spin-orbit switch.

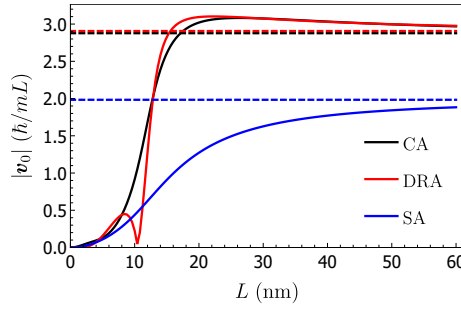


Figure 5.5: Intrinsic spin-orbit velocity  $|v_0|$  as a function of the side length  $L$  of an equilateral FinFET. We compare the effect of the SOHs in wires grown along the orientations in Fig 5.1b) by showing with solid (dashed) lines the values of  $|v_0|$  obtained by the  $6 \times 6$  ( $4 \times 4$ ) LK Hamiltonian that includes (neglects) the SOHs.

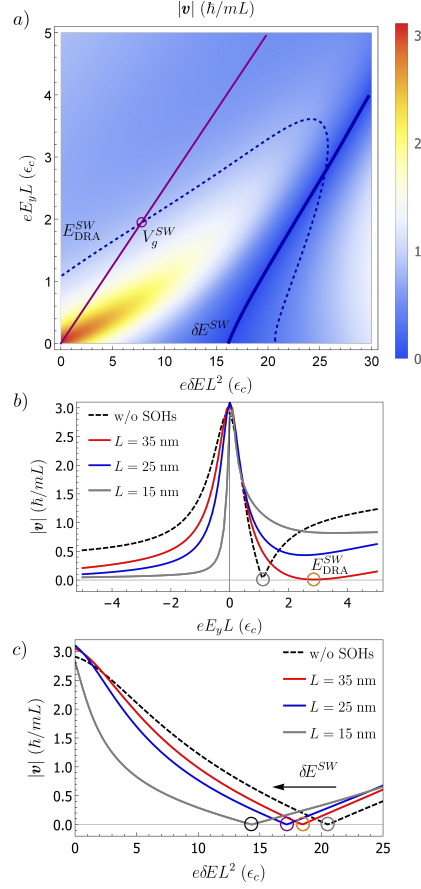


Figure 5.6: Effect of the SOHs on the spin-orbit switch in small equilateral wires grown along the DRA. In a), we show how  $|v|$  varies in a wire with cross-section  $L = 20$  nm as a function of homogeneous and inhomogeneous electric field,  $E_y$  and  $\delta E$ , respectively. When the SOHs are included, the spin-orbit switch driven by  $E_y$  is removed and  $|v|$  vanishes only because of the inhomogeneous field  $\delta E$ . To facilitate the comparison with Fig. 5.4b), we show with a dashed blue line the curve along which  $|v|$  vanishes in large wires. Importantly, when  $\delta E$  and  $E_y$  are constrained on the purple line [see Eq. (5.17)], the SOHs remove the spin-orbit switch at  $V_g^{SW}$ . In b) and c) we study how the SOHs affect the dependence of  $|v|$  on  $E_y$  and  $\delta E$  when the cross-section side  $L$  is varied. While the homogeneous spin-orbit switch  $E_{DRA}^{SW}$  is removed for wires with  $L \lesssim 35$  nm, the inhomogeneous switch  $\delta E^{SW}$  remains and is pushed to lower values as the side length decreases. In the units used, the results obtained without the SOHs are independent of  $L$ .



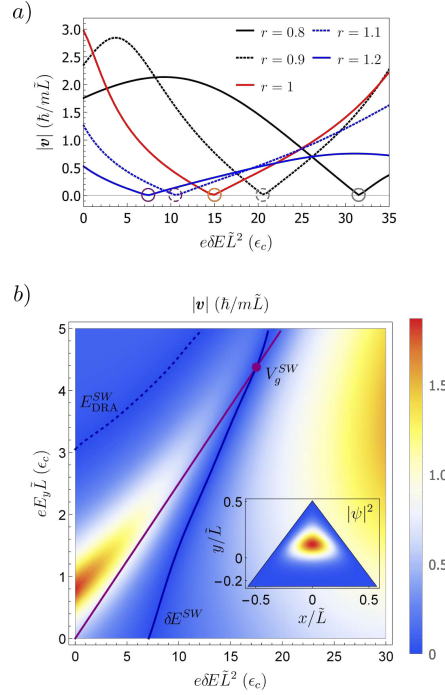


Figure 5.7: Spin-orbit velocity  $|v|$  in a wide FinFET grown along the DRA. In a) we show how the dependence of  $|v|$  on the inhomogeneous electric field  $\delta E$  varies as a function of the aspect ratio  $r$  [see Eq. (5.19)] of the triangular cross-section. We compare triangles with the same area  $\sqrt{3}\tilde{L}^2/4$ , with effective length  $\tilde{L} = 20$  nm. When  $r > 1$  ( $r < 1$ ) the FinFET is wide (narrow). In b) we show  $|v|$  as a function of  $E_y$  and  $\delta E$  for a device with  $r = 1.2$  and  $\tilde{L} = 20$  nm. The solid blue line shows the spin-orbit switch driven by the inhomogeneous field  $\delta E$ . The spin-orbit switch driven by the homogeneous field  $E_y$  is also restored and  $|v|$  vanishes along the dashed blue curve. In the FinFET studied here,  $\delta E$  and  $E_y$  are constrained along the purple line defined by Eq. (5.17). In the inset, we show the density  $|\psi|^2$  of the hole wavefunction in the cross-section at the switching point  $V_g^{SW}$  where purple and blue lines intersect. The hole density vanishes in the blue region and attains maximal value in the red region.

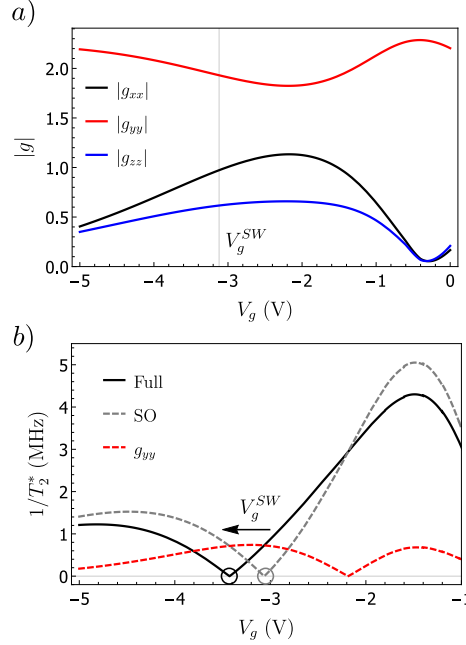


Figure 5.8: Anisotropic  $g$ -factor and dephasing rate  $1/T_2^*$  of a Si FinFET qubit as a function of the gate potential  $V_g$ . We analyze a wide FinFET grown along the DRA with  $r = 1.2$  and  $\tilde{L} = 20$  nm. In a), we show the diagonal entries  $g_{ii}$  of the wire  $g$ -factor matrix derived by considering a small magnetic field  $B_i$  in the  $i$ -direction and diving  $\Delta_i$  in Eq. (5.8) by  $\mu_B B_i$ . In this device, the off-diagonal components of the  $g$ -factor matrix vanish. In b), the dephasing rate  $1/T_2^*$  of the qubit caused by charge noise is obtained by combining Eqs. (5.23) and (5.24) when  $B_y = 100$  mT. The black line represents the total dephasing of the qubit, while with dashed gray and red lines we show the contributions to  $1/T_2^*$  of the spin-orbit coupling and of the  $g$ -factor fluctuations, respectively. Because  $\mathbf{B}$  is applied along the  $y$ -direction,  $\Delta_{\parallel} = 0$  in Eq. (5.23) ( $\mathbf{v}$  points in the  $x$ -direction) and there is no relaxation ( $\Delta'_{\perp} \parallel \Delta_{\perp} \parallel \mathbf{Q}$ ). We fix  $\delta E_{zz}/V_g$  such that at  $V_g^{SW} = -3.12$  V the lateral size of the dot in Eq. (5.20) is  $l = 30$  nm. The dependence of  $l_{so}$  on  $V_g$  is found by combining Eqs. (5.2) and (5.17). Here, we use  $d_B = 100$  nm,  $\sqrt{\langle \delta V^2 \rangle} = 0.3$  mV and  $\omega_{ir} = 1$  Hz.

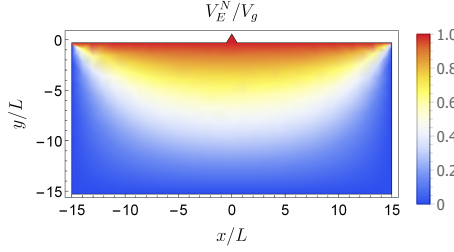


Figure 5.9: Electrostatic potential  $V_E^N$  in the cross-section of a Si FinFET. For the simulation, we used  $d_B = 15L$  and a substrate  $30L$  wide with an equilateral triangular fin of side  $L$  placed on top of it. The top gate covers the whole upper part of the device and is fixed at the potential  $V_g$ ; the rest of the boundary is grounded.

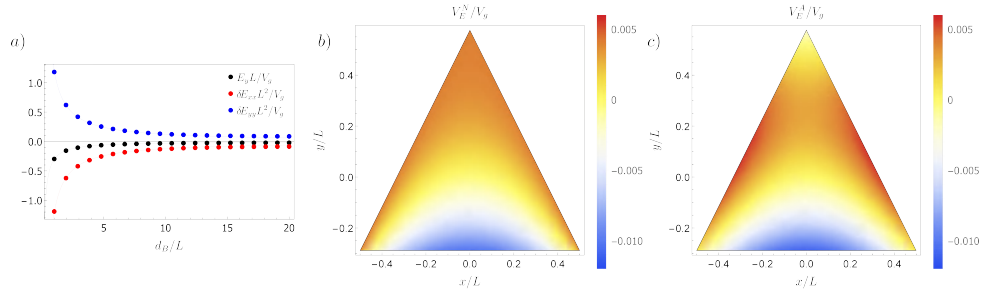


Figure 5.10: Comparison between the electrostatic potential  $V_E^N$  simulated from the Laplace equation and the approximate potential  $V_E^A$ . In a) we show the dependence of the parameters  $\delta E_{ii}$  and  $E_y$  defining  $V_E^A$  on the substrate thickness  $d_B/L$ . The dots are the results of the simulation, while the solid lines are obtained by combining Eqs. (5.25) and (5.26). In b) and c), we show a comparison between the potential in the fin computed numerically (b) and its approximation (c) when  $d_B = 15L$ . To facilitate the comparison, in b), we subtract the constant potential  $V_0 = 0.996$  obtained by averaging the potential in the fin.

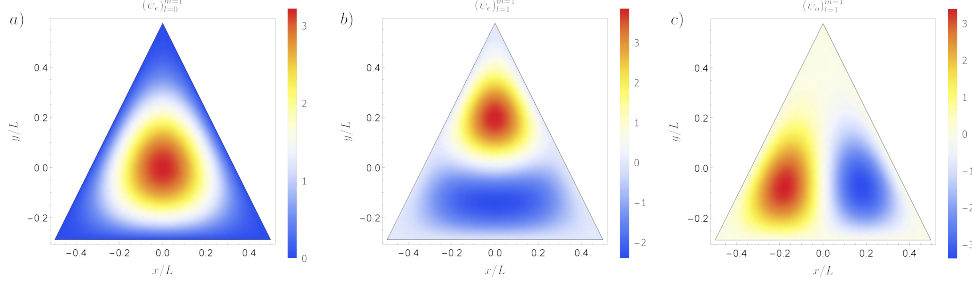


Figure 5.11: First three orbital states in Eq. (5.27) of the Laplace equation in an equilateral triangle. We consider the even solution with  $(l, m) = (0, 1)$  (a) and the solutions with  $(l, m) = (1, 1)$  and even (b) and odd (c) symmetry. The wavefunctions in this plot are normalized. These states are the ones used in App. 5.C.

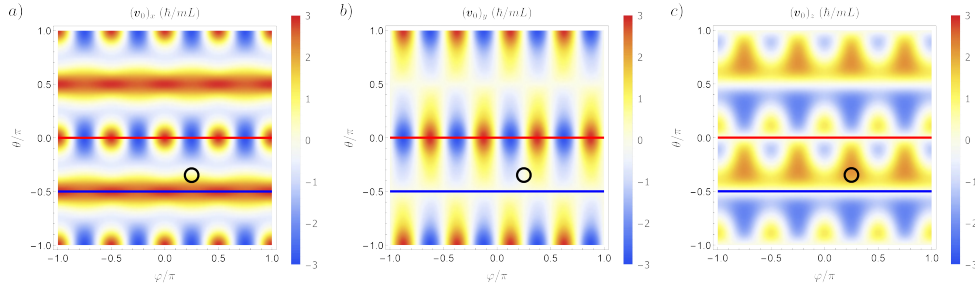


Figure 5.12: Components of the intrinsic spin-orbit vector  $\mathbf{v}_0$  in an equilateral FinFET as a function of the angles  $\theta$  and  $\varphi$  that parametrize the orientation of the wire with respect to the crystallographic axes, see Fig. 5.1. The results shown here are obtained by using a second order Schrieffer-Wolff transformation and including only the lowest 3 orbital states in Eq. (5.27). The wavefunction of these states is shown in Fig. 5.11. We indicate with red and blue lines the cuts  $\theta = 0$  and  $\theta = -\pi/2$ , respectively. These two cases are studied extensively in the main text. The black circle marks the point  $\varphi = \pi/4$  and  $\theta = -\arctan \sqrt{2 + \sqrt{3}}$ , where the wire is grown along the  $z \parallel [111]$  direction, and where  $(\mathbf{v}_0)_{x,y} = 0$  and  $(\mathbf{v}_0)_z$  is maximal.

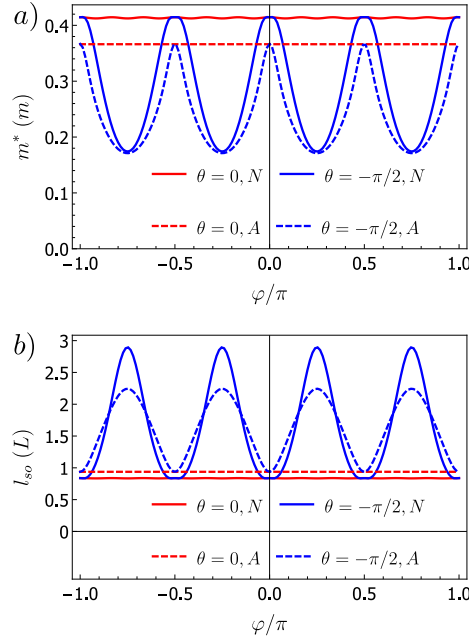


Figure 5.13: a) Effective mass  $m^*$  and b) intrinsic spin-orbit length  $l_{so}$  at zero electric field as a function of  $\varphi$  in an equilateral FinFET. We show with solid lines the results obtained numerically by using Eq. (5.36) for  $m^*$  and by combining Eqs. (5.5), (5.6) and (5.36) for  $l_{so}$ . The dashed lines show the approximate values obtained by a second order Schrieffer-Wolff transformation and including only the lowest three orbital states in Eq. (5.27). For the  $m^*$ , we use Eq. (5.35) and for  $l_{so}$  we combine Eqs. (5.6), (5.35), (5.10) and (5.11). Red and blue lines show results obtained at  $\theta = 0$  and  $\theta = -\pi/2$ , respectively.

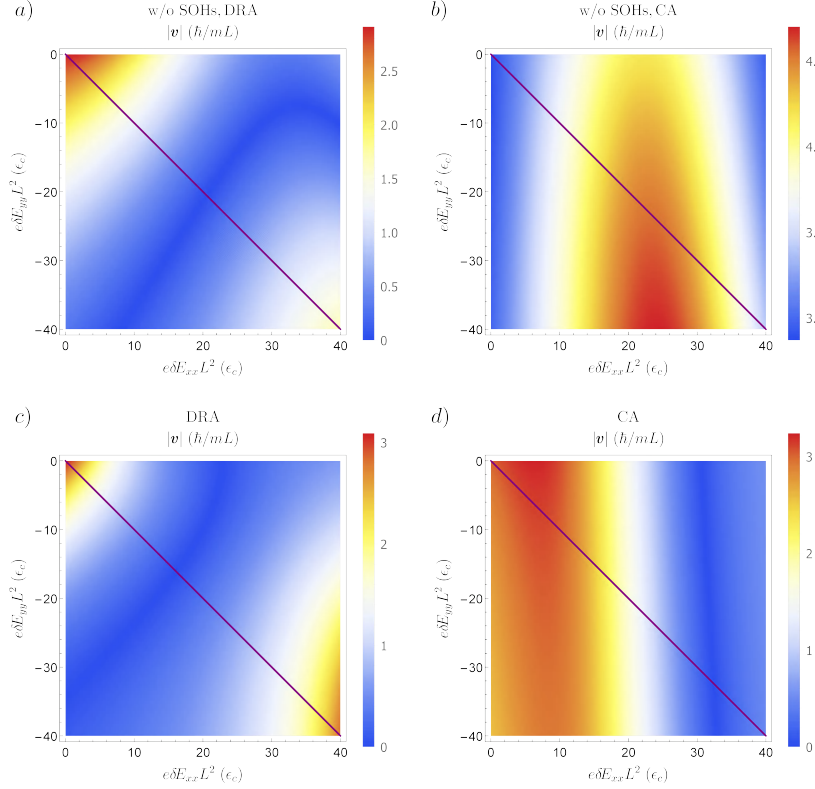


Figure 5.14: Spin-orbit velocity  $|v|$  as a function of  $\delta E_{xx}$  and  $\delta E_{yy}$  when  $\theta = 0$ . Here, we consider an equilateral triangular cross-section. In a) and b) we neglect the SOHs and show results obtained for the DRA and the CA orientations, respectively. In c) and d) we include the SOHs and simulate a wire with cross-section of side  $L = 20$  nm. We show results obtained for the DRA and CA orientations, respectively. The purple lines show the constraint  $\delta E_{xx} = -\delta E_{yy}$ .

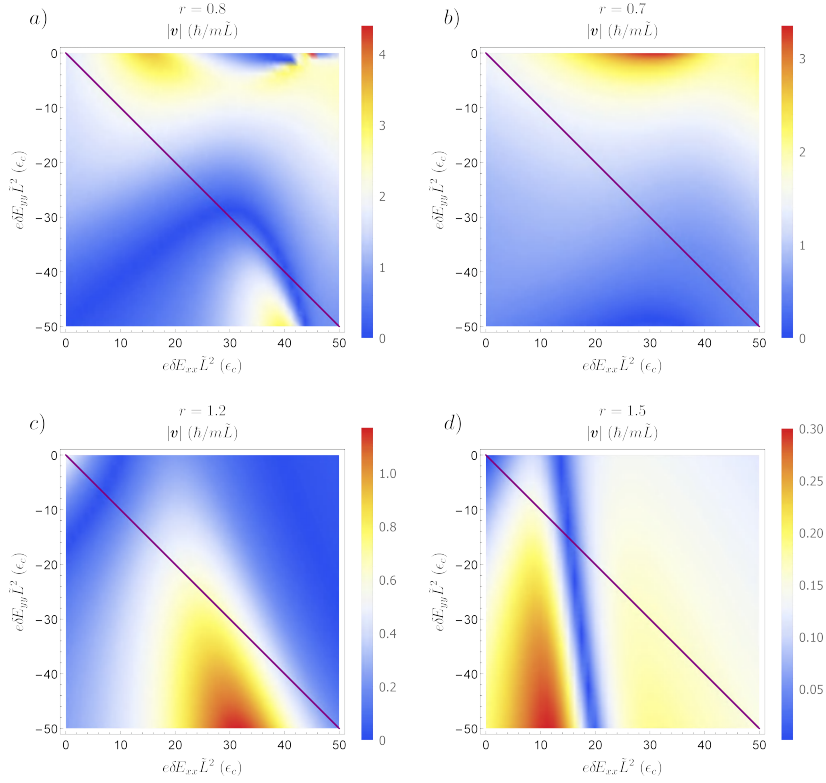


Figure 5.15: Spin-orbit velocity  $|v|$  as a function of  $\delta E_{xx}$  and  $\delta E_{yy}$  for isosceles triangles. Here, we consider wires grown along the DRA orientation whose cross-sections have an effective length  $\tilde{L} = 20$  nm and different aspect ratios  $r = L_y/L_x$ . The SOHs are fully included in these results. In a) and b) we show the spin-orbit coupling obtained for narrow triangles ( $r < 1$ ), while in c) and d) we show the results obtained for wide triangles ( $r > 1$ ). The purple lines show the constraint  $\delta E_{xx} = -\delta E_{yy}$ .

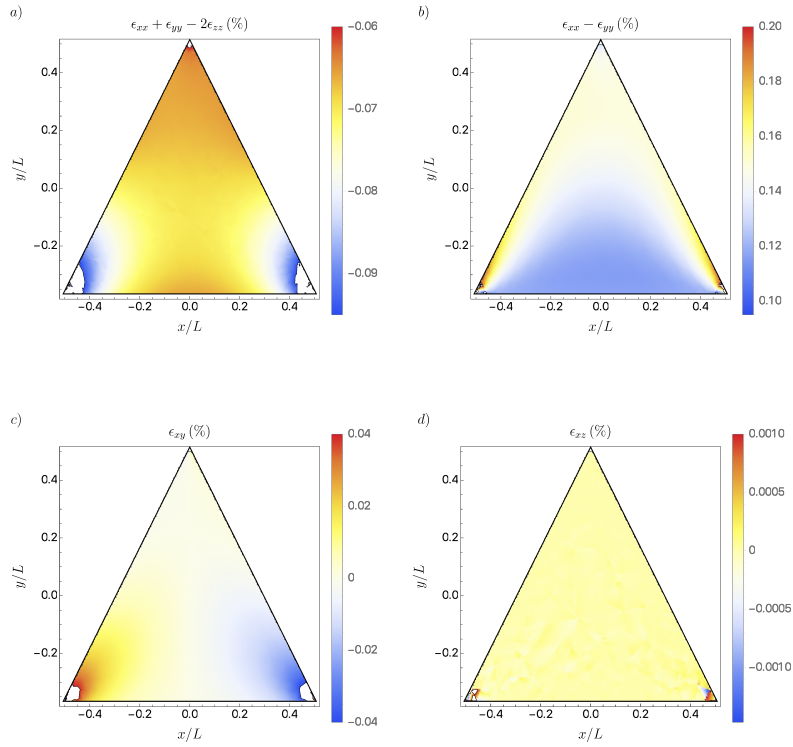


Figure 5.16: Simulation of the strain profile in a Si FinFET. We consider here the strain in a  $L = 20$  nm triangular fin caused by a pressure of 100 MPa applied on the top interface (the two surfaces with side length  $L_y$  in Fig. 5.1), and show the distribution of the relevant combinations of the  $\epsilon_{ij}$  parameters, see Eq. (5.18). The values provided here are given in percentages.



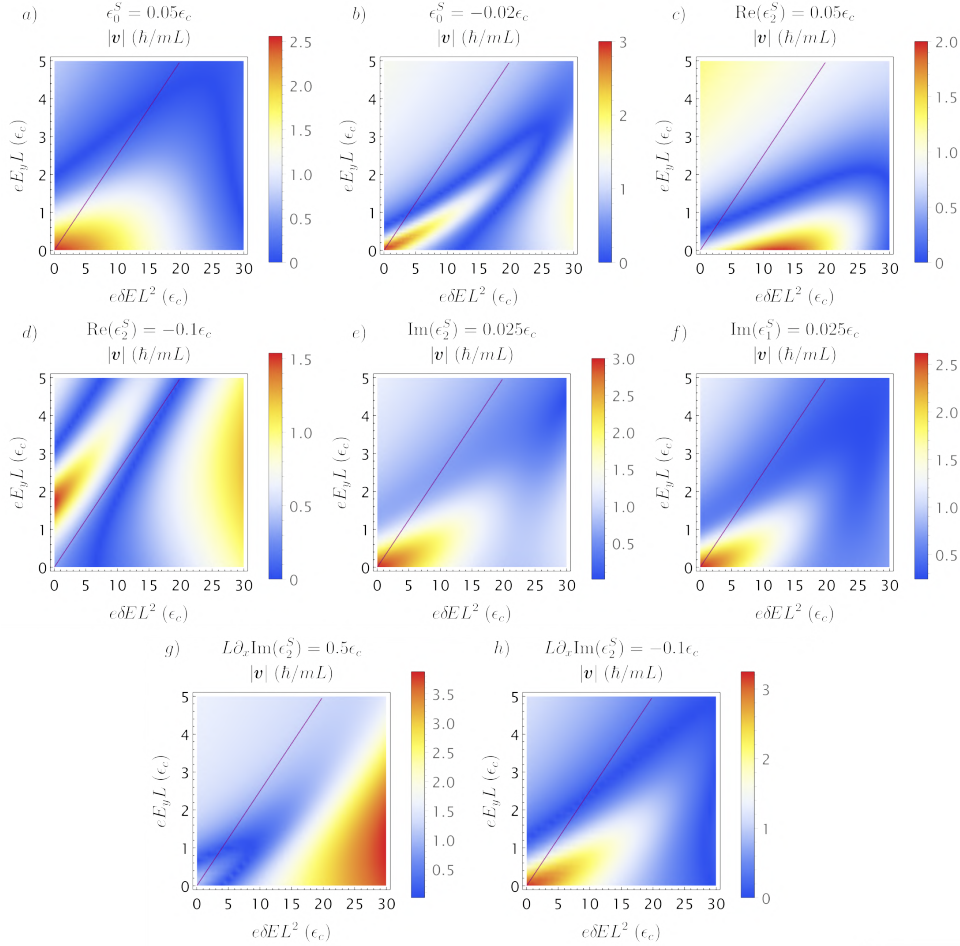


Figure 5.17: Effect of strain on the spin-orbit coupling. We use here the Bir-Pikus Hamiltonian in Eq. (5.44), that is parameterized by the strain energies  $\epsilon_i^S$  related to the strain tensor via Eq. (5.45). The values used in the simulation are given in units of  $\epsilon_c$ , see Eq. (5.9). In a) and b), we show how the dependence of  $|v|$  as a function of  $E_y$  and  $\delta E$  changes by positive and negative values of the energy  $\epsilon_0^S$ , respectively. In c), d) and e), f), we study the effect of positive and negative values of  $\text{Re}(\epsilon_2^S)$  and the effect of  $\text{Im}(\epsilon_2^S)$  and  $\text{Im}(\epsilon_1^S)$ , respectively. In g) and h), we show how the inhomogeneous strain field  $x\partial_x \text{Im}(\epsilon_2^S)$  acts on the spin-orbit coupling for positive and negative values of the gradient.

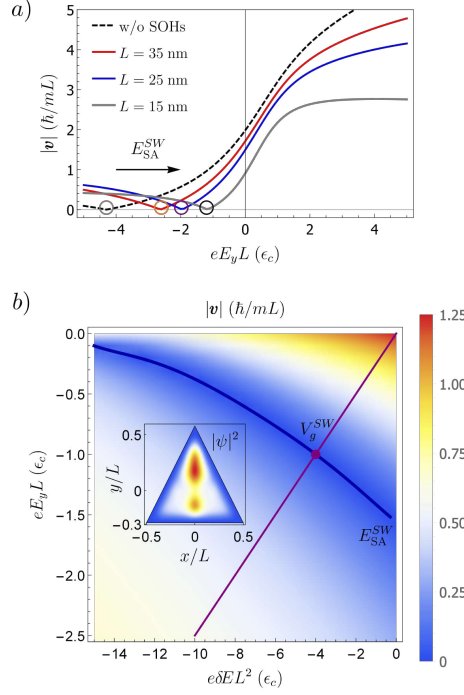


Figure 5.18: Spin-orbit velocity  $|v|$  in an equilateral SOI FinFET grown along the SA. In a), we show how the dependence of  $|v|$  on  $E_y$  varies as a function of  $L$ . The switching field  $E_{SA}^{SW}$  is pushed towards lower values as the triangle becomes smaller. In this device, the spin-orbit coupling is removed by a negative electric field generated by a positive gate potential  $V_g$  that pushes the hole wavefunction to the bottom of the triangle. In the units used, the results obtained without including the SOHs are independent of  $L$ . In b) we show  $|v|$  as a function of  $E_y$  and  $\delta E$  for a device with  $L = 20$  nm. The spin-orbit coupling vanishes along the blue line. The purple line indicates the constraint in Eq. (5.17). In the inset, we show the total density  $|\psi|^2$  of the hole wavefunction in the cross-section at  $V_g^{SW}$ , where purple and blue lines intersect. The density vanishes (is maximal) in the blue (red) region.

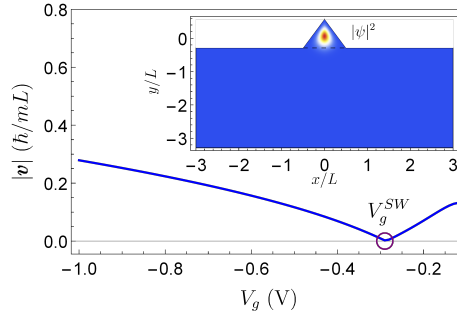


Figure 5.19: Spin-orbit velocity  $|v|$  in a bulk equilateral FinFET grown along the DRA. We show  $|v|$  as a function of the gate potential  $V_g$  in a device where an equilateral triangle with side  $L = 20$  nm is placed on top of a substrate  $6L$  wide and  $3L$  high. The electrostatic potential in this calculation is simulated by solving the Laplace equation as discussed in App. 5.A. In the inset, we show the total density  $|\psi|^2$  of the hole wavefunction at  $V_g = -0.28$  V, where the spin-orbit coupling vanishes. The hole density vanishes in the blue region and attains maximal value in the red region. At this potential, the holes are localised in the fin.

# Bibliography

- [1] R. Winkler, *Spin–Orbit Coupling Effects in Two-Dimensional Electron and Hole Systems*, vol. 191 of *Springer Tracts in Modern Physics*. Berlin, Heidelberg: Springer Berlin Heidelberg, 2003.
- [2] D. Loss and D. P. DiVincenzo, “Quantum computation with quantum dots,” *Phys. Rev. A*, vol. 57, pp. 120–126, Jan 1998.
- [3] R. Hanson, L. P. Kouwenhoven, J. R. Petta, S. Tarucha, and L. M. K. Vandersypen, “Spins in few-electron quantum dots,” *Rev. Mod. Phys.*, vol. 79, pp. 1217–1265, Oct 2007.
- [4] S. Nadj-Perge, S. Frolov, E. Bakkers, and L. P. Kouwenhoven, “Spin–orbit qubit in a semiconductor nanowire,” *Nature*, vol. 468, no. 7327, pp. 1084–1087, 2010.
- [5] K. C. Nowack, F. H. L. Koppens, Y. V. Nazarov, and L. M. K. Vandersypen, “Coherent control of a single electron spin with electric fields,” *Science*, vol. 318, no. 5855, pp. 1430–1433, 2007.
- [6] N. Hendrickx, D. Franke, A. Sammak, G. Scappucci, and M. Veldhorst, “Fast two-qubit logic with holes in germanium,” *Nature*, vol. 577, no. 7791, pp. 487–491, 2020.
- [7] D. V. Bulaev and D. Loss, “Spin relaxation and decoherence of holes in quantum dots,” *Phys. Rev. Lett.*, vol. 95, p. 076805, Aug 2005.
- [8] D. V. Bulaev and D. Loss, “Electric dipole spin resonance for heavy holes in quantum dots,” *Phys. Rev. Lett.*, vol. 98, p. 097202, Feb 2007.
- [9] C. Kloeffer and D. Loss, “Prospects for spin-based quantum computing in quantum dots,” *Annual Review of Condensed Matter Physics*, vol. 4, no. 1, pp. 51–81, 2013.

- [10] M. Marx, J. Yoneda, Á. G. Rubio, P. Stano, T. Otsuka, K. Takeda, S. Li, Y. Yamaoka, T. Nakajima, A. Noiri, D. Loss, T. Koderá, and S. Tarucha, “Spin orbit field in a physically defined p type mos silicon double quantum dot,” *arXiv preprint arXiv:2003.07079*, 2020.
- [11] G. Scappucci, C. Kloeffel, F. A. Zwanenburg, D. Loss, M. Myronov, J.-J. Zhang, S. De Franceschi, G. Katsaros, and M. Veldhorst, “The germanium quantum information route,” *arXiv preprint arXiv:2004.08133*, 2020.
- [12] R. Maurand, X. Jehl, D. Kotekar-Patil, A. Corna, H. Bohuslavskiy, R. Laviéville, L. Hutin, S. Barraud, M. Vinet, M. Sanquer, and S. De Franceschi, “A cmos silicon spin qubit,” *Nature communications*, vol. 7, no. 1, pp. 1–6, 2016.
- [13] R. Li, F. E. Hudson, A. S. Dzurak, and A. R. Hamilton, “Pauli Spin Blockade of Heavy Holes in a Silicon Double Quantum Dot,” *Nano Lett.*, vol. 15, pp. 7314–7318, Nov. 2015.
- [14] N. W. Hendrickx, W. I. L. Lawrie, L. Petit, A. Sammak, G. Scappucci, and M. Veldhorst, “A single-hole spin qubit,” *ArXiv191210426 Cond-Mat*, Dec. 2019.
- [15] C. Kloeffel, M. Trif, and D. Loss, “Strong spin-orbit interaction and helical hole states in ge/si nanowires,” *Phys. Rev. B*, vol. 84, p. 195314, Nov 2011.
- [16] C. Kloeffel, M. J. Rančić, and D. Loss, “Direct rashba spin-orbit interaction in si and ge nanowires with different growth directions,” *Phys. Rev. B*, vol. 97, p. 235422, Jun 2018.
- [17] F. N. M. Froning, L. C. Camenzind, O. A. H. van der Molen, A. Li, E. P. A. M. Bakkers, D. M. Zumbühl, and F. R. Braakman, “Ultrafast hole spin qubit with gate-tunable spin-orbit switch,” *arXiv preprint arXiv:2006.11175*, 2020.
- [18] K. Wang, G. Xu, F. Gao, H. Liu, R.-L. Ma, X. Zhang, T. Zhang, G. Cao, T. Wang, J.-J. Zhang, X. Hu, H.-W. Jiang, H.-O. Li, G.-C. Guo, and G.-P. Guo, “Ultrafast operations of a hole spin qubit in ge quantum dot,” *arXiv preprint arXiv:2006.12340*, 2020.
- [19] F. K. de Vries, J. Shen, R. J. Skolasinski, M. P. Nowak, D. Varjas, L. Wang, M. Wimmer, J. Ridderbos, F. A. Zwanenburg, A. Li,

- S. Koelling, M. A. Verheijen, E. P. A. M. Bakkers, and L. P. Kouwenhoven, "Spin-orbit interaction and induced superconductivity in a one-dimensional hole gas," *Nano letters*, vol. 18, no. 10, pp. 6483–6488, 2018.
- [20] A. P. Higginbotham, F. Kuemmeth, T. W. Larsen, M. Fitzpatrick, J. Yao, H. Yan, C. M. Lieber, and C. M. Marcus, "Antilocalization of coulomb blockade in a ge/si nanowire," *Phys. Rev. Lett.*, vol. 112, p. 216806, May 2014.
- [21] M. Brauns, J. Ridderbos, A. Li, E. P. A. M. Bakkers, and F. A. Zwanenburg, "Electric-field dependent  $g$ -factor anisotropy in ge-si core-shell nanowire quantum dots," *Phys. Rev. B*, vol. 93, p. 121408, Mar 2016.
- [22] F. Gao, J.-H. Wang, H. Watzinger, H. Hu, M. J. Rančić, J.-Y. Zhang, T. Wang, Y. Yao, G.-L. Wang, J. Kukučka, L. Vukušić, C. Kloeffer, D. Loss, F. Liu, G. Katsaros, and J.-J. Zhang, "Site-controlled uniform ge/si hut wires with electrically tunable spin-orbit coupling," *Advanced Materials*, vol. 32, no. 16, p. 1906523, 2020.
- [23] R. Wang, R. Deacon, J. Yao, C. Lieber, and K. Ishibashi, "Electrical modulation of weak-antilocalization and spin-orbit interaction in dual gated ge/si core/shell nanowires," *Semiconductor Science and Technology*, vol. 32, no. 9, p. 094002, 2017.
- [24] F. N. M. Froning, M. J. Rančić, B. Hetényi, S. Bosco, M. K. Rehmann, A. Li, E. P. A. M. Bakkers, F. A. Zwanenburg, D. Loss, D. M. Zumbühl, and F. R. Braakman, "Strong spin-orbit interaction and  $g$ -factor renormalization of hole spins in ge/si nanowire quantum dots," *arXiv preprint arXiv:2007.04308*, 2020.
- [25] F. Maier, C. Kloeffer, and D. Loss, "Tunable  $g$  factor and phonon-mediated hole spin relaxation in ge/si nanowire quantum dots," *Phys. Rev. B*, vol. 87, p. 161305, Apr 2013.
- [26] A. J. Landig, J. V. Koski, P. Scarlino, U. Mendes, A. Blais, C. Reichl, W. Wegscheider, A. Wallraff, K. Ensslin, and T. Ihn, "Coherent spin-photon coupling using a resonant exchange qubit," *Nature*, vol. 560, no. 7717, pp. 179–184, 2018.

- [27] X. Mi, M. Benito, S. Putz, D. M. Zajac, J. M. Taylor, G. Burkard, and J. R. Petta, "A coherent spin-photon interface in silicon," *Nature*, vol. 555, no. 7698, pp. 599–603, 2018.
- [28] C. Kloeffer, M. Trif, P. Stano, and D. Loss, "Circuit qed with hole-spin qubits in ge/si nanowire quantum dots," *Phys. Rev. B*, vol. 88, p. 241405, Dec 2013.
- [29] J. Sun, R. S. Deacon, R. Wang, J. Yao, C. M. Lieber, and K. Ishibashi, "Helical hole state in multiple conduction modes in ge/si core/shell nanowire," *Nano letters*, vol. 18, no. 10, pp. 6144–6149, 2018.
- [30] Y. Oreg, G. Refael, and F. von Oppen, "Helical liquids and majorana bound states in quantum wires," *Phys. Rev. Lett.*, vol. 105, p. 177002, Oct 2010.
- [31] F. Maier, J. Klinovaja, and D. Loss, "Majorana fermions in ge/si hole nanowires," *Phys. Rev. B*, vol. 90, p. 195421, Nov 2014.
- [32] J. Yoneda, K. Takeda, T. Otsuka, T. Nakajima, M. R. Delbecq, G. Allison, T. Honda, T. Koder, S. Oda, Y. Hoshi, N. Usami, K. M. Itoh, and S. Tarucha, "A quantum-dot spin qubit with coherence limited by charge noise and fidelity higher than 99.9%," *Nat. Nanotechnol.*, vol. 13, p. 102, Feb. 2018.
- [33] D. Culcer, X. Hu, and S. Das Sarma, "Dephasing of si spin qubits due to charge noise," *Applied Physics Letters*, vol. 95, no. 7, p. 073102, 2009.
- [34] A. Bermeister, D. Keith, and D. Culcer, "Charge noise, spin-orbit coupling, and dephasing of single-spin qubits," *Applied Physics Letters*, vol. 105, no. 19, p. 192102, 2014.
- [35] Z. Wang, E. Marcellina, A. Hamilton, S. Rogge, J. Salfi, and D. Culcer, "Suppressing charge-noise sensitivity in high-speed ge hole spin-orbit qubits," *arXiv preprint arXiv:1911.11143*, 2019.
- [36] J. Salfi, J. A. Mol, D. Culcer, and S. Rogge, "Charge-insensitive single-atom spin-orbit qubit in silicon," *Phys. Rev. Lett.*, vol. 116, p. 246801, Jun 2016.
- [37] M. Benito, X. Croot, C. Adelsberger, S. Putz, X. Mi, J. R. Petta, and G. Burkard, "Electric-field control and noise protection of the

- flopping-mode spin qubit," *Phys. Rev. B*, vol. 100, p. 125430, Sep 2019.
- [38] T. Tanttu, B. Hensen, K. W. Chan, C. H. Yang, W. W. Huang, M. Fogarty, F. Hudson, K. Itoh, D. Culcer, A. Laucht, A. Morello, and A. S. Dzurak, "Controlling spin-orbit interactions in silicon quantum dots using magnetic field direction," *Phys. Rev. X*, vol. 9, p. 021028, May 2019.
  - [39] B. Venitucci, L. Bourdet, D. Pouzada, and Y.-M. Niquet, "Electrical manipulation of semiconductor spin qubits within the  $sgs$ -matrix formalism," *Phys. Rev. B*, vol. 98, p. 155319, Oct. 2018.
  - [40] T. B. Hook, "Fully depleted devices for designers: Fdsoi and finfets," in *Proceedings of the IEEE 2012 Custom Integrated Circuits Conference*, pp. 1–7, 2012.
  - [41] A. V. Kuhlmann, V. Deshpande, L. C. Camenzind, D. M. Zumbühl, and A. Fuhrer, "Ambipolar quantum dots in undoped silicon fin field-effect transistors," *Applied Physics Letters*, vol. 113, no. 12, p. 122107, 2018.
  - [42] S. Geyer, L. C. Camenzind, L. Czornomaz, V. Deshpande, A. Fuhrer, R. J. Warburton, D. M. Zumbühl, and A. V. Kuhlmann, "Silicon quantum dot devices with a self-aligned second gate layer," *arXiv preprint arXiv:2007.15400*, 2020.
  - [43] L. C. Camenzind, S. Geyer, A. Fuhrer, R. J. Warburton, D. M. Zumbühl, and A. V. Kuhlmann, "A spin qubit in a fin field-effect transistor," *arXiv preprint arXiv:2103.07369*, 2021.
  - [44] C. H. Yang, R. Leon, J. Hwang, A. Saraiva, T. Tanttu, W. Huang, J. C. Lemyre, K. W. Chan, K. Tan, F. E. Hudson, K. M. Itoh, A. Morello, M. Pioro-Ladrière, A. Laucht, and A. S. Dzurak, "Operation of a silicon quantum processor unit cell above one kelvin," *Nature*, vol. 580, no. 7803, pp. 350–354, 2020.
  - [45] L. Petit, M. Russ, H. Eenink, W. Lawrie, J. Clarke, L. Vandersypen, and M. Veldhorst, "High-fidelity two-qubit gates in silicon above one kelvin," *arXiv preprint arXiv:2007.09034*, 2020.
  - [46] M. Veldhorst, C. H. Yang, J. C. C. Hwang, W. Huang, J. P. Dehollain, J. T. Muhonen, S. Simmons, A. Laucht, F. E. Hudson, K. M. Itoh,



- A. Morello, and A. S. Dzurak, "A two-qubit logic gate in silicon," *Nature*, vol. 526, pp. 410–414, Oct. 2015.
- [47] T. F. Watson, S. G. J. Philips, E. Kawakami, D. R. Ward, P. Scarlino, M. Veldhorst, D. E. Savage, M. G. Lagally, M. Friesen, S. N. Coppersmith, M. A. Eriksson, and L. M. K. Vandersypen, "A programmable two-qubit quantum processor in silicon," *Nature*, vol. 555, pp. 633–637, Mar. 2018.
- [48] D. M. Zajac, A. J. Sigillito, M. Russ, F. Borjans, J. M. Taylor, G. Burkard, and J. R. Petta, "Resonantly driven CNOT gate for electron spins," *Science*, vol. 359, pp. 439–442, Jan. 2018.
- [49] X. Xue, T. F. Watson, J. Helsen, D. R. Ward, D. E. Savage, M. G. Lagally, S. N. Coppersmith, M. A. Eriksson, S. Wehner, and L. M. K. Vandersypen, "Benchmarking gate fidelities in a Si/SiGe two-qubit device," *Phys. Rev. X*, vol. 9, p. 021011, Apr 2019.
- [50] W. Huang, C. Yang, K. Chan, T. Tanttu, B. Hensen, R. Leon, M. Fogarty, J. Hwang, F. Hudson, K. M. Itoh, A. Morello, A. Laucht, and A. S. Dzurak, "Fidelity benchmarks for two-qubit gates in silicon," *Nature*, vol. 569, no. 7757, pp. 532–536, 2019.
- [51] K. Takeda, A. Noiri, J. Yoneda, T. Nakajima, and S. Tarucha, "Resonantly Driven Singlet-Triplet Spin Qubit in Silicon," *Phys. Rev. Lett.*, vol. 124, p. 117701, Mar. 2020.
- [52] T. Lundberg, J. Li, L. Hutin, B. Bertrand, D. J. Ibberson, C.-M. Lee, D. J. Niegemann, M. Urdampilleta, N. Stelmashenko, T. Meunier, J. W. A. Robinson, L. Ibberson, M. Vinet, Y.-M. Niquet, and M. F. Gonzalez-Zalba, "Spin quintet in a silicon double quantum dot: Spin blockade and relaxation," *Phys. Rev. X*, vol. 10, p. 041010, Oct 2020.
- [53] G. Zheng, N. Samkharadze, M. L. Noordam, N. Kalhor, D. Brousse, A. Sammak, G. Scappucci, and L. M. K. Vandersypen, "Rapid gate-based spin read-out in silicon using an on-chip resonator," *Nat. Nanotechnol.*, vol. 14, pp. 742–746, Aug. 2019.
- [54] A. West, B. Hensen, A. Jouan, T. Tanttu, C.-H. Yang, A. Rossi, M. F. Gonzalez-Zalba, F. Hudson, A. Morello, D. J. Reilly, and A. S. Dzurak, "Gate-based single-shot readout of spins in silicon," *Nat. Nanotechnol.*, vol. 14, pp. 437–441, May 2019.

- [55] J. Yoneda, K. Takeda, A. Noiri, T. Nakajima, S. Li, J. Kamioka, T. Koder, and S. Tarucha, "Quantum non-demolition readout of an electron spin in silicon," *Nature communications*, vol. 11, no. 1, pp. 1–7, 2020.
- [56] X. Xue, B. D'Anjou, T. F. Watson, D. R. Ward, D. E. Savage, M. G. Lagally, M. Friesen, S. N. Coppersmith, M. A. Eriksson, W. A. Coish, and L. M. K. Vandersypen, "Repetitive quantum nondemolition measurement and soft decoding of a silicon spin qubit," *Phys. Rev. X*, vol. 10, p. 021006, Apr 2020.
- [57] A. Seedhouse, T. Tantt, R. C. C. Leon, R. Zhao, K. Y. Tan, B. Hensen, F. E. Hudson, K. M. Itoh, J. Yoneda, C. H. Yang, A. Morello, A. Laucht, S. N. Coppersmith, A. Saraiva, and A. S. Dzurak, "Parity readout of silicon spin qubits in quantum dots," *arXiv preprint arXiv:2004.07078*, 2020.
- [58] A. V. Khaetskii, D. Loss, and L. Glazman, "Electron spin decoherence in quantum dots due to interaction with nuclei," *Phys. Rev. Lett.*, vol. 88, p. 186802, Apr 2002.
- [59] W. A. Coish and D. Loss, "Hyperfine interaction in a quantum dot: Non-markovian electron spin dynamics," *Phys. Rev. B*, vol. 70, p. 195340, Nov 2004.
- [60] J. Fischer, M. Trif, W. Coish, and D. Loss, "Spin interactions, relaxation and decoherence in quantum dots," *Solid state communications*, vol. 149, no. 35-36, pp. 1443–1450, 2009.
- [61] J. Fischer and D. Loss, "Hybridization and spin decoherence in heavy-hole quantum dots," *Phys. Rev. Lett.*, vol. 105, p. 266603, Dec 2010.
- [62] J. Fischer, W. A. Coish, D. V. Bulaev, and D. Loss, "Spin decoherence of a heavy hole coupled to nuclear spins in a quantum dot," *Phys. Rev. B*, vol. 78, p. 155329, Oct 2008.
- [63] F. Maier and D. Loss, "Effect of strain on hyperfine-induced hole-spin decoherence in quantum dots," *Phys. Rev. B*, vol. 85, p. 195323, May 2012.
- [64] P. Philippopoulos, S. Chesi, and W. A. Coish, "First-principles hyperfine tensors for electrons and holes in gaas and silicon," *Phys. Rev. B*, vol. 101, p. 115302, Mar 2020.

- [65] K. Takeda, J. Kamioka, T. Otsuka, J. Yoneda, T. Nakajima, M. R. Delbecq, S. Amaha, G. Allison, T. Kodera, S. Oda, and S. Tarucha, "A fault-tolerant addressable spin qubit in a natural silicon quantum dot," *Sci. Adv.*, vol. 2, p. e1600694, Aug. 2016.
- [66] R. Zhao, T. Tantt, K. Y. Tan, B. Hensen, K. W. Chan, J. C. C. Hwang, R. C. C. Leon, C. H. Yang, W. Gilbert, F. E. Hudson, K. M. Itoh, A. A. Kiselev, T. D. Ladd, A. Morello, A. Laucht, and A. S. Dzurak, "Single-spin qubits in isotopically enriched silicon at low magnetic field," *Nat. Commun.*, vol. 10, pp. 1–9, Dec. 2019.
- [67] B. Voisin, R. Maurand, S. Barraud, M. Vinet, X. Jehl, M. Sanquer, J. Renard, and S. De Franceschi, "Electrical control of g-factor in a few-hole silicon nanowire mosfet," *Nano letters*, vol. 16, no. 1, pp. 88–92, 2016.
- [68] A. Crippa, R. Maurand, L. Bourdet, D. Kotekar-Patil, A. Amisse, X. Jehl, M. Sanquer, R. Laviéville, H. Bohuslavskyi, L. Hutin, S. Barraud, M. Vinet, Y.-M. Niquet, and S. De Franceschi, "Electrical spin driving by  $g$ -matrix modulation in spin-orbit qubits," *Phys. Rev. Lett.*, vol. 120, p. 137702, Mar 2018.
- [69] M. Reed, R. Bate, K. Bradshaw, W. Duncan, W. Frensley, J. Lee, and H. Shih, "Spatial quantization in gaas–algaas multiple quantum dots," *Journal of Vacuum Science & Technology B: Microelectronics Processing and Phenomena*, vol. 4, no. 1, pp. 358–360, 1986.
- [70] R. J. Warburton, "Self-assembled semiconductor quantum dots," *Contemporary Physics*, vol. 43, no. 5, pp. 351–364, 2002.
- [71] B. Venitucci and Y.-M. Niquet, "Simple model for electrical hole spin manipulation in semiconductor quantum dots: Impact of dot material and orientation," *Phys. Rev. B*, vol. 99, p. 115317, Mar 2019.
- [72] J.-X. Xiong, S. Guan, S.-S. Li, and J.-W. Luo, "Strong and tunable linear rashba spin-orbit coupling of two-dimensional hole gases in ge/si quantum wells," *arXiv preprint arXiv:2008.12523*, 2020.
- [73] B. Hetényi, C. Kloeffel, and D. Loss, "Exchange interaction of hole-spin qubits in double quantum dots in highly anisotropic semiconductors," *Phys. Rev. Research*, vol. 2, p. 033036, Jul 2020.

- [74] J. M. Luttinger, "Quantum theory of cyclotron resonance in semiconductors: General theory," *Phys. Rev.*, vol. 102, pp. 1030–1041, May 1956.
- [75] B. J. McCartin, "Eigenstructure of the equilateral triangle, part i: The dirichlet problem," *Siam Review*, vol. 45, no. 2, pp. 267–287, 2003.
- [76] S. Bravyi, D. P. DiVincenzo, and D. Loss, "Schrieffer–wolff transformation for quantum many-body systems," *Annals of physics*, vol. 326, no. 10, pp. 2793–2826, 2011.
- [77] M. L. Lee, E. A. Fitzgerald, M. T. Bulsara, M. T. Currie, and A. Lochtefeld, "Strained si, sige, and ge channels for high-mobility metal-oxide-semiconductor field-effect transistors," *Journal of applied physics*, vol. 97, no. 1, p. 1, 2005.
- [78] S. Liles, F. Martins, D. Miserev, A. Kiselev, I. Thorvaldson, M. Rendell, I. Jin, F. Hudson, M. Veldhorst, K. Itoh, *et al.*, "Electrical control of the g tensor of the first hole in a silicon mos quantum dot," *Physical Review B*, vol. 104, no. 23, p. 235303, 2021.
- [79] Y.-M. Niquet, C. Delerue, and C. Krzeminski, "Effects of strain on the carrier mobility in silicon nanowires," *Nano letters*, vol. 12, no. 7, pp. 3545–3550, 2012.
- [80] G. Stan, S. Krylyuk, A. Davydov, and R. F. Cook, "Compressive stress effect on the radial elastic modulus of oxidized si nanowires," *Nano letters*, vol. 10, no. 6, pp. 2031–2037, 2010.
- [81] T. Thorbeck and N. M. Zimmerman, "Formation of strain-induced quantum dots in gated semiconductor nanostructures," *AIP Advances*, vol. 5, no. 8, p. 087107, 2015.
- [82] G. L. Bir and G. E. Pikus, *Symmetry and strain-induced effects in semiconductors*, vol. 484. Wiley New York, 1974.
- [83] P. Del Vecchio, M. Lodari, A. Sammak, G. Scappucci, and O. Moutanabbir, "Vanishing zeeman energy in a two-dimensional hole gas," *arXiv preprint arXiv:2006.00102*, 2020.
- [84] L. S. Levitov and E. I. Rashba, "Dynamical spin-electric coupling in a quantum dot," *Phys. Rev. B*, vol. 67, p. 115324, Mar 2003.

- [85] V. N. Golovach, M. Borhani, and D. Loss, "Electric-dipole-induced spin resonance in quantum dots," *Phys. Rev. B*, vol. 74, p. 165319, Oct 2006.
- [86] V. N. Golovach, A. Khaetskii, and D. Loss, "Phonon-induced decay of the electron spin in quantum dots," *Phys. Rev. Lett.*, vol. 93, p. 016601, Jun 2004.
- [87] Y. Makhlin, G. Schön, and A. Shnirman, "Dissipative effects in josephson qubits," *Chemical Physics*, vol. 296, no. 2, pp. 315 – 324, 2004.
- [88] K. D. Petersson, J. R. Petta, H. Lu, and A. C. Gossard, "Quantum coherence in a one-electron semiconductor charge qubit," *Phys. Rev. Lett.*, vol. 105, p. 246804, Dec 2010.
- [89] D. M. Zumbühl. Private communication.
- [90] COMSOL Multiphysics® v. 5.5. COMSOL AB, Stockholm, Sweden.

# CHAPTER 6

## Long-distance coupling of spin qubits via topological magnons

*Adapted from:*  
Bence Hetényi, Alexander Mook, Jelena Klinovaja, and Daniel Loss  
“Long-distance coupling of spin qubits via topological magnons”,  
arXiv:2207.01264 (2022)

We consider two distant spin qubits in quantum dots, both coupled to a two-dimensional topological ferromagnet hosting chiral magnon edge states at the boundary. The chiral magnon is used to mediate entanglement between the spin qubits, realizing a fundamental building block of scalable quantum computing architectures: a long-distance two-qubit gate. Previous proposals for long-distance coupling with magnons involved off-resonant coupling, where the detuning of the spin-qubit frequency from the magnonic band edge provides protection against spontaneous relaxation. The topological magnon mode, on the other hand, lies in-between two magnonic bands far away from any bulk magnon resonances, facilitating strong and highly tuneable coupling between the two spin qubits. Even though the coupling between the qubit and the chiral magnon is resonant for a wide range of qubit splittings, we find that the magnon-induced qubit relaxation is vastly suppressed if the coupling between the qubit and the ferromagnet is antiferromagnetic. A fast and high-fidelity long-distance coupling protocol is presented capable of achieving spin-qubit entanglement over micrometer distances with 1 MHz gate speed and up to 99.9% fidelities. The resulting spin-qubit

entanglement may be used as a probe for the long-sought detection of topological edge magnons.

## 6.1 Introduction

Along the journey towards universal quantum computing several of the milestones [1] have already been reached, such as single-qubit gates with long coherence times and fast readout as well as short-ranged two-qubit gates in multiple platforms [2–13]. Universality, on the other hand, requires coherent logical qubits, that can be achieved in large-scale quantum computers by means of quantum error correction [14, 15]. Owing to the highly developed semiconductor industry qubits defined in semiconductor quantum dots (QDs) [16–18] are increasingly believed to be an exceptionally potent candidate for the long term goal: scalable quantum computers. The challenge incorporates the improvement of single- and two-qubit gate performance as well as the management of the corresponding control electronics [19–21]. Leveraging the industry-standard fabrication techniques, Ref. [20] proposed to accommodate elements of the control electronics on the same chip by arranging small dense qubit arrays and local control electronics in a checkerboard pattern, where the qubit arrays are connected via long-range qubit couplers. For such architectures having means to create entanglement over large distances ( $\gtrsim 1 \mu\text{m}$ ) would be highly desirable.

Long-range entanglement of spin qubits is realizable using a variety of mediators [18] such as floating gates [22, 23], microwave cavities [24], superconducting resonators [25–27] or spin shuttling [28–30]. While the fidelity of the aforementioned protocols may be limited by charge noise, magnetic insulators are versatile platforms to create entanglement among distant spins with low dissipation and no heat generation due to Joule heating [31]. Furthermore, the coupling to magnons does not require spin-orbit interaction (SOI). In such systems the effective coupling between spin qubits can be established using ferromagnetic (FM) magnons [32–34], antiferromagnetic domain walls [35] or magnon waveguides [36]. An other promising approach to mitigate dissipation is to couple spin qubits via topological edge states in quantum Hall systems [37–40].

Herein, as shown in Fig. 6.1, we bring together topological excitations, magnets, and spin qubits by studying long-distance entanglement mediated by topological magnons. The latter are examples of bosonic

topological spin excitations above topologically trivial magnetic ground states. Topological chiral magnons are predicted to exist in a large variety of magnetic systems, ranging from FM [41–49] and antiferromagnets [50–52] to skyrmion crystals [53–58], and from two-dimensional to three-dimensional systems [59–61]. Being nonconserved bosons, chiral edge (or interface [43,62,63]) magnons exist within topological spectral gaps at finite frequencies, typically between a few GHz in (artificially manufactured or self-organized) topological magnonic crystals [43, 44, 47, 53–56, 64–68] up to several THz in magnetic compounds. Examples for the latter are Cu(1,3-benzenedicarboxylate) [69], CrI<sub>3</sub> [70], CrSiTe<sub>3</sub>, and CrGeTe<sub>3</sub> [71]. For recent reviews on topological magnons, see Refs. [72–75].

Once the qubit is brought into proximity to the magnet’s edge (or interface) and its frequency is tuned within the topological magnon gap, the qubit is only resonant with the chiral edge mode. Coupling the qubit to the FM leads to an emission of a *physical* unidirectionally propagating magnon well localized to the edge of the sample. This magnon can be re-absorbed by the second qubit thereby mediating entanglement between the qubits. This nonreciprocal coupling protocol can be exceptionally fast ( $\sim 1$  GHz) and we find high gate fidelities when the inter-qubit distance is well below the magnon mean free path, that is to say, well below  $1\ \mu\text{m}$ .

Importantly, we report a coupling regime that drastically outperforms the aforementioned protocol. If the two qubits are coupled simultaneously with the FM (antiferromagnetically), a *virtual* chiral magnon-mediated process arises, which is proportional to the direct exchange coupling, with the decoherence rates being suppressed by the smallness of the dipole-dipole interaction. In this regime, fidelities of 99.9% of 1 MHz two-qubit gates can be achieved even at distances comparable with the magnon mean free path.

The remainder of this work is structured as follows: in Sec. 6.2 the model of a two-dimensional topological FM in nanoribbon geometry is presented and its chiral edge magnons characterized. In Secs. 6.2–6.2, we consider two planar QDs residing in an adjacent non-magnetic layer, coupled by both direct exchange and dipole-dipole interaction to an arm-chair edge of the FM. In Secs. 6.2–6.2, we identify a coupling regime with antiferromagnetic exchange coupling between the QD and the FM. In this scenario the qubit relaxation is orders of magnitude slower than the effective coupling. In Secs. 6.3–6.3, we present the results of the corresponding numerical study, which we show to agree well with our analytical estimates. Finally, we consider the opposite (ferromagnetic) coupling regime in Sec. 6.4 for which the resonant coupling together with the chiral prop-



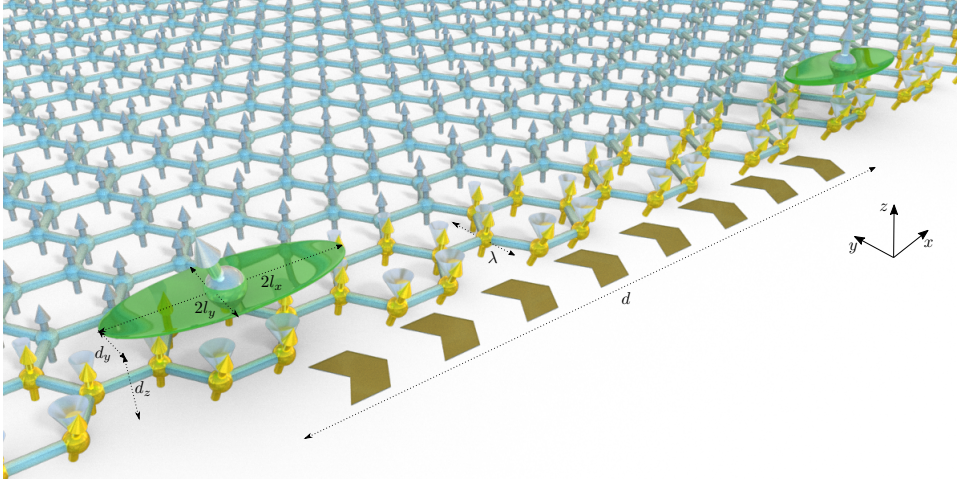


Figure 6.1: Schematic setup for the long-distance spin-qubit entanglement mediated by chiral magnons in a topological ferromagnet. The light blue honeycomb lattice represents the ferromagnet with the arrows indicating the ground state spin polarization. The armchair edge of the ferromagnet hosts the chiral magnon mode propagating along the positive  $x$  direction, indicated by the canted edge spins (gold). The spin qubits (silver arrow embedded in a green ellipse) are lying in a parallel plane close to the FM lattice (qubit layer is not shown explicitly), located near the edge of the magnet.

agation of the magnon facilitates qubit entanglement via the exchange of a physical magnon. After a discussion in Sec. 6.5, we conclude in Sec. 6.6. Several Appendices provide more detailed information.

## 6.2 Theory

### Model of the topological ferromagnet

We consider a two-dimensional honeycomb lattice, as shown in Fig. 6.1, with each lattice site—indexed by  $i$ —hosting a localized spin operator  $\mathbf{S}_i$ . Nearest neighbors interact via ferromagnetic Heisenberg exchange interaction,  $J > 0$ , and next-nearest neighbors are coupled via Dzyaloshinsky-Moriya interaction (DMI) [76,77], originating from spin-orbit interaction.

The spin Hamiltonian of the FM thus reads as

$$H_{\text{FM}} = -\frac{J}{2} \sum_{\langle i,j \rangle} \mathbf{S}_i \cdot \mathbf{S}_j + \frac{D}{2} \sum_{\langle\langle i,j \rangle\rangle} \nu_{ij} \hat{\mathbf{z}} \cdot (\mathbf{S}_i \times \mathbf{S}_j) + H_{\text{ani}}, \quad (6.1)$$

where  $\nu_{ij} = -\nu_{ji} = \pm 1$  depending on the relative position of sites  $i$  and  $j$ . Here, we adopt the convention that  $\nu_{ij} = +1$ , if the bond from site  $i$  to site  $j$  points in anticlockwise direction as seen from the respective hexagon. We also added an anisotropy term  $H_{\text{ani}}$  in Eq. (6.1) that gaps out the Goldstone mode by creating a spin-wave gap. Since its microscopic origin is of no further relevance, we model the anisotropy by a built-in magnetic field,  $H_{\text{ani}} = -\Delta_{\text{F}} \sum_i S_i^z$ , into which potential external fields may be absorbed as well. Then,  $\Delta_{\text{F}}$  comprises the energy of the uniform ferromagnetic resonance.

Spin Hamiltonian (6.1) is well-studied in the context of topological magnons as it realizes the magnonic version of the Haldane model [78], as shown in Ref. [79]. Here, we do not repeat the derivation but only summarize the most important aspects crucial for the coupling of spin qubits. Assuming that the spins in the ground state are pointing in the positive  $z$  direction, we perform a Holstein-Primakoff transformation [80]. To lowest order in the  $1/S$  expansion the spin operators are expressed as

$$S_i^x \approx \sqrt{\frac{S}{2}} (a_i + a_i^\dagger), \quad (6.2a)$$

$$S_i^y \approx -i\sqrt{\frac{S}{2}} (a_i - a_i^\dagger), \quad (6.2b)$$

$$S_i^z = S - a_i^\dagger a_i, \quad (6.2c)$$

where  $a_i^\dagger$  and  $a_i$  are bosonic creation and annihilation operators, respectively, and  $S$  is the spin quantum number. By plugging Eqs. (6.2a)-(6.2c) into Eq. (6.1), the spin Hamiltonian can be expanded in bosonic operators. In the harmonic approximation, only the bilinear piece is retained and found to constitute the bosonic equivalent of the Haldane model. Both nearest-neighbor hopping and onsite potentials are proportional to  $JS$ . The time-reversal symmetry breaking complex next-nearest neighbor hopping is brought about by DMI and, hence,  $\propto DS$  [81]. The latter causes a topologically nontrivial opening of a band gap that—according to the bulk-boundary correspondence [82,83]—supports a chiral magnonic edge mode.

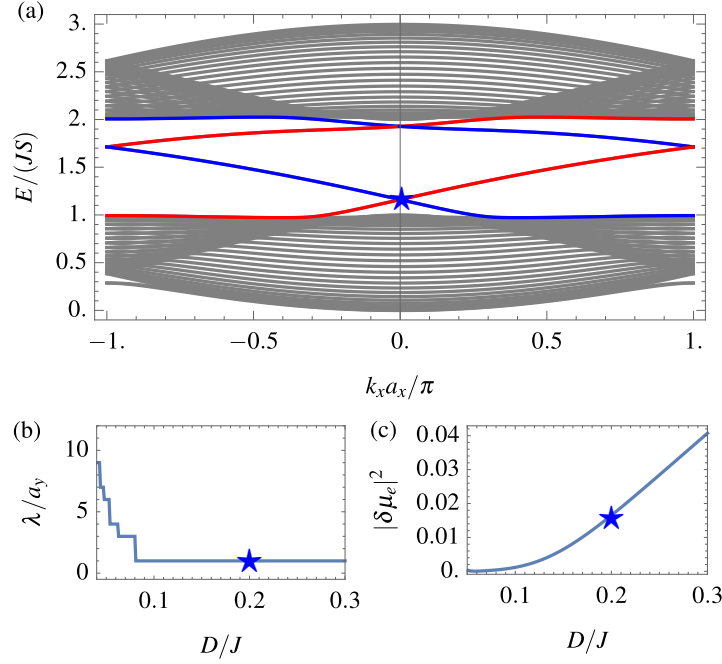


Figure 6.2: (a) Magnon spectrum of a honeycomb-lattice ferromagnetic nanoribbon with armchair termination,  $D = 0.2 J$ , and  $N_y = 20$  unit cells in the  $y$  direction. Left (right) localized edge states are shown in blue (red). (b) Localization length  $\lambda$  of the left localized edge mode [denoted by a blue star on (a)] as a function of DMI strength. (c) Dynamic magnetic moment of the left localized edge mode as a function of DMI strength.

In the rest of this work, we consider a two-dimensional FM in nanoribbon (or “slab”) geometry, infinite along the  $x$  direction, with armchair termination in the  $y$  direction<sup>1</sup>. The elementary unit cell of size  $a_x \times a_y$  contains four atoms (where  $a_x = \sqrt{3}a$  and  $a_y = a$ ), and the slab consists of  $N_y$  unit cells in the  $y$  direction. Using periodic boundary conditions in the  $x$  direction, the momentum  $k_x \in [-\frac{\pi}{a_x}, \frac{\pi}{a_x})$ , is a good quantum number and the eigenvalue equation for a given  $k_x$  reads as

$$\hat{H}_{\text{FM}}(k_x)\varphi_{k_x,n} = \varepsilon_{k_x,n}\varphi_{k_x,n}, \quad (6.3)$$

where  $n$  is the band index running from 1 to  $4N_y$ , where  $4N_y$  is the total number of spins in the nanoribbon unit cell. Here,  $\hat{H}_{\text{FM}}(k_x)$  is the linear

<sup>1</sup>We have chosen armchair rather than zigzag termination because the latter does not support a chiral edge mode at zero momentum, a property that turns out to be crucial to couple the edge mode to a QD.

spin-wave matrix, and  $\varphi_{k_x,n}$  an eigenvector with eigenvalue  $\varepsilon_{k_x,n}$ . The eigenvectors satisfy the usual normalization condition, i.e.,  $\sum_{y_i,\mu} |\varphi_{k_x,n}^\mu(y_i)|^2 = 1$ , where  $y_i \in [1, N_y]$  is the index of the armchair unit cell and  $\mu \in [1, 4]$  a basis site within the armchair unit cell. Furthermore, the eigenvectors are related to the spin waves via  $S_i^+ \approx \sqrt{2S}a_i = \sqrt{2S/N_x} \sum_{k_x} e^{-ik_x x_i} \sum_n \varphi_{k_x,n}^{\mu_i}(y_i) a_{k_x,n}$ , where the second equality defines the annihilation operator of the magnonic eigenmode  $(k_x, n)$ , with  $N_x$  being the number of unit cells in the  $x$  direction (see App. 6.A for further conventions). The spectrum  $\varepsilon_{k_x,n}$  of such a ferromagnetic slab is shown in Fig. 6.2(a), where the left- and right-propagating chiral edge modes are highlighted in blue and red, respectively. For the numerical results to follow the parameters of the FM slab are listed in Tab. 6.1, unless otherwise specified.

Importantly, and in contrast to the electronic Haldane model, the chiral mode is not “particle-hole” symmetric, i.e., its energy is not symmetric with respect to the gap. This is due to missing nearest neighbors at the edges, resulting in a reduction of energy for the edge modes [84–86]. This edge effect does not affect topological protection because the existence of a chiral mode is still dictated by the nontrivial topology of the bulk. However, it does affect other properties of the chiral edge mode that are related to the edge mode’s eigenvector  $\varphi_{k_x,e}$  (subscript “e” for edge mode) and, as we show, crucial for the spin-qubit coupling. These properties are (i) the edge mode localization length  $\lambda = ba_y$ , with  $b$  being the largest integer for which  $\sum_{y_i=1}^b \sum_{\mu=1}^4 |\varphi_{0,e}^\mu(y_i)|^2 \leq 1 - 1/e$ , and (ii) the edge mode dynamic magnetic moment, which reads as

$$\delta\mu_e = \sum_{y_i=1}^{N_y} \sum_{\mu=1}^4 \varphi_{0,e}^\mu(y_i) \quad (6.4)$$

for the left edge. These quantities are shown as a function of  $D/J$  in Figs. 6.2(b) and (c), respectively. In the following, we work at  $D/J = 0.2$ , which ensures that the edge state is well localized within the unit cell width, that is to say,  $\lambda \sim a_y$ .

Later on, we need the transversal spin susceptibility of the topological ferromagnet. In the time domain, we may write it as

$$\chi_{nm}^\perp(t, k_x) \equiv -i\theta(t) \langle [S_{-k_x,n}^-(t), S_{k_x,m}^+(0)] \rangle, \quad (6.5)$$

where  $S_{-k_x,n}^-(t) \equiv \sqrt{2S}e^{i\varepsilon_{k_x,n}t/\hbar}a_{k_x,n}^\dagger$  encompasses the dynamics associated with the  $n$ th magnon normal mode in the linear spin-wave approx-

Table 6.1: Characteristic parameters of the topological ferromagnetic slab assumed for the numerical calculations throughout this work. The slab is assumed to be periodic in the  $x$  direction and has armchair termination in the  $y$  direction.

Parameter	Symbol	Numerical value
Exchange coupling	$J$	1 meV
DMI	$D$	0.2 meV
Spin quantum number	$S$	3/2
$g$ -factor	$g$	2
Ferromagnetic resonance	$\Delta_F$	50 $\mu$ eV
Gilbert damping	$\alpha_G$	$10^{-4}$
Next-nearest-neighbor distance	$a$	1 nm
Slab width	$L_y$	20 nm

imation. In frequency space, we may rewrite it as

$$\chi_{nm}^\perp(\omega, k_x) = -2S \frac{\delta_{nm}}{\varepsilon_{k_x, n}(1 + i\alpha_G) - \hbar\omega}, \quad (6.6)$$

where  $\alpha_G$  is the dimensionless Gilbert damping coefficient [87]. This phenomenological constant accounts for the ubiquitous magnetization damping processes without specifying microscopic origins. It brings about a finite spectral broadening  $\propto \alpha_G \varepsilon_{k_x, n}$  of the magnon line width proportional to the magnon energy [88]. In high-quality magnetic insulators at low temperatures, as considered here,  $\alpha_G \ll 1$ , because metallic Stoner excitations and Landau damping are absent, defect scattering is minimized, magnon-magnon scattering is frozen out, and magnon-phonon scattering suppressed. We take  $\alpha_G = 10^{-4}$  throughout, a value found, for example, in sub-micrometer yttrium iron garnet films [89].

## Model and requirements for the spin qubits

We assume that the spin qubits are defined by electrostatic gates in a 2D (nonmagnetic) layer which is deposited directly on top of the FM layer. The confinement is assumed to be harmonic in both directions with different confinement lengths  $l_x \gg a_x$  and  $l_y \gtrsim a_y$  (see Fig. 6.1). The QD under consideration is in the single-particle filling regime, with the lowest orbital level occupied. An orbital level splitting  $\gtrsim 10$  meV is assumed.

In order to couple resonantly with the chiral magnon the qubit splitting is required to be close enough in energy to the edge states in the

topological gap, approximately at an energy  $E/(JS) = 1.2$  for zero momentum in Fig. 6.2(a). This is ensured by the strong exchange interaction emerging between the FM and the excess electron occupying the QD. This can be achieved if the conduction band edge (hosting the QD) is close enough to the conduction band of the FM allowing for tunnelling, and consequently for exchange interaction between the QD spin and the spins of the FM lattice. Even though the qubit experiences the large exchange field of the FM layer,  $J^\perp \sim 1 \text{ meV}$ , the spectrum of the magnet remains unaffected because the nonmagnetic qubit layer remains unpolarized and the QD spin has only a small weight on the individual lattice sites. Here, the contribution of the dipole field is neglected since it is assumed to be sufficiently small,  $\Delta_{\text{dip}} < 1 \mu\text{eV}$  (see App. 6.B) when compared to the exchange field.

Taking the interlayer exchange interaction into account as an effective Zeeman field, the corresponding qubit Hamiltonian reads

$$H_{\text{SQ}} = -J^\perp \sum_i |\psi_{\text{QD}}(x_i, y_i)|^2 \mathbf{S}_i \cdot \boldsymbol{\sigma} \approx -wJ^\perp S\sigma^z \equiv \Delta\sigma^z, \quad (6.7)$$

where  $J^\perp$  is the interlayer exchange interaction strength (i.e., between the FM and the QD layer),  $\psi_{\text{QD}}$  is the orbital part of the QD wavefunction, and  $\boldsymbol{\sigma}$  is the spin vector-operator with  $\sigma^z = \frac{1}{2}(|\uparrow\rangle\langle\uparrow| - |\downarrow\rangle\langle\downarrow|)$  being the  $z$  component of the QD spin. Furthermore, we used the fact that in the ground state of the FM  $\mathbf{S}_i = S\mathbf{e}_z$ , and therefore the weight of the QD  $w = \sum_i |\psi_{\text{QD}}(x_i, y_i)|^2 \leq 1$  can be factored out. The localized spin on the QD can be identified with a qubit with basis states  $|0\rangle \equiv |\uparrow\rangle$  and  $|1\rangle \equiv |\downarrow\rangle$  and a qubit splitting  $\Delta$ .

The spins of the FM point in the positive  $z$  direction:  $\langle \mathbf{S} \rangle_{T=0} = S\mathbf{e}_z$ . Therefore, if the ground state  $|\downarrow\rangle$  of the qubit is antialigned with the spins of the FM, for example, due to antiferromagnetic interlayer exchange,  $J^\perp < 0$ , the splitting  $\Delta$  is positive. This property is crucial in order to mitigate magnon-induced relaxation from the higher energy qubit state because the transition  $|\uparrow\rangle \rightarrow |\downarrow\rangle$  requires a double spin flip,  $S_i^- \sigma^-$  (where  $S^- \propto a^\dagger$ ). This process cannot be assisted by the strong interlayer exchange but only by dipole-dipole interaction that is orders of magnitude weaker.

For qubit applications, it is essential to have means to control the qubit and to have long enough coherence times, simultaneously. If the spin and orbital degrees of freedom are coupled in the QD (i.e., via spin orbit interaction or magnetic field gradient), coherent flipping of the qubit can be realized by electric-dipole-induced spin resonance (EDSR) [90–

93]. In the present setup, besides intrinsic spin-orbit interaction, the induced dipole-field near the edge of the FM can be leveraged for this purpose<sup>2</sup>. This mechanism opens a channel for relaxation as well, via coupling to charge noise and phonons. Nonetheless, due to the weakness of the dipole-dipole interaction we do not expect this to be a severe limitation.

We note that an additional dephasing mechanism appears near the edge of the FM due to the strong exchange field. Since the exchange field is zero outside the FM, the effective qubit splitting  $\Delta(d_y) = -w(d_y)J^\perp S$  depends on the QD position as  $w(d_y) = [1 + \text{erf}(d_y/l_y)]/2$ , assuming harmonic confinement for the QD, centred around  $y = d_y$ . This sharp dependence on exchange coupling would make the qubit extremely vulnerable against fluctuations of  $d_y$ , e.g., due to charge noise. In the following we assume that this dephasing mechanism is prevented by the device design, an assumption that we return to in Sec. 6.5, and focus on the dynamical (i.e., magnon-induced) contributions of the decoherence rates.

Even though some of the requirements above might seem stringent at first, due to generality of the results to be presented, we believe that there is a large range of materials that are compatible with the criteria above and can be stacked on top of each other. We return to a discussion of materials in Sec. 6.5. For the numerical results in this work the parameters listed in Tab. 6.2 were used, unless specified otherwise.

Table 6.2: Characteristic parameters of the QD used in numerical evaluations.

Parameter	Symbol	Numerical value
Qubit g-factor	$g_{\text{QD}}$	2
QD length along the edge	$2l_x$	20 nm
QD length perpendicular to the edge	$2l_y$	2 nm

Table 6.3: Characteristic parameters of the FM-QD coupling used in numerical evaluations.

Parameter	Symbol	Numerical value
Interlayer exchange interaction	$J^\perp$	$-1.2 \text{ meV}$
QD-QD distance	$d$	$1 \text{ }\mu\text{m}$
QD distance from the FM edge	$d_y$	$-0.4 \text{ nm}$
Interlayer distance	$d_z$	$0.7 \text{ nm}$

## Coupling to the Ferromagnet

Assuming a general, non-local coupling  $\hat{V}_{\text{int}}(\mathbf{r}_i - \mathbf{r})$  between spin  $\mathbf{S}_i$  and QD spin at position  $\mathbf{r}$ , the interaction Hamiltonian between a qubit and the FM spins can be written as  $V_p = \sum_i \mathbf{S}_i \cdot \sum_{\mathbf{r}} \hat{V}_{\text{int}}(\mathbf{r}_i - \mathbf{r}) \boldsymbol{\sigma}_p(\mathbf{r})$ , where  $\boldsymbol{\sigma}_p(\mathbf{r})$  is the spin density of the  $p$ th QD and the interaction matrix  $\hat{V}_{\text{int}}(\mathbf{r}_i - \mathbf{r})$  contains both exchange and dipolar interactions. As long as SOI is negligible in the QD, the spin  $\boldsymbol{\sigma}$  of the particle in the QD is independent of the spatial coordinates and we may make the ansatz

$$\boldsymbol{\sigma}_p(\mathbf{r}) = |\psi_p(\mathbf{r})|^2 \boldsymbol{\sigma}_p, \quad (6.8)$$

where  $\boldsymbol{\sigma}_p$  is acting on the spin space of the  $p$ th QD. The spatial part of the QD wavefunction is  $\psi_p(\mathbf{r}) = \psi(\mathbf{r} - \mathbf{r}_p)$  is localized around  $\mathbf{r}_p = (x_p, d_y, d_z)$  and we assume that the two QD wavefunctions have no common support. Thus, we can introduce the coupling matrix between the  $p$ th QD spin and the  $i$ th FM spin as  $\hat{M}(\mathbf{r}_p - \mathbf{r}_i) = \sum_{\mathbf{r}} \hat{V}_{\text{int}}(\mathbf{r}_i - \mathbf{r}) |\psi(\mathbf{r} - \mathbf{r}_p)|^2$ . For notational convenience we introduce the coupling vector  $\mathbf{M}^\alpha = (M^{\alpha x}, M^{\alpha y}, M^{\alpha z})$  that is the  $\alpha$ th row of the coupling matrix  $\hat{M}$ , and  $\mathbf{M}^\pm = \mathbf{M}^x \pm i\mathbf{M}^y$ , and similarly  $\sigma^\pm = \sigma^x \pm i\sigma^y$ .

Writing the convolution between the FM spins and the coupling matrix  $\hat{M}$  in Fourier space and expanding the coupling terms to first order

<sup>2</sup>Here, we estimate the dipole-field-induced Rabi frequency to be tens of megahertz. In the case of EDSR the Rabi frequency is given by  $\nu_{\text{Rabi}} = \hbar^{-1} E_{\text{SO}}(eE_y l_y) \Delta \Delta_{\text{orb}}^{-2}$ , if the driving field is applied in the  $y$  direction. In order to estimate the dipole-interaction-induced Rabi frequency, we used  $E_y = 0.5 \text{ V}/\mu\text{m}$  for the amplitude of the drive and  $E_{\text{SO}} = 0.2 \text{ }\mu\text{eV}$ , that is the maximal coupling (as a function of  $d_y$  for our set of parameters) that the inhomogeneous dipole-field  $B_{\text{eff}}^y$  can induce between harmonic oscillator basis states in the  $y$  direction.



in magnon creation operators, one obtains

$$V_p = \mu_B S \mathbf{B}_{\text{eff}} \cdot \boldsymbol{\sigma}_p + \frac{1}{2} \sum_{\mathbf{k}_x, n} \left( e^{i\mathbf{k}_x \cdot \mathbf{r}_p} S_{-\mathbf{k}_x, n}^+ \mathbf{M}_{\mathbf{k}_x, n}^- \cdot \boldsymbol{\sigma}_p + h.c. \right) + \mathcal{O}(S^0), \quad (6.9)$$

where  $\mu_B \mathbf{B}_{\text{eff}} \approx -w J^\perp \mathbf{e}_z$  is the effective field of the FM ground state acting on the qubit as in Eq. (6.7), while second order terms in magnon creation operators are neglected. The coupling vector connecting the eigenmodes of the FM to one of the qubits is  $\mathbf{M}_{\mathbf{k}_x, n}^- = \frac{1}{\sqrt{N_x}} \sum_i e^{-i\mathbf{k}_x \cdot \mathbf{r}_i} \varphi_{-\mathbf{k}_x, n}^{\mu_i}(\mathbf{r}_i) \mathbf{M}^-(\mathbf{r}_i, y_i - d_y)$ . Furthermore, owing to the hermiticity of the Hamiltonian, the coupling matrix elements satisfy  $M_{\mathbf{k}_x, n}^{+-} = (M_{-\mathbf{k}_x, n}^{-+})^*$ ,  $M_{\mathbf{k}_x, n}^{++} = (M_{-\mathbf{k}_x, n}^{--})^*$ , and  $M_{\mathbf{k}_x, n}^{+z} = (M_{-\mathbf{k}_x, n}^{-z})^*$ , where  $M^{\pm} = M^x \pm iM^y$ .

Now, let two spin qubits (SQs) be situated near the edge of the FM at positions  $\mathbf{r}_{\text{QD1}} = (-d/2, d_y, d_z)$  and  $\mathbf{r}_{\text{QD2}} = (d/2, d_y, d_z)$ , respectively (see Fig. 6.1). The model Hamiltonian under consideration is then

$$H = \Delta (\sigma_1^z + \sigma_2^z) + H_{\text{FM}} + \tilde{V}, \quad (6.10)$$

where  $\Delta = -J^\perp S$ , assuming  $w = 1$  for simplicity, and

$$\tilde{V} = \sum_{\mathbf{k}_x, n} S_{-\mathbf{k}_x, n}^+ \mathbf{M}_{\mathbf{k}_x, n}^- \cdot \left( e^{-i\mathbf{k}_x \cdot \mathbf{r}_{\text{QD1}}} \boldsymbol{\sigma}_1 + e^{i\mathbf{k}_x \cdot \mathbf{r}_{\text{QD2}}} \boldsymbol{\sigma}_2 \right) + h.c. \quad (6.11)$$

is the coupling between the two qubits and the magnon modes of the FM. Finally, the parameters of the FM-QD coupling used in our numerical results are listed in Tab. 6.3, unless otherwise specified.

## Effective qubit-qubit coupling

In this section we calculate the effective qubit-qubit coupling mediated by the ferromagnet. To this end, we integrate out the magnons from the Hamiltonian by means of a second order Schrieffer-Wolff transformation, and write the effective Hamiltonian as

$$H_{\text{eff}} = \Delta (\sigma_1^z + \sigma_2^z) + W_{\text{eff}}. \quad (6.12)$$

The effective coupling between the qubits assumes the form [32, 94]

$$W_{\text{eff}} = -\frac{i}{2\hbar} \lim_{\eta \rightarrow 0^+} \int_0^\infty dt e^{-\eta t} \left\langle \left[ \tilde{V}(t), \tilde{V} \right] \right\rangle_{\text{FM}}, \quad (6.13)$$

where  $\eta$  is the lifetime of the intermediate virtual excitation (i.e., magnons). The expectation value  $\langle \cdots \rangle_{\text{FM}}$  is taken with the FM ground state  $|0\rangle_{\text{FM}}$ , and  $\tilde{V}(t) = e^{iH_0 t} \tilde{V} e^{-iH_0 t}$  with  $H_0 = H_{\text{FM}} + \Delta(\sigma_1^z + \sigma_2^z)$ .

Within the framework of the Schrieffer-Wolff transformation it is possible to (implicitly) account for the fact that the pure magnons are not the true eigenstates of the FM. Magnons are dressed by other quasiparticles, e.g., by phonons, causing a finite spectral width of the magnon modes. Equation (6.13) can be written in the frequency domain as

$$W_{\text{eff}} = \frac{1}{2\hbar} \int_{-\infty}^{\infty} \frac{d\omega}{2\pi} \frac{\langle [\tilde{V}(\omega), \tilde{V}] \rangle_{\text{FM}}}{\omega + i\eta}, \quad (6.14)$$

where  $\tilde{V}(\omega) = \int_{-\infty}^{\infty} dt \tilde{V}(t) e^{-i\omega t}$  and  $\hbar\eta$  is the linewidth broadening of the corresponding magnon. In our case the linewidth broadening of the magnon mode  $(k_x, n)$  is associated with Gilbert damping and therefore  $\hbar\eta \rightarrow \alpha_G \varepsilon_{k_x, n}$ , which effectively smears out the magnon density of states cutting unphysical singularities. See App. 6.C for more technical arguments.

Expanding  $H_0$  on the eigenbasis of the FM and the qubits, the time evolution of spin and qubit creation operators takes the form  $S_{-k_x, n}^-(t) \sigma^-(t) = \sqrt{2S} e^{i\varepsilon_{k_x, n} t / \hbar - i\Delta t / \hbar} a_{k_x, n}^\dagger \sigma^-$ . The Fourier transform  $\tilde{V}(\omega)$  then contains terms like  $2\pi\hbar\sqrt{2S} M_{k_x, n}^{++} \delta(\hbar\omega - \varepsilon_{k_x, n} + \Delta) a_{k_x, n}^\dagger \sigma^-$ , facilitating the exact evaluation of the integral in Eq. (6.14). Performing the expectation value over magnons, the resulting qubit-qubit interaction can be written as  $W_{\text{eff}} = \sum_{p, q \in \{1, 2\}} W_{pq}$ , where  $W_{pq}$  contains products of qubit operators  $\sigma_p$  and  $\sigma_q$ . Expressing each contribution in terms of the susceptibility in Eq. (6.6), we obtain for  $p \neq q$

$$W_{pq} = \frac{1}{32} \sum_{k_x, n} e^{ik_x(x_p - x_q)} \chi_{nn}^\perp(\Delta/\hbar, k_x) M_{k_x, n}^{++} \sigma_p^- \times (M_{-k_x, n}^{+-} \sigma_q^- + M_{-k_x, n}^{--} \sigma_q^+ + M_{-k_x, n}^{-z} \sigma_q^z) + \text{h.c.}, \quad (6.15)$$

where we have dropped the off-resonant terms proportional to  $\chi_{nm}^\perp(0, k_x)$  and  $\chi_{nm}^\perp(-\Delta/\hbar, k_x)$  because they are highly suppressed for antiferromagnetic interlayer exchange  $J^\perp < 0$  in the relevant limit,  $d \gg l_x \gg a_x$  (see App. 6.D for further details). The diagonal terms  $W_{pp}$  simply give a tiny dynamical contribution  $\delta \mathbf{B}_{\text{eff}}$  to the effective exchange field  $\mathbf{B}_{\text{eff}}$ . Since  $|\delta \mathbf{B}_{\text{eff}}| \ll |\mathbf{B}_{\text{eff}}|$ , we omit  $W_{pp}$  in  $W_{\text{eff}}$ .

The fact that the coupling term of the XY type (i.e.,  $\propto \sigma_1^- \sigma_2^+$ ) is proportional to  $|M^{++}|^2$  instead of  $|M^{-+}|^2$  is a direct consequence of the antiferromagnetic coupling ( $\Delta \propto -J^\perp > 0$ ). Furthermore, we note that the dipole-dipole interaction can contribute to all terms in Eq. (6.15), while the isotropic direct exchange only contributes to the  $M^{-+}$  matrix element. The characteristic energies of these two interactions are strikingly different: for the dipole-dipole interaction  $\frac{\mu_0 \mu_B^2}{a^3} \sim 0.6 \mu\text{eV}$  gives an upper bound, while the direct exchange coupling is  $|J^\perp| \sim 1 \text{ meV}$ . Thus, the strongest coupling term is expected to be  $\propto \sigma_1^- \sigma_2^-$ . The full analytical form of the coupling matrix elements for the exchange and the dipole mechanisms will be shown below in Secs. 6.3-6.3.

### Decoherence rates

In the previous section the (virtual) magnon-mediated effective qubit-qubit interaction has been discussed. However, the coupling of the QD spin to the ferromagnet also gives rise to decoherence of the spin qubits caused by real magnons. In order to calculate the contribution of magnons to the decoherence times, we decompose the FM-QD interaction Hamiltonian of Eq. (6.9) such that  $V = \frac{1}{2}(V^+ \sigma^- + V^- \sigma^+) + V^z \sigma^z$  and define the corresponding noise power spectra as  $\mathcal{S}_{V^b}(\omega) = \int dt \left\{ [V^b(t)]^\dagger, V^b(0) \right\} e^{-i\omega t}$ . The relaxation and dephasing times within the Bloch-Redfield approximation then read as  $\Gamma_1 = \frac{1}{4\hbar^2} \mathcal{S}_{V^-}(\Delta/\hbar)$  and  $\Gamma_2^* = \frac{1}{4\hbar^2} \mathcal{S}_{V^z}(0)$ , respectively [32, 95].

Substituting in the corresponding couplings, to lowest order of the  $1/S$  expansion, we can relate both the longitudinal,  $\mathcal{S}_{V^z}(\omega)$ , and transversal,  $\mathcal{S}_{V^\pm}(\omega)$ , noise spectrum to the transversal magnonic power spectrum  $\mathcal{S}_{k_x, n}^\perp(\omega) = \hbar \coth(\beta \hbar \omega / 2) \text{Im}[\chi_{nn}^\perp(\hbar \omega, k_x)]$ , where  $\beta = (k_B T)^{-1}$  with  $T$  being the temperature. Finally, for the decoherence rates, one obtains

$$\Gamma_1 = \frac{1}{16\hbar^2} \sum_{k_x, n} |M_{k_x, n}^{++}|^2 \mathcal{S}_{k_x, n}^\perp(\Delta/\hbar), \quad (6.16a)$$

$$\Gamma_2^* = \frac{1}{2\hbar^2} \sum_{k_x, n} |M_{k_x, n}^{+z}|^2 \mathcal{S}_{k_x, n}^\perp(0) + \mathcal{O}(S^0). \quad (6.16b)$$

The dephasing rate  $\Gamma_2^*$  can be highly suppressed when the ferromagnetic resonance is shifted to finite energies, for example, by an external magnetic field or an easy-axis anisotropy ( $\Delta_F > 0$ , cf. Sec. 6.2).

The appearance of  $|M_{k_x,n}^{++}|^2$  in the formula for the relaxation rate of Eq. (6.16a) can be understood as follows: for antiferromagnetic coupling ( $\Delta \propto -J^\perp > 0$ ) if no magnons are excited, the excited state of the qubit is  $|0_m \uparrow\rangle$  which can then relax to the qubit ground state  $|1_m \downarrow\rangle$  creating a magnon by means of the coupling  $S^- M^{++} \sigma^-$  (note that  $S^- \propto a^\dagger$ ), where we used the simplified notation  $|0_m\rangle$  for the FM ground state and  $|1_m\rangle$  for a single magnon excitation with energy  $\Delta$ . For the ferromagnetic case ( $\Delta \propto -J^\perp < 0$ ) the qubit states are reversed and the transition  $|0_m \downarrow\rangle \rightarrow |1_m \uparrow\rangle$  describes the relaxation requiring an interaction term of the type  $S^- M^{+-} \sigma^+$ . The relaxation mechanism for ferromagnetic inter-layer coupling is then mediated by direct exchange interaction, as opposed to dipole-dipole interaction in the antiferromagnetic case. For a detailed derivation, we refer the reader to App. 6.E.

One of the central figure of merits in the field of quantum computing is the gate fidelity  $\mathcal{F} = 2\text{Tr}[\rho(t_{\text{op}})\rho_f] - 1 \in [0, 1]$  that describes the deviation of the qubit state after the operation from the targeted final state, quantified by the respective density matrices  $\rho(t_{\text{op}})$  and  $\rho_f$  [1, 96]. Let us consider a two-qubit gate implemented by the time evolution under the static Hamiltonian  $W_{\text{eff}}$ . Neglecting the subleading two-qubit terms and the single qubit terms in the time evolution for simplicity, one may consider only the  $\sigma_1^- \sigma_2^-$  coupling to get  $e^{-iW_{\text{eff}}t_{\text{op}}/\hbar} |00\rangle = (|00\rangle - ie^{i\phi} |11\rangle)/\sqrt{2}$  where  $t_{\text{op}} = \hbar \frac{\pi}{4} |\langle 11 | W_{\text{eff}} | 00 \rangle|^{-1}$  is the operation time and  $\phi = \arg(\langle 11 | W_{\text{eff}} | 00 \rangle)$ . This two-qubit operation, supplemented with single-qubit rotations, i.e.,  $U_{\sqrt{\text{SWAP}}} \sim \sigma_1^x e^{-iW_{\text{eff}}t_{\text{op}}/\hbar} \sigma_1^x$ , is equivalent to a  $\sqrt{\text{SWAP}}$  gate up to a phase. Since the relaxation rate  $\Gamma_1$  describes the decay of the diagonal elements of the density matrix as  $(\rho_{00} - \rho_{11})(t) \propto e^{-\Gamma_1 t}$ , using the operation time in the exponent, the fidelity of the two-qubit gate is obtained as

$$\mathcal{F} = \exp\left(-\frac{\pi}{4} \frac{\hbar \Gamma_1}{|\langle 11 | W_{\text{eff}} | 00 \rangle|}\right) \sim 1 - \frac{\pi}{4} \frac{\hbar \Gamma_1}{|\langle 11 | W_{\text{eff}} | 00 \rangle|}, \quad (6.17)$$

provided that the decoherence is primarily caused by relaxation. As it will be shown later, this is indeed the case for the chiral mode due to the resonant coupling.

### 6.3 Results

A numerical simulation of the effective coupling has been performed by evaluating  $W_{pq}$  in Eq. (6.15). To this end we solved the eigenvalue equa-

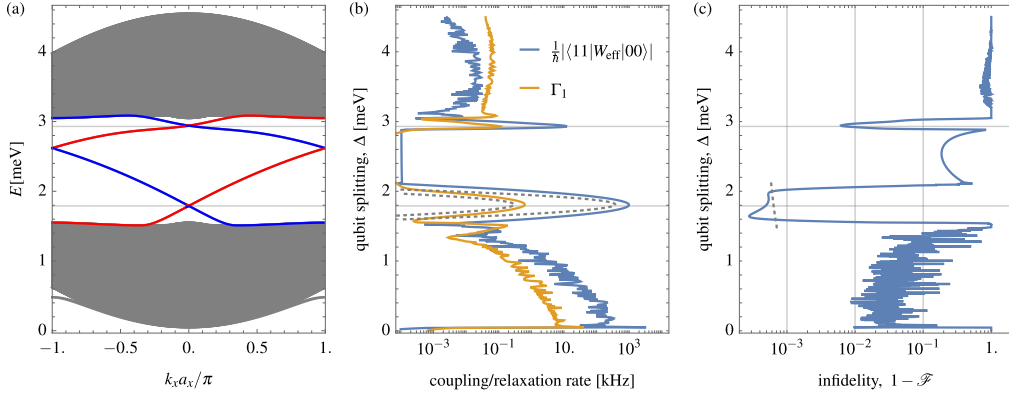


Figure 6.3: (a) Spectrum of the ferromagnetic slab with  $N_y = 1000$  unit cells as a function of momentum  $k_x$ . Chiral edge magnons at opposite edges are indicated by red and blue lines, respectively. (b) Effective qubit-qubit coupling strength (blue) and magnon-induced qubit-relaxation rate (orange) for  $T = 100$  mK, as a function of qubit splitting. Pronounced in-gap resonances are identified and associated with chiral edge magnons. Note that at the two resonances the coupling strength largely exceeds the relaxation rate, making them the optimal operation points for two-qubit gates. (c) Infidelity  $1 - \mathcal{F}$  as a function of qubit splitting. Largest fidelities are found in the energy windows of the chiral edge magnons. Vertical lines correspond to a fidelity of 90%, 99%, and 99.9%, respectively. In (a)-(c), horizontal gray lines indicate the energy of the chiral edge modes at  $k_x = 0$ . Dashed grey lines in (b) and (c) correspond to the result of the analytical formulas, i.e. Eqs. (6.19)-(6.20) with the coupling matrices taken from Eqs. (6.24) and (6.25).

tion of Eq. (6.3) numerically using a slab unit cell consisting of  $N_y = 1000$  armchair cells (i.e., 4000 spins). The resulting eigenvalues  $\varepsilon_{k_x, n}$  were used to obtain the susceptibility according to Eq. (6.6), while the eigenmodes  $\varphi_{k_x, n}$  were used in the explicit expressions for the direct exchange and dipole-dipole couplings [for which we refer the reader to Eqs. (6.75) and (6.83) of the corresponding appendices]. The interlayer exchange was varied together with the qubit splitting as  $J^\perp = -\Delta/S$  to account for the effective exchange field, and the other parameters are listed in Tabs. 6.1-6.3.

We obtained pronounced Gaussian resonances for both the coupling strength and the relaxation rate when the qubit splitting matches the energy of the edge modes at  $k_x = 0$  [see Fig. 6.3(a)-(b)]. The coupling strength for the lower in-gap resonance can reach up to 1 MHz facilitat-

ing fast two-qubit operations over  $\mu\text{m}$  distances with fidelities exceeding 99.9% [see Fig. 6.3(c)]. Further insight into the dependence of the coupling on the various parameters of our model can be obtained via the analytical formulas within the continuum approximation to be presented below. First we obtain the coupling strength as a function of the coupling matrices in Sec. 6.3, then provide analytical formulas for the coupling matrices for both the exchange and dipole-dipole interaction in Secs. 6.3-6.3.

### Chiral edge mode

If the qubit splitting  $\Delta$  lies within the magnonic gap and is close to  $\varepsilon_0 \equiv \varepsilon_{0,e}$ , defined as the energy of the chiral edge mode at  $k_x = 0$ , the effective coupling in Eq. (6.15) simplifies as the contribution of bulk modes ( $n \neq e$ ) are far off-resonant. Since the spin density of the QD is distributed over several lattice sites, the qubit spin  $\sigma$  can only couple to magnon modes with  $k_x \lesssim l_x^{-1}$ , where the spectrum of the edge mode can be written as  $\varepsilon_{k_x,e} = v_x k_x + \varepsilon_0$ , with  $v_x \sim 0.39 \text{ meV}\cdot\text{nm}$ . Finally, the susceptibility near the edge resonance reads as

$$\chi_{nn}^\perp(\Delta, k_x) \approx -2S \frac{\delta_{ne}}{v_x(k_x + i\kappa) - \delta} \quad (6.18)$$

where  $\delta = \Delta - \varepsilon_0$  is the detuning from the edge resonance and  $\kappa^{-1} \approx \frac{v_x}{\alpha_G \varepsilon_0}$  is the mean free path of the chiral magnon. In the continuum approximation we replace the sum over  $k_x$  by an integral [as in Eq. (6.58)]. Furthermore, close to resonance the integration limit can be extended to infinity, provided that  $|\delta/v_x| \ll \pi/a_x$ . Then, exploiting that  $\hat{M}_{k_x,n}$  is an analytic function of  $k_x$ , we can perform the momentum integral using the residue theorem [see Eq. (6.59)] to obtain

$$\langle 01 | W_{\text{eff}} | 10 \rangle \approx -i \frac{S a_x}{16 v_x} e^{i k_0 d - |\kappa| d} |M_{k_0,e}^{++}|^2, \quad (6.19a)$$

$$\langle 11 | W_{\text{eff}} | 00 \rangle \approx i \frac{S a_x}{16 v_x} e^{-i |k_0| d - |\kappa| d} M_{k_0,e}^{++} M_{-k_0,e}^{-+}, \quad (6.19b)$$

$$\langle 10 | W_{\text{eff}} | 00 \rangle \approx i \Theta(v_x) \frac{S a_x}{16 |v_x|} e^{-i |k_0| d - |\kappa| d} M_{k_0,e}^{++} M_{-k_0,e}^{-z}, \quad (6.19c)$$

$$\langle 01 | W_{\text{eff}} | 00 \rangle \approx i \Theta(-v_x) \frac{S a_x}{16 |v_x|} e^{-i |k_0| d - |\kappa| d} M_{k_0,e}^{++} M_{-k_0,e}^{-z}, \quad (6.19d)$$

where  $k_0 = \delta/v_x$  and we neglected  $\kappa$  in the coupling, i.e.,  $M_{k_0+i\kappa,e}^{+\alpha} \approx M_{k_0,e}^{+\alpha} + \mathcal{O}(\kappa d_y)$ . This latter approximation is justified since every length

scale in the coupling is much smaller than  $\kappa^{-1} \approx 2.2 \mu\text{m}$ , for example,  $d_z, d_y \sim 1 \text{ nm}$ .

The Gaussian dependence on the detuning around the resonance in Fig. 6.3(b) can be understood via the spatial averaging effect of the QD. Since the magnetic moment of the particle is equally distributed along the QD, the coupling to magnon modes with  $k_x > l_x^{-1}$  is averaged out leading to  $\hat{M}_{k_x,n} \propto e^{-k_x^2 l_x^2/4}$  (see App. 6.F). Furthermore,  $l_x$  is much larger than the remaining length scales in the coupling (i.e.,  $l_y, d_y, d_z$ , and  $a$ ) and therefore one can expand the coupling as  $\hat{M}_{k_x,n} \approx e^{-k_x^2 l_x^2/4} \hat{M}_{0,n} + \mathcal{O}(l_y/l_x)$ .

Using the same assumptions as for the effective coupling, the contribution of the edge modes to the decoherence rates can also be estimated using Eq. (6.16). If the detuning is close to zero, the relaxation is dominated by the resonant edge mode at  $k_x = 0$  and reads as

$$\Gamma_1 \approx \frac{S a_x}{16 \hbar v_x} |M_{k_0,e}^{++}|^2 \coth(\beta \varepsilon_0/2). \quad (6.20)$$

Since the (pure) dephasing rate is proportional to  $\mathcal{S}_{k_x,n}^\perp(0)$  [see Eq. (6.16b)], the contribution of the edge mode is far off-resonant. In order to estimate it, we expanded the susceptibility in the Gilbert damping  $\alpha_G$  to get  $\mathcal{S}_{k_x,e}^\perp(0) \approx \hbar \coth(\beta \varepsilon_0/2) 2\alpha_G S/\varepsilon_0$ . The dephasing rate can then be written as

$$\Gamma_{2,e}^* \approx \frac{\alpha_G S}{\hbar \sqrt{2\pi \varepsilon_0}} \frac{a_x}{l_x} |M_{0,e}^{-z}|^2 \coth(\beta \varepsilon_0/2), \quad (6.21)$$

where we exploited that  $M_{k_x,n} \approx e^{-k_x^2 l_x^2/4} M_{0,n}$  for every mode. Using Eq. (6.21) we obtain  $\Gamma_2^* \sim 10^{-4} \text{ Hz}$  that is vastly underestimating the dephasing rate (as it will be shown later).

In order to find the leading contribution to dephasing we need to consider the modes that are closest to zero energy. We do this in the 2D limit, which is valid deep in the bulk when the QD is far from the edges of the FM. Here one can replace the coupling  $M_{k_x,n}$  by  $M_{k_x,k_y}$ , that is the coupling to the magnon mode with energy  $\varepsilon_{k_x,k_y}$ , as obtained for periodic boundary conditions along the  $x$  and the  $y$  direction. Since  $l_x \gg a_x$ , we still restrict ourselves to  $k_x = 0$  in the coupling to get

$$\Gamma_2^* \approx \frac{\alpha_G S}{\hbar \sqrt{2\pi} \Delta_F} \frac{a_x}{l_x} \coth(\beta \Delta_F/2) \sum_{k_y} |M_{0,k_y}^{-z}|^2, \quad (6.22)$$

where we neglected the curvature of the magnon band since  $\Delta_F \lesssim \varepsilon_{0,k_y}$ .

Using Eq. (6.19a) and Eq. (6.20), an important relation can be deduced, namely,

$$\frac{|\langle 01 | W_{\text{eff}} | 10 \rangle|}{\hbar \Gamma_1} = e^{-|\kappa|d} \tanh(\beta \varepsilon_0 / 2) \sim \mathcal{O}(1), \quad (6.23)$$

meaning that the relaxation provides an upper bound for the XY coupling, regardless of the strength of the QD-FM coupling. The same formula is valid in the ferromagnetic interlayer coupling regime ( $J^\perp > 0$ ), where both quantities are proportional to  $|M^{+-}|^2$ . Since the  $\langle 01 | W_{\text{eff}} | 10 \rangle$  is the leading coupling in that case, virtual magnon processes are unable to create entanglement between qubits while maintaining the coherence of the two-qubit system. Therefore, we have focused here on the antiferromagnetic case, where the strongest coupling is  $\langle 11 | W_{\text{eff}} | 00 \rangle$ ; we will revisit the ferromagnetic coupling case in Sec. 6.4, where we try to leverage the fast magnon emission/absorption rate ( $\Gamma_1$ ) in a scheme where a real magnon is mediating the coupling between distant spin qubits (as opposed to virtual magnons considered so far).

The dependence of the coupling on the inter-QD distance  $d$  is explicitly defined in Eq. (6.19), however, in order to determine the coupling strength and to identify the dependence on the QD size and position we need to calculate the coupling matrix elements  $M_{k_x, e}$  for the case of direct exchange and dipole-dipole coupling.

## Exchange coupling

Let us first consider the contribution of (isotropic) direct exchange interaction between the FM spin  $S_i$  and the qubit spin  $\sigma$  that is given by the exchange matrix  $-\hat{\mathbf{J}}_i |\psi(\mathbf{r}_i - \mathbf{r}_{\text{QD}})|^2$ , where  $\hat{\mathbf{J}}_i$  is the local spin-spin interaction matrix between the  $i$ th site of the FM and the qubit layer. In this case the effective coupling between the magnonic mode  $(k_x, n)$  and the spin qubit is given by

$$\begin{aligned} M_{-k_x, n}^+ &= -\frac{1}{\sqrt{N_x}} \sum_{\mathbf{r}_i, \mu} e^{ik_x(x_i - x_{\text{QD}})} \varphi_{k_x, n}^\mu(y_i) 2J_i^\perp |\psi(\mathbf{r}_i + \mathbf{r}^\mu - \mathbf{r}_{\text{QD}})|^2 \\ &\approx -e^{-k_x^2 l_x^2 / 4} J^\perp C_{k_x, n}, \end{aligned} \quad (6.24)$$

where we assumed the QD wavefunction to be Gaussian, i.e.,  $|\psi(\mathbf{r}_i)|^2 = \frac{a_x}{\sqrt{\pi} l_x} e^{-x_i^2 / l_x^2} |\psi(y_i)|^2$ , and we defined  $C_{k_x, n} = \frac{1}{2} \sum_{y_i, \mu} \varphi_{k_x, n}^\mu(y_i) e^{ik_x x^\mu} |\psi(y_i - d_y)|^2$ . Furthermore, for simplicity we assumed homogeneous and isotropic coupling,  $\hat{\mathbf{J}}_i \approx J^\perp \mathbb{1}$ .



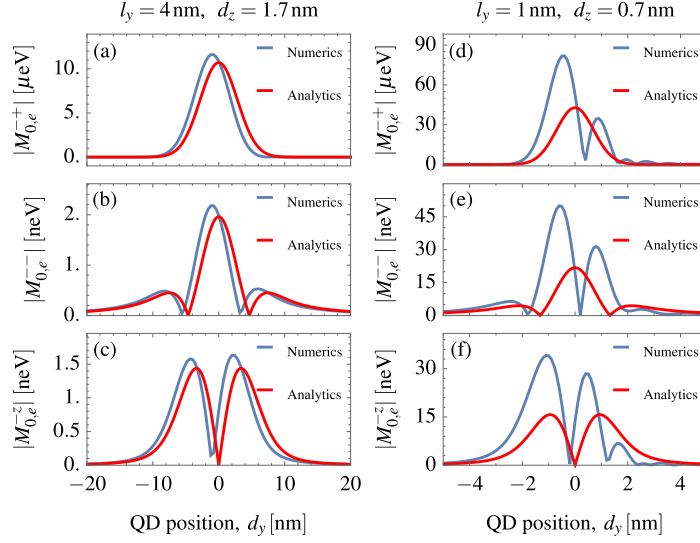


Figure 6.4: Coupling matrix elements  $M_{k_x,e}^{+-}$ ,  $M_{k_x,e}^{--}$ , and  $M_{k_x,e}^{zz}$  at  $k_x = 0$  including both direct exchange and dipole-dipole interactions as a function of the QD position  $d_y$  for (a)-(c)  $l_y = 4$  nm and  $d_z = 1.7$  nm and (d)-(f)  $l_y = 1$  nm and  $d_z = 0.7$  nm. Numerical results (blue lines) are obtained from Eqs. (6.75) and (6.83). Analytical results (red lines) are given in Eqs. (6.24) and (6.25). The rest of the parameters are given in Tabs. 6.1-6.3. Direct exchange interaction only contributes to  $M^{+-}$ , therefore this coupling element is orders of magnitude larger than  $M^{--}$  and  $M^{zz}$ . We observe good quantitative agreement between the numerical and analytical curves in (a)-(c), whereas for smaller  $l_y$  and  $d_z$  values in (d)-(f) the coupling is strongly asymmetric around the FM edge ( $d_y = 0$ ) due to the spatial profile of the edge magnon that is not taken into account in the analytics.

Owing to the Gaussian factor in the coupling the main contribution of the coupling matrix to the qubit-qubit coupling in Eq. (6.19) is given by small momenta ( $k_x \lesssim l_x^{-1}$ ). In this regime,  $C_{k_x,e} \approx C_{0,e}$  is a good approximation for the coefficient in Eq. (6.24). Provided that the DMI is strong enough, i.e.,  $D > 0.1J$ , the localization length of the edge mode is small, i.e.,  $\lambda \ll l_y$  [see Fig. 6.2(c)]. In this limit we can factor out  $\delta\mu_e$  and estimate the corresponding coefficient as  $C_{0,e} \approx \frac{a_y}{2\sqrt{\pi}l_y} \delta\mu_e e^{-d_y^2/l_y^2}$  (see App. 6.F for further details).

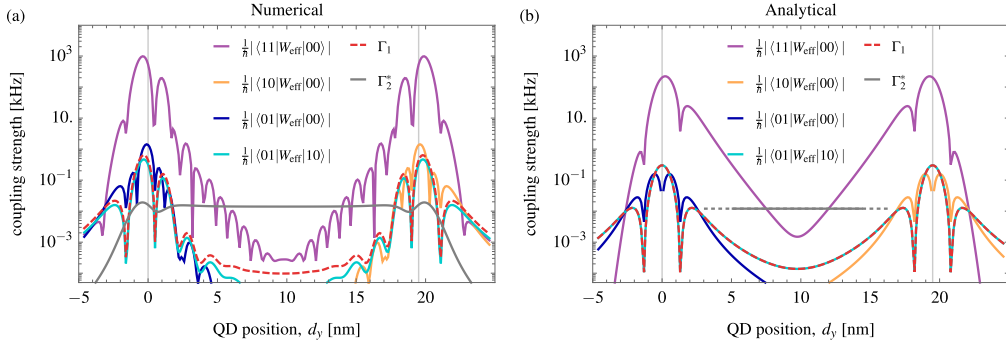


Figure 6.5: Position dependence of the effective qubit-qubit couplings and the qubit relaxation. The parameters are the same as for Fig. 6.3, except for the slab width that is set to  $N_y = 20$  in order to show both edges of the FM simultaneously. (a) Numerical results for the matrix elements of the effective coupling  $W_{\text{eff}}$  of Eq. (6.15) for a constant qubit splitting of  $\Delta = 1.8$  meV. (b) Analytical results of the couplings and the relaxation are given in Eqs. (6.19)-(6.20) by substitution of Eqs. (6.24) and (6.25). The analytical estimate in the bulk for  $\Gamma_2^*$  was calculated using Eq. (6.22) with Eq. (6.27). The excellent quantitative agreement between the numerical simulation (a) and analytical formulas (b) facilitates the estimation of the various coupling and decoherence time scales in different materials without having to perform the heavy numerical calculations.

## Dipole-dipole coupling

Owing to its long-ranged nature, calculations involving the dipole-dipole interaction are unwieldy and deferred to App. 6.G. Here, we only note that the exponential suppression factor in momentum,  $e^{-k_x^2 l_y^2/4}$ , appears regardless of the form of the interaction potential. Therefore, we restrict our attention to the  $k_x = 0$  case and provide an analytical formula, assuming that the other confinement length of the QD,  $l_y$  is sufficiently large, compared to the localization length of the edge magnon,  $\lambda$ , e.g.,  $\lambda \ll l_y$ . The coupling matrix elements in this limit read as

$$M_{0,e}^{-+} = -M_{0,e}^{--} = \frac{\mu_0}{\pi} \frac{g}{a_x l_y^2} g_{\text{QD}} \mu_B^2 \delta \mu_e \text{Re} \left[ I \left( \frac{i d_y - d_z}{l_y} \right) \right], \quad (6.25a)$$

$$M_{0,e}^{-z} = -i \frac{\mu_0}{\pi} \frac{g}{a_x l_y^2} g_{\text{QD}} \mu_B^2 \delta \mu_e \text{Im} \left[ I \left( \frac{i d_y - d_z}{l_y} \right) \right], \quad (6.25b)$$

where we have introduced the complex function  $I(x) = 1 + \sqrt{\pi}xe^{x^2}[1 + \text{erf}(x)]$ . Similarly to the case of the direct exchange interaction, it is the  $\lambda \ll l_y$  assumption that allowed us to factor out the dynamical magnetic moment  $\delta\mu_e$  of the chiral edge mode from the integral.

The analytical estimates for the couplings  $M_{0,e}^{-+}$ ,  $M_{0,e}^{--}$ , and  $M_{0,e}^{-z}$  obtained in Eqs. (6.24) and (6.25) are compared with the numerically evaluated exact expressions given in Eqs. (6.75) and (6.83) as a function of  $d_y$  in Fig. 6.4. The analytical formulas are in very good agreement with the numerics as shown in Fig. 6.4(a)-(c) for  $l_y = 4$  nm and  $d_y = 1.7$  nm. Further parameters of the QD and the FM were set as in Tabs. 6.1-6.3. The only apparent deviation is the slight shift of the peaks in the numerics, compared to the edge ( $d_y = 0$ ). We attribute this effect to the asymmetric nature of the edge mode (i.e., the mode terminates with a sharp maximum at the edge and decays exponentially towards the bulk) that is not taken into account in the analytical estimate which assumes  $\varphi_{0,e}^\mu(y) \sim \frac{1}{4}\delta\mu_e\delta(y)$ .

The FM-QD coupling matrix elements are presented in Figs. 6.4(d)-(f) for the same parameters used in Fig. 6.3, i.e.,  $l_y = 1$  nm and  $d_z = 0.7$  nm. Even though the localization length  $\lambda \sim 1$  nm, is comparable with  $l_y$ , the qualitative behavior is correct and the maximal coupling strength is reliable in order of magnitude. As compared to the analytical prediction, the numerical results exhibit features that are slightly shifted outwards from the edge [similarly to Fig. 6.4(a)-(c)] and small oscillations appear on the side of the FM ( $d_y > 0$ ). These effects appear due to the spatial “fine structure” of the edge mode (exponential decay and oscillations on the scale of  $a_y$ ) that is not accounted for in the analytical approximation.

In order to complement the estimate of the bulk dephasing formula in Eq. (6.22), we provide here the relevant coupling matrix element for  $k_x = 0$  as a function of  $k_y$  (assuming periodic boundary conditions along  $y$  direction). The coupling between the QD spin and the lower-energy acoustic magnon band reads

$$M_{0,k_y}^{-z} \approx \frac{\mu_0\mu_B^2 gg_{\text{QD}}}{2a_x a_y} k_y e^{-k_y^2 l_y^2/4} e^{-|k_y|d_z}, \quad (6.26)$$

where we neglect the contribution of the optical magnon band, since their contribution is suppressed by the negligible dynamical magnetic moment as well as the large energy denominator in Eq. (6.22). The sum over  $k_y$  modes can be evaluated in the continuum limit as

$$\sum_{k_y} |M_{0,k_y}^{-z}|^2 \approx \frac{1}{2\pi} \frac{a_y}{l_y} \left( \frac{\mu_0\mu_B^2 gg_{\text{QD}}}{2a_x a_y l_y} \right)^2 I_2(d_z/l_y), \quad (6.27)$$

where  $I_2(x) = \sqrt{2\pi}(1 + 4x^2)e^{2x^2}[1 + \text{erf}(\sqrt{2}x)] - 4x$ .

## Position dependence of the effective coupling

Choosing a smaller system size of  $N_y = 20$  and considering the various couplings and decoherence rates as a function of  $d_y$  allows us to compare the full analytical formulas with the numerics in Fig. 6.5(a) and (b). For this we have tuned the qubit energy to be on resonance with the  $k_x = 0$  chiral mode i.e.,  $\Delta = 1.8 \text{ meV}$  [see Fig. 6.3(a)]. Even though, in potential experiments if the QD is moved outside the FM (in-situ), the decreasing interlayer exchange experienced by the QD would tune the qubit frequency out of resonance<sup>3</sup>, which is not taken into account in Fig. 6.5.

As shown in Fig. 6.5, the peaks of the effective coupling develop only close to the two edges of the sample at  $d_y = 0$  and  $d_y = 20 \text{ nm}$ , which provides a natural way to tune the qubits in and out of the coupling regime. This property is crucial since the qubit splitting is set by the interlayer exchange interaction that is challenging to tune in-situ. On the other hand  $d_y$  can be changed freely in the range  $d_y \in [0, 20 \text{ nm}]$  since the interlayer exchange is constant to a good approximation in this range.

The strongest coupling is achieved for the  $\langle 11 | W_{\text{eff}} | 00 \rangle$  matrix element because this is the only coupling that is proportional to the interlayer exchange  $J^\perp$ . In order to capture the exponential decay towards the bulk we have used Eq. (6.80) for the analytical curve instead of the simplistic formula for  $C_{0,e}$  given in Sec. 6.3.

The second strongest coupling are the  $\sigma^\pm \sigma^z$ -type of terms that come about three orders of magnitude smaller than the  $\langle 11 | W_{\text{eff}} | 00 \rangle$  term. Importantly, since the propagation direction is opposite along the left and right edges, from Eq. (6.19) we expect only  $\langle 01 | W_{\text{eff}} | 00 \rangle$  coupling on the left edge (because  $v_x < 0$ ) and  $\langle 10 | W_{\text{eff}} | 00 \rangle$  on the right edge (because  $v_x > 0$ ). This is fulfilled up to several orders of magnitude in Fig. 6.5 (cf. yellow and blue lines) and a clear marker of chirality.

The excellent agreement between numerical and analytical results is sustained for the decoherence rates as well. The ratio of the XY coupling and the relaxation rate in Eq. (6.23) being  $\mathcal{O}(1)$  is confirmed by the numerical results close to the edge resonances. The dephasing rate estimate

<sup>3</sup>Within the present assumptions the detuning from resonance would change as  $\delta = \frac{S|J^\perp|}{2} \{ \text{erf}[d_y/l_y] + \text{erf}[(L_y - d_y)/l_y] \} - \varepsilon_0$ . Note that depending on the value  $J^\perp$ , the resonance can be reached at any  $d_y$  in principle.

for the bulk in Eq. (6.22) [using Eq. (6.27)] turns out to be a very good estimate a few nm away from the edges.

## 6.4 Qubit entanglement via chiral magnon transduction

As mentioned in Sec. 6.3, the virtual magnon coupling strength and the relaxation rate are both proportional to the coupling  $|M_{0,e}^{+-}|^2$  in the ferromagnetic interlayer coupling regime ( $J^\perp > 0$ ). Therefore, since  $|\langle 01 | W_{\text{eff}} | 10 \rangle| \sim \Gamma_1$ , the virtual magnon mediated coupling is inefficient in this case. One possibility to overcome this limitation is through coupling by *real* magnons (as opposed to virtual ones described above). Provided that the FM-QD coupling (i.e.,  $J^\perp$ ) can be switched on and off on demand, the first qubit can be used to emit a chiral edge magnon that propagates and is subsequently absorbed by the second qubit, coherently. This protocol is leveraging that the emitted magnon wave packet will propagate towards the second qubit maintaining its shape (quasi-linear dispersion) because it cannot backscatter at defects due to its chirality and the presence of the topological gap.

Previous proposals for such a magnon transduction protocol have focused on the single magnon mode approximation [36]. Such an approximation, however, can only be made if the energy separation from higher magnonic modes is much larger than the coupling strength. For the case of the chiral magnon this energy scale is  $v_x/\mathcal{C} \sim 1$  neV, where  $\mathcal{C} \sim 100 \mu\text{m}$  is a typical circumference of the sample and  $v_x \approx 0.39 \text{ meV}\cdot\text{nm}$ . This energy separation is orders of magnitude smaller than the achievable FM-QD coupling  $g \propto M_{0,e}^{+-}$  in Fig. 6.4(a). Note that we use Fig. 6.4(a) as a reference here, because the coupling is dominated by direct exchange interaction  $J^\perp$  and therefore it agrees up to a sign with the coupling of the ferromagnetic case ( $J^\perp > 0$ ).

In order to discuss the limit where  $g \gg v_x/\mathcal{C}$ , the complete dynamics of the local magnon excitations need to be considered. To model the scenario when the spin qubits are on resonance with the chiral edge mode, we consider a one-dimensional bosonic lattice with the dispersion relation given by the chiral edge mode. In order to reduce the computational cost further, we extend the FM unit cell to several lattice sites,  $a_x \rightarrow 2l_x$ , thereby backfolding the spectrum as depicted in Fig. 6.6(a). We consider only a single mode that used to cross  $k_x = 0$  before the backfolding of

the spectrum, which is the red line in the highlighted area in Fig. 6.6(a). The coupling to higher-energy edge modes (originally at  $k_x = n\pi/l_x$ ) is negligible, since they are suppressed by the factor  $e^{-(n\pi)^2/4}$ . Furthermore, we assume that each spin qubit couples to a single FM unit cell and the coupling is uniform within the unit cell.

In order to mitigate the contribution of the virtual magnon processes, only one of the qubits should be coupled to the magnon mode at any given time. The entangling protocol then consists of three steps, viz., (i) first qubit is coupled and emits a magnon; (ii) both qubits are decoupled and the magnon propagates; (iii) second qubit is coupled and absorbs the magnon. This could be achieved, for example, when the effective coupling strength is  $g = 5 \mu\text{eV}$ , in which case the size of the emitted magnon wave packet  $v_x \hbar/g \sim 80 \text{ nm}$  is indeed much smaller than the distance between the two qubits.

We account for the local coupling and the dynamics of the emitted magnon wave packet by performing a numerical simulation of the system by solving the Lindblad equation [97]

$$\begin{aligned} \dot{\rho} = & -\frac{i}{\hbar}[H(t), \rho] + \frac{1}{2}\Gamma_2^* \sum_{i=\{1,2\}} D[\sigma_i^z] \rho \\ & + \frac{2\alpha_G}{\hbar} \sum_k \varepsilon_k \left\{ (1 + \bar{n}) \mathcal{D}[a_k] \rho + \bar{n} \mathcal{D}[a_k^\dagger] \rho \right\} \end{aligned} \quad (6.28)$$

where  $\mathcal{D}[O]\rho = O\rho O^\dagger - \frac{1}{2}(OO^\dagger\rho + \rho OO^\dagger)$  and  $\bar{n} = [\exp(\beta\varepsilon_k) - 1]^{-1}$ , with  $\varepsilon_k$  being the linear dispersion of the edge mode. The corresponding Hamiltonian is written as

$$\begin{aligned} H(t) = & \Delta(\sigma_1^z + \sigma_2^z) + c_1(t, \delta t) a_1 \sigma_1^+ \\ & + c_2(t - t_{\text{prop}}, \delta t) a_{N_x} \sigma_2^+ + \text{h.c.}, \end{aligned} \quad (6.29)$$

where  $t_{\text{prop}} = \hbar d/v_x$  is the propagation time. The time dependence of the coupling is a smeared out box function, i.e.,  $c_i(t, \delta t) = g_i n_F[t/t_{\text{rise}}] n_F[(t + \delta t)/t_{\text{rise}}]$ , where  $\delta t$  is the length of the pulse,  $n_F(x) = (\exp(x) + 1)^{-1}$  and  $t_{\text{rise}} = 70 \text{ ps}$  is the rise time<sup>4</sup> of the pulse [see Fig. 6.6(b)].

From the time series of the density matrix, we evaluate the von-Neumann entropy of the  $i$ th qubit, defined by

$$\nu_i = -\text{Tr}_{\mathcal{H} \setminus \mathcal{H}_i} [\rho \ln(\rho)], \quad (6.30)$$

<sup>4</sup>The choice of the rise time is a crucial step in order to create a magnon wave packet that can be efficiently absorbed by the second qubit. We found that a pulse with (relatively) long  $t_{\text{rise}}$  time creates a more symmetric wave packet that can be absorbed with a higher accuracy (i.e., magnon number reduces close to zero after absorption).

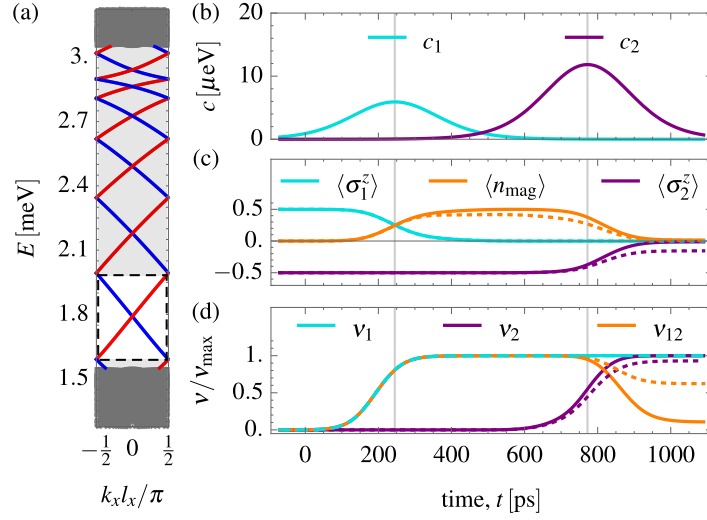


Figure 6.6: (a) Backfolded topological magnonic bandgap of the ferromagnet with a unit cell size of  $2l_x = 5a_x$ . Only the coupling to the highlighted bands are relevant (dashed white box), as discussed in the main text. (b) Coupling strength  $c_{1,2}$  as a function of time for the first and second qubit, respectively. (c) Expectation value of the qubit spins  $\sigma_1^z$  and  $\sigma_2^z$  and the total magnon number  $n_{\text{mag}}$  in the edge of the ferromagnet. (d) von Neumann entropy of the first qubit  $\nu_1$ , the second qubit  $\nu_2$ , and the two-qubit system  $\nu_{12}$ . Solid lines correspond to the dissipationless process and dotted lines to  $\alpha_G = 10^{-4}$  and  $\Gamma_2^* = 100$  kHz. It is apparent from (c) and (d) that even small dissipation has a detrimental effect on the entanglement of the qubits with the environment (i.e.,  $\nu_{12} \neq 0$  in the end of the protocol) suggesting that efficient preparation of a two-qubit entangled state requires a magnon mean-free-path that is much longer than the qubit-to-qubit distance.

where  $\text{Tr}_{\mathcal{H} \setminus \mathcal{H}_i}$  denotes the partial trace, excluding the subspace of the corresponding qubit. Additionally,  $\nu_{12}$  and  $\nu_m$  are the entropies of the two-qubit system and the magnons with the environment, respectively. The spin expectation value of the  $i$ th qubit is then calculated as

$$\langle \sigma_i \rangle = \text{Tr}_{\mathcal{H} \setminus \mathcal{H}_i} [\rho \sigma_i], \quad (6.31)$$

and the magnon occupation number is

$$\langle n_{\text{mag}} \rangle = \text{Tr}_{\mathcal{H} \setminus \mathcal{H}_m} [\rho \sum_l a_l^\dagger a_l]. \quad (6.32)$$

The time-evolution of the entanglement entropy  $\nu_i$  of Eq. (6.30), the spin expectation value  $\langle \sigma_i \rangle$  of Eq. (6.31), and the magnon number  $\langle n_{\text{mag}} \rangle$  of Eq. (6.32) are presented in Fig. 6.6(c)-(d). The density matrix  $\rho(t)$  in the definition of these quantities were obtained by numerically integrating Eq. (6.28). We set  $2l_x = 14a_x$  and consider  $N_x = 11$  lattice sites along the one-dimensional chain. After the emission of the magnon, the wave packet propagates along the chain twice, traveling a total distance of  $42l_x \approx 510$  nm before it is reabsorbed by the second qubit (periodic boundary conditions have been assumed). Two cases are differentiated: dissipationless [ $\alpha_G = 0$  and  $\Gamma_2^* = 0$ ; see solid lines in Fig. 6.6(c)-(d)] and dissipative evolution [ $\alpha_G = 10^{-4}$  and  $\Gamma_2^* = 100$  kHz; see dotted lines in Fig. 6.6(c)-(d)]

The dissipationless case can be discussed straightforwardly in the state vector representation. At  $t = 0$ , the time evolution starts from a pure state of each subsystems i.e.,  $|\uparrow\rangle_1 |\downarrow\rangle_2 |0\rangle_m$ . Between  $t = 200$  ps and  $t = 300$  ps the first qubit emits a magnon with 50% probability leading to an entangled state  $\frac{1}{\sqrt{2}}[|\uparrow\rangle_1 |\downarrow\rangle_2 |0\rangle_m + |\downarrow\rangle_1 |\downarrow\rangle_2 |\psi(x)\rangle_m]$  where  $|\psi(x)\rangle_m$  is a spatially extended wavepacket of a single magnon. At this point the first qubit has a vanishing spin expectation value and the magnon occupation number is  $1/2$ . The entanglement is created between the first qubit and the magnon, therefore  $\nu_1 = \nu_{\text{max}} \equiv \ln 2$  and  $\nu_{12} = \nu_m = \nu_{\text{max}}$  [see solid lines in Fig. 6.6(c)-(d)]. Until  $t = 700$  ps the magnon wave packet propagates through the lattice and reaches the position of the second qubit ( $|\psi(x)\rangle_m \rightarrow |\psi(x-d)\rangle_m$ <sup>5</sup>). In the final step of the protocol the second qubit needs to absorb the incoming magnon with 100% probability [thus the doubled coupling strength in Fig. 6.6(b)] creating a pure state of the two qubit system  $\frac{1}{\sqrt{2}}[|\uparrow\rangle_1 |\downarrow\rangle_2 + |\downarrow\rangle_1 |\uparrow\rangle_2] |0\rangle_m$  with  $\nu_1 = \nu_2 = \nu_{\text{max}}$  and  $\nu_{12} = \nu_m = 0$ .

When the qubit decoherence and the Gilbert damping in Eq. (6.28) is included, the main difference compared to the dissipationless case is the damping of the magnon wavepacket during its propagation, i.e.,  $\langle n_{\text{mag}} \rangle < 1/2$  at  $t = 700$  ps in Fig. 6.6(c). The entanglement with the environment can be tracked via the entanglement entropies in Fig. 6.6(d). Since the magnon number goes to zero, the corresponding entanglement  $\nu_m$  needs to vanish (the vacuum of magnons is a pure state). Nonetheless  $\nu_{12} \neq 0$ , meaning that the two qubits are still entangled with another subsystem, the environment. Therefore, considering  $\nu_1 = \nu_{\text{max}}$  or  $\nu_2 \approx \nu_{\text{max}}$

<sup>5</sup>Since the first qubit is coupled to the first unit cell and the second to the last unit cell, the effective qubit-qubit distance in the simulation is  $d = 42l_x \sim 510$  nm.



gives a false impression about  $\nu_{12}/\nu_{\max} \approx 0.6$  becomes the only appropriate measure for the infidelity.

We conclude this section by noting that even though qubit-qubit entanglement can be created through magnon transduction, the fidelity of the operation is seriously limited by the magnon mean free path (as also pointed out in Ref. [36]). Moreover, we note that such a resonant coupling protocol does not correspond to universal two-qubit logic [98] with the chirality of the edge magnon restricting the quantum computing applications of the magnon transduction protocol even further.

## 6.5 Discussion

In the setup considered in this Paper, the QD needs to be close to the FM edge in order to achieve sufficiently strong coupling. However, at this position, due to the large exchange field gradient, the qubit is susceptible to fluctuations of its position (i.e.,  $\delta d_y$ ), which would lead to a fluctuating qubit splitting and thus dephasing. In order for the dephasing rate to stay well below the two-qubit operation frequencies, the fluctuations  $\delta d_y$ , need to be small enough; we estimate that  $e^{-d_y^2/l_y^2}(\langle \delta d_y^2 \rangle / l_y^2)^{-1/2} \ll 10^{-6}$ . There are different ways to overcome this limitation: (i) The QD can be confined in a narrow nanowire along the FM edge that fixes its position and therefore the effective exchange field. In that case, it is required that the qubit splitting is tuneable by other means (e.g., via an external field if  $g_{\text{QD}} \neq g_{\text{FM}}$ ) and thereby the qubit-qubit coupling can be switched on and off on demand [as in Fig. 6.3(b)]. (ii) The qubit can be located close to a domain-wall in DMI instead of the edge, where the magnetization is constant throughout but the DMI strength  $D$  changes sign. Since the chirality of the edge mode is given by  $\text{sign}(D)$ , for a given ground state magnetization [79], two well-localized edge modes are propagating in the same direction along such a domain wall, potentially increasing the coupling strength by a factor of two. (iii) The QD layer can be terminated as well at the edge of the FM layer. In this case the QD experiences a constant interlayer exchange  $J^\perp$ , and therefore the decoupling has to be performed by moving the QD towards the bulk of the lattice. Additionally, option (i) and (iii) might offer a solution to achieve a QD that is narrow enough  $l_y \sim 1$  nm to efficiently couple to the edge mode.

Throughout this work we concentrated on a honeycomb-lattice topological magnon insulator. This model is approximately realized in monolayers of the van der Waals materials  $\text{CrI}_3$  [70],  $\text{CrSiTe}_3$ , and  $\text{CrGeTe}_3$  [71].

These materials support chiral edge magnons in the low THz range. The honeycomb-lattice model is also realized in artificial arrays of magnetic disks hosting topological magnetic solitons that interact magnetostatically; chiral modes are found in the low GHz range [99]. The general formulas for the effective two-qubit coupling derived here, for example, in Eq. (6.19), are agnostic to the actual realization of the platform hosting topological magnons. As such, they apply to any topological-magnon host—be it on the honeycomb or other lattices, in the GHz or THz range—and provide a guide for the identification of suitable materials.

Finally, we point out that the long-range spin-qubit entanglement may also be used as a probe for the experimental detection of topological chiral edge magnons, one of the key challenges in the field of topological magnons [72–75]. Chiral magnetic edge excitations are notoriously hard to detect with common probes of magnetism that are nonlocal and mostly bulk-sensitive, such as inelastic neutron scattering. In contrast, the *local* coupling to quantum-dot spin qubits, as shown above, can be considerably large. A single spin qubit probes the local magnonic density of states via relaxation processes. By taking the difference of detuning-resolved relaxation times at the edges with that in the bulk, one can verify the existence of edge-located in-gap magnon modes. Moreover, the detuning dependence of the relaxation time is remarkably distinct for linearly dispersing bands, as expected for a chiral mode, and trivial parabolic bands (see Appendix 6.D). On top of that, the two-qubit setup, in particular the transduction protocol in Sec. 6.4, provides a direct experimental handle on chirality because the entanglement protocol is unidirectional.

## 6.6 Conclusion

We have presented a two-layer setup where the FM bottom layer hosts a chiral magnon mode with energy lying in the magnonic band gap. Coupling spin qubits to the chiral magnon facilitates two different long range qubit-qubit coupling protocols, both of which have been studied in detail.

Two-qubit coupling can be mediated by virtual magnons. We found that this protocol is efficient if the interlayer exchange interaction  $J^\perp$  is antiferromagnetic. For  $1\ \mu\text{m}$  qubit separation, 1 MHz coupling strength has been found with a  $\sqrt{\text{SWAP}}$  gate fidelity up to 99.9%. We also pre-

sented general analytical formulas for coupling of two-dimensional spin qubits with chiral edge magnons that can be of great use trying to identify the optimal materials and dimensions for such a system.

Finally, we have investigated the magnon transduction protocol in the ferromagnetic interlayer coupling regime. The coupling is highly fast ( $\sim 1$  GHz), owing to the excitation of a physical magnon. Even though the mean-free path of the edge magnon seriously limits the fidelity of such a two-qubit coupling, the transduction protocol can be used as an experimental probe of the chirality of topological edge magnons.

## 6.A Conventions

In this appendix we guide the reader through the conventions we used throughout the main text and give explicit formulas as examples. First we define the Fourier transformation of an operator  $O = \sum_i O_i$  as follows

$$O_k \equiv \frac{1}{\sqrt{N}} \sum_{i=1}^N e^{-ikr_i} O_i. \quad (6.33)$$

For the bosonic creation and annihilation operators, this convention results in

$$a_k \equiv \frac{1}{\sqrt{N}} \sum_{i=1}^N e^{-ikr_i} a_i, \quad (6.34a)$$

$$a_k^\dagger \equiv \frac{1}{\sqrt{N}} \sum_{i=1}^N e^{ikr_i} a_i^\dagger = (a_k)^\dagger, \quad (6.34b)$$

where the corresponding commutation relation is  $[a_k, a_{k'}^\dagger] = \delta_{kk'}$ . For the Fourier transformation of the FM spin operators in the  $x$  direction this leads to

$$S_i^+ \approx \sqrt{\frac{2S}{N_x}} \sum_{k_x} e^{ik_x x_i} \sum_{n=1}^{4N_y} \varphi_{k_x, n}^{\mu_i}(y_i) a_{k_x, n}, \quad (6.35a)$$

$$S_i^- \approx \sqrt{\frac{2S}{N_x}} \sum_{k_x} e^{ik_x x_i} \sum_{n=1}^{4N_y} [\varphi_{-k_x, n}^{\mu_i}(y_i)]^* a_{-k_x, n}^\dagger. \quad (6.35b)$$

where we have performed a transformation from the band index  $n$  to the index pair  $(y_i, \mu)$  as well, with  $y_i$  being the armchair unit cell index, and

$\mu$  is the index within the unit cell. Furthermore, the transformed spin operators can be expressed with the Holstein-Primakoff bosons as

$$S_{k_x,n}^+ \approx \sqrt{2S} a_{k_x,n}, \quad (6.36a)$$

$$S_{k_x,n}^- \approx \sqrt{2S} a_{-k_x,n}^\dagger. \quad (6.36b)$$

Consequently, the time evolution of the transformed spin operators reads as

$$S_{k_x,n}^+(t) \approx e^{-i\varepsilon_{k_x,n}t} S_{k_x,n}^+, \quad (6.37a)$$

$$S_{k_x,n}^-(t) \approx e^{i\varepsilon_{-k_x,n}t} S_{k_x,n}^-, \quad (6.37b)$$

where we point out that  $S_{k_x,n}^+(t) = [S_{-k_x,n}^-(t)]^\dagger$ .

We define the susceptibility of the transformed spin operators as

$$\begin{aligned} \chi_{nm}^\perp(t, k_x) &\equiv -i\theta(t)\delta_{nm}\langle [S_{-k_x,n}^-(t), S_{k_x,n}^+] \rangle \\ &= i\theta(t)2S\delta_{nm}e^{i\varepsilon_{k_x,n}t}, \end{aligned} \quad (6.38)$$

where we used the time evolution of the spin operators in Eq. (6.37).

Furthermore, in frequency space the susceptibility assumes the form

$$\begin{aligned} \chi_{nm}^\perp(\omega, k_x) &= \int_{-\infty}^{\infty} dt e^{-i\omega t - \eta t} \chi_{nm}^\perp(t, k_x) \\ &= \frac{-2S\hbar}{\varepsilon_{k_x,n} - \hbar\omega + i\eta} \delta_{nm}, \end{aligned} \quad (6.39)$$

where one can substitute the linewidth as  $\eta \rightarrow \alpha_G \varepsilon_{k_x,n}$  in the case of Gilbert damping.

## 6.B Effective qubit-magnon coupling: analytical formulas

Assuming a general, non-local coupling between the qubit and the ferromagnet spins, the interaction Hamiltonian can be written as  $V_p = \sum_i S_i \cdot \hat{M}(\mathbf{r}_p - \mathbf{r}_i) \boldsymbol{\sigma}_p$ . Writing the convolution between the FM spins and the coupling matrix  $\hat{M}$  in Fourier space, and expanding the coupling terms to first order in magnon creation operators one obtains

$$\begin{aligned} V_p &= \frac{1}{2} \sum_{k_x,n} e^{ik_x x_{\text{QD}}} (S_{-k_x,n}^+ \mathbf{M}_{k_x,n}^- + S_{-k_x,n}^- \mathbf{M}_{k_x,n}^+) \cdot \boldsymbol{\sigma}_p \\ &\quad + \mu_B S \mathbf{B}_{\text{eff}} \cdot \boldsymbol{\sigma}_p + \mathcal{O}(S^0), \end{aligned} \quad (6.40)$$

where  $B_{\text{eff}}$  is the effective magnetic field of the FM ground state felt by the qubit. The couplings  $M_{k_x,n}^{\pm} = M_{k_x,n}^x \pm iM_{k_x,n}^y$  have three vector components  $x, y, z$  and can be expressed with the real space coupling matrix elements as

$$M_{k_x,n}^{-} = \frac{1}{\sqrt{N_x}} \sum_{x_i, y_i} \sum_{\mu} e^{-ik_x x_i} \varphi_{-k_x,n}^{\mu}(y_i) \times M^{-}(x_i + x^{\mu}, y_i + y^{\mu} - y_{\text{QD}}), \quad (6.41)$$

$$M_{k_x,n}^{+} = \frac{1}{\sqrt{N_x}} \sum_{x_i, y_i} \sum_{\mu} e^{-ik_x x_i} [\varphi_{k_x,n}^{\mu}(y_i)]^{*} \times M^{+}(x_i + x^{\mu}, y_i + y^{\mu} - y_{\text{QD}}), \quad (6.42)$$

$$B_{\text{eff}} = \sum_{x_i, y_i} \sum_{\mu} M^z(x_i + x^{\mu}, y_i + y^{\mu} - y_{\text{QD}}), \quad (6.43)$$

provided that  $x_{\text{QD}}$  is commensurate with the lattice and therefore, the index  $x_i$  can be shifted by  $x_{\text{QD}}$ .

Assuming that the QD is very narrow, i.e.,  $l_y^2 \ll d_y^2 + d_z^2$ , the QD is subjected to a homogeneous magnetic field that is given by the dipole field of the FM slab at its position. For the parameters used in the main text  $l_y \sim d_y, d_z$ , but the approximation above can still be used to estimate the contribution of the dipole-field to the qubit splitting as shown in Fig. 6.4. The dipole-field of the FM ground state may be estimated by that of a magnetized ribbon substituting  $\mathbf{m}_1(\mathbf{r}) = \Theta(y)\Theta(L_y - y)S\mathbf{e}_z$  into Eq. (6.81), where  $\Theta(y)$  is the Heaviside step function. The dipole field felt by the qubit at a position  $\mathbf{r} = (x, d_y, d_z)$  is then given by

$$\mu_B B_{\text{eff}}^x = 0, \quad (6.44a)$$

$$\mu_B B_{\text{eff}}^y = -\frac{\mu_0}{4\pi} \frac{z_0 g g_{\text{QD}} \mu_B^2}{a_x a_y} \left[ \frac{d_z}{d_y^2 + d_z^2} - \frac{d_z}{(L_y + d_y)^2 + d_z^2} \right], \quad (6.44b)$$

$$\begin{aligned} \mu_B B_{\text{eff}}^z = -J^{\perp} - \frac{\mu_0}{4\pi} \frac{z_0 g g_{\text{QD}} \mu_B^2}{a_x a_y} \\ \times \left[ -\frac{d_y}{d_y^2 + d_z^2} + \frac{L_y + d_y}{(L_y + d_y)^2 + d_z^2} \right], \end{aligned} \quad (6.44c)$$

where  $L_y = N_y a$ , the magnetic moment density of the ribbon is given by  $z_0 \mu_B^2 / a_x a_y$  ( $z_0 = 4$  is the number of spins in the FM unit cell), and we included the exchange field as well in the last equation. The contribution of the  $z$ -component of the dipole field is  $\sim 0.6 \mu\text{eV}$  for the parameters presented in the main text, and therefore one might neglect it compared

to the exchange field. We note that the  $g$ -tensor anisotropy in the QD layer can be straightforwardly accounted for, by replacing  $g_{\text{QD}}\sigma$  with  $\hat{g}\sigma$ , where  $\hat{g}$  is the  $g$ -tensor of the QD.

## 6.C Including spectral broadening in the Schrieffer-Wolff transformation

In this appendix we revisit the formula for the second order Schrieffer-Wolff transformation and show how spectral broadening can be included in the subspace to be projected out. For simplicity, in this section we consider a single qubit coupled to the magnons via the effective coupling  $V$  of Eq. (6.40), but the calculations we provide here can be extended straightforwardly to the two-qubit system. Starting from the definition of  $W_{\text{eff}}$  in the Fourier space given in Eq. (6.14) of the main text, assuming that the linewidth broadening of the qubit is negligible compared to the broadening of the magnons we get

$$W_{\text{eff}} = \frac{1}{2\hbar} \sum_{\alpha, \beta} \int_{-\infty}^{\infty} \frac{d\omega}{2\pi} \frac{\langle 0 |_{\text{FM}} [V_{\alpha\beta}(\omega) |\alpha\rangle \langle \beta|, V] |0\rangle_{\text{FM}}}{\omega + i\Gamma[\varepsilon_{\alpha\beta}(\omega)]}, \quad (6.45)$$

where  $|\alpha\rangle, |\beta\rangle$  are qubit basis states corresponding to the energies  $\varepsilon_{\alpha}, \varepsilon_{\beta}$ , respectively. The state  $|0\rangle_{\text{FM}}$  is the vacuum of magnons and  $\varepsilon_{\alpha\beta}(\omega) = |\hbar\omega - (\varepsilon_{\alpha} - \varepsilon_{\beta})|$  is the contribution of the magnons to the total excitation energy  $\hbar\omega$ . Furthermore, the relaxation rate  $\Gamma[\varepsilon]$  is the inverse lifetime of the magnon.

Physically the motivation behind this substitution is the following: the magnons are coupled to the phonons of the FM lattice and thereby these modes are dressed. However, the qubits are coupled to each other via the "pure" magnon modes. Therefore, we need to account for the indirect coupling of the two-qubit system to the phonons of the FM lattice through the finite lifetime  $\Gamma[\varepsilon]$  of the magnons.

Rewriting the coupling  $V$  on the eigenbasis of each subsystems (e.g., the qubits and the ferromagnet) and substituting the corresponding time dependence we get

$$V_{\alpha\beta}(t) = \sqrt{\frac{S}{2}} \sum_{k_x, n} \left[ e^{i\varepsilon_{k_x, n} t / \hbar} a_{k_x, n}^{\dagger} (M_{k_x, n}^{+} \cdot \sigma)_{\alpha\beta} + e^{-i\varepsilon_{k_x, n} t / \hbar} a_{k_x, n} (M_{-k_x, n}^{-} \cdot \sigma)_{\alpha\beta} \right] e^{i(\varepsilon_{\alpha} - \varepsilon_{\beta}) t / \hbar}. \quad (6.46)$$

Taking the Fourier transform in time leads to

$$V_{\alpha\beta}(\omega) = \sqrt{2S\pi\hbar} \sum_{k_x,n} \left[ (M_{k_x,n}^+ \cdot \sigma)_{\alpha\beta} \delta(\Delta_{\alpha\beta} + \varepsilon_{k_x,n} - \hbar\omega) a_{k_x,n}^\dagger + (M_{-k_x,n}^- \cdot \sigma)_{\alpha\beta} \delta(\Delta_{\alpha\beta} - \varepsilon_{k_x,n} - \hbar\omega) a_{k_x,n} \right], \quad (6.47)$$

with  $\Delta_{\alpha\beta} = \varepsilon_\alpha - \varepsilon_\beta$ . Substituting  $V_{\alpha\beta}(\omega)$  into Eq. (6.45), one obtains

$$W_{\text{eff}} = \frac{S}{4} \sum_{\alpha,\beta} |\alpha\rangle \langle\beta| \sum_{k_x,n} \sum_{\gamma} (M_{-k_x,n}^- \cdot \sigma)_{\alpha\gamma} (M_{k_x,n}^+ \cdot \sigma)_{\gamma\beta} \times \left( \frac{1}{\Delta_{\alpha\gamma} - \varepsilon_{k_x,n} + i\hbar\Gamma(\varepsilon_{k_x,n})} + \frac{1}{\Delta_{\beta\gamma} - \varepsilon_{k_x,n} - i\hbar\Gamma(\varepsilon_{k_x,n})} \right), \quad (6.48)$$

that is the usual 2nd order perturbative formula extended with the linewidth broadening of the intermediate state.

The range of validity can be determined from Eq. (6.48) by requiring that the second order correction  $\delta\varepsilon_\alpha = \langle\alpha| W_{\text{eff}} |\alpha\rangle$  to the qubit energy level  $\varepsilon_\alpha$  is much smaller than the orbital level splitting of the QD, assumed to be  $\Delta_{\text{orb}} \sim 10$  meV, and the bandwidth of the respective magnonic subband  $W \propto JS \approx 2$  meV. In particular, we consider (i) the magnon mode  $n$  that is closest to the qubit splitting; (ii) the transition  $\alpha = \uparrow$  and  $\gamma = \downarrow$ , for which  $\Delta_{\uparrow\downarrow} = \Delta$ . We neglect transitions  $\alpha = \gamma$  because there are no resonant transitions for  $\Delta_{\alpha\alpha} = 0$  due to the FM resonance gap ( $\varepsilon_{k_x,n} \geq \Delta_F$ ). The correction to the qubit splitting due the magnon mode  $n$  reads as

$$\delta\Delta_n = \frac{Sa_x}{16\pi} \int dk |M_{k_x,n}^{++}|^2 \frac{\Delta - \varepsilon_{k_x,n}}{(\Delta - \varepsilon_{k_x,n})^2 + \hbar^2\Gamma^2(\varepsilon_{k_x,n})}, \quad (6.49)$$

which we then rewrite in terms of the density of states  $\rho_n(\varepsilon) = dk_x/d\varepsilon_{k_x,n}$  as

$$\delta\Delta_n = \frac{Sa_x}{16\pi} \int_{\varepsilon_{\min}}^{\varepsilon_{\max}} d\varepsilon \rho_n(\varepsilon) \sum_{\gamma} |M_{k_{\varepsilon,n}}^{++}|^2 \frac{\Delta - \varepsilon}{(\Delta - \varepsilon)^2 + \hbar^2\Gamma^2(\varepsilon)}, \quad (6.50)$$

where the integration boundaries correspond to the lowest- and highest-energy magnon state of  $\varepsilon_{k_x,n}$ . We first consider the case, when the qubit splitting is renormalized by a quadratic mode  $\varepsilon_{k_x,n} = \varepsilon_0 + D_x k_x^2$  with the density of states  $\rho_n(\varepsilon) = [4D_x(\varepsilon - \varepsilon_{0,n})]^{-1/2}$ . We exploit that for long QDs

the coupling can be estimated as  $|M_{k_x,n}^{++}|^2 \approx |M_{0,n}^{++}|^2 e^{-k_x^2 l_x^2/2}$ . Then, the renormalization of the qubit splitting is given by

$$\delta\Delta_n \approx \frac{S a_x}{16\pi} |M_{0,n}^{++}|^2 \int_0^{D_x l_x^{-2}} d\varepsilon' \frac{1}{2\sqrt{D_x \varepsilon'}} \frac{\delta - \varepsilon'}{(\delta - \varepsilon')^2 + \hbar^2 \Gamma^2}, \quad (6.51)$$

where  $\delta = \Delta - \varepsilon_{0,n}$  and we have cut the frequency integral at  $D_x l_x^{-2}$  to account for the decay of the coupling  $V$  in  $k$ -space and approximated  $\Gamma(\varepsilon)$  with a constant linewidth  $\Gamma$ . First, we note that for  $\Gamma = 0$  the above integral diverges as  $1/\sqrt{\delta}$  near resonance. Evaluating the correction in Eq. (6.51) for finite linewidth  $\Gamma$  and small detunings  $\delta$ , we get

$$\delta\Delta_n \approx \frac{S}{32} \frac{|M_{0,n}^{++}|^2}{\sqrt{2D_x a_x^{-2} \hbar \Gamma}} [1 + \mathcal{O}(\delta/\hbar\Gamma)], \quad (6.52)$$

where we omitted terms that are  $\Gamma l_x^2/D_x$  and  $\delta l_x^2/D_x$ . Importantly, the correction is no longer divergent on resonance, owing to the linewidth that acts as a low-frequency cutoff in this case. For a very conservative estimate we substitute  $|M_{k_x,n}^{++}| \sim \frac{\mu_0 \mu_B^2}{a^3} \sim 0.6 \mu\text{eV}$  and the FM resonance mode with  $\Gamma = \alpha_G \Delta_F \sim 5 \text{ neV}$  that leads to  $\delta\Delta_n \lesssim 30 \text{ neV}$  on resonance, that is well within the  $\sim 0.5 \text{ meV}$  bandwidth of the respective magnon mode. Moreover, we note that the density of states is not singular in the 2D limit ( $\alpha_G N_y \gg 1$ ) leading to even larger range of validity for the bulk modes.

Now, we turn to the discussion of the chiral magnon mode  $\varepsilon_{k_x,e} = \varepsilon_0 + v_x k_x$  that plays a central role in our work. Following similar considerations as in Eq. (6.51) for the linear mode we get

$$\delta\Delta_e \approx \frac{S a_x}{16\pi v_x} |M_{0,e}^{++}|^2 \int_{-v_x/l_x}^{v_x/l_x} d\varepsilon' \frac{\delta - \varepsilon'}{(\delta - \varepsilon')^2 + \hbar^2 \Gamma^2}, \quad (6.53)$$

where we get a finite contribution even for  $\Gamma = 0$ . In fact for  $\delta = 0$ , the correction is  $\delta\Delta_e = 0$  in Eq. (6.53) because the spectrum is symmetric around the qubit splitting leading to no renormalization of the excited qubit state. However, note that the upper ( $\varepsilon > \Delta$ ) and the lower ( $\varepsilon < \Delta$ ) parts of the integral are both logarithmically divergent if  $\Gamma = 0$ . Taking the contribution of the magnon modes above resonance ( $\varepsilon > \Delta$ ) into



consideration we get

$$\begin{aligned}\delta\Delta_{e,\varepsilon>\Delta} &\approx \frac{Sa_x}{16\pi v_x} |M_{0,e}^{++}|^2 \int_0^{v_x/l_x} d\varepsilon' \frac{\delta - \varepsilon'}{(\delta - \varepsilon')^2 + \hbar^2 \Gamma^2} \\ &\approx -\frac{Sa_x}{32\pi v_x} |M_{0,e}^{++}|^2 \left[ \log \left( 1 + \frac{v_x^2}{\hbar^2 \Gamma^2 l_x^2} \right) + \mathcal{O}(l_x \delta / v_x) \right],\end{aligned}\quad (6.54)$$

where we assume  $\delta = 0$  to arrive at the second line. In a very pessimistic estimate we might replace the logarithm with  $-2 \log \alpha_G \approx 18$ , which leads to  $\delta\Delta_{e,\varepsilon>\Delta} \sim 10^{-2} \text{ neV}$  for  $|M_{0,e}^{++}| \sim 100 \text{ neV}$  and the parameters used in the main text. This qubit splitting correction is several orders of magnitude smaller than the bandwidth of the chiral mode.

## 6.D Effective qubit-qubit coupling

Here, we show first how to obtain Eq. (6.15) of the main text and the analytical formulas for linear and quadratic magnon modes in the subsequent subsections. To this we use the real time expression for  $W_{\text{eff}}$  defined in Eq. (6.13) and the coupling  $V$  defined in Eq. (6.40) in the Heisenberg representation as

$$\begin{aligned}\tilde{V}(t) = \frac{1}{2} \sum_{p \in \{1,2\}} \sum_{k_x, n} e^{ik_x x_p} & (e^{i\varepsilon_{k_x, n} t} S_{-k_x, n}^+ \mathbf{M}_{k_x, n}^- \\ & + e^{-i\varepsilon_{-k_x, n} t} S_{-k_x, n}^- \mathbf{M}_{k_x, n}^+) \cdot \boldsymbol{\sigma}_p(t),\end{aligned}\quad (6.55)$$

where we dropped terms of  $\mathcal{O}(S^0)$ , furthermore  $\sigma^\pm(t) = e^{\pm i\Delta t} \sigma^\pm$  and  $\sigma^z(t) = \sigma^z$ . Using Eqs. (6.38) and (6.39), we can identify the susceptibility in each terms of the coupling in the form of  $\chi_{nn}^\perp(\omega, k_x) = \frac{i}{\hbar} \int_0^\infty dt e^{-i(\omega - \varepsilon_{k_x, n})t - \eta t}$ . As it is shown in App. 6.C, the linewidth  $\eta$  can be replaced by the Gilbert damping  $\hbar\Gamma(\varepsilon_{k_x, n}) = \alpha_G \varepsilon_{k_x, n}$ . Finally, we get

$$\begin{aligned}W_{\text{eff}} = \frac{1}{8} \sum_{p, q} \sum_{k_x, n} e^{ik_x x_{pq}} & \mathbf{M}_{-k_x, n}^- \cdot \boldsymbol{\sigma}_q \\ & \times \left\{ \frac{1}{2} M_{k_x, n}^{++} \sigma_p^- \chi_{nn}^\perp(\Delta/\hbar, k_x) + \frac{1}{2} M_{k_x, n}^{+-} \sigma_p^+ \chi_{nn}^\perp(-\Delta/\hbar, k_x) \right. \\ & \left. + M_{k_x, n}^{+z} \sigma_p^z \chi_{nn}^\perp(0, k_x) \right\} + h.c.,\end{aligned}\quad (6.56)$$

where  $x_{pq} = x_p - x_q$ . Dropping the off-resonant terms  $\chi_{nn}^\perp(-\Delta/\hbar, k_x)$  and  $\chi_{nn}^\perp(0, k_x)$  and expanding  $\mathbf{M}_{-k_x, n}^- \cdot \boldsymbol{\sigma}_q$  leads to Eq. (6.15). For ferromagnetic interlayer coupling, i.e.,  $J^\perp > 0$  (that is  $\Delta < 0$ ), the  $\chi_{nn}^\perp(-\Delta/\hbar, k_x)$

term becomes the resonant contribution. In this latter case the leading contribution to the coupling would be  $\propto |M^{+-}|^2$  that is of the same order as the magnon-induced relaxation rate in the ferromagnetic coupling case [see Eq. (6.68)]. This is a reason why in our work we focus on the antiferromagnetic interlayer coupling.

We note that the off-resonant terms cannot be dropped for the qubit splitting corrections [i.e., the  $p = q$  terms in Eq. (6.56)]. Considering  $\Delta \approx \varepsilon_0$ , where  $\varepsilon_0$  is the energy of the chiral mode at  $k_x = 0$ , the resonant term gives a contribution on the order of the coupling strength ( $\sim 1$  neV), and the  $\chi_{nn}^\perp(0, k_x)$  term is expected to be even smaller. The contribution of  $\chi_{nn}^\perp(-\Delta/\hbar, k_x)$  on the other hand contains terms of the order of  $|M^{+-}|^2/(2\Delta)$  (second order in exchange) that are orders of magnitude stronger than the formers, i.e.,  $|M^{+-}| \sim 100 \mu\text{eV}$ , leading to a dynamical contribution to the effective field of the order of  $1 \mu\text{eV}$ . Since this contribution is still a small corrections to the static exchange field one can simply redefine  $B_{\text{eff}}$  accordingly.

## Linear spectrum

The chiral edge mode has a linear dispersion around  $k_x \sim 0$  and it is well separated in energy from the bulk modes. Therefore the main contribution to the susceptibility at the corresponding energy range is given by

$$\chi_{nn}^\perp(\Delta/\hbar, k_x) \approx -2S\hbar \frac{\delta_{ne}}{v_x(k_x + i\kappa) - \delta} \quad (6.57)$$

where  $\delta = \Delta - \varepsilon_0$  and  $\kappa^{-1} \approx \frac{v_x}{\alpha_G \Delta}$  is the mean free path of the chiral magnon. The other chiral branch with opposite group velocity is localized on the other edge of the sample and therefore is neglected in the effective qubit-qubit coupling.

First we convert the sum over  $k_x$  to an integral as

$$W_{pq} = \frac{1}{16} \frac{a_x}{2\pi} \int_{-\pi/a_x}^{\pi/a_x} dk_x e^{ik_x x_{pq}} M_{k_x, n}^{++} \sigma_p^- \chi_{ee}^\perp(\Delta/\hbar, k_x) \quad (6.58)$$

$$\times M_{-k_x, n}^- \cdot \sigma_q + h.c.,$$

assuming that the sample is large enough, i.e.,  $2\pi/L_x \rightarrow 0$ . If the integral is extended to infinity, i.e.,  $a_x \rightarrow 0$ , it can be performed using the

residue theorem. However, this approximation is only valid in the low-energy limit, or in our specific case for  $|\delta| \ll |v_x/a_x| \sim JS$ , such that the pole of the integrand remains at finite  $k_x$ . The integral of interest can be evaluated using residue theorem as

$$\begin{aligned} -\frac{Sa_x}{\pi} \int_{-\infty}^{\infty} dk_x \frac{e^{ik_x x_{ij}}}{v_x(k_x + i\kappa) - \delta} f(k_x) \\ = \Theta(-v_x x_{ij}) \frac{2iSa_x}{|v_x|} e^{ik_0 x_{ij} - |\kappa x_{ij}|} f(k_0 - i\kappa), \end{aligned} \quad (6.59)$$

where  $k_0 = \delta/v_x$ . Furthermore, we have assumed that  $f(k_x)$  is a holomorphic function and the contribution of the upper arc goes to zero if the contour is extended to infinity. Thus, for the two-qubit couplings ( $p \neq q$ ) we have

$$\begin{aligned} W_{12} + W_{21} = \frac{iSa_x}{8|v_x|} e^{-|\kappa|d} M_{k_0,n}^{++} M_{-k_0,n}^{-} \\ \times [\Theta(v_x) e^{-ik_0 d} \sigma_1^- \sigma_2 + \Theta(-v_x) e^{ik_0 d} \sigma_2^- \sigma_1] + h.c., \end{aligned} \quad (6.60)$$

which can be rewritten as

$$\begin{aligned} W_{12} + W_{21} = \frac{iSa_x}{16|v_x|} e^{-|\kappa|d} (M_{k_0,n}^{++} M_{-k_0,n}^{-+} e^{-i|k_0|d} \sigma_1^- \sigma_2^- \\ + \text{sgn}(v_x) |M_{k_0,n}^{++}|^2 e^{-ik_0 d} \sigma_1^- \sigma_2^+ + M_{k_0,n}^{++} M_{-k_0,n}^{-z} \\ \times e^{-i|k_0|d} (\Theta(v_x) \sigma_1^- \sigma_2^z + \Theta(-v_x) \sigma_1^z \sigma_2^-) + h.c. \end{aligned} \quad (6.61)$$

The individual two-qubit matrix elements can be read off directly to obtain Eq. (6.19) of the main text.

## Quadratic spectrum

Similarly to the case of the chiral edge magnon, we can discuss the effect of a topologically trivial magnonic mode that is localized at the edge of the FM. To this, we assume that the energy of the trivial mode  $\varepsilon_{k_x,e} = \varepsilon_0 + D_x k_x^2$  is well separated from the two bulk bands and therefore the single mode approximation is adequate. The effective interaction matrix elements then read as

$$\langle 01 | W_{12} | 10 \rangle \approx -\frac{Sa_x}{D_x} \text{Re} \left[ \frac{e^{-K|d|}}{K} \right] |M_{-K,e}^{++}|^2, \quad (6.62a)$$

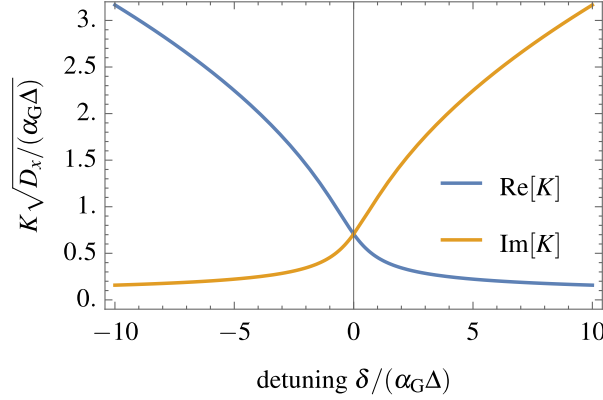


Figure 6.7: Real and imaginary parts of the complex wave number  $K = D_x^{-1/2} \sqrt{-\delta + i\alpha_G \Delta}$ , describing the decay and the period of the oscillations in the effective coupling of Eq. (6.62), respectively.

$$\langle 11 | W_{12} | 00 \rangle \approx -\frac{S a_x}{D_x K} e^{-K|d|} M_{-K,e}^{++} (M_{-K,e}^{+-})^*, \quad (6.62b)$$

$$\langle 10 | W_{12} | 00 \rangle \approx -\frac{S a_x}{D_x K} e^{-K|d|} M_{-K,e}^{++} (M_{-K,e}^{+z})^*, \quad (6.62c)$$

$$\langle 01 | W_{12} | 00 \rangle = \langle 10 | W_{12} | 00 \rangle, \quad (6.62d)$$

where  $K = D_x^{-1/2} \sqrt{-\delta + i\alpha_G \Delta}$  is a complex wave number, the real and imaginary parts of which describe the decay and the oscillations of the effective couplings, respectively. In Fig. 6.7, the real and imaginary parts of  $K$  are shown as a function of the detuning,  $\delta$ . We see that below resonance ( $\delta < 0$ ) the real part of  $K$  is large and positive, leading to fast decay of the effective couplings in Eq. (6.62) as a function of qubit-qubit distance  $d$ , whereas the imaginary part becomes larger above resonance ( $\delta > 0$ ) leading mostly to oscillations in the coupling strength.

Furthermore we note that the formulas above are only valid for  $|K| \ll \pi/a_x$ , or equivalently  $\delta \ll D_x/a_x^2 \sim JS$ . Therefore in the case of the bulk modes (harmonic spectrum) the exponential decay in the coupling is only valid close enough to the corresponding resonance. Consequently, the finite coupling in the middle of the gap is not captured by these analytic formulas.

## 6.E Decoherence

In this section we show how to relate the transversal  $\mathcal{S}_{V^-}$  and longitudinal  $\mathcal{S}_{V^z}$  qubit noise spectra to the transversal noise spectrum of the magnons. The transversal noise spectrum of magnons is defined as

$$\mathcal{S}_{k_x,n}^\perp(\omega) \equiv \int_{-\infty}^{\infty} dt e^{-i\omega t} \langle \{S_{-k_x,n}^-(t), S_{k_x,n}^+\} \rangle, \quad (6.63)$$

substituting the time dependence of the FM spin operators in Eq. (6.37) the integral can be evaluated as

$$\mathcal{S}_{k_x,n}^\perp(\omega) = 2\pi\hbar\delta(\hbar\omega - \varepsilon_{k_x,n}) \langle \{S_{-k_x,n}^-, S_{k_x,n}^+\} \rangle, \quad (6.64)$$

where we can replace  $2\pi\hbar\delta(\hbar\omega - \varepsilon_{k_x,n})$  by  $\frac{1}{S}\text{Im}[\chi_{nn}^\perp(\omega, k_x)]$  in the dissipative case. Furthermore, using the time dependence of the FM spin operators in Eq. (6.37) and substituting it into Eq. (6.63), one can easily show that

$$\mathcal{S}_{k_x,n}^\perp(-\omega) = \int_{-\infty}^{\infty} dt e^{-i\omega t} \langle \{S_{k_x,n}^+(t), S_{-k_x,n}^-\} \rangle. \quad (6.65)$$

Exploiting the commutation relations between the magnon creation and annihilation operators one obtains

$$\mathcal{S}_{k_x,n}^\perp(\omega) = \text{Im}[\chi_{nn}^\perp(\omega, k_x)] \coth(\beta\varepsilon_{k_x,n}/2), \quad (6.66)$$

as stated in the main text. We note that this is just a form of the well-known fluctuation-dissipation theorem.

Writing down the transversal qubit noise spectrum according to its definition as  $\mathcal{S}_{V^-}(\omega) = \int dt \left\{ [V^-(t)]^\dagger, V^-(0) \right\} e^{-i\omega t}$ , where  $V^-$  is the term multiplying  $\sigma_p^+$  in Eq. (6.40), leads to

$$\begin{aligned} \mathcal{S}_{V^-}(\omega) = \frac{1}{4} \sum_{k_x,n} \int_{-\infty}^{\infty} dt e^{-i\omega t} & \left[ |M_{k_x,n}^{++}|^2 \langle \{S_{-k_x,n}^-, S_{k_x,n}^+\} \rangle \right. \\ & \left. + |M_{k_x,n}^{--}|^2 \langle \{S_{k_x,n}^+, S_{-k_x,n}^-\} \rangle \right], \end{aligned} \quad (6.67)$$

where we exploited that  $\langle \{S_{-k_x,n}^-, S_{k'_x,n'}^+\} \rangle \propto \delta_{k_x,k'_x} \delta_{nn'}$ . In the equation above, the perpendicular magnon noise spectrum appears in the form of Eqs. (6.63) and (6.65). Finally we get

$$\begin{aligned} \mathcal{S}_{V^-}(\omega) = & \frac{1}{4} \sum_{k_x,n} \coth(\beta \varepsilon_{k_x,n}/2) [|M_{k_x,n}^{++}|^2 \text{Im}[\chi_{nn}^\perp(\omega, k_x)] \\ & + |M_{k_x,n}^{-+}|^2 \text{Im}[\chi_{nn}^\perp(-\omega, k_x)]] , \end{aligned} \quad (6.68)$$

where the second term can be dropped for  $\omega = \Delta/\hbar$  as it is strongly suppressed even in the dissipative case. An analogous derivation leads to the longitudinal qubit noise spectrum as

$$\begin{aligned} \mathcal{S}_{V^z}(\omega) = & \sum_{k_x,n} \coth(\beta \varepsilon_{k_x,n}/2) |M_{k_x,n}^{+z}|^2 \\ & \times [\text{Im}[\chi_{nn}^\perp(\omega, k_x)] + \text{Im}[\chi_{nn}^\perp(-\omega, k_x)]] . \end{aligned} \quad (6.69)$$

Afterwards, the noise power spectra obtained in Eqs. (6.68) and (6.69) can be used to obtain the decoherence rates in Bloch-Redfield approximation as

$$\Gamma_1 = \frac{1}{4\hbar^2} \mathcal{S}_{V^-}(\Delta/\hbar) , \quad (6.70a)$$

$$\Gamma_2^* = \frac{1}{4\hbar^2} \mathcal{S}_{V^z}(0) , \quad (6.70b)$$

where  $\Gamma_1$  is the qubit relaxation rate and  $\Gamma_2^*$  is called pure dephasing.

## Decoherence due to a quadratic magnon mode

In the main text we focused on the decoherence rates due to the resonant interaction with the chiral magnon mode. Here we provide analogous formulas for the case of a quadratic mode, e.g., a bulk mode or a topologically trivial edge mode. We start the discussion with the non-dissipative limit  $\alpha_G = 0$ , where the noise spectrum of the edge mode assumes the form  $\mathcal{S}_{k_x,e}^\perp(\omega) \propto \delta(D_x k_x^2 + \varepsilon_0 - \hbar\omega)$  [see Eq. (6.64)], and the decoherence rates of Eqs. (6.70a)-(6.70b) become

$$\Gamma_1 = \Theta(\delta) \frac{S a_x}{2\hbar D_x k_0} (|M_{k_0,e}^{++}|^2 + |M_{-k_0,e}^{++}|^2) , \quad (6.71a)$$

$$\Gamma_2^* \sim \mathcal{O}(S^0) , \quad (6.71b)$$

where we used Eqs. (6.68) and (6.69) and substituted them into Eqs. (6.70a)-(6.70b). Furthermore,  $k_0 = \sqrt{\delta/D_x}$  and we assumed that the FM spectrum is gapped (e.g., via external magnetic field) and therefore  $\mathcal{S}_{k_x,e}^\perp(0) = 0$ . The divergent behaviour at  $k_0 = 0$  is due to the van Hove singularity of the density of states that can be observed in Fig. 6.8.

In order to account for the effect of Gilbert damping we assume  $d_y, d_z \ll l_x$  and neglect the dependence of the coupling on  $k_x$  except for the Gaussian factor  $e^{-k_x^2 l_x^2/2}$ . In contrast to Eqs. (6.71a) and (6.71b), we consider the imaginary part of the susceptibility with quadratic dispersion in Eq. (6.39) with a finite linewidth  $\eta = \alpha_G \varepsilon_{k_x,e}$ , the integral over momentum is exactly solvable leading to

$$\Gamma_1 = -\frac{S a_x}{\hbar D_x} |M_{0,e}^{++}|^2 \text{Im} \left[ \frac{e^{K^2 l_x^2/2} \text{Erfc}(\frac{K l_x}{\sqrt{2}})}{K} \right], \quad (6.72a)$$

$$\Gamma_2^* \approx \frac{\alpha_G}{2\sqrt{\pi}} \frac{a_x}{l_x} \frac{|M_{0,F}^{-z}|^2}{\hbar \Delta_F} \left( 1 + \frac{D_F}{l_x^2 \Delta_F} \right), \quad (6.72b)$$

where we listed the relaxation rate for a trivial edge mode, assuming  $|M_{0,e}^{++}|^2 \sim 100 \mu\text{eV}$  for the coupling matrix element, and the dephasing rate for the FM resonance mode. Furthermore,  $\Delta_F$  is the ferromagnetic resonance energy and  $D_F$  is the curvature of the lowest magnonic band

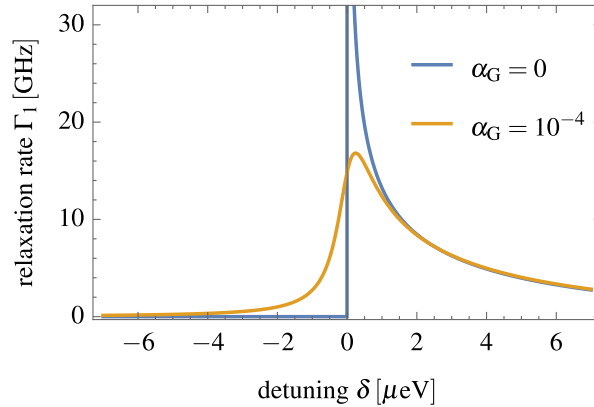


Figure 6.8: Relaxation rate  $\Gamma_1$  from Eq. (6.71a) plotted as a function detuning  $\delta$ . The relaxation is caused by to a trivial (1D) edge magnon for  $D_x = 0.5 \text{ meV} \cdot \text{nm}^2$ . The effect of the van Hove singularity at zero detuning is smoothed out by the finite Gilbert damping.

at  $k_x = 0$ . Even though the damping smoothes out the divergence of the density of states at resonance, the relaxation rate is still highly enhanced (see Fig. 6.8) rendering the trivial edge mode unfavourable in practical applications.

## 6.F Exchange interaction — Analytical formulas

In this section we provide details of the direct exchange-induced FM-QD coupling and derive the effective analytical formula presented in Eq. (6.24) of the main text. Since the QD layer is adjacent to the FM layer, the wavefunction of the particle on the QD can have a finite overlap with the FM spins. In real space the interaction can be written as

$$- \sum_{i,\mu} \mathbf{S}_{i,\mu} \cdot \hat{\mathbf{J}}_{i,\mu} \boldsymbol{\sigma} |\psi(\mathbf{r}_i + \mathbf{r}^\mu - \mathbf{r}_{\text{QD}})|^2. \quad (6.73)$$

Assuming that the interlayer exchange interaction  $\hat{\mathbf{J}}_i$  is homogeneous and isotropic with a strength of  $J^\perp$  and keeping the leading terms only in the  $1/S$  expansion we get

$$-SJ^\perp \sigma^z + \frac{1}{4} \sum_{k_x, n} (S_{-k_x, n}^+ M_{k_x, n}^{-+} \sigma^- + S_{-k_x, n}^- M_{k_x, n}^{+-} \sigma^+). \quad (6.74)$$

Here, the first term provides the effective magnetic field as  $\mathbf{B}_{\text{eff}} = -\frac{1}{\mu_B} SJ^\perp \mathbf{e}_z$  as well as we get

$$M_{k_x, n}^{-+} = -2J^\perp \sum_{i,\mu} e^{-ik_x x_i} \varphi_{-k_x, n}^\mu(y_i) \times |\psi(x_i + x^\mu, y_i + y^\mu - y_{\text{QD}})|^2. \quad (6.75)$$

In what follows, the QD wave function is assumed to be Gaussian in both spatial directions, i.e.,

$$|\psi(x_i + x^\mu, y_i + y^\mu)|^2 = \frac{a_x a_y}{4\pi l_x l_y} e^{-(x_i + x^\mu)^2 l_x^{-2}} e^{-(y_i + y^\mu)^2 l_y^{-2}}. \quad (6.76)$$

Next we derive the estimate for the coupling to the chiral edge mode in the continuum approximation. To this end we convert the sum over  $x$



to an integral and evaluate it as

$$\frac{1}{\sqrt{\pi}l_x} \int_{-\infty}^{\infty} dx e^{-ik_x x} e^{-(x+x^\mu)^2 l_x^{-2}} = e^{-k_x^2 l_x^2 / 4 + ik_x x^\mu}. \quad (6.77)$$

The coupling matrix element then reads as

$$M_{k_x, e}^{-+} \approx -\frac{J^\perp a_y}{2\sqrt{\pi}l_y} e^{-k_x^2 l_x^2 / 4} \sum_{y_i, \mu} e^{-ik_x x^\mu} \varphi_{-k_x, e}^\mu(y_i) e^{-(y_i + y^\mu - d_y)^2 l_y^{-2}}. \quad (6.78)$$

Next, we exploit that the edge state is well localized around  $y_i \sim 0$  and neglect  $x^\mu \ll l_x$  and  $y^\mu \ll l_y$  in the formulas to arrive at

$$M_{k_x, e}^{-+} \approx -\frac{J^\perp a_y}{2\sqrt{\pi}l_y} e^{-k_x^2 l_x^2 / 4} e^{-d_y^2 l_y^{-2}} \sum_{y_i, \mu} \varphi_{-k_x, e}^\mu(y_i). \quad (6.79)$$

Finally, since  $k_x \lesssim l_x^{-1} \ll \pi/a_x$  the last sum can be replaced by  $\delta\mu_e$  leading to Eq. (6.24) of the main text.

We can also account for the exponential envelope of the edge mode and arrive at

$$M_{k_x, e}^{-+} \approx -\frac{J^\perp a_y}{4\lambda} e^{-k_x^2 l_x^2 / 4} e^{-d_y / \lambda + l_y^2 / (4\lambda^2)} \left[ 1 + \operatorname{erf} \left( \frac{l_y}{2\lambda} - \frac{d_y}{l_y} \right) \right]. \quad (6.80)$$

This approximation is necessary to capture the qualitative dependence of the coupling for large  $d_y$  due to the short-ranged nature of the direct exchange interaction.

## 6.G Dipole-dipole interaction analytical formulas

In this section we provide details of the dipole-induced FM-QD coupling and derive the effective analytical formula presented in Eqs. (6.25) and (6.26) of the main text. The dipole-dipole interaction between localized magnetic moments reads as

$$H_{d-d} = -\frac{\mu_0}{4\pi} \frac{3(\mathbf{m}_1 \cdot \hat{\mathbf{r}})(\mathbf{m}_2 \cdot \hat{\mathbf{r}}) - \mathbf{m}_1 \cdot \mathbf{m}_2}{|\mathbf{r}_1 - \mathbf{r}_2|^3} + \mu_0 \frac{2}{3} \mathbf{m}_1 \cdot \mathbf{m}_2 \delta(\mathbf{r}_1 - \mathbf{r}_2), \quad (6.81)$$

where the magnetic moments are  $\mathbf{m}_1 = -\mu_B g \mathbf{S}_i$  with  $\mathbf{S}_i$  being the FM spin at position  $\mathbf{r}_1$  and  $\mathbf{m}_2 = -\mu_B g_{\text{QD}} |\psi(\mathbf{r}_2)|^2 \boldsymbol{\sigma}$ , and we define  $\hat{\mathbf{r}} = (\mathbf{r}_1 - \mathbf{r}_2)/|\mathbf{r}_1 - \mathbf{r}_2|$ . Using the wavefunction of the QD,  $\psi(x', y')$ , given in Eq. (6.76), the coupling between the QD and a lattice spin at position  $(x, y)$  is given by

$$M^{-+}(x, y) = -\frac{\mu_0 \mu_B^2 g g_{\text{QD}}}{4\pi} \sum_{x', y'} |\psi(x', y')|^2 \times \frac{(x - x')^2 + (y - y')^2 - 2d_z^2}{[(x - x')^2 + (y - y')^2 + d_z^2]^{5/2}}, \quad (6.82a)$$

$$M^{--}(x, y) = -\frac{\mu_0 \mu_B^2 g g_{\text{QD}}}{4\pi} \sum_{x', y'} |\psi(x', y')|^2 \times \frac{3[(x - x') - i(y - y')]^2}{[(x - x')^2 + (y - y')^2 + d_z^2]^{5/2}}, \quad (6.82b)$$

$$M^{-z}(x, y) = -\frac{\mu_0 \mu_B^2 g g_{\text{QD}}}{4\pi} \sum_{x', y'} |\psi(x', y')|^2 \times \frac{3[(x - x') - i(y - y')]d_z}{[(x - x')^2 + (y - y')^2 + d_z^2]^{5/2}}, \quad (6.82c)$$

where  $d_z$  is the distance between the QD and the FM planes. Furthermore we note that  $M^{+-}(x, y) = M^{-+}(x, y)$ ,  $M^{++}(x, y) = [M^{--}(x, y)]^*$ , and  $M^{+z}(x, y) = [M^{-z}(x, y)]^*$ .

Using the couplings in Eq. (6.82), we write the coupling of the QD to a given magnon mode  $(k_x, n)$  as

$$\mathbf{M}_{k_x, n}^- = \sum_{i, \mu} e^{-ik_x x_i} \varphi_{-k_x, n}^\mu(y_i) \sum_{i', \mu'} |\psi(\mathbf{r}'_i + \mathbf{r}^{\mu'})|^2 \times \mathbf{D}^-(\Delta x, \Delta y, d_z), \quad (6.83)$$

where we have used Eq. (6.41). Furthermore we defined

$$\mathbf{D}^-(\Delta x, \Delta y, d_z) = -\frac{\mu_0 \mu_B^2 g g_{\text{QD}}}{4\pi(\Delta x^2 + \Delta y^2 + d_z^2)^{5/2}} \times \begin{pmatrix} \Delta x^2 + \Delta y^2 - 2d_z^2 \\ 3(\Delta x - i\Delta y)^2 \\ 3(\Delta x + i\Delta y)d_z \end{pmatrix} \begin{matrix} + \\ - \\ z \end{matrix}, \quad (6.84)$$

with  $\Delta x = x_i - x'_i + x^\mu - x^{\mu'}$  and  $\Delta y = y_i - y'_i + y^\mu - y^{\mu'}$ . Note that  $\mathbf{D}^-$  is not given in a vector form, but the first (second, third) element of the column correspond to the  $D^{-+}$  ( $D^{--}$ ,  $D^{-z}$ ) coupling elements. This notation is emphasized next to the corresponding row.

In order to obtain the formulas for the edge mode in the continuum approximation we convert the sums over  $x$  coordinates to integrals, switch to the center-of-mass frame, and neglect  $x^\mu, x^{\mu'} \sim a_x$  since the QD wavefunction changes slowly on this scale. Furthermore, we make use of Eq. (6.77) to get

$$\begin{aligned} & \sum_{x_i, x'_i} e^{-ik_x x_i} |\psi(x'_i)|^2 \mathbf{D}^-(\Delta x, \Delta y, d_z) \\ &= e^{-k_x^2 l_x^2 / 4} \frac{1}{a_x} \int_{-\infty}^{\infty} dx e^{-ik_x x} \mathbf{D}^-(x, \Delta y, d_z), \end{aligned} \quad (6.85)$$

where the Fourier transformation of the  $\mathbf{D}^-$  is analytically solvable and reads as

$$\begin{aligned} & \frac{1}{a_x} \int_{-\infty}^{\infty} dx e^{-ik_x x} \mathbf{D}^-(x, \Delta y, d_z) = -\frac{\mu_0 \mu_B^2 g g_{\text{QD}}}{4\pi a_x} \\ & \times \begin{pmatrix} -\frac{2}{3} k_x^2 K_0 + \frac{2}{3} \left| \frac{k_x}{d_\perp} \right| K_1 + \frac{2}{3} \frac{k_x^2}{d_\perp^2} (\Delta y^2 - 2d_z^2) K_2 \\ -2k_x^2 K_0 + 2 \left| \frac{k_x}{d_\perp} \right| (1 - 2k_x \Delta y) K_1 + \frac{2}{3} \frac{k_x^2 \Delta y^2}{d_\perp^2} K_2 \\ -2id_z \left( \left| \frac{k_x}{d_\perp} \right| k_x K_1 + \frac{k_x^2}{d_\perp^2} \Delta y K_2 \right) \end{pmatrix} \begin{matrix} + \\ - \\ z \end{matrix}, \end{aligned} \quad (6.86)$$

with  $K_n \equiv K_n(|k_x|d_\perp)$  being the  $n$ th modified Bessel functions of the second kind, and  $d_\perp = \sqrt{\Delta y^2 + d_z^2}$ .

From this point onwards, we will be focusing on the  $k_x \sim 0$  case since  $l_x \gg d_y, d_z, l_y$ . In this case, Eq. (6.86) for  $k_x = 0$  simplifies to

$$\frac{1}{a_x} \int_{-\infty}^{\infty} dx \mathbf{D}^-(x, \Delta y, d_z) = \frac{\mu_0 \mu_B^2 g g_{\text{QD}}}{2\pi a_x d_\perp^4} \begin{pmatrix} d_z^2 - \Delta y^2 \\ \Delta y^2 - d_z^2 \\ 2i\Delta y d_z \end{pmatrix} \begin{matrix} + \\ - \\ z \end{matrix}. \quad (6.87)$$

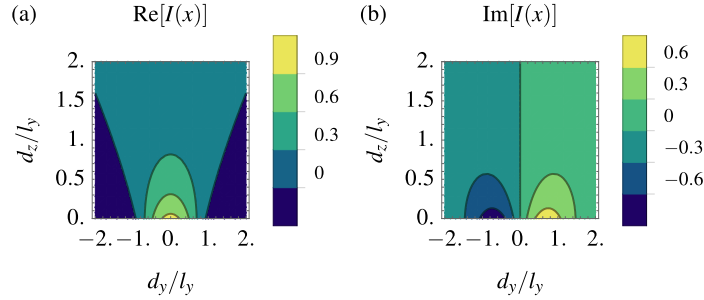


Figure 6.9: (a) Real and (b) imaginary part of the function  $I(x)$  in Eq. (6.90) with  $x = (id_y - d_z)/l_y$ . These functions determine the dependence of the dipolar FM-QD coupling of Eq. (6.89) on the relative length scales  $d_y/l_y$  and  $d_z/l_y$ .

Assuming  $y_i, y'_i \ll l_y$  we substitute Eq. (6.87) back into Eq. (6.83) to get

$$\begin{aligned}
 M_{k_x \sim 0, e}^- &= \frac{\mu_0 \mu_B^2 g g_{\text{QD}}}{2\pi a_x} e^{-k_x^2 l_y^2 / 4} \sum_{y_i, \mu} \varphi_{0, e}^\mu(y_i) \\
 &\times \frac{a_y}{\sqrt{\pi} l_y} \sum_{y'_i} e^{-(y'_i - d_y^2) l_y^{-2}} \frac{1}{d_\perp^4} \left( \frac{d_z^2 - \Delta y^2}{2i \Delta y d_z} \right) \frac{+}{z}. \quad (6.88)
 \end{aligned}$$

Once again we assume that the edge mode is well localized around  $y_i \sim 0$  and therefore  $\Delta y = y'_i$ . Then the sum over  $y'_i$  can be converted to an integral and coupling acquires its final form

$$\begin{aligned}
 M_{k_x \sim 0, e}^- &= \frac{\mu_0 \mu_B^2 g g_{\text{QD}}}{\pi a_x l_y^2} e^{-k_x^2 l_y^2 / 4} \delta \mu_e \\
 &\times \left( \frac{1 + \sqrt{\pi} \text{Re}[x e^{x^2} (1 + \text{erf}(x))]}{-1 - \sqrt{\pi} \text{Re}[x e^{x^2} (1 + \text{erf}(x))]} \right) \frac{+}{z}, \quad (6.89) \\
 &\quad -i \sqrt{\pi} \text{Im}[x e^{x^2} (1 + \text{erf}(x))] \frac{-}{z}
 \end{aligned}$$

where  $x = (id_y - d_z)/l_y$  and the formula is valid for  $k_x^{-1} \gg l_y, d_y, d_z$ , if the QD covers several lattice sites i.e.,  $l_x, l_y \gg a$  and the edge mode is very well localized e.g.,  $l_y \gg \lambda$ . Furthermore we note that for  $d_z \lesssim a$  the coupling starts to depend on the lattice structure  $\mathbf{r}^\mu$  that we have neglected in the calculation above. Finally, we introduce the complex function

$$I(x) = 1 + \sqrt{\pi} x e^{x^2} [1 + \text{erf}(x)], \quad (6.90)$$

in order to simplify the formula for the dipole interaction-induced couplings  $M_{0,e}^{-+}$ ,  $M_{0,e}^{--}$ , and  $M_{0,e}^{-z}$  in Eq. (6.25) of the main text. The real and imaginary parts of  $I(x)$  determine the dependence of the coupling matrix elements  $M_{0,e}^{-}$  on the relative length scale  $x = (id_y - d_z)/l_y$ . This functional dependence is shown in Fig. 6.9.

Lastly, we show the derivation of the dipole coupling to the FM resonance mode deep in the bulk, where the magnonic eigenmodes can be labelled by the quantum numbers  $k_x$  and  $k_y$ . The final result for this coupling has been shown in Eq. (6.26) of the main text. Starting from

$$M_{k_x, k_y}^{-z} = \sum_{x_i, y_i} e^{-ik_x x_i - ik_y y_i} \sum_{i', \mu'} |\psi(\mathbf{r}'_i + \mathbf{r}^{\mu'})|^2 \times D^{-z}(\Delta x, \Delta y, d_z), \quad (6.91)$$

we separate center-of-mass and relative coordinates obtaining the Gaussian factors  $e^{-k_x^2 l_x^2/4} e^{-k_y^2 l_y^2/4}$  from the center-of-mass integrals. Considering  $k_x = 0$  in the relative coordinates we are left with the integral

$$\frac{1}{a_x a_y} \int dx dy e^{-ik_y y} D^{-z}(x, y, d_z) = \frac{\mu_0 \mu_B^2 g g_{\text{QD}}}{2 a_x a_y} e^{-|k_y| d_z} k_y, \quad (6.92)$$

which together with the Gaussian factors yield Eq. (6.26). Finally we note that the  $g$ -tensor anisotropy in the QD layer can be taken into account as in Eq. (6.44) for the dipole field, by replacing  $g_{\text{QD}} \boldsymbol{\sigma}$  with  $\hat{\mathbf{g}} \boldsymbol{\sigma}$ , where  $\hat{\mathbf{g}}$  is the  $g$ -tensor of the QD.

# Bibliography

- [1] D. Loss and D. P. DiVincenzo, “Quantum computation with quantum dots,” *Phys. Rev. A*, vol. 57, pp. 120–126, Jan 1998.
- [2] P. Kok, W. J. Munro, K. Nemoto, T. C. Ralph, J. P. Dowling, and G. J. Milburn, “Linear optical quantum computing with photonic qubits,” *Rev. Mod. Phys.*, vol. 79, pp. 135–174, Jan 2007.
- [3] X. Qiang, X. Zhou, J. Wang, C. M. Wilkes, T. Loke, S. O’Gara, L. Kling, G. D. Marshall, R. Santagati, T. C. Ralph, J. B. Wang, J. L. O’Brien, M. G. Thompson, and J. C. F. Matthews, “Large-scale silicon quantum photonics implementing arbitrary two-qubit processing,” *Nature Photonics*, vol. 12, no. 9, pp. 534–539, 2018.
- [4] C. J. Ballance, T. P. Harty, N. M. Linke, M. A. Sepiol, and D. M. Lucas, “High-fidelity quantum logic gates using trapped-ion hyperfine qubits,” *Phys. Rev. Lett.*, vol. 117, p. 060504, Aug 2016.
- [5] G. Waldherr, Y. Wang, S. Zaiser, M. Jamali, T. Schulte-Herbrüggen, H. Abe, T. Ohshima, J. Isoya, J. F. Du, P. Neumann, and J. Wrachtrup, “Quantum error correction in a solid-state hybrid spin register,” *Nature*, vol. 506, no. 7487, pp. 204–207, 2014.
- [6] F. Dolde, V. Bergholm, Y. Wang, I. Jakobi, B. Naydenov, S. Pezzagna, J. Meijer, F. Jelezko, P. Neumann, T. Schulte-Herbrüggen, J. Biamonte, and J. Wrachtrup, “High-fidelity spin entanglement using optimal control,” *Nature Communications*, vol. 5, no. 1, p. 3371, 2014.
- [7] R. Barends, J. Kelly, A. Megrant, A. Veitia, D. Sank, E. Jeffrey, T. C. White, J. Mutus, A. G. Fowler, B. Campbell, Y. Chen, Z. Chen, B. Chiaro, A. Dunsworth, C. Neill, P. O’Malley, P. Roushan, A. Vainsencher, J. Wenner, A. N. Korotkov, A. N. Cleland, and J. M. Martinis, “Superconducting quantum circuits at the surface code

- threshold for fault tolerance," *Nature*, vol. 508, no. 7497, pp. 500–503, 2014.
- [8] F. Arute, K. Arya, R. Babbush, D. Bacon, J. C. Bardin, R. Barends, R. Biswas, S. Boixo, F. G. S. L. Brandao, D. A. Buell, B. Burkett, Y. Chen, Z. Chen, B. Chiaro, R. Collins, W. Courtney, A. Dunsworth, E. Farhi, B. Foxen, A. Fowler, C. Gidney, M. Giustina, R. Graff, K. Guerin, S. Habegger, M. P. Harrigan, M. J. Hartmann, A. Ho, M. Hoffmann, T. Huang, T. S. Humble, S. V. Isakov, E. Jeffrey, Z. Jiang, D. Kafri, K. Kechedzhi, J. Kelly, P. V. Klimov, S. Knysh, A. Korotkov, F. Kostritsa, D. Landhuis, M. Lindmark, E. Lucero, D. Lyakh, S. Mandrà, J. R. McClean, M. McEwen, A. Megrant, X. Mi, K. Michielsen, M. Mohseni, J. Mutus, O. Naaman, M. Neeley, C. Neill, M. Y. Niu, E. Ostby, A. Petukhov, J. C. Platt, C. Quintana, E. G. Rieffel, P. Roushan, N. C. Rubin, D. Sank, K. J. Satzinger, V. Smelyanskiy, K. J. Sung, M. D. Trevithick, A. Vainsencher, B. Villalonga, T. White, Z. J. Yao, P. Yeh, A. Zalcman, H. Neven, and J. M. Martinis, "Quantum supremacy using a programmable superconducting processor," *Nature*, vol. 574, no. 7779, pp. 505–510, 2019.
- [9] M. Veldhorst, C. H. Yang, J. C. C. Hwang, W. Huang, J. P. Dehollain, J. T. Muhonen, S. Simmons, A. Laucht, F. E. Hudson, K. M. Itoh, A. Morello, and A. S. Dzurak, "A two-qubit logic gate in silicon," *Nature*, vol. 526, no. 7573, pp. 410–414, 2015.
- [10] T. F. Watson, S. G. J. Philips, E. Kawakami, D. R. Ward, P. Scarlino, M. Veldhorst, D. E. Savage, M. G. Lagally, M. Friesen, S. N. Copper-smith, M. A. Eriksson, and L. M. K. Vandersypen, "A programmable two-qubit quantum processor in silicon," *Nature*, vol. 555, no. 7698, pp. 633–637, 2018.
- [11] Y. He, S. K. Gorman, D. Keith, L. Kranz, J. G. Keizer, and M. Y. Simmons, "A two-qubit gate between phosphorus donor electrons in silicon," *Nature*, vol. 571, no. 7765, pp. 371–375, 2019.
- [12] N. W. Hendrickx, W. I. L. Lawrie, M. Russ, F. van Riggelen, S. L. de Snoo, R. N. Schouten, A. Sammak, G. Scappucci, and M. Veldhorst, "A four-qubit germanium quantum processor," *Nature*, vol. 591, no. 7851, pp. 580–585, 2021.

- [13] A. Alfieri, S. B. Anantharaman, H. Zhang, and D. Jariwala, “Nanomaterials for quantum information science and engineering,” *Advanced Materials*, p. 2109621, 2022.
- [14] A. G. Fowler, M. Mariantoni, J. M. Martinis, and A. N. Cleland, “Surface codes: Towards practical large-scale quantum computation,” *Phys. Rev. A*, vol. 86, p. 032324, Sep 2012.
- [15] J. R. Wootton and D. Loss, “High threshold error correction for the surface code,” *Phys. Rev. Lett.*, vol. 109, p. 160503, Oct 2012.
- [16] C. Kloeffer and D. Loss, “Prospects for spin-based quantum computing in quantum dots,” *Annual Review of Condensed Matter Physics*, vol. 4, pp. 51–81, 2022/05/29 2013.
- [17] A. Chatterjee, P. Stevenson, S. De Franceschi, A. Morello, N. P. de Leon, and F. Kuemmeth, “Semiconductor qubits in practice,” *Nature Reviews Physics*, vol. 3, no. 3, pp. 157–177, 2021.
- [18] G. Burkard, T. D. Ladd, J. M. Nichol, A. Pan, and J. R. Petta, “Semiconductor spin qubits,” *arXiv preprint arXiv:2112.08863*, 2021.
- [19] M. Veldhorst, H. G. J. Eenink, C. H. Yang, and A. S. Dzurak, “Silicon cmos architecture for a spin-based quantum computer,” *Nature Communications*, vol. 8, no. 1, p. 1766, 2017.
- [20] L. M. K. Vandersypen, H. Bluhm, J. S. Clarke, A. S. Dzurak, R. Ishihara, A. Morello, D. J. Reilly, L. R. Schreiber, and M. Veldhorst, “Interfacing spin qubits in quantum dots and donors—hot, dense, and coherent,” *npj Quantum Information*, vol. 3, no. 1, p. 34, 2017.
- [21] R. Li, L. Petit, D. P. Franke, J. P. Dehollain, J. Helsen, M. Steudtner, N. K. Thomas, Z. R. Yoscovits, K. J. Singh, S. Wehner, L. M. K. Vandersypen, J. S. Clarke, and M. Veldhorst, “A crossbar network for silicon quantum dot qubits,” *Science Advances*, vol. 4, 2022/05/29 2018.
- [22] L. Trifunovic, O. Dial, M. Trif, J. R. Wootton, R. Abebe, A. Yacoby, and D. Loss, “Long-distance spin-spin coupling via floating gates,” *Phys. Rev. X*, vol. 2, p. 011006, Jan 2012.
- [23] P. Szumniak, J. Pawłowski, S. Bednarek, and D. Loss, “Long-distance entanglement of soliton spin qubits in gated nanowires,” *Phys. Rev. B*, vol. 92, p. 035403, Jul 2015.



- [24] C. Kloeffel, M. Trif, P. Stano, and D. Loss, "Circuit QED with hole-spin qubits in Ge/Si nanowire quantum dots," *Phys. Rev. B*, vol. 88, p. 241405, Dec 2013.
- [25] S. E. Nigg, A. Fuhrer, and D. Loss, "Superconducting grid-bus surface code architecture for hole-spin qubits," *Phys. Rev. Lett.*, vol. 118, p. 147701, Apr 2017.
- [26] F. Borjans, X. G. Croot, X. Mi, M. J. Gullans, and J. R. Petta, "Resonant microwave-mediated interactions between distant electron spins," *Nature*, vol. 577, no. 7789, pp. 195–198, 2020.
- [27] P. Harvey-Collard, J. Dijkema, G. Zheng, A. Sammak, G. Scappucci, and L. M. K. Vandersypen, "Coherent spin-spin coupling mediated by virtual microwave photons," *Phys. Rev. X*, vol. 12, p. 021026, May 2022.
- [28] R. P. G. McNeil, M. Kataoka, C. J. B. Ford, C. H. W. Barnes, D. Anderson, G. A. C. Jones, I. Farrer, and D. A. Ritchie, "On-demand single-electron transfer between distant quantum dots," *Nature*, vol. 477, no. 7365, pp. 439–442, 2011.
- [29] J. M. Boter, J. P. Dehollain, J. P. G. van Dijk, T. Hensgens, R. Versluis, J. S. Clarke, M. Veldhorst, F. Sebastiano, and L. M. K. Vandersypen, "A sparse spin qubit array with integrated control electronics," in *2019 IEEE International Electron Devices Meeting (IEDM)*, 2019.
- [30] J. Yoneda, W. Huang, M. Feng, C. H. Yang, K. W. Chan, T. Tanttu, W. Gilbert, R. C. C. Leon, F. E. Hudson, K. M. Itoh, A. Morello, S. D. Bartlett, A. Laucht, A. Saraiva, and A. S. Dzurak, "Coherent spin qubit transport in silicon," *Nature Communications*, vol. 12, no. 1, p. 4114, 2021.
- [31] A. Barman, G. Gubbiotti, S. Ladak, A. O. Adeyeye, M. Krawczyk, J. Gräfe, C. Adelman, S. Cotozana, A. Naeemi, V. I. Vasyuchka, B. Hillebrands, S. A. Nikitov, H. Yu, D. Grundler, A. V. Sadovnikov, A. A. Grachev, S. E. Sheshukova, J.-Y. Duquesne, M. Marangolo, G. Csaba, W. Porod, V. E. Demidov, S. Urazhdin, S. O. Demokritov, E. Albisetti, D. Petti, R. Bertacco, H. Schultheiss, V. V. Kruglyak, V. D. Poimanov, S. Sahoo, J. Sinha, H. Yang, M. Münzenberg, T. Moriyama, S. Mizukami, P. Landeros, R. A. Gallardo, G. Carlotti, J.-V. Kim, R. L. Stamps, R. E. Camley, B. Rana, Y. Otani, W. Yu, T. Yu,

- G. E. W. Bauer, C. Back, G. S. Uhrig, O. V. Dobrovolskiy, B. Budinska, H. Qin, S. van Dijken, A. V. Chumak, A. Khitun, D. E. Nikonov, I. A. Young, B. W. Zingsem, and M. Winklhofer, "The 2021 magnonics roadmap," *Journal of Physics: Condensed Matter*, vol. 33, p. 413001, aug 2021.
- [32] L. Trifunovic, F. L. Pedrocchi, and D. Loss, "Long-distance entanglement of spin qubits via ferromagnet," *Phys. Rev. X*, vol. 3, p. 041023, Dec 2013.
- [33] D. R. Candido, G. D. Fuchs, E. Johnston-Halperin, and M. E. Flatté, "Predicted strong coupling of solid-state spins via a single magnon mode," *Materials for Quantum Technology*, vol. 1, p. 011001, dec 2020.
- [34] I. C. Skogvoll, J. Lidal, J. Danon, and A. Kamra, "Tunable anisotropic quantum rabi model via a magnon–spin-qubit ensemble," *Phys. Rev. Applied*, vol. 16, p. 064008, Dec 2021.
- [35] B. Flebus and Y. Tserkovnyak, "Entangling distant spin qubits via a magnetic domain wall," *Phys. Rev. B*, vol. 99, p. 140403, Apr 2019.
- [36] M. Fukami, D. R. Candido, D. D. Awschalom, and M. E. Flatté, "Opportunities for long-range magnon-mediated entanglement of spin qubits via on- and off-resonant coupling," *PRX Quantum*, vol. 2, p. 040314, Oct 2021.
- [37] G. Yang, C.-H. Hsu, P. Stano, J. Klinovaja, and D. Loss, "Long-distance entanglement of spin qubits via quantum hall edge states," *Phys. Rev. B*, vol. 93, p. 075301, Feb 2016.
- [38] S. J. Elman, S. D. Bartlett, and A. C. Doherty, "Long-range entanglement for spin qubits via quantum hall edge modes," *Phys. Rev. B*, vol. 96, p. 115407, Sep 2017.
- [39] G. Wagner, D. X. Nguyen, D. L. Kovrizhin, and S. H. Simon, "Driven quantum dot coupled to a fractional quantum hall edge," *Phys. Rev. B*, vol. 100, p. 245111, Dec 2019.
- [40] S. Bosco and D. P. DiVincenzo, "Transmission lines and resonators based on quantum hall plasmonics: Electromagnetic field, attenuation, and coupling to qubits," *Phys. Rev. B*, vol. 100, p. 035416, Jul 2019.

- [41] F. Meier and D. Loss, "Magnetization transport and quantized spin conductance," *Phys. Rev. Lett.*, vol. 90, p. 167204, Apr 2003.
- [42] H. Katsura, N. Nagaosa, and P. A. Lee, "Theory of the thermal hall effect in quantum magnets," *Phys. Rev. Lett.*, vol. 104, p. 066403, Feb 2010.
- [43] R. Shindou, R. Matsumoto, S. Murakami, and J.-i. Ohe, "Topological chiral magnonic edge mode in a magnonic crystal," *Phys. Rev. B*, vol. 87, p. 174427, May 2013.
- [44] R. Shindou, J.-i. Ohe, R. Matsumoto, S. Murakami, and E. Saitoh, "Chiral spin-wave edge modes in dipolar magnetic thin films," *Phys. Rev. B*, vol. 87, p. 174402, May 2013.
- [45] L. Zhang, J. Ren, J.-S. Wang, and B. Li, "Topological magnon insulator in insulating ferromagnet," *Phys. Rev. B*, vol. 87, p. 144101, Apr 2013.
- [46] A. Mook, J. Henk, and I. Mertig, "Magnon hall effect and topology in kagome lattices: A theoretical investigation," *Phys. Rev. B*, vol. 89, p. 134409, Apr 2014.
- [47] R. Shindou and J.-i. Ohe, "Magnetostatic wave analog of integer quantum hall state in patterned magnetic films," *Phys. Rev. B*, vol. 89, p. 054412, Feb 2014.
- [48] A. Mook, J. Henk, and I. Mertig, "Edge states in topological magnon insulators," *Phys. Rev. B*, vol. 90, p. 024412, Jul 2014.
- [49] K. Nakata, J. Klinovaja, and D. Loss, "Magnonic quantum hall effect and wiedemann-franz law," *Phys. Rev. B*, vol. 95, p. 125429, Mar 2017.
- [50] K. Nakata, S. K. Kim, J. Klinovaja, and D. Loss, "Magnonic topological insulators in antiferromagnets," *Phys. Rev. B*, vol. 96, p. 224414, Dec 2017.
- [51] A. Mook, B. Göbel, J. Henk, and I. Mertig, "Taking an electron-magnon duality shortcut from electron to magnon transport," *Phys. Rev. B*, vol. 97, p. 140401, Apr 2018.

- [52] A. Mook, J. Henk, and I. Mertig, "Thermal hall effect in non-collinear coplanar insulating antiferromagnets," *Phys. Rev. B*, vol. 99, p. 014427, Jan 2019.
- [53] K. A. van Hoogdalem, Y. Tserkovnyak, and D. Loss, "Magnetic texture-induced thermal hall effects," *Phys. Rev. B*, vol. 87, p. 024402, Jan 2013.
- [54] A. Roldán-Molina, A. S. Nunez, and J. Fernández-Rossier, "Topological spin waves in the atomic-scale magnetic skyrmion crystal," *New Journal of Physics*, vol. 18, p. 045015, Apr. 2016.
- [55] M. Garst, J. Waizner, and D. Grundler, "Collective spin excitations of helices and magnetic skyrmions: review and perspectives of magnonics in non-centrosymmetric magnets," *Journal of Physics D: Applied Physics*, vol. 50, p. 293002, jun 2017.
- [56] S. A. Díaz, J. Klinovaja, and D. Loss, "Topological magnons and edge states in antiferromagnetic skyrmion crystals," *Phys. Rev. Lett.*, vol. 122, p. 187203, May 2019.
- [57] S. K. Kim, K. Nakata, D. Loss, and Y. Tserkovnyak, "Tunable magnonic thermal hall effect in skyrmion crystal phases of ferrimagnets," *Phys. Rev. Lett.*, vol. 122, p. 057204, Feb 2019.
- [58] S. A. Díaz, T. Hirose, J. Klinovaja, and D. Loss, "Chiral magnonic edge states in ferromagnetic skyrmion crystals controlled by magnetic fields," *Phys. Rev. Research*, vol. 2, p. 013231, Feb 2020.
- [59] F.-Y. Li, Y.-D. Li, Y. B. Kim, L. Balents, Y. Yu, and G. Chen, "Weyl magnons in breathing pyrochlore antiferromagnets," *Nature Communications*, vol. 7, no. 1, p. 12691, 2016.
- [60] A. Mook, J. Henk, and I. Mertig, "Tunable magnon weyl points in ferromagnetic pyrochlores," *Phys. Rev. Lett.*, vol. 117, p. 157204, Oct 2016.
- [61] A. Mook, S. A. Díaz, J. Klinovaja, and D. Loss, "Chiral hinge magnons in second-order topological magnon insulators," *Phys. Rev. B*, vol. 104, p. 024406, Jul 2021.
- [62] A. Mook, J. Henk, and I. Mertig, "Magnon waveguide with nanoscale confinement constructed from topological magnon insulators," *Phys. Rev. B*, vol. 91, p. 174409, May 2015.

- [63] A. Mook, J. Henk, and I. Mertig, "Topologically nontrivial magnons at an interface of two kagome ferromagnets," *Phys. Rev. B*, vol. 91, p. 224411, Jun 2015.
- [64] B. Xu, T. Ohtsuki, and R. Shindou, "Integer quantum magnon hall plateau-plateau transition in a spin-ice model," *Phys. Rev. B*, vol. 94, p. 220403, Dec 2016.
- [65] E. Iacocca and O. Heinonen, "Topologically nontrivial magnon bands in artificial square spin ices with dzyaloshinskii-moriya interaction," *Phys. Rev. Applied*, vol. 8, p. 034015, Sep 2017.
- [66] Z.-X. Li, C. Wang, Y. Cao, and P. Yan, "Edge states in a two-dimensional honeycomb lattice of massive magnetic skyrmions," *Phys. Rev. B*, vol. 98, p. 180407, Nov 2018.
- [67] Y.-M. Li, J. Xiao, and K. Chang, "Topological magnon modes in patterned ferrimagnetic insulator thin films," *Nano Letters*, vol. 18, pp. 3032–3037, May 2018.
- [68] P. Mellado, "Intrinsic topological magnons in arrays of magnetic dipoles," *Scientific Reports*, vol. 12, no. 1, p. 1420, 2022.
- [69] R. Chisnell, J. S. Helton, D. E. Freedman, D. K. Singh, R. I. Bewley, D. G. Nocera, and Y. S. Lee, "Topological magnon bands in a kagome lattice ferromagnet," *Phys. Rev. Lett.*, vol. 115, p. 147201, Sep 2015.
- [70] L. Chen, J.-H. Chung, B. Gao, T. Chen, M. B. Stone, A. I. Kolesnikov, Q. Huang, and P. Dai, "Topological spin excitations in honeycomb ferromagnet  $\text{CrI}_3$ ," *Phys. Rev. X*, vol. 8, p. 041028, Nov 2018.
- [71] F. Zhu, L. Zhang, X. Wang, F. J. dos Santos, J. Song, T. Mueller, K. Schmalzl, W. F. Schmidt, A. Ivanov, J. T. Park, J. Xu, J. Ma, S. Lounis, S. Blügel, Y. Mokrousov, Y. Su, and T. Brückel, "Topological magnon insulators in two-dimensional van der waals ferromagnets  $\text{CrSiTe}_3$  and  $\text{CrGeTe}_3$ : Toward intrinsic gap-tunability," *Science Advances*, vol. 7, no. 37, 2021.
- [72] M. Malki and G. S. Uhrig, "Topological magnetic excitations," *Europhysics Letters*, vol. 132, p. 20003, oct 2020.
- [73] Z.-X. Li, Y. Cao, and P. Yan, "Topological insulators and semimetals in classical magnetic systems," *Physics Reports*, vol. 915, pp. 1–64, jun 2021.

- [74] P. A. McClarty, "Topological magnons: A review," *Annual Review of Condensed Matter Physics*, vol. 13, pp. 171–190, 2022/05/29 2022.
- [75] X. S. Wang and X. R. Wang, "Topological magnonics," *Journal of Applied Physics*, vol. 129, p. 151101, apr 2021.
- [76] I. Dzyaloshinsky, "A thermodynamic theory of "weak" ferromagnetism of antiferromagnetics," *Journal of Physics and Chemistry of Solids*, vol. 4, pp. 241–255, Jan. 1958.
- [77] T. Moriya, "Anisotropic superexchange interaction and weak ferromagnetism," *Phys. Rev.*, vol. 120, pp. 91–98, Oct 1960.
- [78] F. D. M. Haldane, "Model for a quantum Hall effect without landau levels: Condensed-matter realization of the "parity anomaly"," *Phys. Rev. Lett.*, vol. 61, pp. 2015–2018, Oct 1988.
- [79] S. A. Owerre, "A first theoretical realization of honeycomb topological magnon insulator," *J. Phys.: Condens. Matter*, vol. 28, p. 386001, Jul 2016.
- [80] T. Holstein and H. Primakoff, "Field dependence of the intrinsic domain magnetization of a ferromagnet," *Phys. Rev.*, vol. 58, pp. 1098–1113, Dec 1940.
- [81] P. A. Pantaleón and Y. Xian, "Analytical study of the edge states in the bosonic haldane model," *Journal of Physics: Condensed Matter*, vol. 29, no. 29, p. 295701, 2017.
- [82] Y. Hatsugai, "Chern number and edge states in the integer quantum Hall effect," *Phys. Rev. Lett.*, vol. 71, pp. 3697–3700, Nov. 1993.
- [83] Y. Hatsugai, "Edge states in the integer quantum Hall effect and the Riemann surface of the Bloch function," *Phys. Rev. B*, vol. 48, pp. 11851–11862, Oct. 1993.
- [84] S. S. Pershoguba, S. Banerjee, J. C. Lashley, J. Park, H. Ågren, G. Aeppli, and A. V. Balatsky, "Dirac magnons in honeycomb ferromagnets," *Phys. Rev. X*, vol. 8, p. 011010, Jan 2018.
- [85] P. A. Pantaleón and Y. Xian, "Effects of edge on-site potential in a honeycomb topological magnon insulator," *Journal of the Physical Society of Japan*, vol. 87, p. 064005, June 2018.

- [86] P. A. Pantaleón and Y. Xian, "Edge states in a ferromagnetic honeycomb lattice with armchair boundaries," *Physica B: Condensed Matter*, vol. 530, pp. 191–194, 2018.
- [87] A. D. Karenowska, A. V. Chumak, A. A. Serga, and B. Hillebrands, *Magnon Spintronics*, pp. 1505–1549. Dordrecht: Springer Netherlands, 2016.
- [88] A. Prabhakar and D. D. Stancil, *Spin waves: Theory and applications*, vol. 5. Springer, 2009.
- [89] C. Dubs, O. Surzhenko, R. Linke, A. Danilewsky, U. Brückner, and J. Dellith, "Sub-micrometer yttrium iron garnet LPE films with low ferromagnetic resonance losses," *Journal of Physics D: Applied Physics*, vol. 50, p. 204005, apr 2017.
- [90] V. N. Golovach, M. Borhani, and D. Loss, "Electric-dipole-induced spin resonance in quantum dots," *Phys. Rev. B*, vol. 74, p. 165319, Oct 2006.
- [91] K. C. Nowack, F. H. L. Koppens, Y. V. Nazarov, and L. M. K. Vandersypen, "Coherent control of a single electron spin with electric fields," *Science*, vol. 318, pp. 1430–1433, 2022/05/29 2007.
- [92] S. Nadj-Perge, S. M. Frolov, E. P. A. M. Bakkers, and L. P. Kouwenhoven, "Spin-orbit qubit in a semiconductor nanowire," *Nature*, vol. 468, no. 7327, pp. 1084–1087, 2010.
- [93] M. D. Schroer, K. D. Petersson, M. Jung, and J. R. Petta, "Field tuning the  $g$  factor in inas nanowire double quantum dots," *Phys. Rev. Lett.*, vol. 107, p. 176811, Oct 2011.
- [94] S. Bravyi, D. P. DiVincenzo, and D. Loss, "Schrieffer–Wolff transformation for quantum many-body systems," *Annals of Physics*, vol. 326, pp. 2793–2826, oct 2011.
- [95] Y. Makhlin, G. Schön, and A. Shnirman, "Dissipation in josephson qubits," *New Directions in Mesoscopic Physics (Towards Nanoscience)*, pp. 197–224, 2003.
- [96] J. F. Poyatos, J. I. Cirac, and P. Zoller, "Complete characterization of a quantum process: The two-bit quantum gate," *Phys. Rev. Lett.*, vol. 78, pp. 390–393, Jan 1997.

- [97] G. Lindblad, "On the generators of quantum dynamical semi-groups," *Communications in Mathematical Physics*, vol. 48, no. 2, pp. 119–130, 1976.
- [98] A. Blais, A. L. Grimsmo, S. M. Girvin, and A. Wallraff, "Circuit quantum electrodynamics," *Rev. Mod. Phys.*, vol. 93, p. 025005, May 2021.
- [99] S. K. Kim and Y. Tserkovnyak, "Chiral edge mode in the coupled dynamics of magnetic solitons in a honeycomb lattice," *Phys. Rev. Lett.*, vol. 119, p. 077204, Aug 2017.



# Acknowledgments

I would like to express my gratitude to Prof. Daniel Loss for all the discussions and support of the past four years. I consider myself very fortunate, having had the opportunity to work with him, to learn from him not only through the projects we had together but also during research seminars and discussions. After I finished my masters one of my teachers said, that I will have lot of opportunity to learn about physics with Daniel. After almost four years in his research group, I see how right he was.

I first met Prof. Oded Zilberberg during a QSIT meeting in Arosa, where he explained to me one of his recent works at a poster session. I really enjoyed that discussion and therefore I was delighted that he agreed to review my thesis and join the doctoral committee on the defense. I would like to thank my second supervisor Prof. Jelena Klinovaja as well, for the additional support.

During my PhD I had the opportunity to work with exceptional researchers and also great friends, Christoph Kloeffer, Dmitry Miserev, Stefano Bosco, Marko Rančić, Alexander Mook, Jelena Klinovaja, Flavio Ronetti, and Tamás Haidekker Galambos. I am also very grateful for the experimental groups of Dominik Zumbühl, Richard Warburton and Andreas Kuhlmann. In particular Floris Braakman, Florian Froning, Leon Camenzind, Raffael Eggli, and Simon Geyer. I am also happy getting to know Jonas Amport and Linus Arnold, not only over teaching but also through discussions about their master theses.

In the last few years Basel has become a second home to me, for which I am very thankful for every member of the research group: Marko, Sebastian, Alex, Peng, Mónica, Pierre, Ferdinand, Daniel M., Pawel, Marcel, Christina, Silas, Maria, Tomoki, Yuhao, Chris, Yanick, Katharina, Christoph A., Christoph K., Henry, Valera, Stefano, Aleks, Denis, James, Viktor, Pavel, Vardan, Manisha, Flavio, Kirill, Aksel, Zhe, Vardan, Renato, Melina, Dima, Even, Tamás, Richard, Oindrila, Olesia, Joel, Jelena, and Daniel.

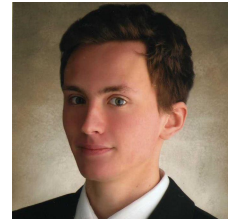
I would like to thank Rafael Eggli for the enlightening discussion on charge readout, Christoph Adelsberger and Daniel Miller for reading and giving feedback on the first version of this thesis.

Furthermore, I am thankful to my former supervisors András Pályi and János Asbóth as well as my friends from the Eötvös University: Ádam, Tamás, Zsolt, Áron, Dani, Döme, Milán, and Aurél.

Finally, I would like to say thank you to my friends and family, especially my girlfriend Eszti who accompanied and supported me throughout my doctoral studies.

# Curriculum Vitae

## Bence Hetényi



University of Basel  
Department of Physics  
Klingelbergstrasse 82,  
CH-4056 Basel, Switzerland

Email: bence.hetenyi@gmail.com  
Phone: +41 79 963 3604  
Skype: hetenyibence

### Education

#### **University of Basel (Basel, Switzerland)**

- PhD student, Condensed Matter Physics, 2018 -
- Condensed Matter Theory & Quantum Computing Group
- Supervisor: Prof. Daniel Loss

#### **Eötvös Lóránd University (Budapest, Hungary)**

- MSc, Condensed Matter Physics, 2016 - 2018
  - Thesis: 'Quantumbits in silicon nanostructures'
- BSc, Physics, 2013 - 2016
  - Thesis: 'Optomechanical multistability in elastic structures'

### Teaching activity

- Master student co-supervision (Jonas Amport, Yanik Linus Arnold)
- Quantum mechanics, Spin based quantum information science, Quantum computation
- Golden chalk (teaching award): 3rd place, 2019-spring; 2nd place 2019-fall

### Languages

- english (advanced / C1)
- german (intermediate / B2)
- hungarian (native language)

### IT skills

Python, Wolfram Mathematica, C,  
COMSOL Multiphysics, L<sup>A</sup>T<sub>E</sub>X, Adobe Photoshop

### Publications

- B. Hetényi, A. Mook, J. Klinovaja, and D. Loss, arXiv:2207.01264 (2022)
- B. Hetényi, S. Bosco, and D. Loss, arXiv:2205.02582 (2022)
- T. Haidekker Galambos, F. Ronetti, B. Hetényi, D. Loss, J. Klinovaja, arXiv:2203.05894 (2022)
- S. Bosco, B. Hetényi, and D. Loss, PRX Quantum **2**, 010348 (2021)
- F.N.M. Froning, M.J. Rančić, B. Hetényi, S. Bosco, M.K. Rehmann, A. Li, E.P.A.M. Bakkers, F.A. Zwanenburg, D. Loss, D.M. Zumbühl, F.R. Braakman, Phys. Rev. Research **3**, 013081 (2021)
- B. Hetényi, C. Kloeffer, and D. Loss, Phys. Rev. Research **2**, 033036 (2020)
- B. Hetényi, P. Boross, and A. Pályi, Phys. Rev. B **100**, 115435 (2019)